Feasibility Studies on Large-Current Capacity HTS Conductors for Fusion Magnets

Gourab Bansal

Department of Fusion Science
School of Physical Sciences
The Graduate University for Advanced Studies

2008

Dedicated to my wife, Sonika and my daughter, Vidhi

Abstract

The feasibility study of large-current capacity High Temperature Superconducting (HTS) conductors suitable for fusion reactor magnets has been carried out in this thesis.

Presently, well-established low-temperature superconductors (LTS), such as NbTi and Nb_3Sn, operating at ~ 4 K are being used for producing high magnetic fields in fusion devices like Tore-Supra, LHD, EAST, SST-1, KSTAR, W7-X and are being planned to be used in near future machines such as JT-60SA and ITER. However, the LTS conductors are prone to quench due to the lower specific heats of the materials and therefore lower stability margin at 4 K. The stability margin of LTS conductors further degrades due to non-uniform current distribution among strands, such as observed in Demo Poloidal Coils (DPC). The future fusion energy reactors such as LHD-type force-free helical reactor (FFHR) cannot allow their huge magnets to quench and therefore there is a need to develop high stability conductors to have safer operations. Compared to LTS, HTS possess rather higher stability as they can be operated at elevated temperatures above 20 K, which assures higher specific heats and therefore lower risk of quench. In addition to high stability, high critical current density is expected for HTS materials in high magnetic fields even at elevated temperatures. Moreover, lower refrigeration power is required due to elevated temperature operations.

Owing to the above-mentioned advantages, HTS conductors are considered to be a potential candidate for future fusion energy reactor magnets. However, HTS conductors are presently available only in the wire and tape forms and no large-current (> 10 kA) capacity HTS conductor that can be used for magnet windings (not for current-leads) has been developed yet. Toward the development of large-current capacity HTS conductors, feasibility of large-current capacity HTS conductors suitable for fusion energy reactors is studied in this thesis. We hereby make a new proposal of simple stacking of HTS wires in the conductor form and the focus of this research is on the cryogenic stability of this type of conductors. Due to simple stacking of HTS wires, it is probable to observe inductance mismatching among HTS wires and therefore non-uniform current distribution is supposed to be formed in the conductor. As mentioned above, non-uniform current

distribution is a serious problem for LTS conductors especially with insulated strands. Even though we are proposing HTS conductors, suitable for DC magnets, without insulation between wires to assure good current re-distribution, it is considered to be an important task to investigate the effect of non-uniform current distribution on the conductor stability. In this respect, as the artificial introduction of non-uniform current distribution is rather easy in cable-in-conduit conductors (CICC), the present research was initiated by critically examining the stability of the non-insulated strand LTS CICC with non-uniform current distribution in the conductor. Secondly, we developed a method to examine the effect of non-uniform current distribution on HTS conductors rather directly by utilizing the LTS/HTS hybrid conductor concept. Thirdly, we fabricated 10 kA-class HTS conductors and tested them extensively. Finally, we carried out the HTS conductor design study for the helical coils of FFHR.

We carried out stability margin measurement experiments on a full-scale CICC with non-insulated NbTi/Cu strands by artificially introducing non-uniform current distribution in a controlled way. In our experiments, we found that the stability margin of the conductor reduced significantly due to the non-uniform current distribution, which indicates that non-uniform current distribution is a problem even for non-insulated strand conductors where current re-distribution can take place rather easily. We found that with the non-uniform current distribution, the stability margin reduced by more than one order of magnitude, especially in the transition region between the well-cooled and ill-cooled regions. The limiting current, which separates the well-cooled and ill-cooled regions, was found to be shifted toward lower current values due to non-uniform current distribution in the conductor. We have carried out numerical calculations to simulate the experimental data of stability margin with uniform and non-uniform current distributions and found good consistency between experimental and calculated results.

We carried out ramp rate limitation (RRL) experiments as well and found that the quench current reduced due to non-uniform current distribution for faster ramp rates ranging from 100 A/s to 800 A/s. Hence, our experiments of stability margin measurements with non-uniform current distribution on non-insulated strand CICC clearly suggest that non-uniform current distribution is an important factor to be

considered for large-current capacity LTS conductors. Therefore, the effect of non-uniform current distribution on the stability of HTS conductors should also be examined even though the stability of HTS conductors is supposed to be quite high compared to LTS conductors.

Then, we proposed a unique and innovative experimental method to examine the effect of non-uniform current distribution on the stability of HTS conductors. We prepared an LTS/HTS hybrid conductor, which was the world's first superconducting conductor using both LTS and HTS together. In a hybrid conductor, layers of Bi-2223/Ag HTS tapes were soldered to form a stabilizer for the LTS wires. Once a normal-zone appears in the LTS wires, the transport current transfers into the HTS part from one layer to another and so on. This is supposed to be a case of extreme non-uniform current distribution in the HTS part. In our experiments at 4.2 K and 7 T bias field, we found that even with this extreme non-uniform current distribution, the HTS part was stable and the conductor did not quench fully even though the transport current was close to the critical current of the HTS part in the hybrid conductor. These experimental results suggest that non-uniform current distribution may not be a problem for the stability of HTS conductors even though many of the HTS wires carry the currents equal to critical currents. However, examination of this problem by direct experiments on real full HTS conductors might be an important future task.

The experiments on LTS/HTS hybrid conductors confirmed that non-uniform current distribution may not be a problem for HTS conductors and therefore the freedom of conductor configuration can be increased for HTS conductors. Thus, we proposed a large-current capacity HTS conductors consisting of simple stacks of HTS wires, which are presently available in tape forms. This is regarded as a new but a controversial proposal, since simple stacking of superconducting strands without transpositions has never been allowed for LTS conductors. As a first step, we fabricated a 10 kA-class (at 20 K, 8 T) HTS conductor using Bi-2223/Ag tapes. The conductor was prepared by stacking HTS tapes in two bundles and then encasing them inside a copper jacket. The conductor size is 12 mm (width) × 7.5 mm (thickness). An innovative technique was

applied to test the HTS conductor at different temperatures from 4.2 K to 30 K. Thin stainless steel heaters were attached to the conductor surface to elevate the temperature and then conductor was insulated by epoxy and GFRP to obtain similar conduction cooling conditions as in future magnets made of HTS conductors. We measured the critical currents of the HTS conductor at 4.2 K, 10 K, 20 K, and 30 K and the results were found to be close to our expectations. We calculated the critical currents of the HTS conductor at different temperatures and a bias field of 8 T (parallel to the ab-plane of the HTS tapes) by taking account of the self-field generated by the transport current in the conductors. The calculated results are found to be in good agreement with the measured critical current, which shows no degradation in HTS conductors due to the handling during the fabrication process.

The stability margin of the HTS conductor was also measured at different temperatures. The conductor was found to be highly stable, as it was expected from the high heat capacity of the conductor at elevated temperatures. The stability test results suggest that HTS conductors possess much higher stability margin compared to their LTS counterparts and therefore are the potential candidates for stable operations of future fusion energy reactors.

We also carried out ramp rate limitation (RRL) tests on the HTS conductors. The results are very encouraging. The conductor did not show any ramp rate limitation behavior even at 1.5 kA/s ramp rate, which was completely different from the observations in the CICC experiment described above. For HTS conductors, the critical currents were found to increase by increasing the ramp rate. This was because the conductor temperature showed lower increase due to the shorter duration of joule heating associated with the appearance of flux-flow resistance. Hence, our preliminary results suggest that RRL may not be a problem for HTS conductors unlike the LTS counterparts. It is considered that the increase of stability also gives this improvement. As our near future tasks, we will test a 10 kA-class HTS conductor using YBCO tapes. The conductor fabrication and sample development work is underway.

Looking at the encouraging results of 10 kA-class HTS conductors, we have started the HTS conductor design as an option for the helical coils of the LHD-type fusion

energy reactor FFHR. We have carried out several studies such as structural, quench detection and protection on the proposed 100 kA-class HTS conductors using YBCO tapes. We have considered aluminum-alloy or stainless-steel as the jacket material options for the HTS conductors. It is found that stainless-steel jacket is more suitable due to its higher strength and larger heat capacity. Our preliminary results suggest that HTS conductors might be promising candidates for the helical coils of FFHR. However, when considering the application of HTS conductors for fusion magnets, many difficult issues, such as the error magnetic fields generated by superconducting shielding currents in HTS tapes and how to make robust coil structures using fragile HTS materials, should be solved. One also has to optimize the cooling method for HTS coils. At the same time, owing to the higher stability of HTS conductors, a new design philosophy for HTS coils should be established unlike the LTS coils, which are primarily based on the cryogenic stability. In these connections, an innovative idea of having rather thin layers of HTS wires within the conductor is also proposed in the present study. By having such a configuration, the bending strain can be minimized to be ~0.05% level so that the winding of coils using these conductors is feasible. Moreover, the problem of error magnetic field generated by shielding currents in the HTS tapes and/or by the occurrence of non-uniform current distribution among tapes due to inductance mismatching is considered to be equivalent as the shift of current centers in the conductors. If the HTS part can be confined in thin layers, the current shift is supposed to be in an acceptable level within the tolerance of winding accuracy.

As a conclusion, through this thesis, it has been found that considering HTS conductors to be used for fusion energy reactor magnets is feasible though a number of issues associated with their development should be solved one by one.

Acknowledgements

It is my great pleasure to acknowledge all the people who helped and encouraged me to complete my thesis research. It would have not been possible to complete my thesis without the support and nice hospitality from the staff at the Graduate University for Advanced Studies (Sokendai) and National Institute for Fusion Science (NIFS).

I am deeply grateful to Dr. Nagato Yanagi who gave me an opportunity to study at Sokendai/NIFS and patiently guided me throughout my thesis research.

I am greatly indebted to Prof. Osamu Motojima for having given me an opportunity to study at the Department of Fusion Science at Sokendai/NIFS. I am also thankful to Prof. Akio Komori, Prof. Noriyoshi Nakajima, Prof. Shoichi Okamura and many other staff at the department for having assisted me to complete my research.

Particularly, I am deeply grateful to Prof. Akio Sagara and Prof. Toshiyuki Mito for giving me a great help by suggesting many modifications to improve my thesis. They suggested us to stress on our own idea of using simple-stacked configuration of HTS tapes for the large-current application, which really made an impact and boosted our confidence. I give my wholehearted thanks to Prof. Yuichi Ogawa for his fruitful comments, as well as for letting me learn about levitated fusion machines using HTS coils. I also appreciate the useful comments given by Prof. Yasuyuki Shirai.

I would like to give my many thanks to Dr. Kazutaka Seo for his steadfast teaching, informative suggestions and kind helps to me, especially to conduct the experiments on SST-1 CICC and to improve my publications. A number of fruitful suggestions and continuous encouragement given by Prof. Kazuya Takahata are highly appreciated. I thank Dr. Tsutomu Hemmi for his continuous help and support, especially for my experiments and numerical calculations using ANSYS and FEM analysis.

I would like to thank many other staff at NIFS, Prof. Shinsaku Imagawa, Prof. Arata Nishimura, Prof. Takeo Muroga, Prof. Motoyasu Sato, Prof. Yasuji Kozaki, Dr. Shuichi Yamada, Dr. Hirotaka Chikaraishi, Dr. Ryuji Maekawa, Dr. Hitoshi Tamura, Dr. Akifumi Iwamoto, Dr. Shinji Hamaguchi, Dr. Tetsuhiro Obana, Dr. Yoshimitsu Hishinuma and Mr. Sadatomo Moriuchi for giving me many good suggestions and encouragement to improve my experiments, presentations, and thesis.

I am grateful to Ms. Shihomi Kato for taking care of my administrative and personal documents. I would like to give my thanks to our lab staff, Ms. Ai Okada, Mr. Hiroshi Kitano and Mr. Kenji Ueda for their kind helps during my experiments. Special thanks are given to administration staff Mr. Satoshi Ido, Ms. Satona Urushihara, Ms. Kazuko Mizuno, Ms. Kyoko Shimazaki and others for their kind support and help. I am thankful to Ms. Naho Hayashi who taught me Japanese language, which helped me a lot in my daily life and to learn Japanese culture. I would like to give my special thanks to Ms. Emiko Yanagi for her kind supports to my family throughout the last three years.

Special thanks are given to Dr. Teruo Izumi, Dr. Yuh Shiohara, Dr. Yutaka Yamada and Dr. Takashi Saitoh for having provided the YBCO and GdBCO HTS tapes.

I am deeply indebted to the financial support provided by Kakuyugo-Kagaku-Kenkyu-kai, Gifu Prefecture, and Japan Society for the Promotion of Science.

I am deeply grateful to Institute for Plasma Research (IPR) in India and Director-General Prof. Predhiman K. Kaw for granting me a three-year leave to complete my Ph.D. I am grateful to my project leader Prof. Yogesh C. Saxena for his support and encouragement. I would also like to give my thanks to all of my friends for their friendship and support, especially Mr. Malay Chowdhuri, Mr. Dashrath Sonara, Mr. Akhilesh Singh, Mr. Ashu Sharma, Dr. Mainak Bandyopadhyay, Dr. Biswanath Sarkar, Mr. Amit Srivastava, Mr. Ananta K. Sahu, Mr. Ravi Duggar, and Dr. Vipul Tanna.

I am indebted to my members in India for their moral support to me and to my family, especially my parents, my elder brothers Mr. Sanjay Kumar, Mr. Ajay Kumar, Mr. Rajkumar and my younger sisters and brother Ms. Rachna Mittal, Ms. Ritu Garg, Mr. Manish, and my parents in law.

I sincerely dedicate this thesis to my beloved wife Sonika and my sweet daughter Vidhi for their unconditional love and support to me.

Contents

Chapter 1

Introduction

1.1 Low temperature superconductors (LTS)

Low temperature superconductors (LTS) refer to those practical superconductors, which are generally operated at around 4 K using liquid or supercritical helium. These superconductors are generally Nb based, such as NbTi, Nb_3Sn, and recently developed Nb_3Al [1.1, 1.2, 1.3]. Another superconductor V_3Ga, which comes under the LTS category, is also being developed [1.4]. This superconductor is supposed to be a promising candidate for fusion machines as it has less radioactivation by neutron irradiations compared to others in the LTS category. The below table 1.1 gives the critical properties of some of the well-known low temperature superconductors. The relationship between the critical field and critical temperatures are shown in Fig. 1.1 for several superconductors [1.2].

Table 1.1: Critical properties of some LTS conductors

Superconductor	**T_c (K) at B = 0 T**	**B_{c2} (T) at T = 0 K**	**Typical critical current density, J_c (A/mm^2), superconductor area only**
NbTi	9.2	14.5	~2000 (4.2 K, 5 T)
Nb_3Sn	18.3	27.9	~1200 (4.2 K, 10 T)
Nb_3Al	18.02	~ 32	~ 1500 (4.2 K, 12 T)
V_3Ga	16.5	~ 26	~ 1000 (4.2 K, 10 T)

NbTi and Nb_3Sn superconductors are the most widely used materials in many applications. NbTi can generally be used below 10 T field, whereas Nb_3Sn can be used up to about 20 T without significant degradation in critical current density. Nb_3Al and V_3Ga superconductors are still in the developing phase and have shown good prospects. NbTi is the most ductile material out of all the LTS superconductors. It is almost insensitive to the bending, compressive and tensile strains. On the other hand, A15 materials (Nb_3Sn, Nb_3Al, V_3Ga) are brittle and sensitive to strain. Their critical current properties degrade with strain as shown in Fig. 1.2 [1.3].

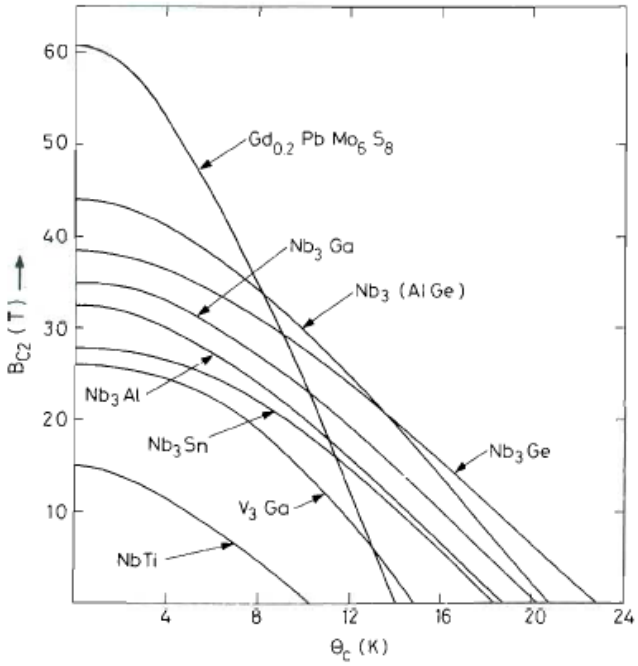

Fig. 1.1: Relationship between critical field and critical temperatures of several low temperature superconductors [1.2].

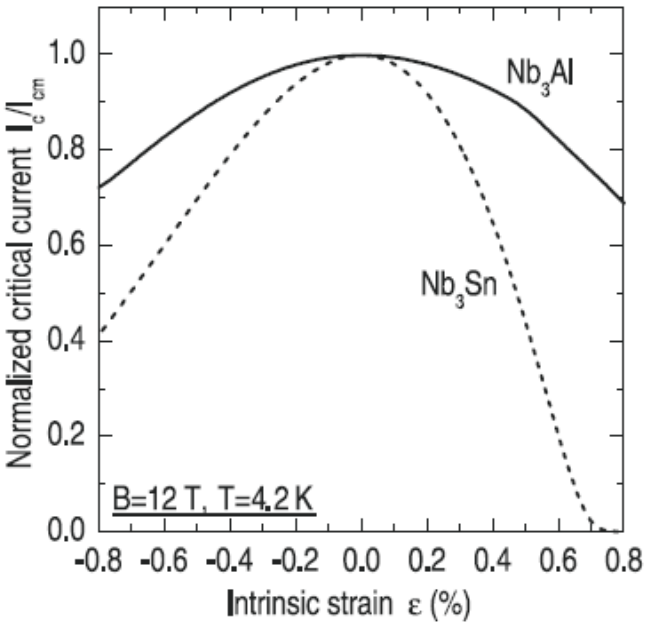

Fig. 1.2: Strain dependence of Nb_3Sn and Nb_3Al on critical currents [1.3].

The typical cross-sectional views of multifilamentary practical NbTi and Nb_3Sn strands are shown in Fig. 1.3. The detailed schematic of the major stages of a process route for the fabrication of multifilamentary NbTi composite strands can be found in reference [1.2]. The starting materials are a cylindrical billet of NbTi alloy and an extrusion can of high-purity copper. After chemical cleaning, these components are assembled and the interior of the extrusion can is evacuated and sealed. After preheating to ~550^0C, the billet is extruded to reduce its size by a factor of ~20. Billet sizes range from 100 – 250 mm diameter and 15 – 200 kg in weight. Cold drawing is used to convert the extruded bar into a hexagonal rod, which is then cut to length and chemically cleaned. Depending on the number of filaments, the appropriate number of hexagonal rods is then stacked in another extrusion can, which is again evacuated, sealed and extruded. The extruded bar is then drawn down to strand size. Precipitation heat treatments are applied at the appropriate sizes to produce optimum J_c. Just before the final size, the wire is twisted to decouple the filaments. A final drawing pass serves to set the twist in place and a low temperature heat treatment is used to anneal the copper. Fig. 1.3(a) shows the cross-section of a 61-filament NbTi strand.

Unlike NbTi alloy, Nb_3Sn is an intermetallic compound with a precise chemical composition Nb_3Sn. The crystallographic structure of Nb_3Sn is known as A15 or Cr_3Si type. The mechanical properties of Nb_3Sn pose serious problems in the fabrication of practical conductors. Nb_3Sn is hard and brittle and bulk samples of it will fracture at elongations of only 0.3 %. Conventional fabrication techniques cannot be used and therefore it was necessary to devise new techniques for the production of practical Nb_3Sn conductors. Filamentary composites of Nb_3Sn first became possible with the invention of the bronze process for producing Nb_3Sn via a solid-state reaction [1.2]. Filaments of pure Nb are drawn down in a matrix of bronze using a process very similar to that for NbTi discussed before. Multiple stacking procedure is often used for Nb_3Sn, in which rods of Nb are put into the holes drilled in a bronze cylinder which may then be extruded and drawn or simply drawn directly. After reaching its final size, heat treatment is done, typically for 1 – 10 days at about 700 ^{o}C. During this heat treatment, tin diffuses through the bronze and reacts with niobium. Since all constituents remain in solid state, the filamentary structure is perfectly preserved. Pure copper is usually added to bronze composites in order to promote dynamic stability and protection from quenching.

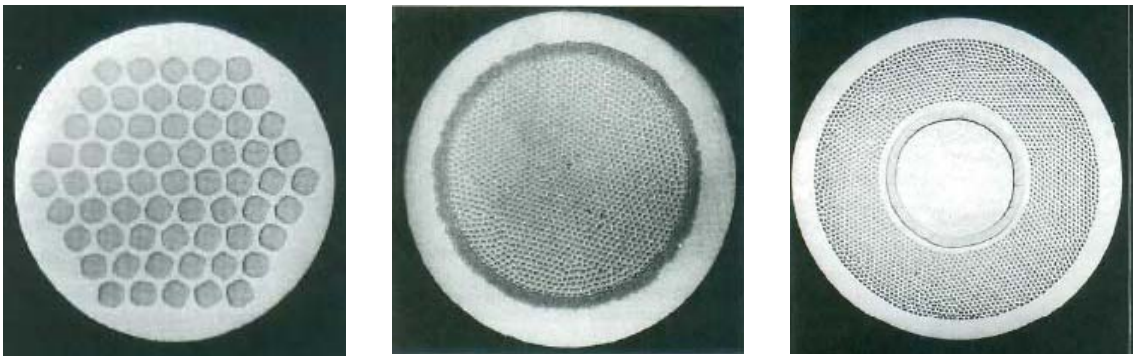

Fig. 1.3: Cross-sectional views of (a) 61 filaments NbTi strand; (b) Nb_3Sn strand with copper jacket; (c) Nb_3Sn strand with copper at the core [1.2].

Figure 1.3(b) shows an Nb_3Sn composite in which copper has been added in the form of a jacket. Alternatively, copper cores may also be used as shown in Fig. 1.3(c). In either case, copper must be protected from contamination by tin, which would otherwise diffuse into it during heat treatment and spoil its high conductivity. A diffusion barrier, usually, tantalum or niobium, is therefore, interposed between copper and bronze.

There are several other methods to produce Nb_3Sn strands such as external tin diffusion, internal tin diffusion, In Situ and powder metallurgical processes. The internal tin diffusion method is economic and reliable compared to other methods. In this method, composites of elementary Cu, Nb, and Sn are co-reduced up to the final size and then heat treated to produce Nb_3Sn [1.5]. As a consequence of good ductility of these constituents before reaction, the composite wire can be drawn to final size without any intermediate annealing. In addition, it is also possible to introduce higher tin content into the matrix, which consequently produces larger volume of Nb_3Sn and then larger critical current strands compared to bronze processed strands. Figure 1.4 shows the cross-section of an internal tin Nb_3Sn strand.

Hundreds or thousands of such small diameter (typically 1 mm) strands are then combines and twisted to form a large-current capacity superconducting conductor. Generally, these large-current capacity conductors are divided into two categories, normally, “cable-in-conduit conductors” and “composite type conductors”. Figure 1.5 shows the examples of both types of conductors. In cable-in-conduit conductors, superconducting strands are twisted in multiple stages and then housed in a high-strength material conduit such as stainless steel [1.6]. The coolant (generally supercritical helium) flows in the void area inside the conduit to cool the superconducting strands and the method is called force flow cooling. Sometimes, an additional cooling channel at the center of the conductor is also introduced to enhance the cooling of the conductor as shown in Fig. 1.5 (b) [1.7].

In case of composite type conductors, the superconducting strands are twisted and soldered together. The conductor is extra-stabilized by low resistivity materials such as pure aluminum [1.8]. The conductor is cooled by surrounded liquid helium and the method is called bath-cooling. Cable-in-conduit conductors provide higher rigidity and higher stability (due to large cooling perimeter) to the magnets and therefore most widely

used. The ITER will be using NbTi and Nb_3Sn cable-in-conduit conductors for its superconducting magnets. Fig. 1.5 (a) shows the LHD poloidal field coil NbTi conductor whereas Fig. 1.5 (b) shows the ITER central solenoid Nb_3Sn conductor. Figure 1.5 (c) shows the LHD helical coil conductor.

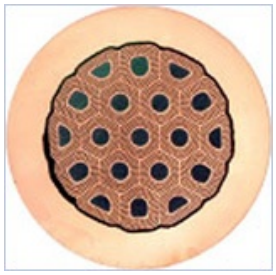

Fig. 1.4: Cross-section of an internal tin Nb_3Sn strand. The central black portion is tin, which diffuses into Nb and produces Nb_3Sn during heat treatment.

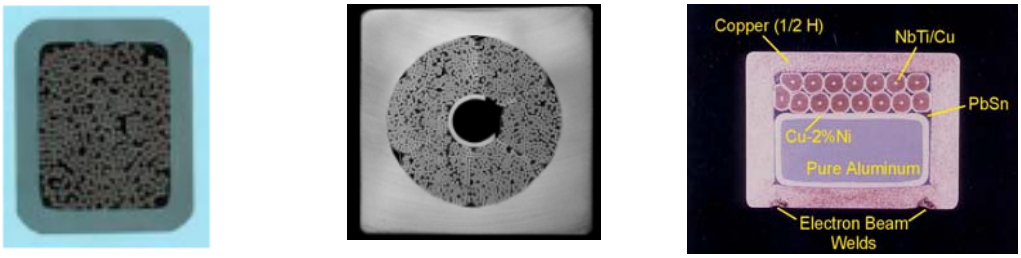

(a) (b) (c)

Fig. 1.5: Cross-sectional views of (a) typical cable-in-conduit conductor [1.6]; (b) cable-in-conduit conductor with central cooling channel [1.7]; (c) composite type conductor [1.8].

1.2 High temperature superconductors (HTS)

The modern age of the so-called high-T_c superconductors began in April 1986 with a report by Karl A. Muller and Johannes G. Bednortz of superconductivity in lanthanum-barium copper oxide at 30 K [1.9]. This led to the discovery of $La_{2-x}Sr_xCuO_4$ with T_c of ~ 34 K and then many other high temperature superconductors, which are basically, copper oxide ceramics with perovskite lattice structures. There are several ceramics, based on copper oxide, which remain superconducting near ~100 K. For example, yttrium barium copper oxide (YBCO) has been found to be superconducting up to 92 K [1.10]. YBCO was the first superconductor with T_c higher than boiling temperature of liquid nitrogen and then came bismuth strontium calcium copper oxides (BSCCO) with even higher critical temperatures up to 110 K [1.11]. The high temperature superconductor with highest known T_c of 133 K is mercury barium calcium copper oxide (HBCCO).

The commercially available superconductors based on BSCCO are known as first generation high-T_c superconductors. Two members of BSCCO family commonly known as Bi-2223 with T_c = 110 K and Bi-2212 with T_c = 85 K are already available in long lengths and are being used in many applications such as maglev, transmission cables, fault current limiters, current leads etc. The Bi-2223 is available in tape form whereas Bi-2212 is available in both round wire and tape forms [1.12, 1.13]. The cross-sectional views of these superconductors are shown in Fig. 1.6. During last few years, the critical current properties of Bi-2223 superconductors have improved tremendously and therefore are being used widely in many applications compared to Bi-2212. The Bi-2223 superconducting tapes are fabricated by the so-called powder in tube (PIT) method [1.14]. The schematic of BSCCO wire fabrication method is shown in Fig. 1.7. In this method, first the oxides of key elements are treated at high temperature to make the powder of the superconducting compound. The powder is then packed into a tube of silver. The wire making process of drawing, rolling, or swaging follows, leaving it into a final shape of a tape or round wire. To restore the ceramic core to the superconducting state, it is heat treated further at 800 – 900 ^oC. Finally, the wire is annealed in oxygen very slowly (typically 100 hours) in order to allow oxygen atoms to slowly recover their proper positions in the crystal lattice. Due to the high content of silver in Bi-2223 tapes and

labor intensive manufacturing processes, these superconductors are quite expensive compared to their low temperature counterparts. At the moment, this is one of the disadvantages toward the industrial applications of these superconductors.

(a)

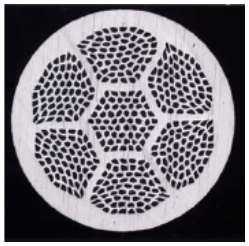

(b)

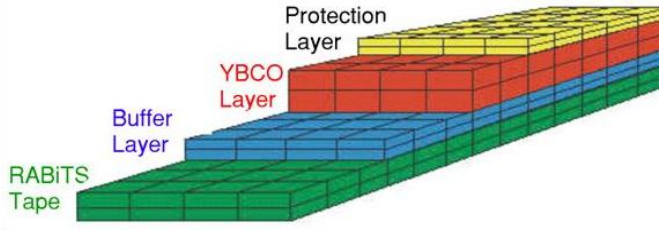

(c)

Fig. 1.6: Cross-sectional views of (a) Bi-2223/Ag tape [1.12]; (b) Bi-2212/Ag strand [1.13]; (c) YBCO tape.

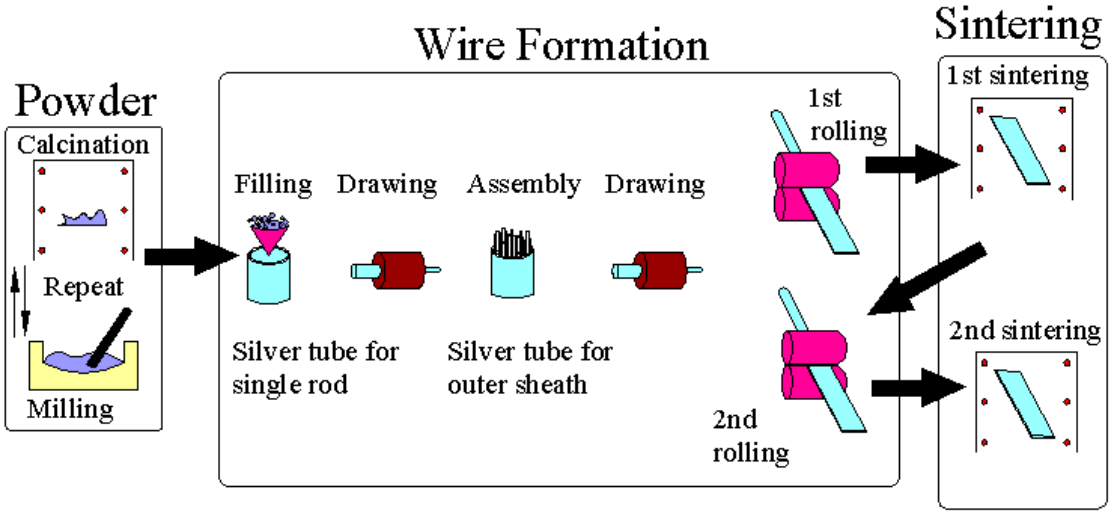

Fig. 1.7: Schematic of BSCCO powder in tube (PIT) wire making process.

More recently, a good progress in yttrium based coated high-T_c conductors (YBCO) has been made. These coated conductors show very good properties under high magnetic fields and therefore are the potential candidates for high field applications such as fusion reactor magnets. These conductors are produced by surface coating and are in fact very difficult to produce compared to BSCCO wires and tapes [1.15]. A typical architecture of an YBCO tape is shown in Fig. 1.6(c). The typical cross-section of an YBCO tape is 10 mm (width) ×0.1 mm (thickness) whereas for Bi-2223/Ag tapes it is typically 4.2 mm (width) ×0.22 mm (thickness).

The ceramic superconductors are very anisotropic compounds; that is, their properties are quite different in different crystalline directions. For that reason, researchers have struggled to obtain good grain alignment in finite-sized samples. Figure 1.8 shows the molecular structure of YBCO. The structure is essentially that of a sandwich, with planes of copper oxide in the center, and that is where the superconducting current flows [1.16]. In fact, the role of the elements other than copper and oxygen is secondary. In YBCO, yttrium is only a spacer and a contributor of charge carriers and nearly any of the rare earth elements (holmium, erbium, gadlium, etc.) can be substituted for yttrium without changing T_c significantly. Therefore, often the formula is written as $(RE)_1Ba_2Cu_3O_7$, to emphasize the interchangeability of other rare earth (RE) with yttrium. Compared to YBCO, the BSCCO compounds are more pronounced in their anisotropy; in fact, very little current can flow perpendicular to the copper oxide planes in those lattices. Therefore, in order to achieve high critical currents, the c-axis orientation of the grains in BSCCO compounds is very necessary so that current can easily flow in the direction of ab-plane. The c-axis orientation is best achieved by rolling process (shown in Fig. 1.9) and therefore the BSCCO wires are available in tape form with enhanced critical current properties.

Similarly, to achieve high critical currents in YBCO tapes, the grains of YBCO should be properly aligned for easy current transfer from one grain to another. Therefore, the bi-axially textured substrates are used to grow YBCO thin films with high critical currents [1.17]. Typically, the thickness of the YBCO film is 1-2 μm. Up to present, there have been developed some crucial technologies to produce high quality YBCO tapes: One is the so-called IBAD (Ion Beam Assisted Deposition Process) [1.15] to produce

high-quality biaxial grain alignment for buffer layers of YSZ or GZO. PLD (Pulse Laser Deposition) or MOD (Metal Organic Deposition) are used for producing YBCO layers. To prepare high-quality textured substrates, RABiTS (Rolling Assisted Bi-axially Textured Process) is used [1.18]. The critical properties of the HTS conductors are discussed in details in the following sections.

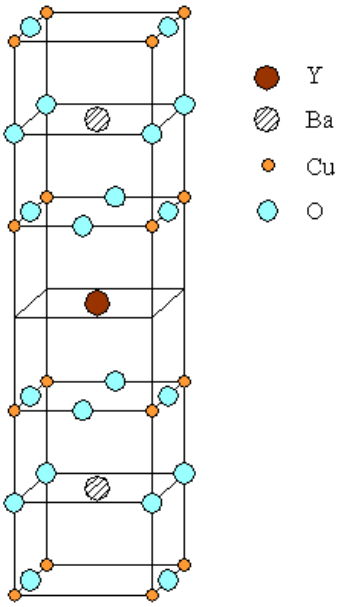

Fig. 1.8: Lattice structure of YBCO superconductors.

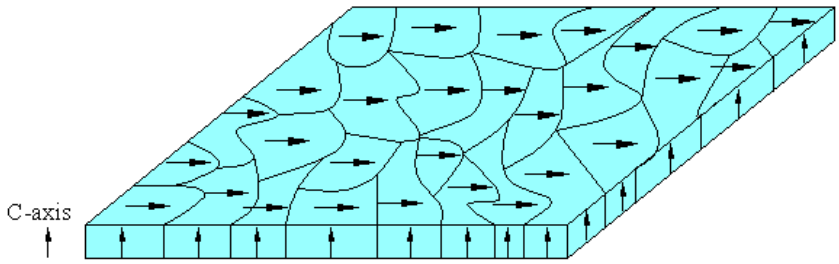

Fig. 1.9: c-axis oriented grains after rolling.

1.3 Application of superconductors in fusion devices

Superconducting magnets are inevitable in a fusion energy reactor based on magnetic confinement of hot plasma. The required magnetic field is in the range of 13 ~ 20 T for a fusion energy reactor, which is almost impossible to attain using resistive magnets due to the large joule heating and huge size of the magnets [1.2]. Therefore, the superconducting magnets are being used in fusion devices, which are free from heating (except AC losses and joule heating at the joints). Also, due to the large current carrying capacity of superconductors, the sizes of the superconducting magnets are much smaller than resistive magnets for the same magnetic fields.

The fusion device, first time using a superconductor for its magnets, was built in Russia during 1968-78 and was named T-7. This machine used NbTi based superconductor producing a maximum magnetic field of ~ 4 T at the winding. Later on, another device named T-15 (in Russia) used Nb_3Sn superconducting conductors and produced a maximum field of about 6.5 T. T-7 and T-15 superconductors were cooled by force flowing helium at 4.5 K. The first bath cooled superconducting Tokamak, Tore-Supra, was built in France. The NbTi based superconducting magnets of this Tokamak are cooled by He-II at 1.8 K and produce a maximum field of ~8.5 T. Another Tokamak, TRIAM-1M, based on bath cooled Nb_3Sn superconducting magnets producing a maximum field of ~ 11 T was built in Japan.

Later on, the concept of cable-in-conduit conductor (CICC) was developed at MIT in USA. This conductor concept solved many problems such as mechanical rigidity of windings, thermal stability of magnets, insulation etc. The first large-volume superconducting magnet using CICC was tested in a multinational project “Large Coil Task (LCT)” [1.19]. Now, several countries have started their own fusion plasma projects and are building their fusion devices using superconducting CICC such as SST-1 in India, KSTAR in Korea, EAST in China, and JT-60 SA in Japan [1.20, 1.21, 1.22, 1.23].

The Large Helical Device (LHD), which is based on helical or heliotron concept, uses NbTi based bath cooled helical coils at 4.4 K and CICC for force flow cooled poloidal field magnets at 4.5 K [1.24, 1.25]. Another helical machine, or a stellarator, W-7X, which is under construction in Germany, also uses NbTi based CICC for its planner

and non-planner modular coils [1.26]. The magnets are cooled by force flowing supercritical helium at 4.5 K.

Now, a multinational project, ITER, based on tokamak concept is underway. ITER also uses NbTi and Nb_3Sn CICC for its toroidal field (TF) and poloidal field (PF) magnets and the maximum field at the conductor is ~13 T [1.7, 1.27-1.30].

Following the fast developments in high temperature superconductors, helical machines have already been started being used in fusion devices. Other than tokamak and helical machines, the levitated ring coils based fusion devices such as Mini-RT, RT-1, and LDX have also been developed. Mini-RT and RT-1 devices (in Japan) use BSCCO wires for their floating coils whereas LDX (in USA) uses Nb_3Sn conductor for its floating coil [1.31-1.33].

Other than the magnets in fusion devices, there are several auxiliary systems such as current feeder systems to feed the current into magnets, current-leads to transfer the currents form room temperature to low temperature also use superconductors. In SST-1 and LHD, the current feeder systems are made of NbTi based conductors and ITER will also be utilizing superconducting current feeder system [1.34, 1.35]. The conventional current leads use LTS conductors, however, to reduce the consumption of liquid helium by current leads, HTS current leads have been developed using BSCCO wires [1.36-1.39]. There is already a discussion to use HTS current leads in ITER. Figure 1.10 shows some examples of the fusion devices using LTS and HTS superconductors.

(a)

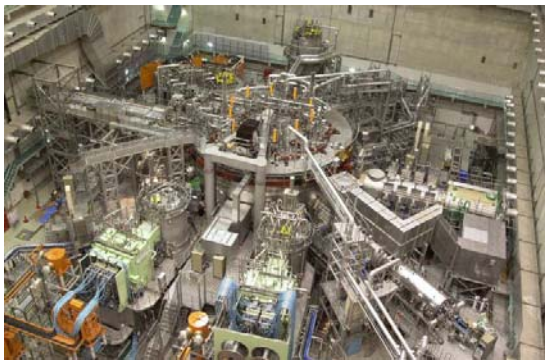

(b)

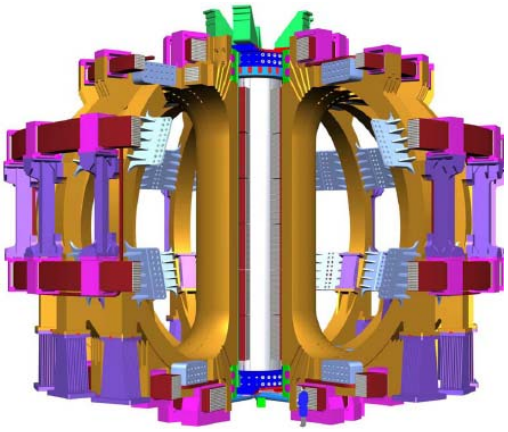

(c)

(d)

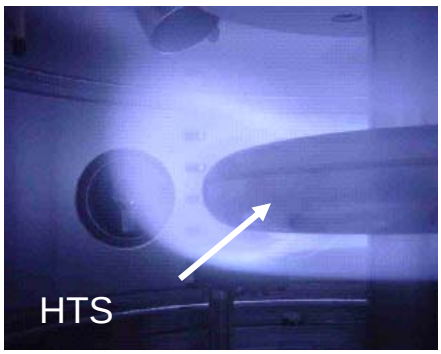

(e)

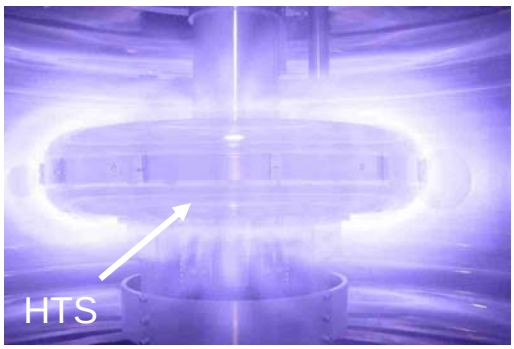

(f)

Fig. 1.10: (a) SST-1; (b) LHD; (c) ITER; (d) RT-1. Figures (e) and (f) show the HTS floating coils (using Bi-2223/Ag wires) of Mini-RT and RT-1 devices whereas other devices use NbTi and Nb_3Sn LTS conductors.

1.4 Issues associated with large-current capacity superconducting conductors

Presently, the so-called low temperature superconductors (LTS) such as NbTi, Nb_3Sn are being used in fusion magnets to confine the hot plasma. The typical operating temperature of LTS magnets is ~ 4 K using liquid or supercritical helium. At low temperatures of about 4 K, the stability margins of LTS conductors are quite lower as the specific heats of the materials at 4 K are quite small and therefore small heat inputs to the magnet conductors can increase the temperature beyond the critical temperature of the superconductors. Due to this increased temperature, the superconductor quenches (a superconductor turns into a normal conductor) and large joule heating occurs in the magnets. To protect the magnets from burning due to the excessive joule heating, the stored magnetic energy should be dumped safely outside the magnets (usually by using external dump resistors). To dump the huge magnetic energy, stored in fusion magnets, is generally a challenging and risky task. If a quench is not detected in time (e.g. due to the failure of the quench detection circuit) or if the protection circuit fails, the magnets can be damaged rather easily. Secondly, during the dumping process, large voltages appear across the magnet winding, which is always a danger for the insulation system of magnets. And, of course, due to the quench and dumping of the magnetic energy, the device operation should be stopped immediately until the magnets are ready again. Hence, a quench in the magnet is an absolutely unwanted event, which invites many problems to the magnet system itself and delays in the operation of the fusion machine. A commercial fusion energy reactor can never afford such kind of problems and therefore the superconducting magnets will never be allowed to quench. Hence, there is a strong demand to improve the stability of the superconducting magnets so that they do not quench and fusion reactors are operated safely without any trouble [1.40].

The stability margin of a superconducting conductor largely depends on the temperature margin (difference between operating and current sharing temperatures). At a current sharing temperature, a part of the operating current starts to flow in surrounding matrix materials (usually copper) and therefore joule heating occurs. If this joule heating

is higher than available cooling, the conductor quenches. The current sharing temperature reduces by increasing the magnetic fields and therefore the stability margin also reduces by increasing the magnetic fields. Hence, LTS conductors are more prone to quench in higher magnetic fields.

Apart from the reduction of stability margins in high magnetic fields, another phenomenon known as "non-uniform current distribution (NUCD)" in the conductor also reduces the stability margin, sometimes, substantially. The effect of NUCD on the stability margin of conductors was first observed in Demo Poloidal Coils (DPC) [1.41, 1.42]. Two 30 kA, NbTi Demo Poloidal Coils, DPC-U1 and DPC-U2 were fabricated and tested aimed at the development of large, forced-flow cooling, superconducting poloidal and toroidal coils for the next generation fusion reactors such as ITER. DPC coils were designed to be capable of both DC and pulsed operations up to 7 T and pulsed operation of 7 T/s with a design current of 30 kA. To reduce AC losses, formvar insulation was applied over the strands to reduce interstrand coupling currents. DPC coils reached their design currents, but exhibited serious instability during the charging, in many cases resulting in coil quenches. Such a quench occurred even at a current one-tenth of the conductor critical current. Later, the detailed analysis showed that this reduced performance of the conductor was caused by the existence of the non-uniform current distribution among strands of the conductor [1.43, 1.44]. The quench starts from the strand which carries the highest current in the conductor and then it propagates to other neighboring strands and then to the whole conductor, which is sometimes called avalanche-like quenches [1.45].

In multiple-strand superconducting cables, the current in each strand is determined by the inductance, as the resistance of superconducting wires is zero. Simple electrical circuit schematics for 3 strand superconducting conductor are shown in Fig. 1.11. Figure 1.11 (a) shows that during the charging of the conductor, if the inductances (or inductive reactances) are different, the current in each strand will be different and finally non-uniform current distribution is established [1.44]. Therefore, to have a uniform current distribution in a multiple strand superconducting conductor, the inductances of all the strands should be uniform. To get this condition, all the strands in superconducting conductors are usually twisted and fully transposed in multiple stages as shown in Fig.

1.12. However, the non-uniform current distribution in a conductor can still occur due to the non-uniformity in the inductances of strands caused by imperfect transposition during the conductor fabrication. On the other hand, the non-uniform current distribution can occur due to the mismatch in contact resistances at the joint locations also [1.46, 1.47] as shown in Fig. 1.11 (b).

During the charging of coils, large circulation currents can be induced due to the non-uniformity in the inductances, which by superimposing on the transport current cause the non-uniform current distribution in the conductor. When the strands are insulated, the contact resistance among the strands (as shown in Fig. 1.11 (c)) is large, and therefore the time constant of the current re-distribution becomes large, which makes the problem even more serious.

Table 1.2 shows the DPC coil parameters and Fig. 1.13 shows the DPC strand and conductor cross-sectional views [1.42]. Figure 1.14 shows the load line of the DPC single coil charging. The solid circles show the quench points during the charging of the coil, which are well below the desired operation point of 5.29 T (maximum field at the conductor) and 30 kA. As indicated in Fig. 1.14, it was revealed that non-uniform current distribution is a serious problem for stability of conductors and should be considered for designing conductors. Several other researchers also carried out similar studies on the effect of non-uniform current distribution on stability using reduced-scale conductors and found similar results of instabilities due to non-uniform current distributions [1.48, 1.49]. Hence, one can say that non-uniform current distribution is an important issue and should be considered for large-current capacity conductors.

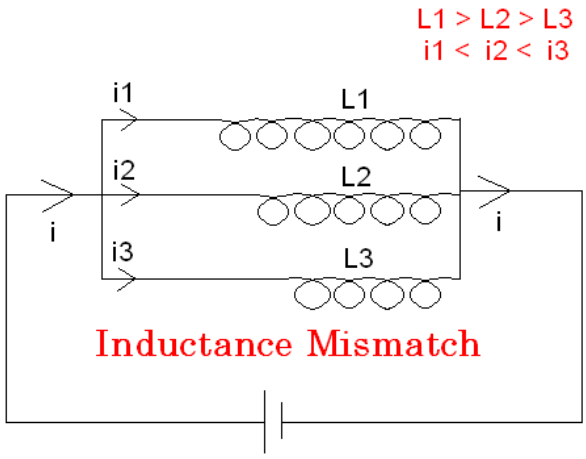

(a)

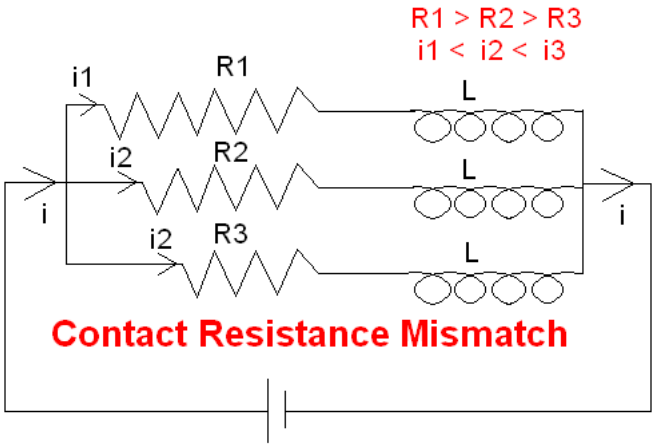

(b)

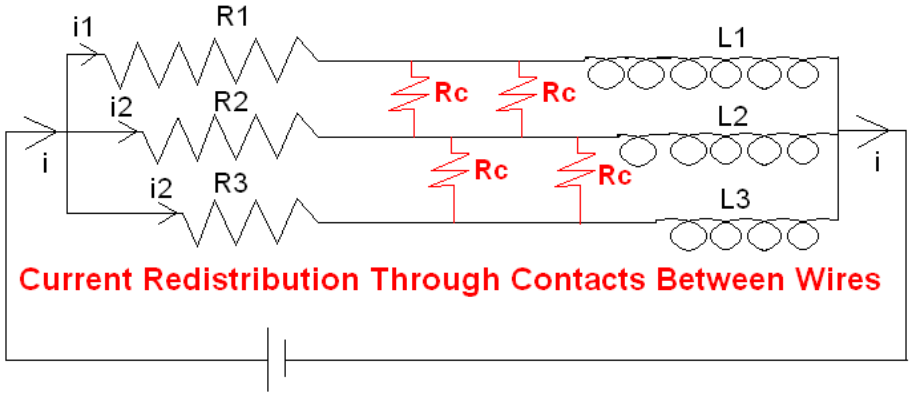

(c)

Fig. 1.11: Schematic of electrical circuit for 3 strands superconducting cable showing (a) inductance mismatch; (b) contact resistance mismatch at the joint locations; (c) contact resistances among strands.

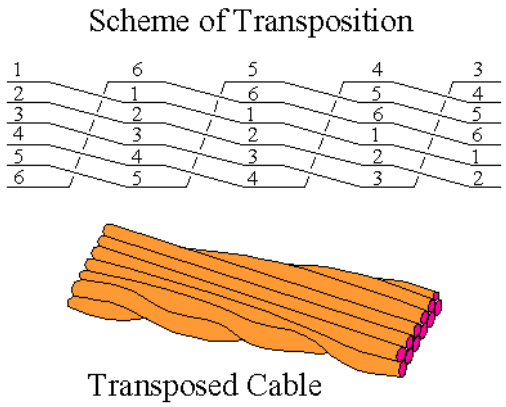

(a)

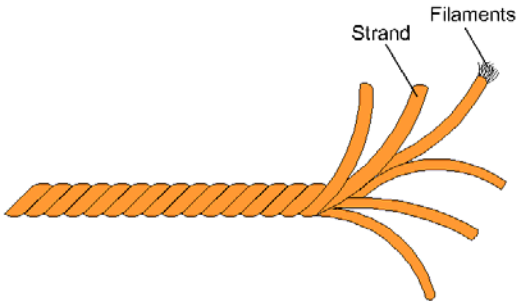

(b)

(c)

Fig. 1.12: (a) schematic of principal scheme of transposition and fully transposed cable; (b) fully transposed cable by twisting the strands; (c) a proposed HTS conductor in Germany.

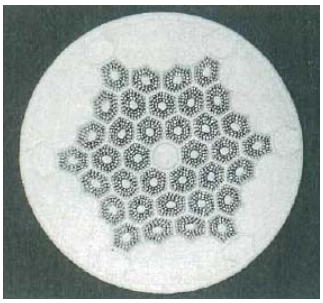

(a)

(b)

Fig. 1.13: Cross-sectional views of (a) the DPC coil strand and (b) the DPC coil conductor [1.47].

Table 1.2: Parameters of the DPC coil [1.47].

Coil	
Winding inner diameter	1000 mm
Winding outer diameter	2000 mm
Winding width	300 mm
Number of coils	2
Design field	7 T
Design current	30 kA
Number of turns	254
Cooling path length	80 m
Conductor	
Outside dimension	31 × 35 mm
Strand diameter	1.12 mm
Strand surface	Formvar
Number of strands	486
NbTi cross-section area	85 mm^2
Cu cross-section area	228 mm^2
CuNi cross-section area	49 mm^2
Coolant cross-section area	303 mm^2
Void fraction	38%
Hydraulic diameter	0.665 mm

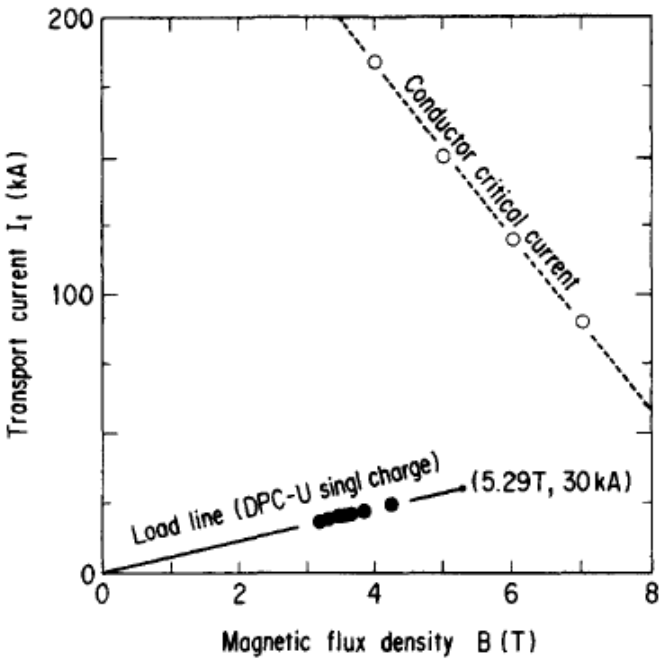

Fig. 1.14: Load line of DPC single coil charge. Solid circles show the quench points [1.42].

1.5 Advantages of high temperature superconductors

In contrast to LTS conductors, high temperature superconductors have several advantages, which make them promising candidates for future fusion energy reactor magnets. Some of them are discussed here.

Critical magnetic field

High temperature superconductors are basically Type-II superconductors. Generally, the critical magnetic field of HTS conductors are quite high compared to LTS conductors, which make them suitable for high field applications. HTS conductors can be used quite effectively in a bias field of 20 T or higher, and therefore, can be promising candidates for fusion energy reactor magnets where the field will be in the range of 13 – 20 T.

Figure 1.15 shows the critical magnetic fields of some of the high temperature superconductors as a function of operation temperature. For comparison, conventional LTS conductors, such as NbTi and Nb_3Sn are also shown.

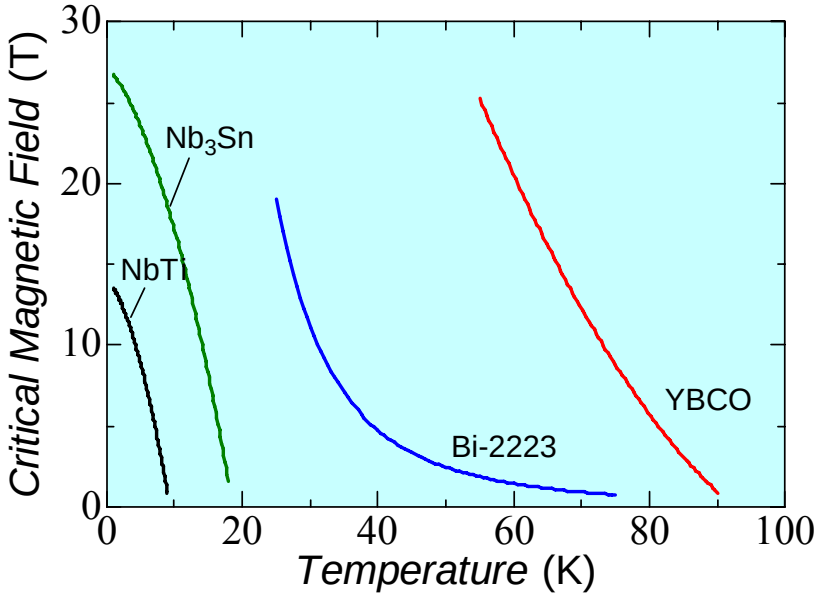

Fig. 1.15: Critical magnetic field of superconductors as a function of operation temperature.

Critical current density

Higher critical current densities in superconductors are required to fabricate high magnetic field magnets with smaller volumes. HTS conductors offer quite high critical current densities compared to conventional LTS conductors in high magnetic fields, which is one of the biggest advantages of HTS conductors. HTS conductors offer high critical current densities even at elevated temperatures of about 20 K which make them suitable to be operated at 20 K or higher unlike the conventional LTS conductors operating at ~ 4 K. Figure 1.16 shows the critical current characteristics of some of HTS conductors [1.40]. For comparison, critical current densities of NbTi, Nb_3Sn, and Nb_3Al conductors' critical current densities are also plotted.

As shown in Fig. 1.16, the critical current density of YBCO is much higher compared to conventional LTS conductors even at elevated temperature of 20 K. YBCO is the most promising candidates among all HTS conductors, as it degrades less in higher magnetic fields.

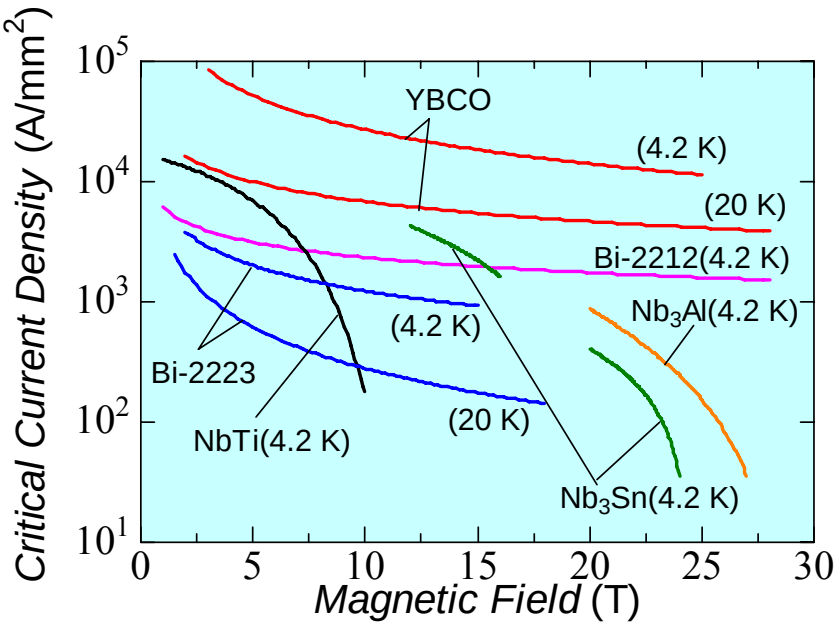

Fig. 1.16: Critical current densities of the superconductors as a function of magnetic field.

Specific heat

As discussed above, HTS conductors, especially YBCO, can be used at elevated temperatures of ~ 20 K or higher in high magnetic fields. The specific heats of the materials are much higher at 20 K compared to them at 4 K. Figure 1.17 shows the specific heat of typical superconducting magnet materials as a function of temperature [1.50]. It clearly indicates that the specific heats are 10 – 100 times larger at 20 K compared to those at 4 K. This increased specific heat at 20 K makes HTS conductors invulnerable to thermal disturbances coming from wire motions, epoxy crackings, etc. in superconducting magnet and therefore improves the stability of HTS magnets. This is

another big advantage in HTS conductors, which make HTS magnets almost quench free and promise to provide safe and interruption free operations of a fusion reactor.

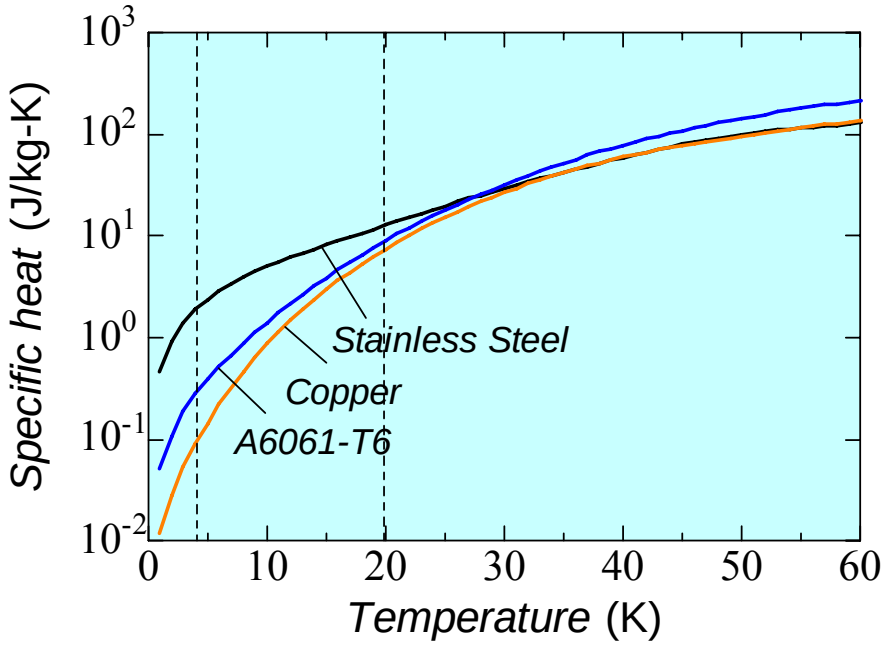

Fig. 1.17: Specific heat of typical superconducting magnet materials as a function of temperature. A6061-T6 is an aluminum alloy.

Thermal conductivity

At elevated temperature of ~20 K, the thermal conductivity of materials is also improved. This improved thermal conductivity helps in removing the heat quickly, especially when the magnets are indirect or conduction cooled. Due to the increased stability of HTS conductors at ~20 K, the active cooling may not be required for HTS magnets unlike conventional LTS magnets where magnets are actively cooled by liquid or supercritical helium at ~ 4 K. Figure 1.18 shows the thermal conductivity of some materials as a function of temperature [1.50]. It clearly indicates that the thermal conductivities are 5 – 10 times higher at 20 K compared to those at 4 K.

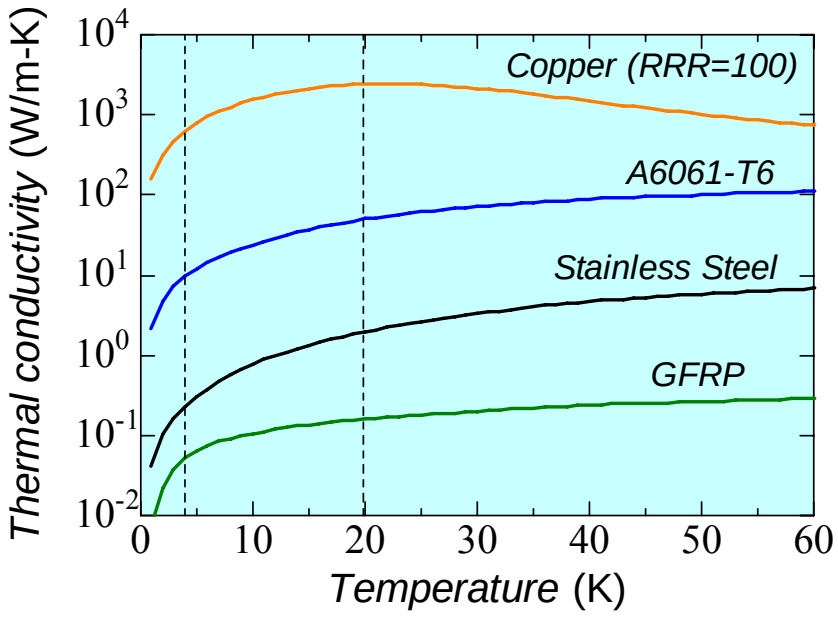

Fig. 1.18: Thermal conductivity of the materials as a function of temperature. A6061-T6 is an aluminum alloy.

Refrigeration power

As discussed before, HTS magnets can be operated at ~20 K or higher temperatures and therefore much less refrigeration power is required compared to LTS magnets which are operated at ~ 4 K. Figure 1.19 shows the ideal input power per Watt of refrigeration considering 100% efficient Carnot cycle [1.16]. It clearly indicates that the input power is about 5 times less at 20 K whereas it is about 15 times less at 50 K compared to 4 K. This reduced input power requirement makes a fusion reactor economically more viable as it is operated continuously over a long period of time.

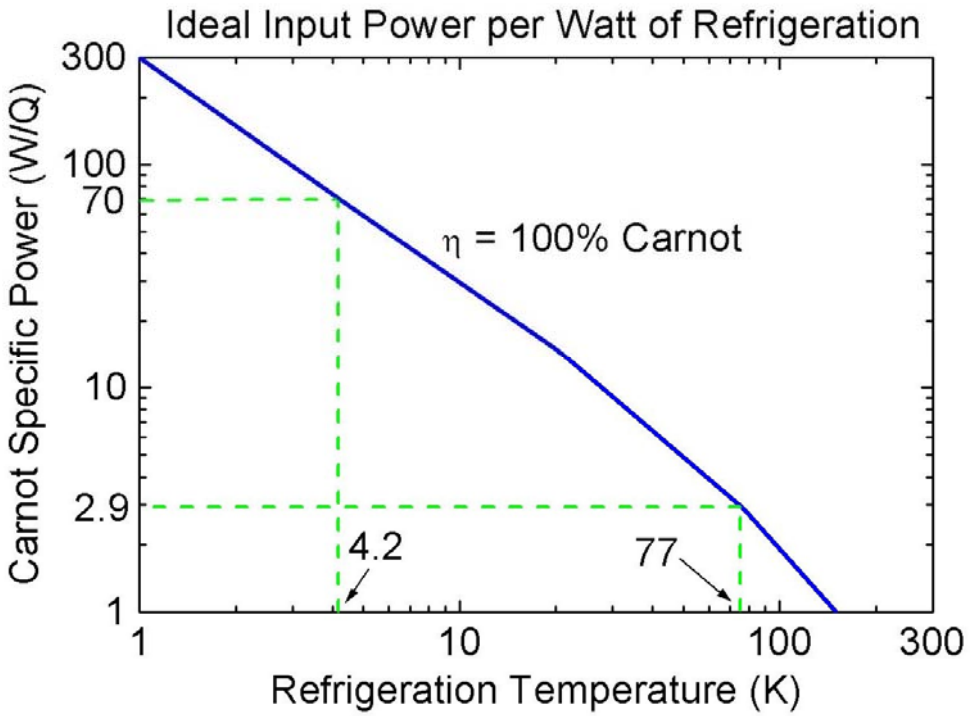

Fig. 1.19: Carnot specific power as a function of refrigeration temperature.

1.6 Proposal of large-current capacity HTS conductors

Owing to several advantages of HTS conductors as discussed above, HTS conductors are promising candidates for future fusion energy reactor magnets [1.51 – 1.54]. Compared to LTS conductors, HTS conductors possess higher stability due to large temperature margin. The typical operating temperature for a HTS conductor magnet may be about 20 K and the temperature margin is supposed to be more than 10 K (typical temperature margin of LTS conductors is ~1 K) in a magnetic field of 13 ~ 20 T. The higher stability of HTS conductors can be exploited in developing a high stability conductor or virtually a quench free conductor suitable for fusion energy reactors. Due to the increased stability of conductors, the reliable and safer operations of fusion energy reactors can be assured and problems related with quench and energy dump can be mitigated.

Unlike LTS conductors, HTS conductors are available only in primitive forms (tape and strand) and no large-current capacity HTS conductor suitable for fusion reactor magnets has been developed yet. Through this thesis research, our objective is to examine the feasibility of a 100 kA-class HTS conductor suitable for fusion energy reactor magnets, especially the DC magnets, such as the helical coils in a heliotron-based fusion reactor or toroidal coils in tokamak-based fusion reactors.

As discussed before, HTS materials are basically ceramic materials and are mostly available in tape forms and thus, it is not easy to twist or transpose many of them to form a large-current capacity conductor. As is also discussed before, transposition is necessary to avoid non-uniform current distribution in conductors. However, opposite to this idea, we propose a large-current capacity HTS conductor with simple stacking of HTS tapes. This idea is rather bold as there has been no such conductor so far without any transposition of wires. It is quite natural to have non-uniform current distribution in such kind of conductors due to the inductance mismatching. Therefore, our main focus during this research is on the stability of large-current capacity HTS conductors and the effect of non-uniform current distribution on the stability of the HTS conductor with simple stacking of tapes.

During this research, we developed and studied 10 kA-class (at 20 K and 8 T) YBCO and Bi-2223/Ag HTS conductors by simply stacking them inside copper sheaths. In this thesis, we design and propose 100 kA-class (20 K, 13 T) HTS conductors for the LHD-type force-free helical reactor (FFHR). The major design parameters of FFHR machine are given in Table 1.3 [1.55]. A bird eye view of FFHR is shown in Fig. 1.20.

The major specifications of the proposed 100 kA HTS conductor are shown in Table 1.4 and the cross-sectional view of the conductor is shown in Fig. 1.21.

Table 1.3: Major parameters of the LHD type helical reactor FFHR

Major radius	14.0 – 18.0 m
Minor radius	3.0 – 4.0 m
Plasma central field	~ 6 T
Maximum field at the helical coil conductor	~13 T
Helical coil conductor current	100 kA
Total current in the helical coil	40 – 50 MA
Stored energy	~150 GJ

Table 1.4: Major Specifications of the proposed 100 kA HTS conductor

Superconductor	YBCO
Operating temperature	20 – 25 K
Maximum field on the conductor	13.25 T
Critical current of HTS tape	100 A per mm width (25 K, 13 T)
Operating current	100 kA
Current density	~ 40 A/mm^2
Copper to HTS ratio	7
Cooling method	Indirect cooled

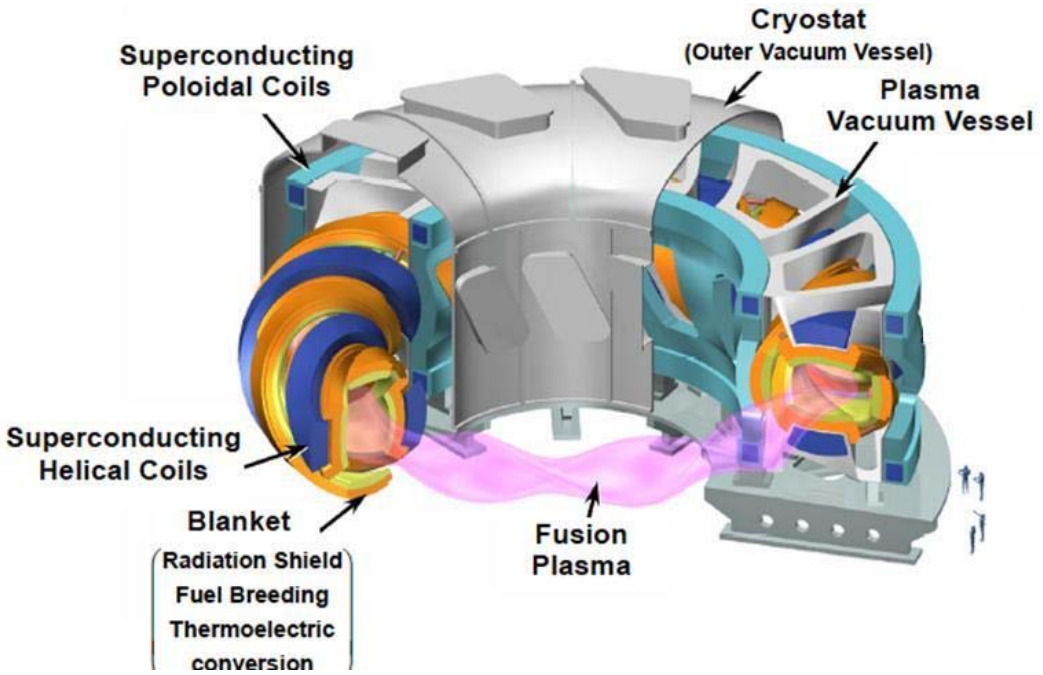

Fig. 1.20: Bird's-eye view of the LHD-type force-free helical reactor FFHR [1.55].

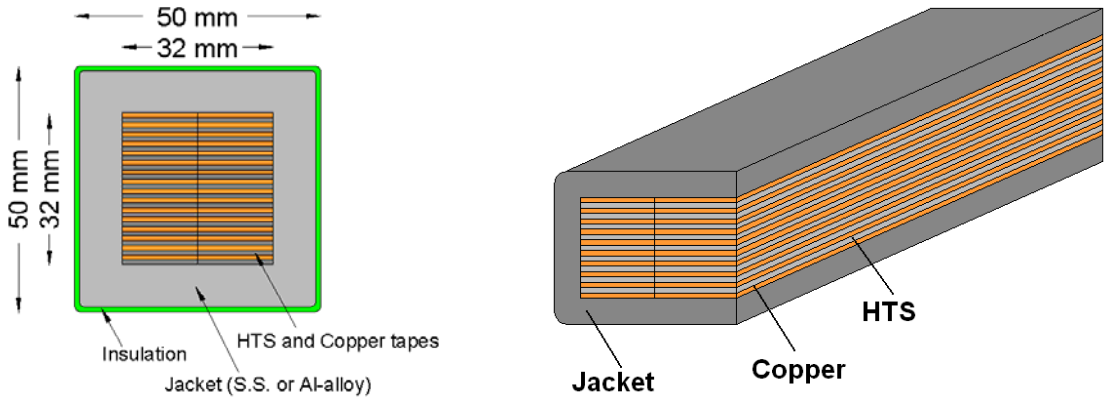

(a) (b)

Fig. 1.21: (a) Cross-sectional and (b) 3-D views of the 100 kA HTS conductor proposed for the helical coils of FFHR.

Chapter 2

Cryogenic stability of cable-in-conduit conductors (CICC)

As introduced in Chapter 1, the stability of a large-current capacity conductor is affected by non-uniform current distribution (NUCD), especially in insulated strand conductors where the current redistribution is not easy. The proposed HTS conductor with simple stacking of the HTS tapes without any insulation between them will also be subjected to non-uniform current distribution due to the inductance mismatching. Though the current redistribution among the HTS tapes might be easier due to the absence of any insulation, it is still an important task to examine the stability of a HTS conductor with non-uniform current distribution. Before developing and examining the stability with non-uniform current distribution of HTS conductors, it was thought to be a good idea to examine the stability of presently available with bare strands full-scale LTS conductor with controlled non-uniform current distribution. Secondly, it was also thought that this research might provide some valuable information to some of the ongoing projects such as ITER and JT-60SA whose magnets are based on LTS conductors. Therefore, the research on the examination of stability of bare strand cable-in-conduit conductors (CICC) with controlled non-uniform current distribution has been carried out. The results of this research activity are discussed in this chapter.

2.1 Stability of a typical CICC

The typical cross-sectional view of a cable-in-conduit conductor (CICC) is shown in Fig. 2.1. Hundreds of superconducting strands, twisted in multiple stages, are housed in a high strength conduit (generally stainless steel). The coolant (usually supercritical helium) flows in the voids between the conduit and superconducting strands. Due to the direct contact of the coolant with each strand increases the stability of the conductor against thermal disturbances. The typical stability margin of a CICC (usually measured in mJ/cm^3) as a function of operation current is shown in Fig. 2.2 [2.1]. The stability margin line is divided in two parts: the so-called well-cooled and ill-cooled regions. In the well-cooled region, the stability is higher which is mainly governed by the enthalpy of the coolant whereas it is lower in ill-cooled region where it is mainly governed by the enthalpy of the strands. The operation current dividing these two regions is generally called as limiting current, which can be determined by the following equation [2.2].

$$I_{\lim} = \sqrt{\frac{hp_w A_{cu}(T_c - T_{op})}{\rho_{cu}}} \tag{2.1}$$

where h, p_w, T_c, T_{op}, A_{cu}, ρ_{cu} are heat transfer coefficient, wetted perimeter, critical temperature, operation temperature, copper area, and copper resistivity respectively. Generally, limiting current criterion is used to design a cable-in-conduit conductor to ensure high stability of the conductor, which is basically applicable for steady state conditions and assumes the uniform current distribution in the conductor. Usually, the normalized operation current (I_{op}/I_c) of a CICC in a magnet is ~ 0.4 to ensure high stability [2.1]. Here, I_{op} and I_c are the operational and critical currents of the conductor.

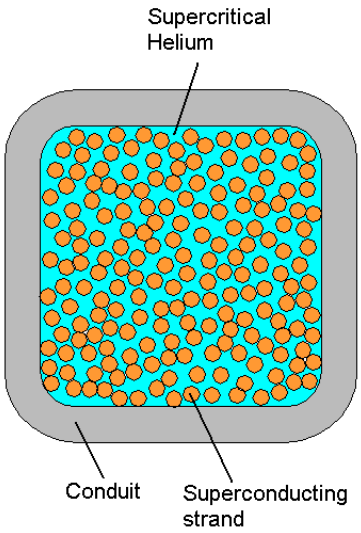

Fig. 2.1: Schematic cross-sectional view of a typical cable-in-conduit conductor (CICC).

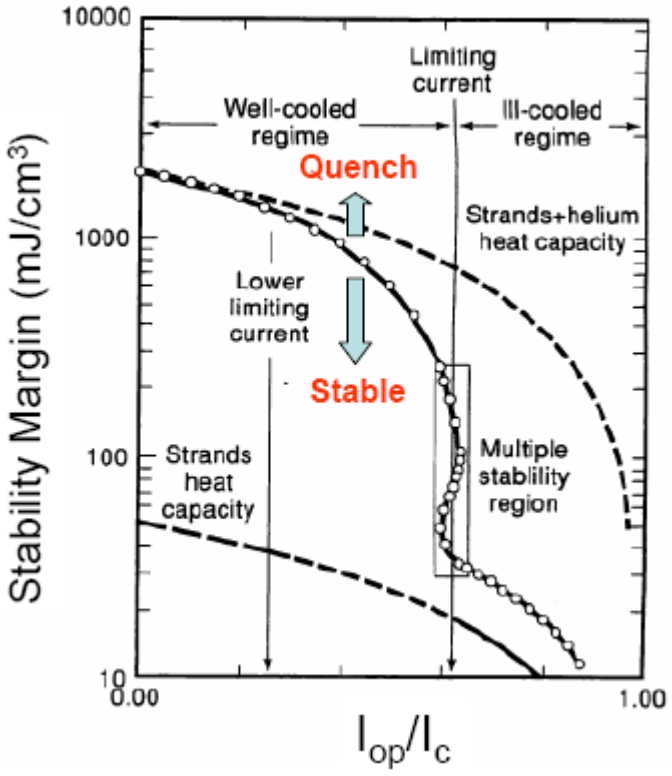

Fig. 2.2: Stability margin of a typical CICC as a function of normalized operation current (I_{op}/I_c). I_c is the critical current of the conductor. The so-called well-cooled and ill-cooled regions are indicated along with the limiting current [2.1].

2.2 Experimental set-up for the stability measurement of a CICC with NUCD

As discussed before, stability of bare strands CICC was measured with non-uniform current distribution in the conductor. This section describes the details of the experimental setup and measurement method.

2.2.1 Conductor specifications

The CICC for Steady State Tokamak (SST-1) magnets in India was used for preparing the short samples for this research [2.3]. The major specifications of the conductor are shown in Table 2.1 [2.4]. A cross-sectional view of the conductor and the schematic of different twisting stages of the conductor are shown in Fig. 2.3.

Table 2.1: Major specifications of the SST-1 CICC

Strands		
	Diameter (mm)	0.86 ± 0.005
	Copper / SC ratio	4.88
	Surface Condition	Bare
	Critical Current, I_c, at 5 T (A)	≥ 272
	RRR	≥ 100
	Index n	≥ 25
Cabling		
	Cabling Scheme	3 × 3 × 3 × 5
	Twist Pitch Lengths (mm)	40, 75, 130, 290
Conduit		
	Outer Dimensions (mm)	14.8 × 14.8
	Thickness (mm)	1.5
	I_c at 5 T (kA)	≥ 35
	Void fraction (%)	40 ± 2

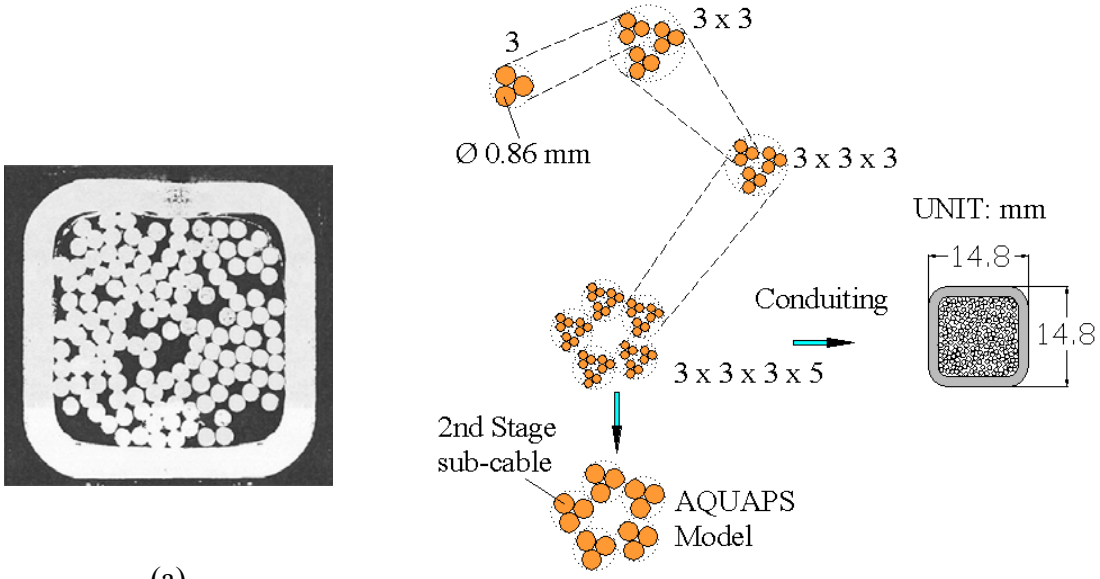

Fig. 2.3: (a) Cross-sectional view of the SST-1 CICC [2.3]; (b) schematic of different twisting stages in the SST-1 CICC.

2.2.2 Experimental sample

An experimental set-up with a sophisticated current feeder system was prepared to study the influence of NUCD on the stability of bare strands NbTi/Cu CICC for SST-1. This project was named INNOCENTS (INstabilities due to NOn-uniform Current distribution experimENTS). The schematic of the experimental set-up is shown in Fig. 2.4. The conductor was wound non-inductively in two turns with a radius of ~180 mm. The CICC has 135 strands of a diameter 0.86 mm twisted in 3 × 3 × 3 × 5 pattern with 40, 75, 130, and 290 mm twist pitch lengths as shown in Fig. 2.3b. The last two twisting stages of the CICC were opened up into 15 sub-cables of 9 strands each at both ends of the sample winding. In a terminal box, these 15 sub-cables were individually soldered with 15 thick high-current capacity NbTi/Cu wires (as shown in Fig. 2.5), which were finally connected with current leads as shown in Fig. 2.6. The feeders were arranged in one layer in the terminal block to avoid any non-uniform current distribution caused by the terminal joint itself.

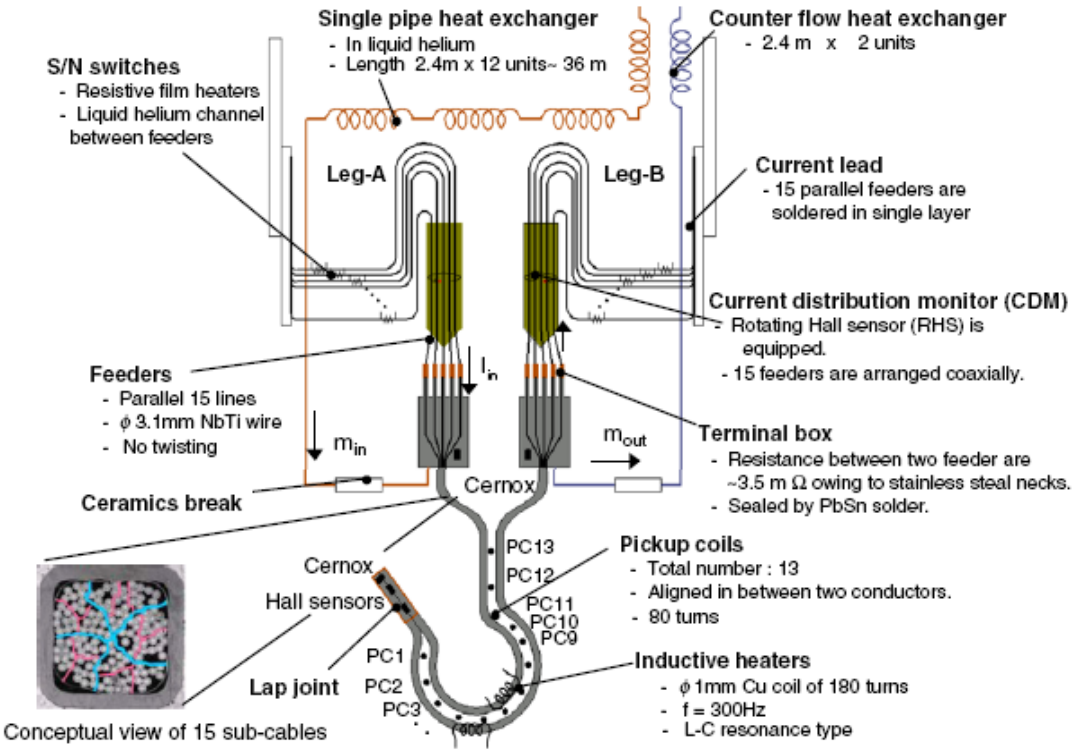

Fig. 2.4: Schematic view of the experimental setup for stability measurement of the CICC with non-uniform current distribution.

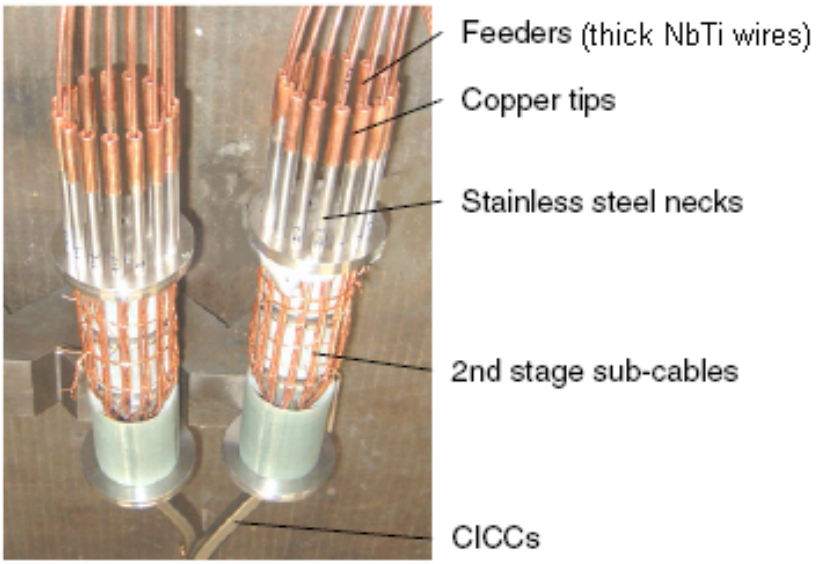

Fig. 2.5: Connection of 15 numbers of 2nd stage sub-cables with 15 thick high-current capacity NbTi/Cu wires (feeders) in terminal boxes.

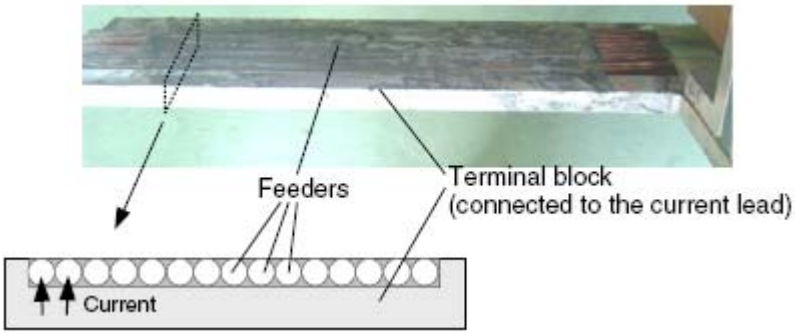

Fig. 2.6: Connection of 15 NbTi/Cu feeders with a terminal block, which connects the current lead to supply the current into the sample. The feeders are arranged in one layer to avoid any non-uniformity in the current distribution from the terminal itself.

Resistive heaters for artificial introduction of NUCD

Thin film heaters were mounted on the thick NbTi/Cu feeders individually to initiate normal-zones in them and thereby establishing a NUCD in the CICC as indicated in the Fig. 2.4. These NbTi/Cu wires were thermally isolated from the testing area and therefore did not affect the stability measurements. The arrangement of thin film heaters over feeders is shown in Fig. 2.7. By turning on the selective heaters, different kinds of controlled NUCD patterns can be established in the conductor. Figure 2.8 shows some examples of NUCD patterns, which were established before the stability measurements. Here, Step-0, Step-1, Step-3, and Step-6 correspond to 0, 20, 47, and 67% strands of the whole conductor, which were initially prevented to carry any current.

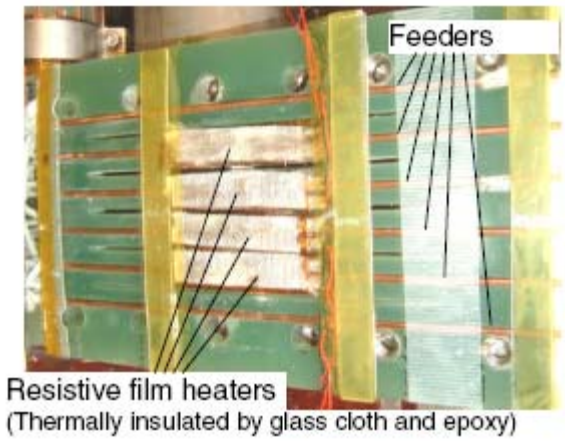

Fig. 2.7: Arrangement of thin film resistive heaters on the NbTi/Cu feeders to introduce different kinds of NUCD patterns in a controlled way.

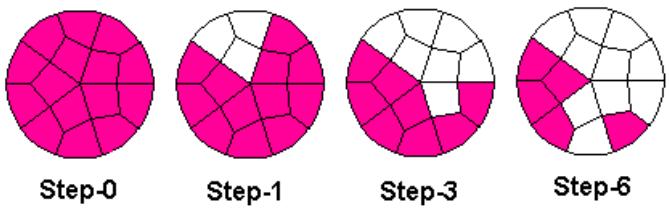

Fig. 2.8: Different NUCD patterns established by using thin film resistive heaters. Step-0 shows the uniform current distribution in the conductor. The current in white-portioned sub-cables was prevented by resistive heaters.

Current distribution measurement system (CDMS)

From terminal boxes, the feeder lines go through the current distribution measurement system (CDMS). In CDMS, the feeder lines are arranged equidistantly around a GFRP hollow pipe. Inside this hollow pipe, rotating Hall sensors were arranged. These hall sensors rotate 360 degrees and measure the magnetic field generated by the feeder lines.

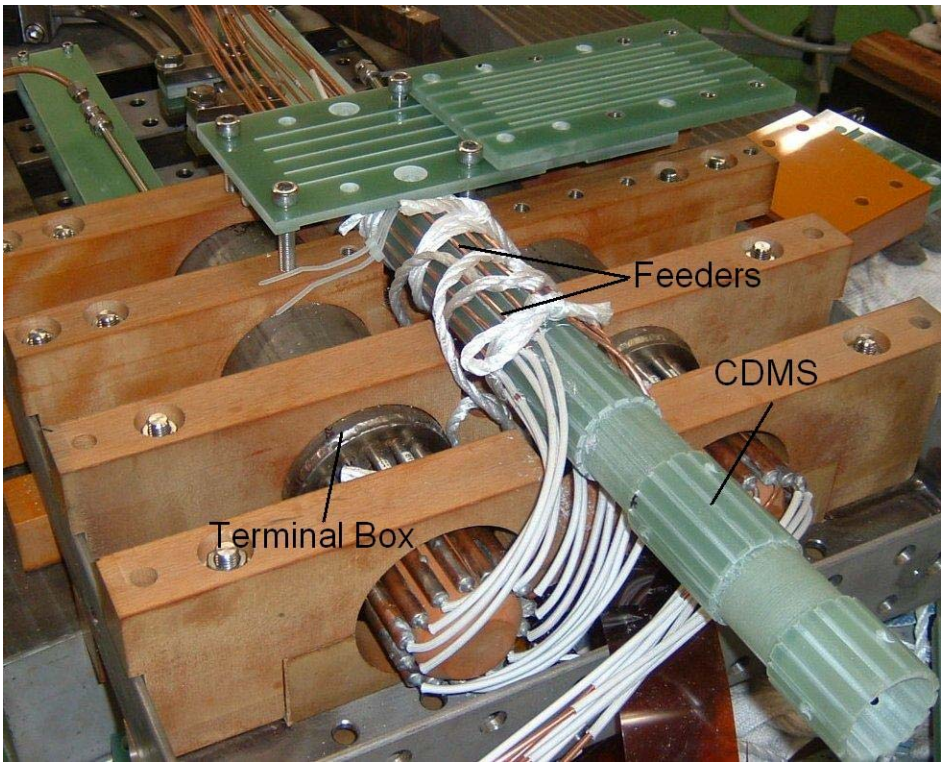

Fig. 2.9: Arrangement of feeder lines over GFRP hollow pipe of the current distribution measurement system (CDMS). The rotating Hall sensors were inside the hollow pipe to measure the field distribution according to individual current distribution pattern.

According to individual current distribution pattern as shown in Fig. 2.8, the field distribution is different which is measured by rotating Hall sensors and hence the current distribution is measured in the conductor. Figure 2.9 shows the arrangement of feeder lines over CDMS.

Induction heaters for stability margin measurements

Induction heaters were wound around each turn of the winding to initiate normal-zones. Induction heater consisted of 180 turns of insulated copper wire of about 1 mm diameter. During the experiments, after establishing the desired current distribution, the induction heater was turned on by discharging a capacitor to initiate a normal-zone in the conductor.

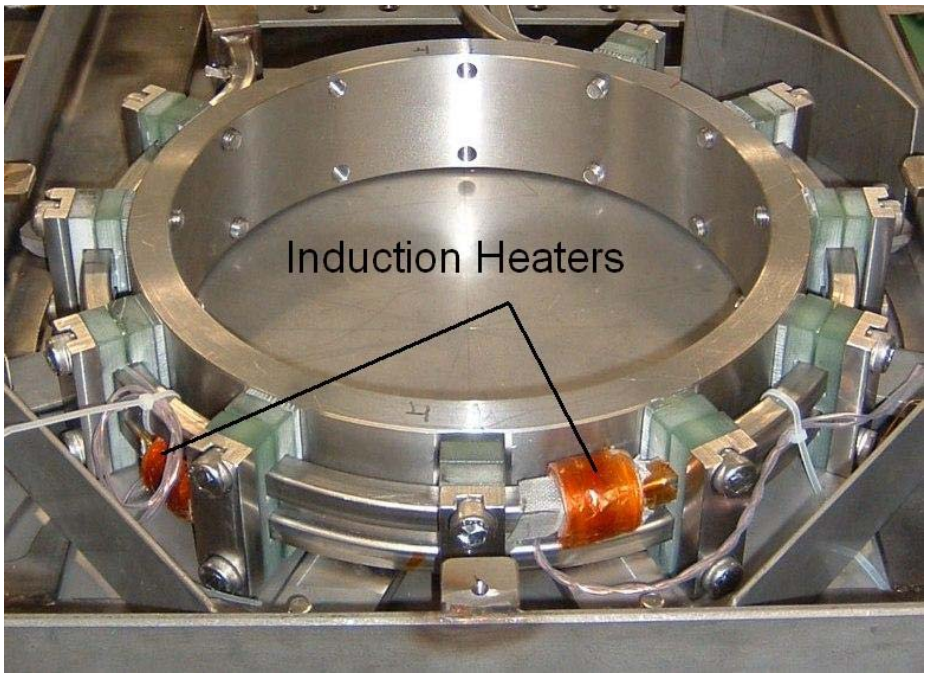

Fig. 2.10: Induction heaters wound over both turns of the CICC.

Figure 2.10 shows the induction heater wound over the CICC. The length of the induction heater was about 30 mm.

Cooling scheme

The CICC sample was cooled by supplying the pure He gas from outside through the counter flow and single pipe heat exchangers, which were immersed in liquid helium.

The pure He gas was supplied at 0.4 MPa into the sample which then flows through the heat exchangers and then condenses into the supercritical helium at 0.4 MPa and 4.2 K. The experiments were carried out at stagnant helium conditions and therefore outlet of helium line at room temperature was kept closed using a safety release valve. Figure 2.11 shows the single pipe heat exchanger used in the experiment.

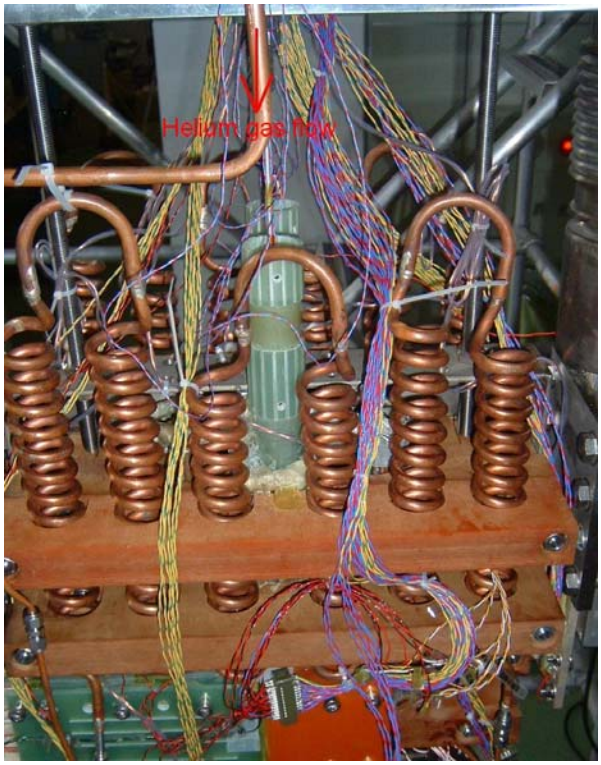

Fig. 2.11: Single pipe heat exchanger to condensate the pure helium gas.

Diagnostics

Lots of diagnostic sensors were installed which include Cernox temperature sensors, Hall sensors, pick-up coils, pressure sensor, flow meter, and voltage taps. To insure appropriate temperature conditions during experiments, Cernox temperature sensors were installed in the terminal boxes and at the joint location as shown in Fig. 2.4. As discussed above, rotating Hall sensors were installed to measure current distribution in the

conductor. Apart from these Hall sensors, some Hall sensors were installed at the joint to measure the current diffusion in the joint. Lots of pick-up coils were installed between two turns of the winding as indicated in Fig. 2.4 as PC1 to PC13. These pick-up coils were installed to monitor the current redistribution process after a normal zone appearance in the conductor. Pressure sensor and flow meter were installed in the outlet of the helium line to monitor the pressure and flow rate during the experiments. Flow meter was installed to monitor the helium flow rate for the stability experiments with different flow rates in the conductor. But later on it was decided to carry out the experiments with only stagnant helium conditions as the stability of an NbTi conductor is not significantly affected by steady state flow rate [2.5]. Secondly, all the measurements with uniform and non-uniform current distributions were carried out at the same operating conditions, it was not difficult to draw a conclusion about the effect on non-uniform current distribution on the stability and therefore the flow rate was not important for this experiment.

Many voltage tap pairs were installed to monitor the voltage development during the normal zone event in the conductor. A decision of quench was made by measuring the voltage rise only. Voltages were measured across the whole sample without including current leads, across the whole sample by including current leads, across each sample leg, and across the current leads.

9-T split coil facility and experimental conditions

For these experiments, the 9-T split coil facility was used to apply a bias field at the conductor [2.6]. Fig. 2.12 shows the schematic of the 9-T split coil facility. Fig. 2.13 shows the magnetic field profile generated by the split coil. The field at the conductor (~180 mm) is 6.1 T with a peak field of 9 T at the center of the split coil.

The experiments were mainly carried out at 6.1 T bias field, 4.2 K temperature, and 0.4 MPa helium pressure. Some tests were carried out by varying the helium pressure as well but maintaining the temperature and magnetic fields. The photographs of the experimental sample are shown in Fig. 2.14.

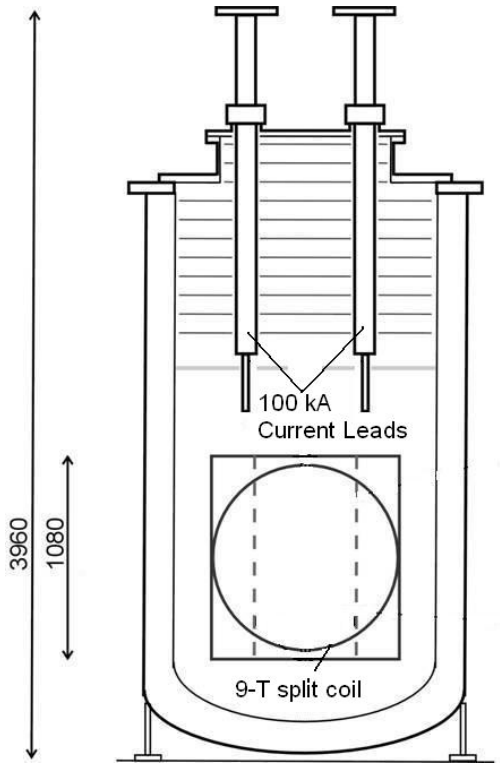

Fig. 2.12: Schematic of 9-T split coil facility. Dimensions are in mm.

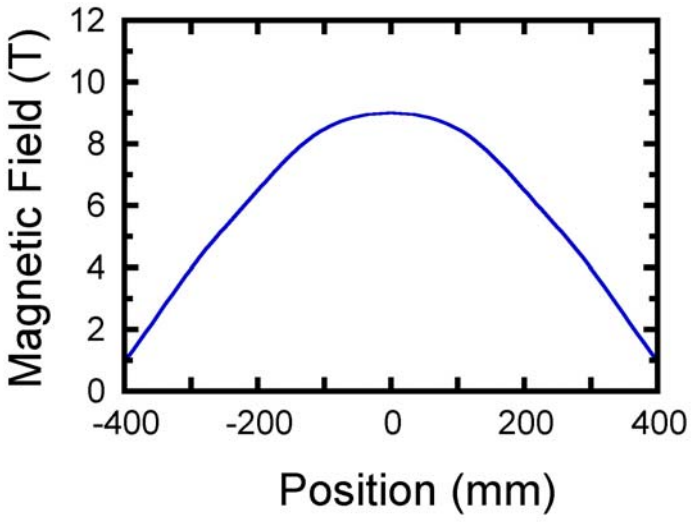

Fig. 2.13: Magnetic field profile generated by the 9-T split coil. The zero position in the horizontal axis indicates the center of the coil.

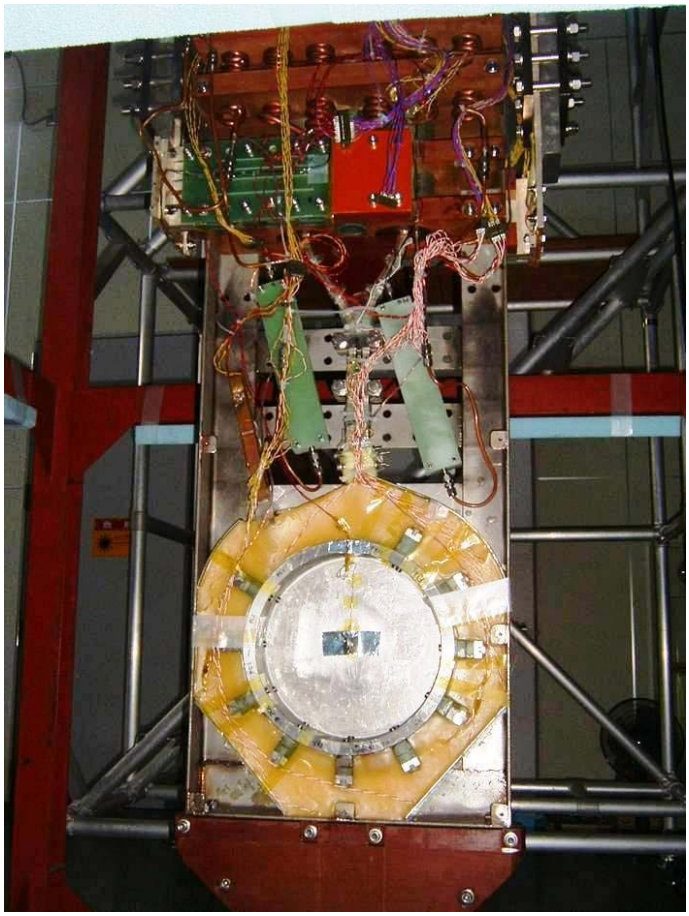

(a)

(b)

Fig. 2.14: Photos of (a) the completed test sample and (b) during the installation work.

2.3 Experimental method, results and analyses

The experimental method, experimental results and analyses of stability measurement and ramp rate limitation tests are discussed in this section.

2.3.1 Experimental method

During the experiments, initially, the sample was charged up to the desired current and then some of the thin film resistive heaters were tuned on to obtain the desired NUCD in the conductor as shown in Fig. 2.8. After reaching the steady-state, the input energy by induction heater was applied to initiate a normal-zone in the conductor.

At first, the time required (after turning on the resistive heaters) for establishing NUCD in the conductor was measured. For this measurement, the resistive heaters corresponding to Step-6 NUCD pattern were turned on after the charging of the sample up to the desired current and then after 0, 5, 15, 20, 30, 45 and 60 seconds, the input energy by induction heater was injected. Figure 2.15 shows the results of these measurements. It was found that the typical time required for establishing NUCD in the conductor was about 30 s as the required input energy for initiating a quench becomes almost constant thereafter. Hence, during the stability measurements with NUCD in the conductor, the input energy by induction heater was injected after 30 s from the resistive heaters were turned on.

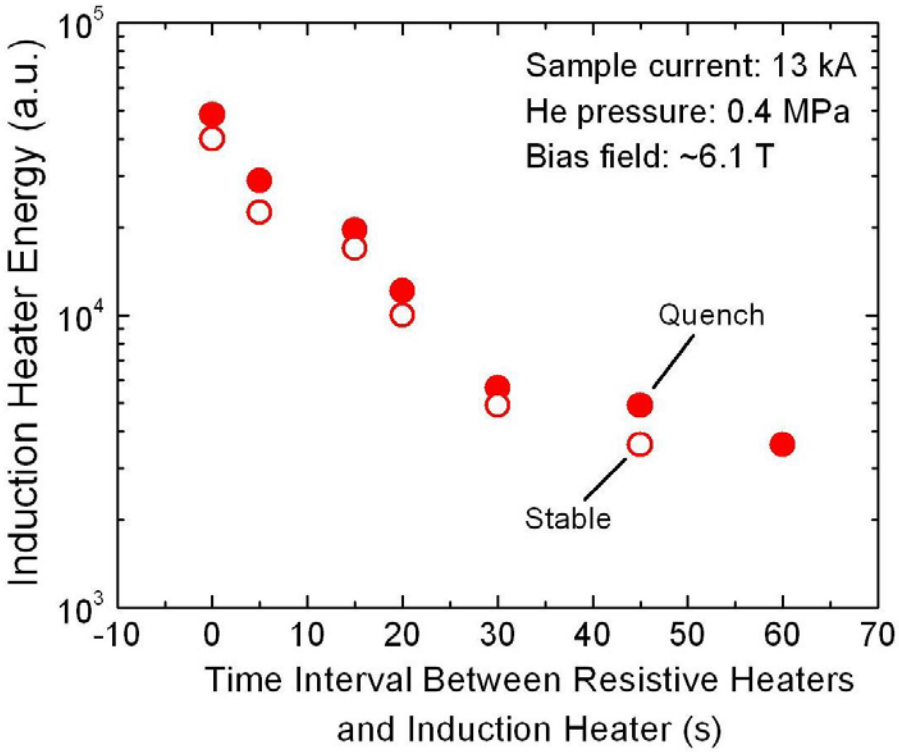

Fig. 2.15: Induction heater energy vs. time interval between NUCD heaters and induction heater operations to initiate a quench. The results show that a time delay of ~ 30 s was required to establish the NUCD in the conductor.

2.3.2 Current distribution measurements and verification with numerical calculations

As discussed before, the current distribution inside the conductor was measured by rotating Hall sensors in the current distribution measurement system (CDMS). Figure 2.16 shows the 2-D view of the feeder lines at the CDMS location and at the terminal boxes. The trajectory of the Hall sensors is also mentioned. The magnetic field profile at the Hall sensor location was affected by terminal boxes as well and therefore this effect has also been considered in numerical calculations. Figure 2.17 shows the measured and numerically calculated results of the magnetic fields by rotating Hall sensors. These results show that the desired NUCD was successfully established before each experiment.

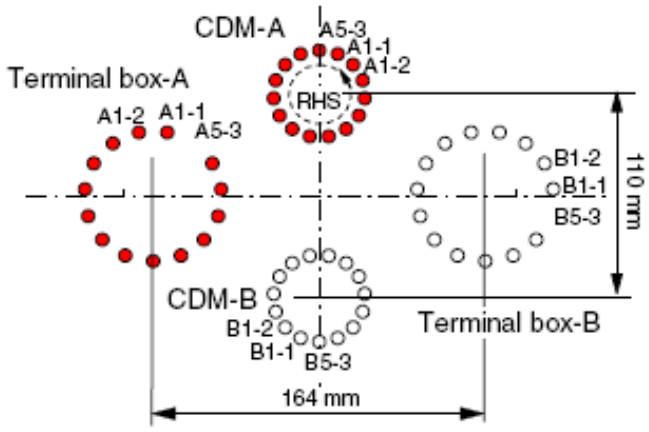

Fig. 2.16: 2-D view of the feeder lines at current distribution measurement system (CDMS) and terminal boxes. The trajectory of the rotating Hall sensors is shown by the arrow.

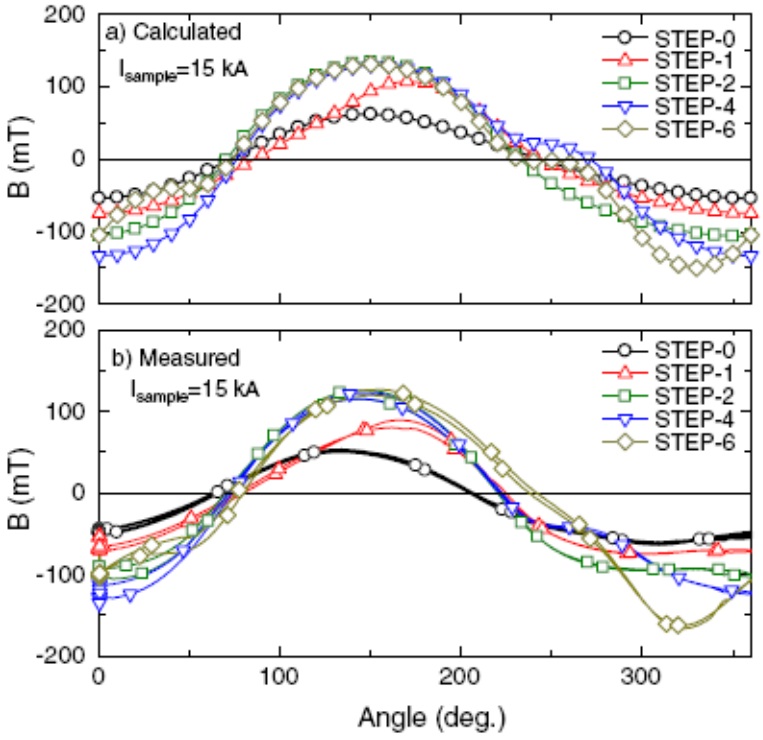

Fig. 2.17: (a) Calculated and (b) measured rotating Hall sensor signals. In (b), the clockwise and counter clockwise measurements are plotted.

2.3.3 Stability margin with uniform and non-uniform current distributions in the conductor

The stability margin measurements were carried out with uniform and non-uniform current distributions in the conductor to directly examine the effects of non-uniformity of the current on the stability. The experimental conditions were kept same for all these measurements. Figure 2.18 shows the experimental results of the stability margin measurements.

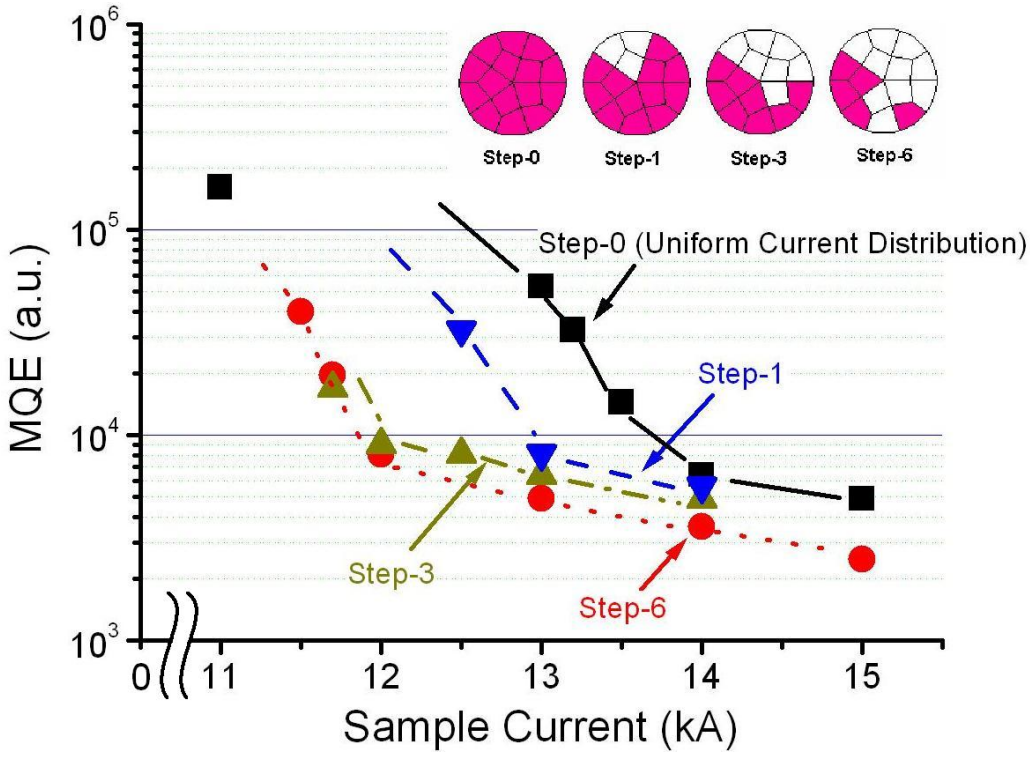

Fig. 2.18: Minimum Quench Energy (MQE) vs. sample current with uniform current and different patterns of non-uniform current distributions in the conductor. Here MQE refers to the minimum induction heater energy, which causes a quench in the conductor. The induction heater was not calibrated and therefore the unit is shown as arbitrary unit. MQE is determined as the square of the discharge voltage of the capacitor through induction heater. The bias field at the conductor was 6.1 T.

As shown in Fig. 2.18, the stability of the conductor was found to decrease significantly due to non-uniform current distribution, especially in the so-called transition region from well-cooled to ill-cooled region. This is a very important result, which clearly indicates that the stability of a bare strands conductor also suffers from non-uniformity in the current even though the current redistribution among the strands is rather easy compared to insulated strands conductor such as DPC coil conductor.

Figure 2.19 is the reproduction of Fig. 2.18 showing the experimentally observed limiting currents with uniform and non-uniform current distributions.

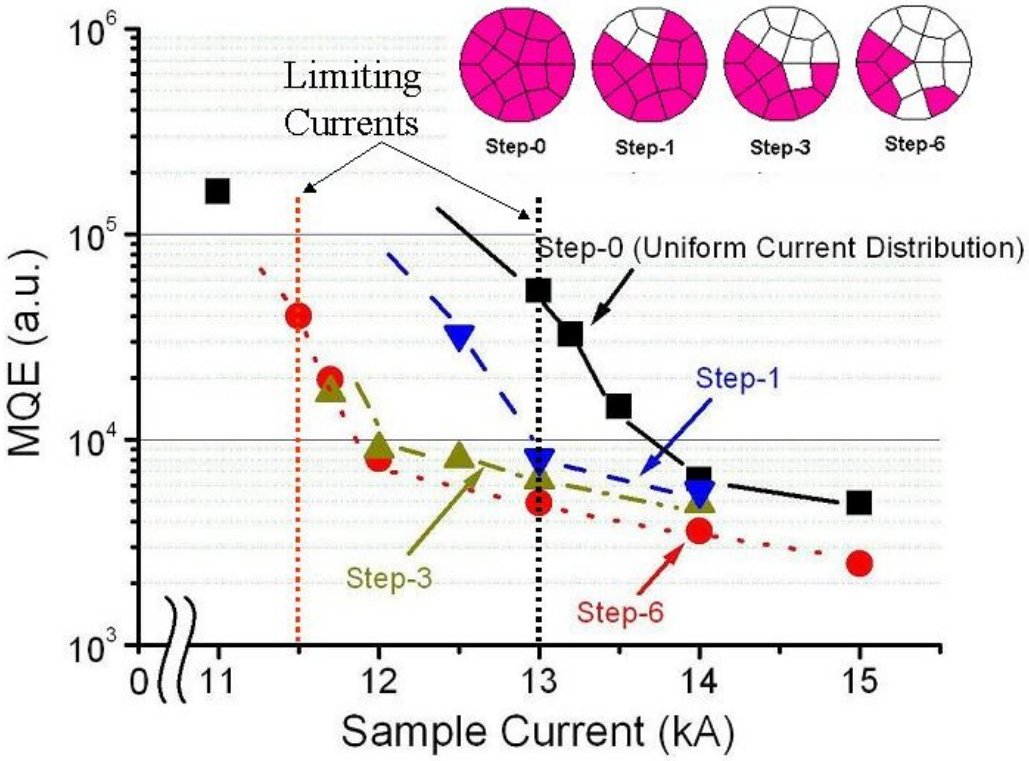

Fig. 2.19: Limiting currents with uniform and non-uniform current distributions in the conductor. Limiting currents are approximately 13 kA and 11.5 kA with uniform and step-6 non-uniform current distributions, respectively. The bias field at the conductor was 6.1 T.

Figure 2.19 indicates that the limiting current, which separates the well-cooled region and ill-cooled regions, decreases from about 13 kA in uniform current distribution case to about 11.5 kA with step-6 non-uniform current distribution case. This means that if this conductor is planned to be used at about 13 kA in 6 T, it may not perform as per expectation due to the non-uniformity in the current, which reduces the stability margin and the limiting current. Hence, these results suggest that the non-uniform current distribution should be considered even for non-insulated conductors as well. However, the operating current in SST-1 is 10 kA, and therefore it is expected that SST-1 magnets should be operated stably in steady state conditions.

2.3.4 Stability margin at different coolant pressures

As an academic interest, the stability margin of the CICC was measured also by varying the coolant pressure. Hence, the stability margin was measured in supercritical and liquid helium conditions.

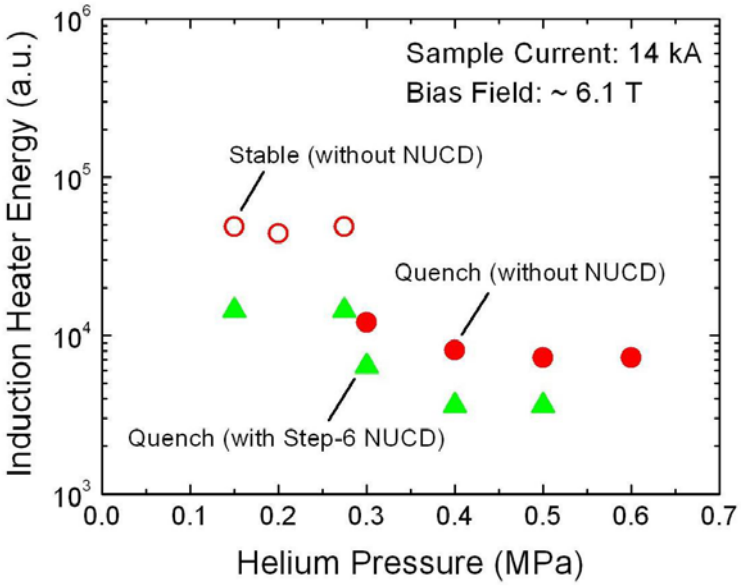

Fig. 2.20: Measured stability margin at different helium pressures. The stability margin increases significantly in liquid helium below critical pressure of 0.23 MPa. The quench was not observed in liquid helium due to the limitation on induction heater. The sample current was kept at 14 kA under a bias field of 6.1 T during these measurements.

Figure 2.20 shows the results of these measurements with uniform and step-6 non-uniform currents in the conductor. No significant change in stability margin was observed with increased helium pressure above 0.4 MPa. However, the conductor showed high stability in liquid helium below the critical pressure of 0.23 MPa. In case of uniform currents, the quench was not observed in liquid helium from the limitation of the induction heater voltage. The increased stability of CICC in liquid helium might be due to the large latent heat of vaporization (~ 20 J/g) of liquid helium [2.7]. Since there is no latent heat of vaporization of supercritical helium, the supercritical helium temperature increases much higher as compared with that of liquid helium for the same amount of heat input. Therefore, the superconductor quenches in supercritical helium while it remains stable in liquid helium for the same amount of induction heater energy input.

Also, in these measurements, we confirmed the reduction of stability margin due to the non-uniform current distribution.

2.3.5 Quench propagation velocity with uniform and non-uniform current distributions

Several stability measurements were done with uniform and non-uniform current distributions in the conductor. The voltage rise data observed from voltage taps attached to the sample during these measurements have been used to estimate the quench propagation velocity in the conductor. Figure 2.21 (a) shows one example of the voltage development with time after a quench initiation in the conductor at 6.1 T bias field and 14 kA with uniform current distribution. The quench velocity is estimated as 5 m/s as the quench propagated into the whole one turn sample length of 1.5 m in 0.3 s. The voltage development, in case of step-6 NUCD, at 14 kA and 6.1 T is shown in Fig. 2.21 (b). By comparing both curves, it is interesting to note that there is almost no difference in propagation velocity between two cases of uniform current and non-uniform current distribution. This might be due to the good electrical contacts between strands, which allow the current to re-distribute quickly near the quench front.

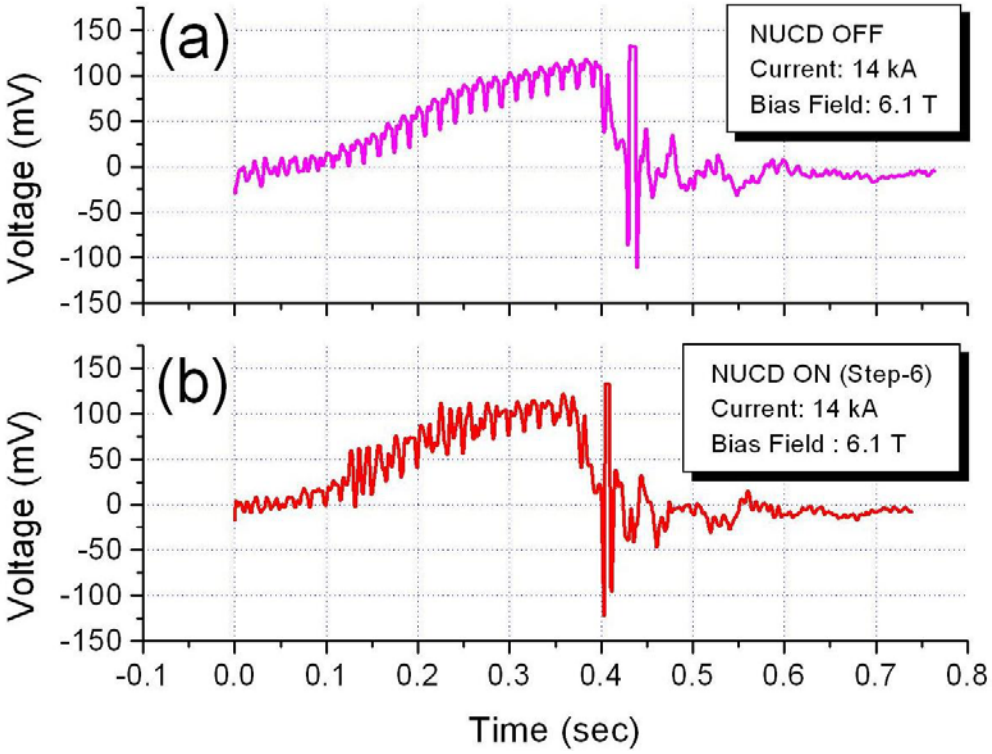

Fig. 2.21: Voltage development along the conductor length after a quench initiation at 14 kA current and 6.1 T bias field, (a) uniform current distribution case; (b) step-6 NUCD case.

The quench velocity is evaluated using well-known analytical expressions [2.8]:

$$V_p = V_{ad} \frac{(1-2y)}{[yz^2 + z + 1 - y]^{1/2}} \tag{2.2}$$

where V_{ad} represents the quench velocity under adiabatic conditions and is given by equation (2.3) whereas other terms take into account the cooling effects.

$$V_{ad} = \frac{J}{\gamma C}\{\frac{\rho k}{\theta_s - \theta_0}\}^{1/2} \tag{2.3}$$

$$y = \frac{hP(\theta_s - \theta_0)}{AJ^2\rho} \tag{2.4}$$

where J is the current density in copper, γC the specific heat per unit volume, ρ the copper resistivity, k the thermal conductivity of copper, θ_0 the bath temperature, θ_s the average of current sharing and critical temperatures, h the heat transfer coefficient, P the cooling perimeter, and A the copper cross-sectional area. The terms y and z are from steady state and transient heat transfer respectively. In this calculation, the parameter $z=0$ and therefore only y is used.

Using parameter values as J (current density in copper) = 0.215×10^{9} Am^{-2}, γC (volumetric specific heat of the strands) =3.64×10^{3} $Jm^{-3}K^{-1}$, ρ (copper resistivity) = 3.85×10^{-10} Ωm, θ_0 (bath temperature) = 4.2 K, θ_s (= T_c+T_{cs}/2) = 5.9 K, P (cooling perimeter) =0.304 m, A (copper area) = 65.07×10^{-6} m^2, h (heat transfer coefficient) = 900 $Wm^{-2}K^{-1}$, k (thermal conductivity of copper) = 400 $Wm^{-1}K^{-1}$, the propagation velocity is estimated to be 4.5 m/s, which is in agreement with the experimentally observed value of 5 m/s at 14 kA. Here, the steady state heat transfer coefficient, h, was used as a fitting parameter. The heat transfer coefficient of 900 $Wm^{-1}K^{-1}$ provides good agreement between experimentally observed propagation velocity and calculated propagation velocity at other operating currents as well. The heat transfer coefficient of 900 $Wm^{-1}K^{-1}$ has been used in numerical calculations as well discussed in the following sections.

2.3.6 Ramp rate limitation (RRL) tests

Ramp rate limitation (RRL) has been a problem for large-current capacity conductors, especially, for cable-in-conduit conductors (CICC) [2.9 – 2.12]. It has been observed by many researchers that magnets made of CICC cannot be charged rapidly up to the desired current. They happen to quench at much lower current than design current value as was observed in DPC coils. The phenomenon was called as ramp rate limitation (RRL). The origin of RRL was not known and initially AC losses were suspected to be the reason for it. However, it was found that AC losses could not explain this RRL behavior. After the

DPC coil tests, the non-uniform current distribution was suspected to be the reason for RRL. Koizumi et al. gave the plausible explanations of the degraded performance of the DPC coils based on non-uniform current distribution in the conductor.

We have carried out the RRL tests with uniform and controlled non-uniform current distributions in the present conductor. Figure 2.22 shows the NUCD patterns, which were supposed to be established in the conductor for RRL tests. Figure 2.23 shows the measurement results of the RRL tests.

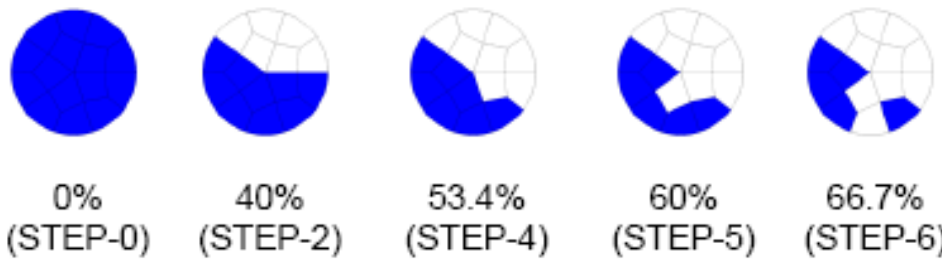

Fig. 2.22: Different NUCD patterns tried for RRL tests. Here, the indicated numbers are the percentages of strands in the conductor, which were not initially allowed to carry any current by turning on the thin film resistive heaters.

For RRL tests, the conductor was first charged up to 14 kA current and then thin film resistive heaters were turned on according to the desired NUCD pattern. The heaters were kept on for about 40 s to establish the NUCD in the conductor. Once, NUCD was established in the conductor, the current was increased up to the quench point. The ramp rates were varied from 100 A/s to maximum 800 A/s.

As shown in Fig. 2.23, the quench point decreased by increasing the ramp rate and the degree of NUCD in the conductor. These results clearly indicate that non-uniform current distribution affects the ramp rate performance of the conductor as well.

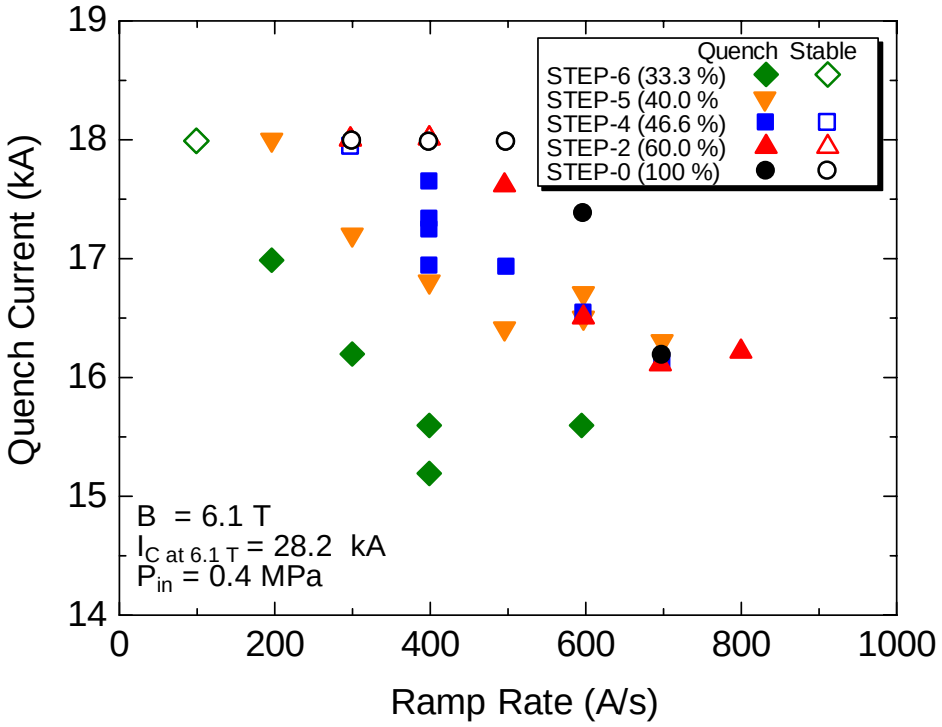

Fig. 2.23: The ramp rate limitation (RRL) performance of the conductor with different ramp rates and NUCD patterns as shown in Fig. 2.22. The initial current was always set at 14 kA. The operating conditions are indicated inside the graph itself.

The reduced performance is believed to be due to the early saturation of some of the strands with critical currents. The stability margin of the saturated strands becomes very small and therefore they quench quite easily. Then, the current of the quenching strands distributes to the neighboring strands making their currents also close or equal to the critical currents. These strands also then quench and distribute their currents to other strands. This way, the whole conductor quenches and this kind of phenomenon is called as avalanche-like quenches.

2.4 Numerical calculations for the stability margin of the CICC

Numerical calculations have been carried out to validate the experimentally observed stability margins of the CICC. This section discusses the method of numerical calculations and results.

2.4.1 Calculation of stability margin with uniform current distribution using 1-D finite element code "GANDALF"

The one dimensional finite element computer code GANDALF, developed by L. Bottura, for calculating thermo-hydraulic and electromagnetic properties of a superconducting CICC is used to calculate the stability margin of our CICC sample with uniform current distribution [2.13]. GANDALF is the numerical implementation of 1-D model for the simulation of quench initiation and quench propagation in CICC's with cooling channels. The basic conductor scheme modeled by GANDALF is shown in Fig. 2.24. The 1-D model consists of a maximum of four independent components at different thermodynamic states.

1. The strands, consisting of stabilizer and superconductor
2. The conduit, including insulation and jacket
3. The bundle helium, surrounding the strands in the cable
4. The hole helium, flowing in an independent passage

The temperatures of these four components are treated separately and the energy balances are coupled through heat transfer coefficients at the contact (wetted) surfaces. If a CICC doesn't have any central channel for helium flow (like the one we used in our experiment), the hole area can be set to zero for excluding the differential equations associated with the central channel flow. The conductor length, or flow path, is modeled

along its length using linear finite elements. At each node, 8 degrees of freedom are defined as shown in Fig. 2.25.

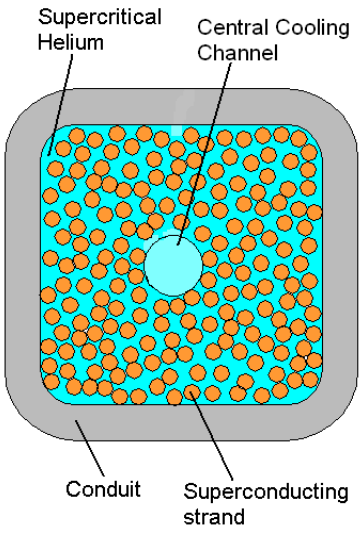

Fig. 2.24: Schematic of a CICC (with central cooling channel) modeled in GANDALF.

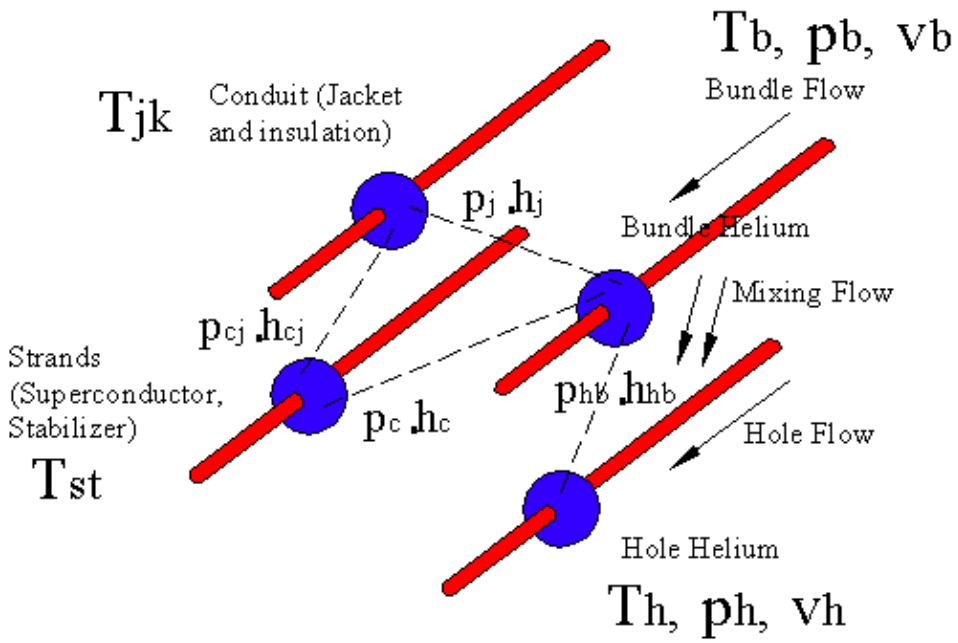

Fig. 2.25: Basic finite element, used in GANDALF, showing the degrees of freedom and the thermal and flow couplings among components.

The choice of superconductor, material properties, boundary conditions, current and field conditions etc. are incorporated into the input file by choosing appropriate flags. GANDALF allows incorporating the user subroutines for heat transfer coefficients, heat input to the conductor, magnetic field conditions, boundary conditions, current conditions, material properties etc.

GANDALF treats the conductor as a monolith with an equivalent stabilizer and superconductor area and therefore cannot treat the non-uniform current distribution among the strands of the conductor. Therefore, the stability margins have been calculated using GANDALF for uniform current distribution cases only.

The bias field distribution along the conductor (Fig. 2.26), large copper area at the lap joint, external heater pulse (half-cycle sinusoidal pulse of 2 ms duration, Fig. 2.27), and heat transfer coefficient are incorporated by using external user subroutines.

The heat transfer coefficient, h, between the conductor bundle and surrounding supercritical helium is considered either $h_t h_k/(h_t+h_k)$ $Wm^{-2}K^{-1}$ or 900 $Wm^{-2}K^{-1}$, whichever is higher. The symbols h_t and h_k represent the transient heat transfer coefficient and Kapitza conductance respectively. Steady state heat transfer is included as a lower limit on the value of h as 900 $Wm^{-2}K^{-1}$ as obtained from quench propagation velocity data, discussed in the previous section. A cosine square shaped external heat pulse is modeled, which describes the heat input from a half-cycle sinusoidal magnetic field pulse [2.14]. The GANDALF calculations have been done by assuming closed system to simulate the real experimental conditions. GANDALF and experimental results are compared in Fig. 2.25. GANDALF results with default heat transfer coefficient (~280 $Wm^{-2}K^{-1}$) are also plotted in Fig. 2.28 for comparison. In our experiments, the induction heater was not calibrated separately and therefore experimental results are calibrated by GANDALF results at 15 kA current in ill-cooled region.

As shown in Fig. 2.28, the GANDALF results are in good agreement with experimental results when steady state heat transfer coefficient is considered as 900 $Wm^{-2}K^{-1}$. Therefore, the same value of heat transfer coefficient is used in another code, AQUAPS for calculating the stability margin of the conductor with NUCD, discussed in the next section.

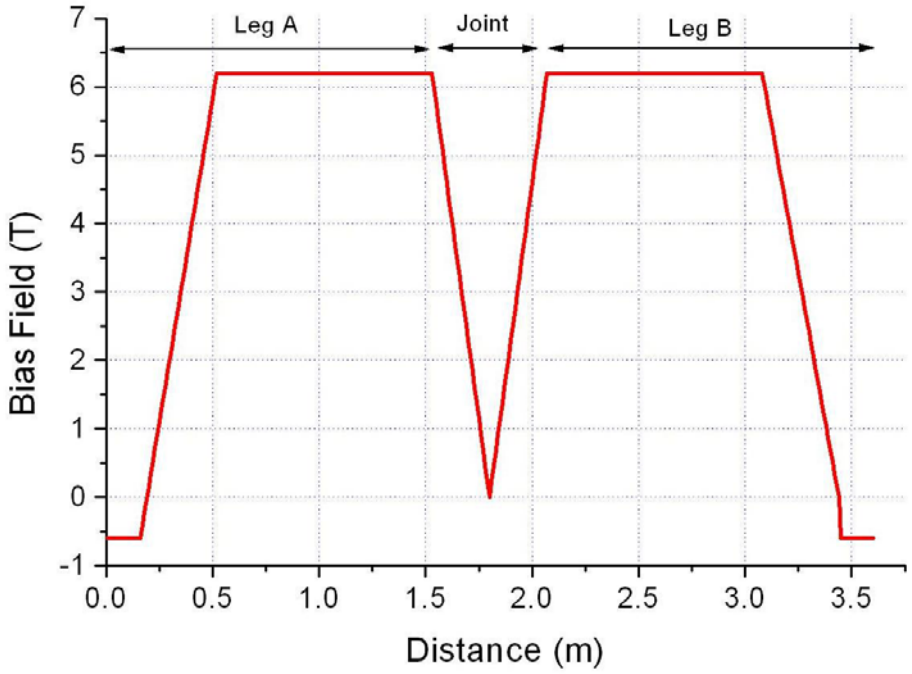

Fig. 2.26: Bias magnetic field distribution along the length of the conductor used for GANDALF calculations.

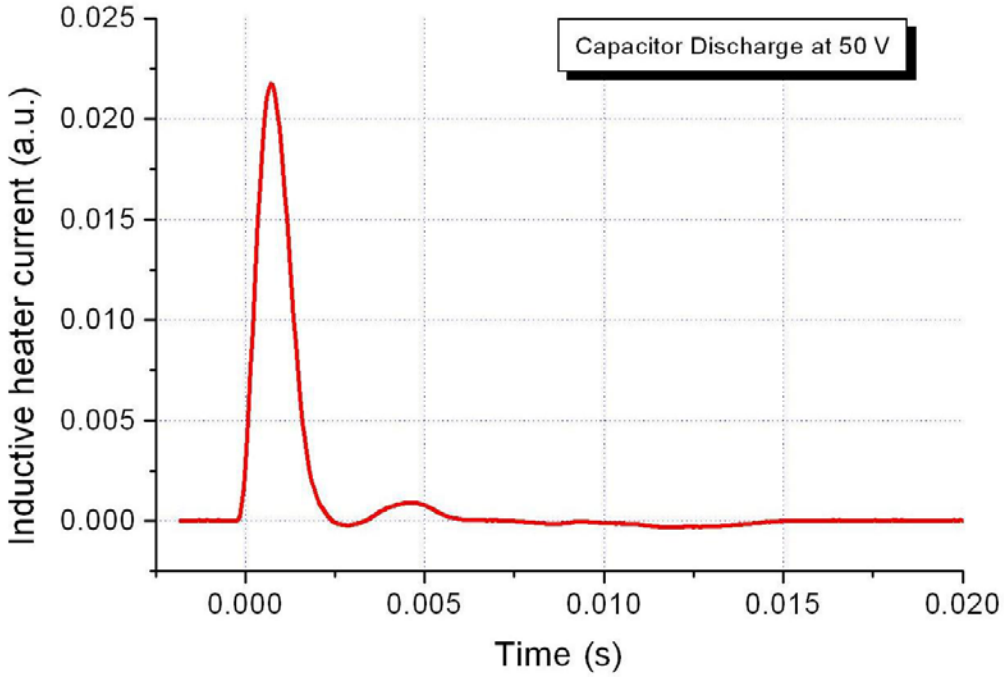

Fig. 2.27: An example of measured induction heater current after a discharge of a capacitor at 50 V.

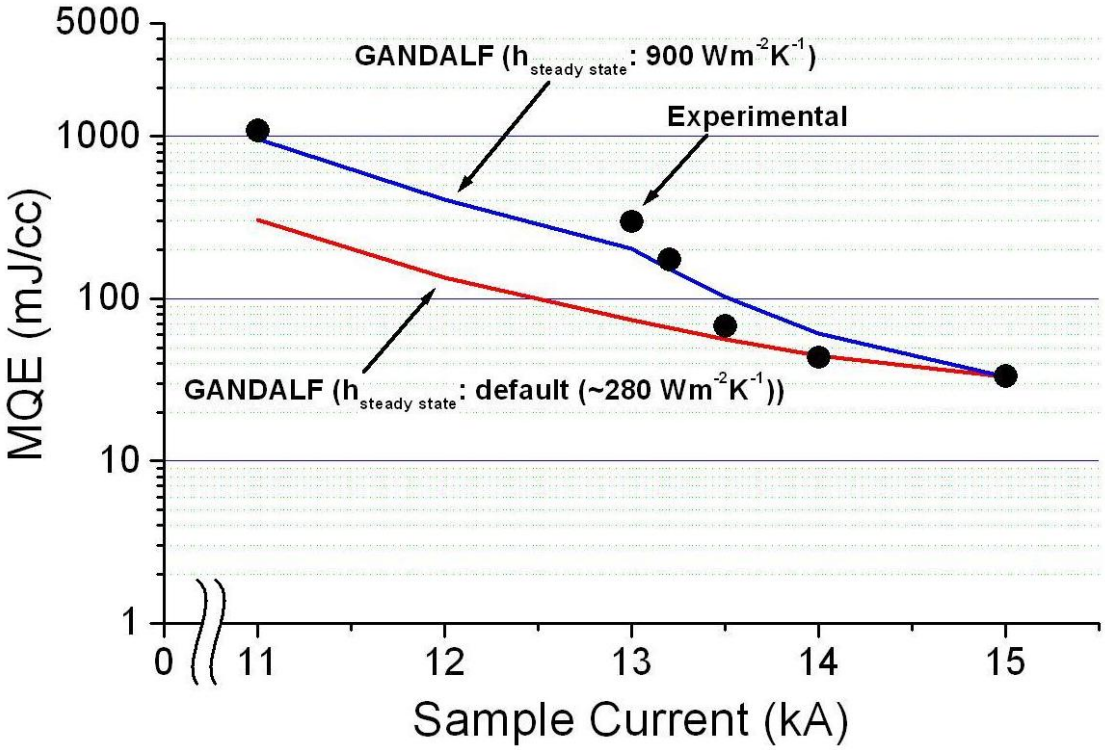

Fig. 2.28: GANDALF calculation results of stability margin. The heat transfer coefficient is used as a fitting parameter. The experimental results are calibrated with the GANDALF results at 15 kA and are shown for comparison. Numerical and experimental results are in good agreement.

2.4.2 Calculation of stability margin with non-uniform current distribution using "AQUAPS" code

Since GANDALF cannot consider NUCD in the CICC, the stability margin of the conductor with NUCD are calculated by another code AQUAPS, developed by K. Seo [2.15]. The CICC is modeled as a distributed electric circuit to calculate the current re-distribution and voltage developments along the conductor length. The superconducting strands are modeled as non-linear resistances as a function of temperature, current, and

magnetic field. The heat accumulation rate, q, in the strands is calculated by

$$q = R_{sc}(I,B,T)I^2 + q_{cont} + q_{ext} - Ph(T - T_0) \tag{2.5}$$

where q_{ext}, q_{cont}, P, h and T_0 are the external heat, heat generation due to the contact resistances between strands, cooling perimeter, heat transfer coefficient to helium and bath temperature, respectively. No heat conduction along the strands is considered. To make the calculations simple and time effective, the second stage sub-cables are assumed to be single superstrands, which are twisted into two final stages as 3 × 5 with 130 mm and 290 mm twist pitch lengths as shown in Fig. 2.3 (b). The self and mutual inductances between superstrands are calculated by Neumann's formula.

$$M = \frac{\mu_0}{4\pi}\iint \frac{\vec{ds}_1 . \vec{ds}_2}{\vec{r}} \tag{2.6}$$

where ds_1, ds_2 are two current elements and r is the distance between them.

The electric contact conductance per meter and heat transfer coefficient between two superstrands are calculated as a function of distance between them and are considered as 10^5 siemens and 6000 $Wm^{-2}K^{-1}$, respectively when they are in contact (the contact area is assumed as 1/16 of the whole surface area of the superstrand). A constant heat transfer coefficient between superstrands and liquid helium is considered as 900 $Wm^{-2}K^{-1}$, which is deduced from quench propagation velocity data as discussed in the previous sections. The cooled perimeter of one superstrand is considered as 5/6 of the total surface area of 9 basic strands of the CICC.

Figure 2.29 shows the calculated stability margin for uniform and non-uniform current distributions. The calculated results are qualitatively consistent with experimental results shown in Fig. 2.18. The stability margin decreases due to NUCD in the conductor and limiting current shifts towards the lower current values. The step-6 NUCD is the most severe and degrades stability margin significantly even in the well-cooled region.

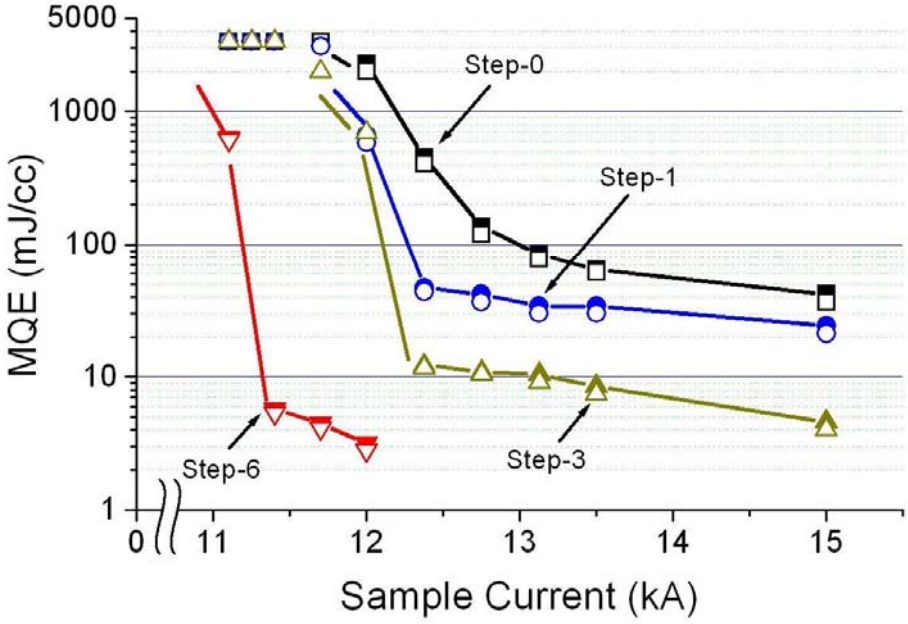

Fig. 2.29: Calculated stability margin using AQUAPS code for different NUCD patterns. Open and close symbols correspond to the stable and quench conditions respectively. The numerical results are consistent with experimental results as shown in Fig. 2.17.

2.5 Summary

Stability margin of the bare strands NbTi/Cu cable-in-conduit conductor has been measured as a function of current with uniform and non-uniform current distributions in the conductor. The ramp rate performance of the conductor was also checked with uniform and non-uniform current distributions. Numerical calculations using GANDALF and AQUAPS codes have been carried out and have been found to be consistent with the experimental results. Broadly, the following conclusions can be drawn.

1. Despite good electrical contacts between strands for current re-distribution (in bare strands conductor), it was found that non-uniform current distribution affects the stability margin of the conductor significantly, especially in ill-cooled and transition regions.
2. Due to non-uniform current distribution, the limiting current shifts towards the lower current values.
3. In our experiments, the step-6 NUCD was the most severe case and degrades stability margin significantly even in well-cooled region. Hence, this kind of situation should be avoided in a CICC magnet, for example, by having a good terminal joint design [2.16]. This information might be useful for ongoing projects like ITER and JT-60SA.
4. Based on the results of bare strands CICC, it is recommended to examine the stability of a simple stacked HTS conductor where NUCD might occur due to the inductance mismatching. The stability of the HTS conductor is supposed to be high at elevated temperature of 20 K, but it is recommended to examine whether avalanche-like quenches happen in HTS conductors as well or not which eventually can degrade the overall stability of the HTS conductor.

The next chapter discusses some issues of the HTS conductor stability with non-uniform current distributions.

Chapter 3

LTS/HTS hybrid conductors

As discussed in Chapter 2, the non-uniform current distribution affects the stability of bare strands large-current capacity conductors even though the current redistribution is rather easy compared to insulated strand conductors, which are more likely to suffer from non-uniform current distribution. Our experimental results showing the degradation in stability margin due to non-uniform current distribution in a bare strands cable-in-conduit conductor suggest examining the effect of non-uniform current distribution in the proposed simple stacked non-insulated HTS conductor as well even though the stability of the HTS conductor is supposed to be high even with indirect cooling. This chapter discusses the method and results of the stability tests of HTS conductor with non-uniform current distribution.

3.1 Purpose and concept of LTS/HTS hybrid conductors

The main purpose of LTS/HTS hybrid conductor was to test the stability of a HTS conductor with non-uniform current distribution. For this purpose, we devised an innovative approach and proposed a completely new idea of LTS/HTS hybrid conductor. LTS/HTS hybrid conductor is made by replacing the conventional stabilizer, such as pure aluminum, from solid type conductor, by HTS tapes. Hence, the LTS/HTS hybrid conductor uses both LTS and HTS superconductors together. Here, the transport current flows in LTS whereas HTS is used only as a stabilizer to LTS in a way as pure aluminum is used. In fact, our proposed LTS/HTS hybrid conductor is the world's first superconducting conductor using both LTS and HTS together.

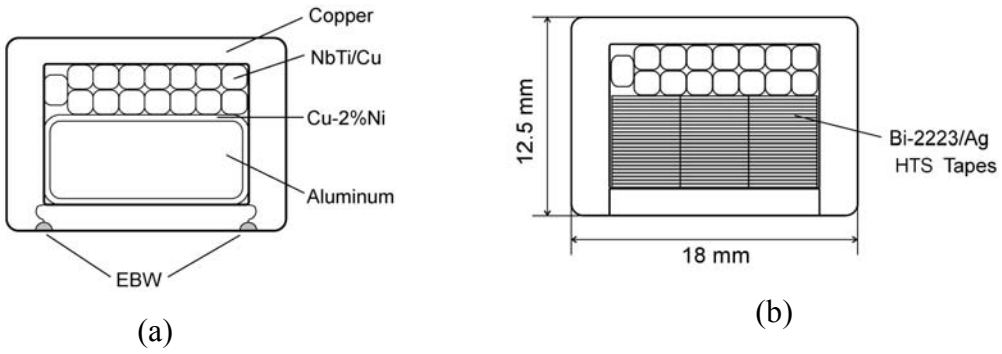

Fig. 3.1: Cross-sectional views of (a) the conventional pure aluminum-stabilized solid-type superconducting conductor used for the LHD helical coils; (b) LTS/HTS hybrid conductor. In the hybrid conductor, the original pure aluminum is replaced by HTS tapes.

Figure 3.1 shows the conventional solid type LTS conductor stabilized by pure aluminum as well as the LTS/HTS hybrid conductor after replacing pure aluminum by HTS tapes. The HTS tapes are just soldered to the LTS part. The HTS tapes are first bundled by simply stacking them together and then soldered to LTS part of the conductor. This way, the HTS part in hybrid conductor is just like the proposed simple stacked HTS conductor. The main idea to test HTS part in hybrid conductor is as follows.

Initially, the transport current flows in the LTS part of the conductor (the HTS part is missing at the current lead terminals and therefore current goes to LTS part only). After charging the conductor up to a desired current value, the heat input (using thin film resistive heaters) into the conductor induces a normal zone in the LTS part and therefore the transport current starts to transfer in stabilizer, which is the bundle of HTS tapes. The current first transfers to the HTS layer nearest to the LTS part until it is saturated with critical current and then transfers to other layers of HTS tapes. This way, the HTS part in hybrid conductors experiences the extreme non-uniform current distribution. The details of the experimental sample, method and results are discussed in the following sections.

Second purpose of the hybrid conductor concept during this research was to improve the stability of the solid type conductors after replacing the pure aluminum stabilizer by HTS tapes. The next section discusses the stability of the solid type conductors and LTS/HTS hybrid conductors.

3.2 Stability of solid-type superconductors

Large current capacity with high current density is supposed to be achieved by solid composite-type low-temperature superconducting (LTS) conductors when they are extra-stabilized with low resistive metals. Such an example is seen in the aluminum-stabilized superconductor used for the helical coils of the Large Helical Device (LHD) [3.1]. However, it was found in this conductor that the cold-end recovery current was lower than the expected value due to the enhancement of the magnetoresistivity of aluminum-copper composites by the generation of "Hall currents" under high magnetic field. A CuNi insulating layer was added as a cladding material around the pure aluminum in order to mitigate the generation of Hall currents [3.2], and the effective resistivity was reduced and the recovery current was increased to meet the required specification for the LHD operation point of 13 kA at 7 T. Fig. 3.2 shows the schematics of the Hall current generation with and without CuNi layer. However, it was later found that in the transient process, the minimum propagation current of this conductor was lower than the recovery current (which can be found only in the steady-state). This is due to the long magnetic diffusion time constant in the pure aluminum (~50 ms with 5N purity and 6 mm thickness), and asymmetrical propagation velocity was found. With a transport current just above the minimum propagation current, it has been also found that the normal-zone propagates only in one direction along the conductor by forming a "traveling normal-zone" [3.3, 3.4]. Due to this fact, partial and transient normal-transitions have been observed with the LHD helical coils [3.5].

The magnetic diffusion time constant, τ, can be estimated by the following equation.

$$\tau = \frac{\mu_0 d^2}{\pi^2 \rho} \tag{3.1}$$

where d and ρ are the thickness and resistivity of the aluminum respectively.

Figure 3.3 shows the experimental result of the magnetic diffusion time constant of the LHD conductor. Figure 3.4 shows the observation of asymmetrical and one side traveling normal zone propagations.

If these problems with composite-type LTS conductors are solved, the cryogenic

stability could be sufficiently improved, and this type of conductors may still be used in the future middle-scale or large-scale magnets. In this connection, for the purpose of extending the basic research on the cryogenic stability of composite-type superconductors, high-temperature superconducting (HTS) tapes were examined as stabilizers in place of pure aluminum. Since HTS wires have effectively zero resistivity as long as the transport current is lower than the critical current, they can be regarded as ideal stabilizers. For the HTS, we used Bi-2223/Ag wires that have been developed in recent years for many applications [3.6, 3.7].

Though it is not our intention to apply hybrid conductors for real magnets at the moment, one may consider a sufficiently long hybrid conductor, and its properties, especially concerning the cryogenic stability, can be examined in comparison to the conventional metal-stabilized conductors. Here, we may assume that the stabilizing HTS wires are to be used in pieces (subdivided in the longitudinal direction) so that the mechanical brittleness and relatively large AC loss generation of the HTS wires can be mitigated. In this situation, we may also assume that the transport current initially flows only in the LTS wires. When there is a normal-transition in the LTS wires due to some disturbances, the transport current may immediately transfer to the HTS, and thus, the heat generation can be suppressed and a full quench might be avoided.

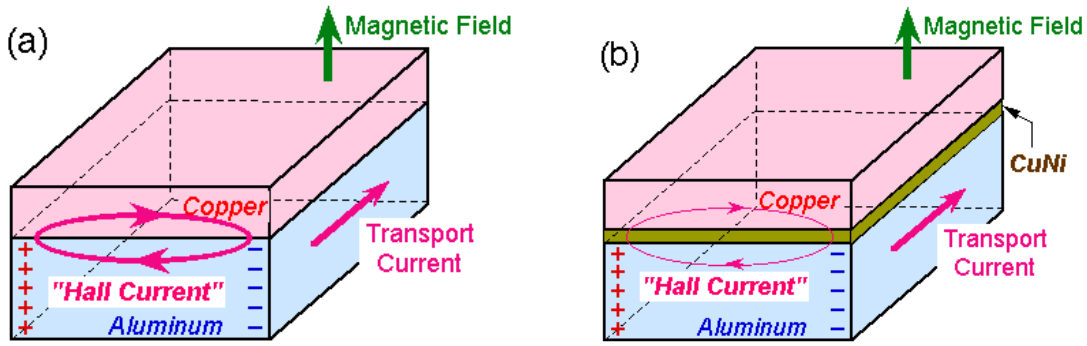

Fig. 3.2: Schematic presentation of generation of Hall currents at the interface of pure aluminum and copper (a) without CuNi layer between copper and aluminum; (b) with CuNi layer between copper and aluminum. Due to the CuNi layer, Hall currents are reduced.

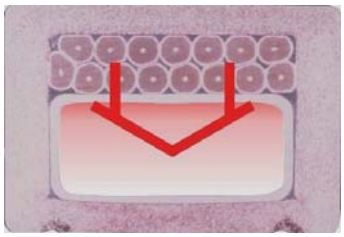

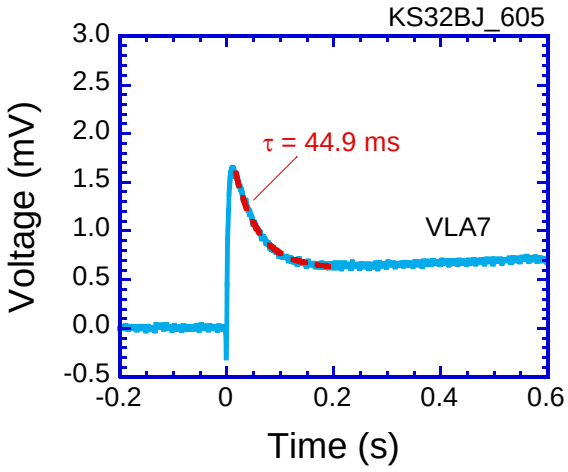

(a) (b)

Fig. 3.3: (a) Schematic representation of current diffusion from the superconducting wires to the pure aluminum stabilizer in the LHD conductor; (b) Voltage rise after a normal-zone appearance. The estimated current diffusion time constant is ~ 45 ms.

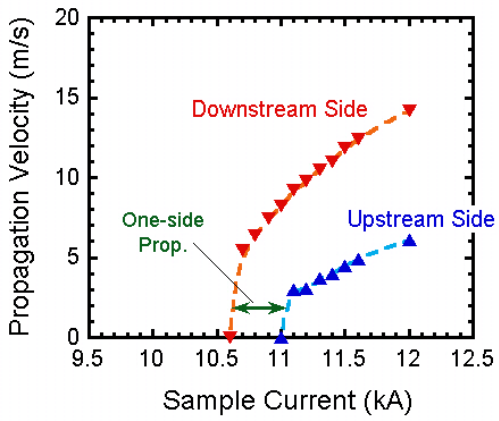

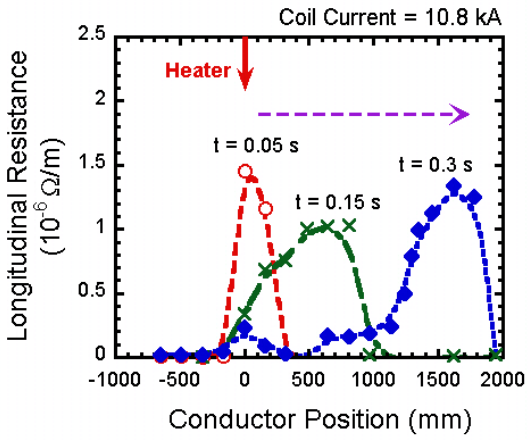

(a) (b)

Fig. 3.4: (a) Measured quench propagation velocity in LHD conductor. Propagation velocity is different in upstream and downstream current directions and therefore called as asymmetrical normal zone propagation [3.4]; (b) Observed longitudinal resistance (or voltage) only in one direction at 10.8 kA current. The spatial profile of longitudinal resistance indicates it as a traveling normal zone [3.4].

To validate the concept of LTS/HTS hybrid conductor toward the improvement in the stability of the solid type conductors, the proof of principle experiments on small scale samples were carried out, which are discussed in the next section.

3.3 Proof-of-principle (POP) experiments on small-scale LTS/HTS hybrid conductors

For the proof-of-principle (POP) experiments, small scale NbTi/Cu Rutherford cable was used to prepare different samples of hybrid conductors as well as the pure aluminum stabilized conductors. The details are discussed in the following sections.

3.3.1 Experimental set-up

The experimental set-up including the bias magnet, conductor samples, and experimental methods are discussed in this section.

Bias field magnet and test facility

A solenoid wound of NbTi/Cu wire and producing a central field of 9 T was used to carry out the experiments. Figure 3.5 shows the cross-sectional view of the solenoid with dimensions. The solenoid has about 93 layers with about 339 turns in each layer. The wire cross-section used in the solenoid is about 0.27 mm^2. The nominal current to produce 9 T field at the center of the solenoid is 49 A.

Test conductors and sample coils

The cross-sectional views of an NbTi/Cu conductor and corresponding aluminum stabilized conductor and hybrid conductors are shown in Fig. 3.6. The aluminum stabilized conductor and hybrid conductors are prepared by soldering the pure aluminum (RRR ~ 7000) and Bi-2223/Ag HTS tapes onto the NbTi/Cu conductor. First, the

NbTi/Cu conductor was wound onto a Bakelite bobbin and tested. This test coil consisted of one layer of 9 turns with a self-inductance of 3.6 μH. The solder was filled into the voids of the NbTi/Cu cable to limit the wetted perimeter. After the NbTi/Cu conductor testing, two HTS tapes were soldered onto the NbTi/Cu winding throughout the 9 turns to make the hybrid conductor test coil. The aluminum stabilized conductor test coil was prepared by soldering the pure aluminum tape onto the NbTi/Cu winding on another Bakelite bobbin. This time, the aluminum was soldered only onto the central turn of the NbTi/Cu winding. The same test coil was used to prepare another hybrid conductor test sample with three HTS tapes to see the effect of number of HTS tapes in hybrid conductors. Like the aluminum conductor sample, this time, the three HTS tapes were soldered only onto one turn of NbTi/Cu winding just below the aluminum conductor test turn. To have the same cooling conditions for all the test conductors, the space between the walls of the bobbin and NbTi/Cu cable was filled with epoxy and only the top surface of the conductors was exposed to liquid helium. The parameters of the test conductors and test coils are given in Table 3.1. The schematics of the test coil arrangement are shown in Fig. 3.7.

Experimental method and diagnostics

The schematic of the experimental set-up is shown in Fig. 3.5. The conductor samples were tested in a bias field up to 8 T using a 9 T solenoid. Because of the limited size of the cryostat, it was not possible to supply the sample current using an external power supply through current leads. Therefore, an induction method was used to charge the test coils using the bias field solenoid itself. For this purpose, the ends of the test coil windings were lap jointed. The joint resistance was evaluated to be approximately 2 nΩ. One calibrated Hall sensor was placed at the center of the test coil to measure the magnetic field during the experiments. The evaluated flux change provides the test coil currents. A Rogowski coil was also installed in the joint area for direct measurements of the test coil currents.

A thin film resistive heater attached to the lap joint of the test coil was kept turned on during the charging of the bias field solenoid so that no current was induced in the test

coil. Once the bias field solenoid was charged up to the desired magnetic field, the lap joint heater was turned off. The test coil was now charged by changing the current in the bias field solenoid. Since the winding ratio of the bias field solenoid and test coil was very large, a small current change in the bias field solenoid induced a large current in the test coil. One resistive heater attached to the test conductor, as shown in Fig. 3.8, was used for initiating a normal-zone in the test conductor. The voltage taps attached to the test coil at various locations as shown in Fig. 3.8 provide information of normal-zone growth in the test conductor. After each heater test, the test coil current was completely reduced to zero by turning on the lap joint heater. The test coil current was deduced by calculating the change of the magnetic flux linkage to the test coil using the Hall sensor.

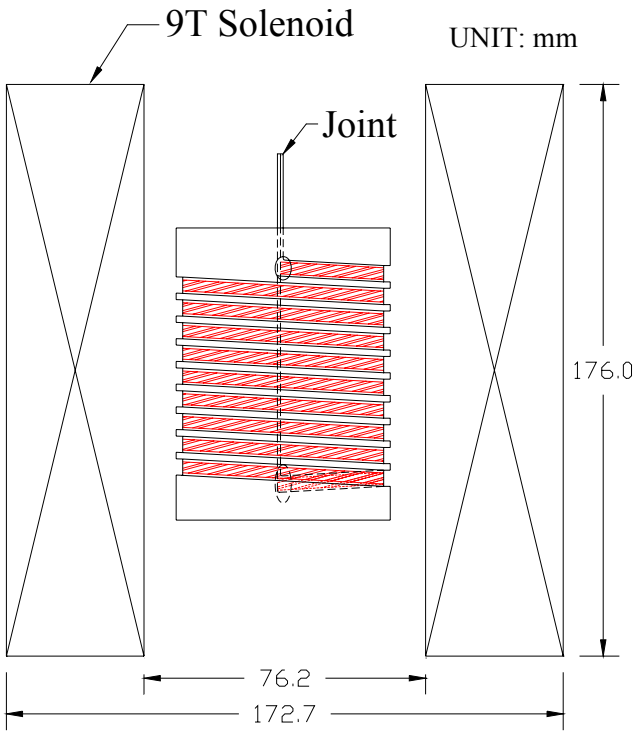

Fig. 3.5: Schematic side-view of the 9-T solenoid used for the proof-of-principle hybrid conductor experiments. The conductor sample coil is also shown. The conductor sample coil was charged by induction method by changing the current in the bias 9-T solenoid.

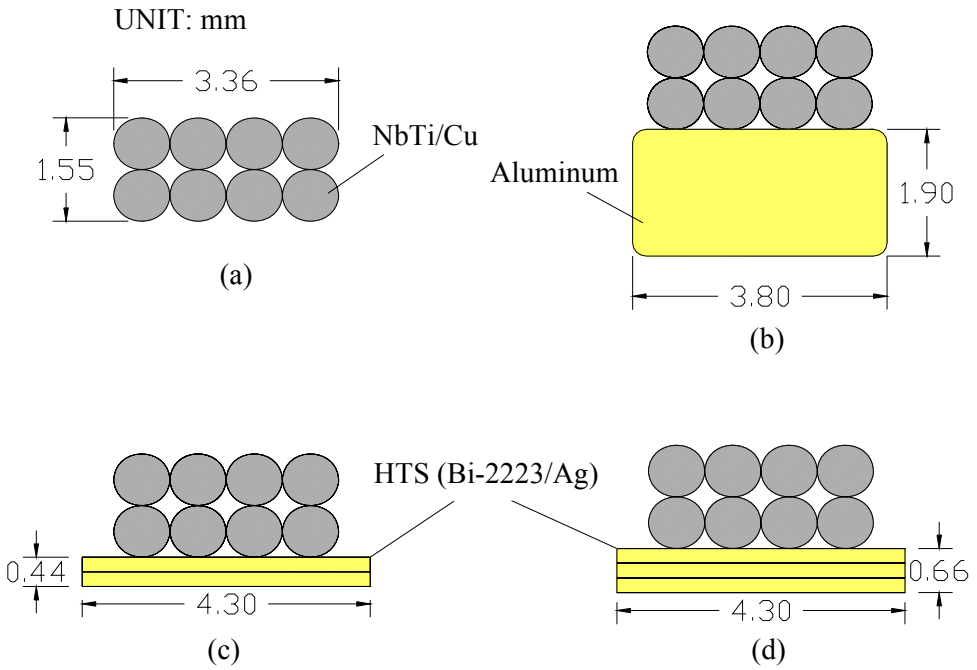

Fig. 3.6: Cross-sectional views of (a) a NbTi/Cu conductor; (b) NbTi/Cu conductor stabilized with pure aluminum; (c) NbTi/Cu conductor stabilized with two HTS tapes; (d) NbTi/Cu conductor stabilized with three HTS tapes.

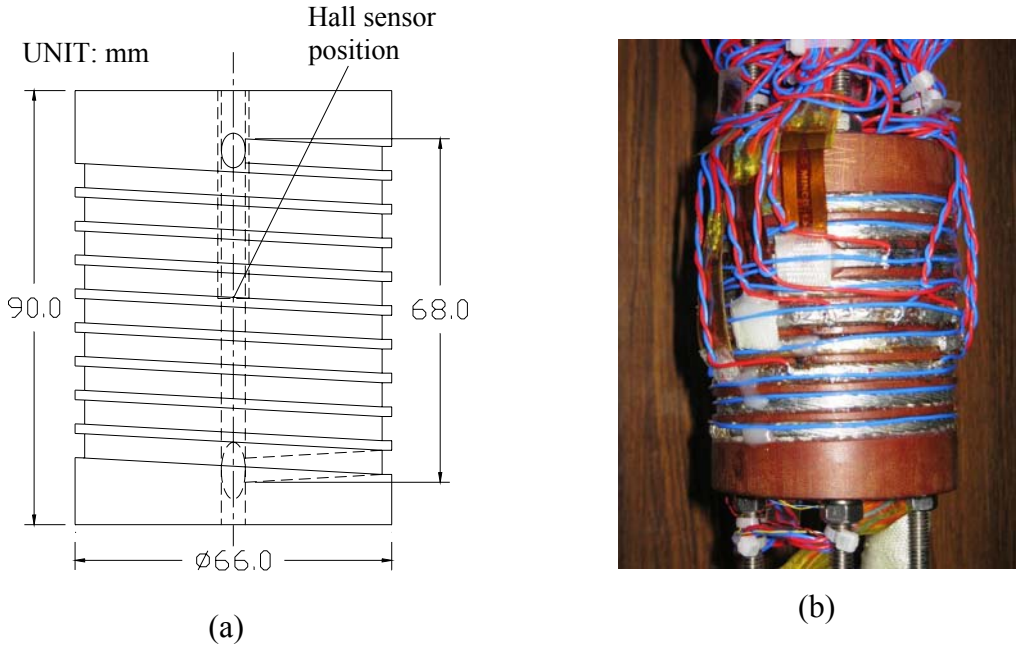

Fig. 3.7: (a) Test coil bobbin; (b) Test coil on the sample holder.

Table 3.1: Parameters of the test conductors and test coils

NbTi/Cu conductor	
Number of strands	8
Strand diameter	0.823 mm
Copper ratio	1.98
Strand Surface	Bare copper
NbTi/Cu/Al conductor	
Superconductor	NbTi/Cu
Aluminum dimensions	1.9 mm × 3.8 mm
RRR of Aluminum	7000
HTS Tape	
Superconductor	Bi-2223/Ag
Dimension	4.3 mm × 0.22 mm
Critical current at 8 T (parallel field) and 4.2 K	480 A
LTS/HTS hybrid conductors	
Superconductor	NbTi/Cu + Bi-2223/Ag
Number of Bi-2223/Ag tapes	2 or 3
Joining method	Soldering
Test sample coil	
Coil diameter	66 mm
Coil length	~ 90 mm
Number of turns	9
Bobbin material	Bakelite
Inductance	~ 3.6 μH
Mutual inductance with the 9 T bias field solenoid	~ 5.23 mH

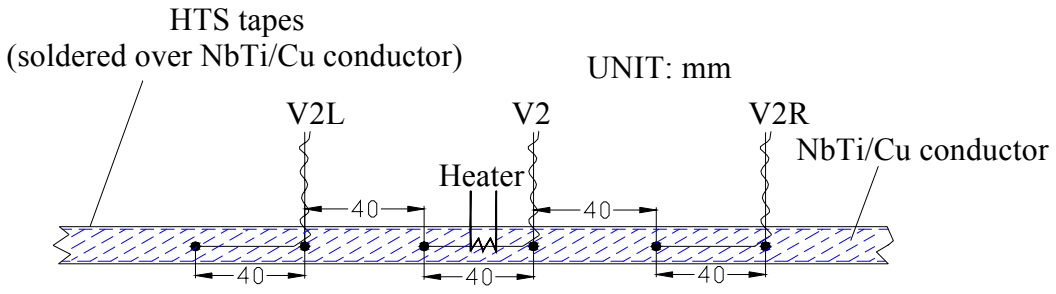

Fig. 3.8: Schematic of the heater and voltage taps arrangements on the small-scale hybrid conductor.

3.3.2 Experimental results and analyses

The experimental results of minimum quench energy (MQE) or stability margin, normal-zone propagation velocity and minimum propagation currents of different samples are discussed in this section.

Minimum quench energy (MQE)

First, the minimum quench energy (MQE) of the test conductors was measured. Fig. 3.9 shows an example of the typical waveforms observed during a normal-zone growth in the hybrid conductor. Here, V0 is the total voltage across the whole winding whereas V2, V2R, and V2L are indicated in Fig. 3.8. The magnetic field at the center of the coil is also shown. The measured magnetic field rises during the voltage developments in the test conductor. This is due to the decrease of the test coil current by the appearance of resistance. The estimated change in the test coil current during the normal-zone growth is about 5% of the initial current. Fig. 3.10 shows the measured minimum quench energies for a hybrid conductor at 7 T bias field. The MQE values were measured for all the conductor samples at 6, 7 and 8 T bias fields. The appearance of V2L or V2R was considered as quench propagation in the conductor and hence MQE was measured.

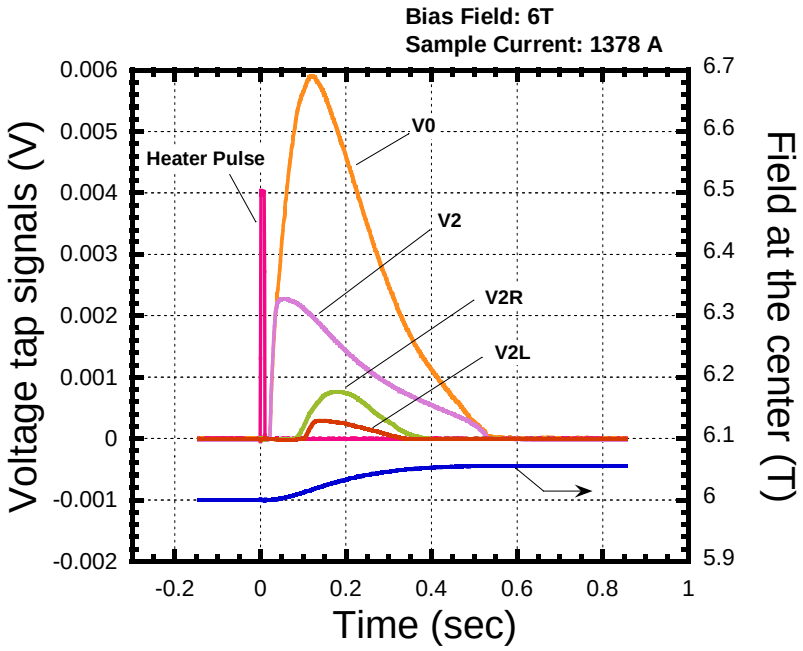

Fig. 3.9: Typical waveforms observed during the hybrid conductor (NbTi/Cu conductor stabilized with 2 HTS Bi-2223/Ag tapes) experiments

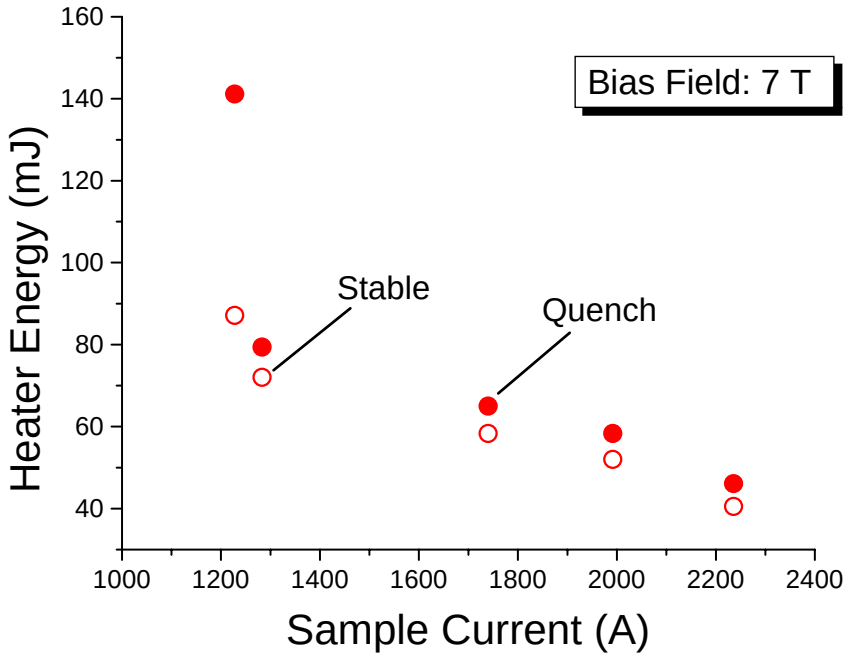

Fig. 3.10: Minimum Heater Energy to observe a quench in hybrid conductor (NbTi/Cu conductor stabilized with 2 HTS Bi-2223/Ag tapes).

Normal-zone propagation velocity

The experimental shots of minimum quench energy measurements were used to estimate the normal-zone propagation velocities in both directions along and opposite to the transport current. As shown in Fig. 3.9, we observe time delays between V2, V2R, and V2L voltage signals. The distance between the voltage taps and the time delay in the corresponding signals was used to estimate the propagation velocity. Fig. 3.11 shows the propagation velocities in both directions along and opposite to the transport current at 7 T bias field of a hybrid conductor. Here, VPR indicates the propagation from V2 towards V2R (in the same direction as the transport current) whereas VPL indicates propagation from V2 towards V2L (opposite to the transport current). Unlike above described hybrid conductors, we observed traveling normal zones in Al-stabilized NbTi/Cu conductor, which is discussed in later section.

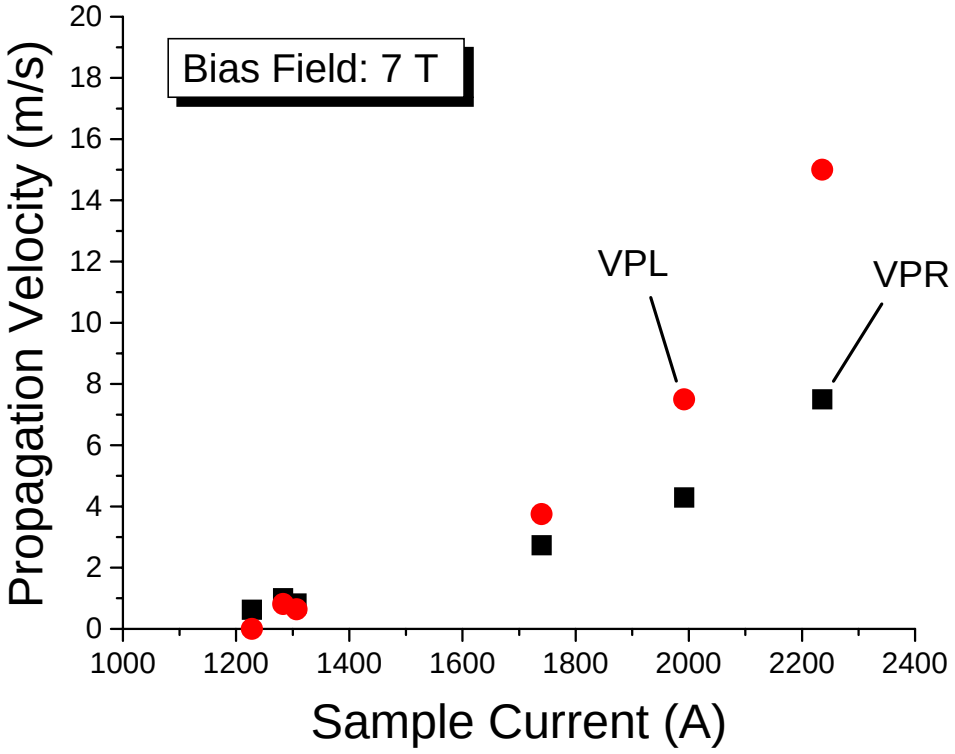

Fig. 3.11: Propagation velocities evaluated in the hybrid conductor (NbTi/Cu conductor stabilized with 2 HTS Bi-2223/Ag tapes).

Minimum propagation currents

The minimum propagation currents are the defined as the minimum transport currents over which a normal-zone just propagates along the conductor and leads to a quench. The minimum propagation currents at different bias fields for all the conductors are shown in Fig. 3.12. Here, we should note that, for the hybrid conductors, the average values of the extrapolated currents with zero velocities in both sides of normal-zone propagation are taken as the minimum propagation currents. The calculated steady-state cold end recovery currents (using Maddock's equal-area theorem) and critical currents of NbTi/Cu conductor at 4.2 K are also plotted for comparison. As shown in Fig. 3.12, the minimum propagation currents of the NbTi/Cu conductor increase significantly when it is stabilized with HTS tapes. It should be noted that the measured minimum propagation currents of the hybrid conductors were more than 1.3 times the critical currents of the HTS tapes at 17 K. The temperature rise of the hybrid conductors near the heater position was measured using Cernox temperature sensors, which increased up to around 17 K. The critical currents of the HTS tapes at different temperatures and parallel magnetic fields are shown in Fig. 3.13 [3.8].

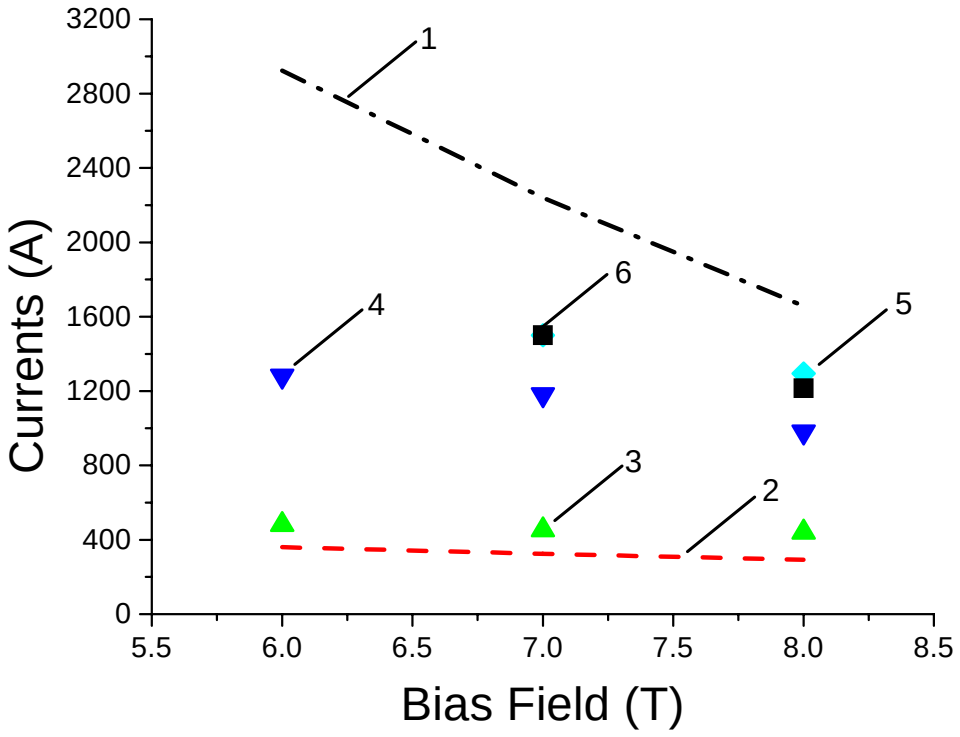

Fig. 3.12: (1) Critical currents of NbTi/Cu conductor expected at 4.2 K; (2) Calculated I_{mp} of NbTi/Cu conductor; (3) Measured I_{mp} of NbTi/Cu conductor; (4) Measured I_{mp} hybrid conductor (NbTi/Cu stabilized with 2 HTS tapes); (5) Measured I_{mp} of hybrid conductor (NbTi/Cu stabilized with 3 HTS tapes); (6) Measured I_{mp} of pure aluminum stabilized NbTi/Cu conductor.

The high-purity aluminum-stabilized NbTi/Cu conductor also showed high minimum propagation currents. But the minimum propagation currents of the NbTi/Cu conductor stabilized with 3 HTS tapes are comparable with aluminum stabilized conductor and the current density is much higher, as the cross-sectional area of HTS tapes is much lower than pure aluminum.

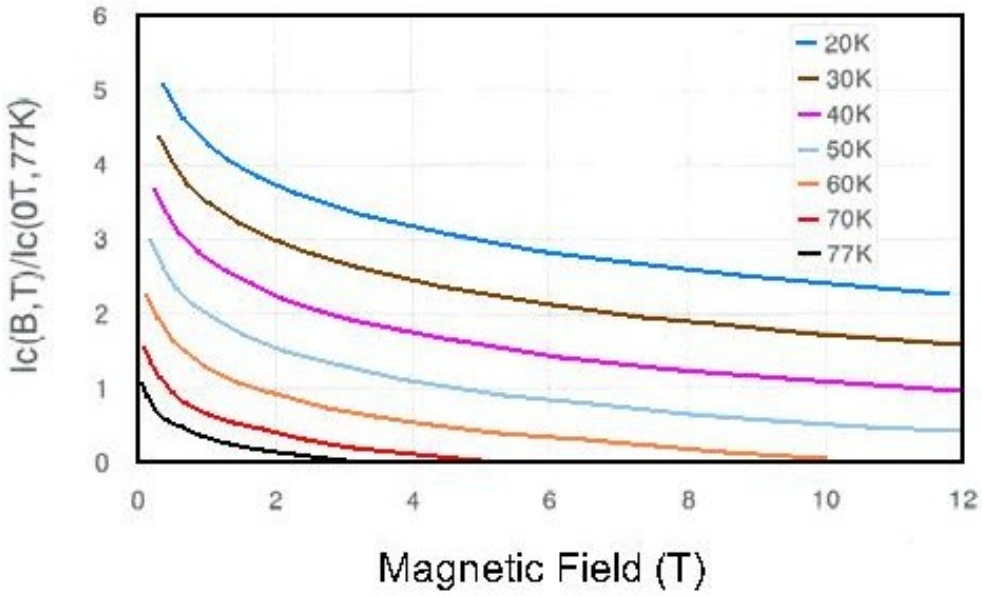

Fig. 3.13: Critical currents of the HTS tapes (used in hybrid conductors) at different temperatures and parallel bias magnetic fields [3.8].

From these experimental results, we can conclude that for the same current density, the minimum propagation currents might be significantly higher in hybrid conductors as compared with pure aluminum stabilized conductors. In other words, we can say that the stability of the stability of a solid type conductor can be improved significantly after replacing the pure aluminum stabilizer by HTS tapes.

After validating the hybrid conductor concept through POP experiments on small-scale conductors, we have also successfully carried out experiments on LTS/HTS hybrid conductors prepared by modifying the helical coil conductor for the Large Helical Device (LHD). The experimental results of these big hybrid conductors are discussed in the next section. In the big hybrid conductors, the current transfer from the LTS to the stabilizing HTS during normal-transitions and then back to the LTS after the recovery of the LTS was clearly observed by an array of Hall sensors, which confirms that the nature of stabilization in hybrid conductors is similar to the conventional normal metal-stabilized low-temperature superconductors.

Traveling normal zone in aluminum stabilized conductor

We have observed traveling normal-zones in the aluminum-stabilized conductor. The observed voltage waveforms during the normal-zone propagation are shown in Fig. 3.14. The voltage taps pair V4 is across the heater. The voltage taps pairs V5, V6, and V7 are next to V4 in the direction of the current whereas V3, V2, and V1 are next to V4 in the opposite direction. The voltage tap length is 20 mm and the distance between the consecutive voltage tap pairs is also 20 mm. As shown in Fig. 3.14, the voltage evolution with time clearly indicates a spatial profile of traveling normal-zone, which propagates only in one direction. At currents higher than 1950 A, the traveling normal-zones were observed in both directions. The reason of this behavior is under investigation. One explanation might be the Hall voltage generation as suggested for the LHD conductor [3.4].

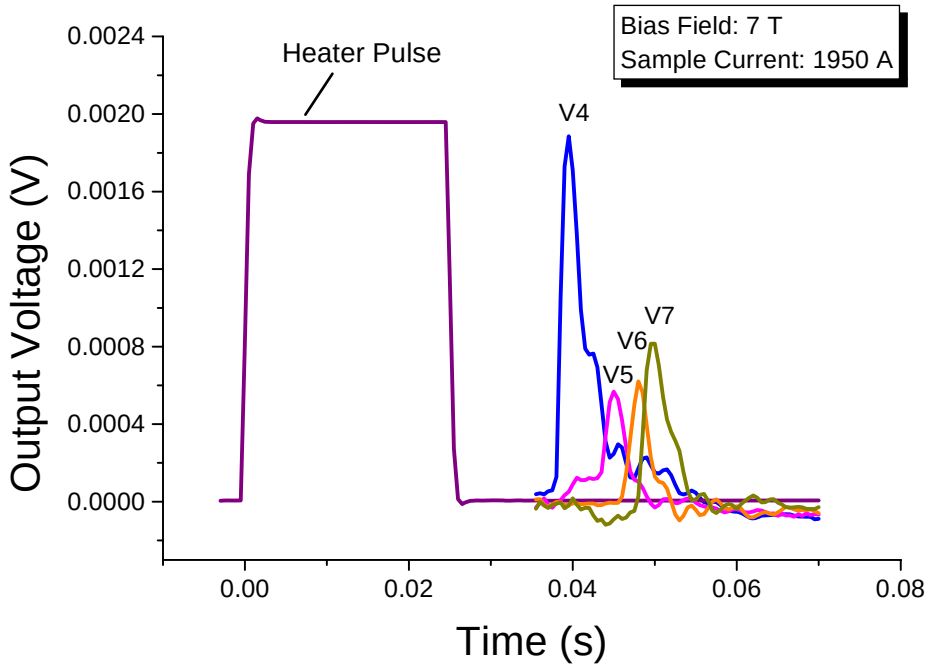

Fig. 3.14: Voltage waveforms observed during normal-zone propagation in aluminum stabilized NbTi/Cu conductor.

3.4 Experiments on large-scale LTS/HTS hybrid conductors

The concept of hybrid conductor and the improvement in stability or minimum propagation currents of the solid type conductors was validated by POP experiments as discussed in previous section. However, due to the small size of the conductors in POP experiments, it was not possible to observe the current transfer process (for example by Hall sensors) from LTS to HTS part of the hybrid conductor. The current transfer process was observed by an array of Hall sensors in large-scale hybrid conductor tests and current transfer from LTS to HTS was confirmed by numerical calculations. The details of the experimental set-up, experimental method and results are discussed in this section.

3.4.1 Experimental set-up

The experimental set-up including the conductor samples, experimental samples, and experimental method and sensors are discussed in this section.

The 9-T split coil facility was used for these experiments. The details of the 9-T facility are discussed in chapter 2.

Test conductors and experimental samples

Figure 3.15 shows the cross-sectional views of the original pure aluminum stabilized LHD helical coil conductor and two types of LTS/HTS hybrid conductors, which were tested simultaneously. Type-A hybrid conductor consists of 3 layers of HTS tapes with 10 tapes in each layer whereas Type-B hybrid conductor consists of 3 layers with 25 HTS tapes in each layer. The major specifications of the original LHD conductor and hybrid conductors are shown in Table 3.2.

Both, Type-A and Type-B, hybrid conductors were fabricated by modifying the original aluminum-stabilized conductor used for the LHD helical coils. The aluminum-stabilizer was replaced by a bundle of Bi-2223/Ag tapes. For both conductors, the

aluminum stabilizer was first removed from the original conductor and stacks of HTS tapes were inserted into the grooves where the aluminum stabilizer was originally situated. For each conductor, the HTS tapes were prepared with 900 mm length at the central region where the external magnetic field was applied, and the stacks of tapes were soldered together. The total length of each conductor was about 2 m, and the HTS tapes were imbedded also in the end regions of the conductor samples (~500 mm each). As there were gaps between the central HTS bundles and the other ones, the transport current could be initially supplied only to the (continuous) NbTi/Cu cables from the current leads. For the Type-A hybrid conductor, copper strips were also used in addition to the HTS tapes in order to fill the remaining vacant space after removing the original aluminum stabilizer. Finally, the two samples were jointed together by overlapping 200 mm length at one end of each conductor so that a hairpin like configuration was formed. The samples were tested in the bias magnetic field simultaneously, as is illustrated in Fig. 3.16. The photographs of the hybrid conductor sample are shown in Fig. 3.17.

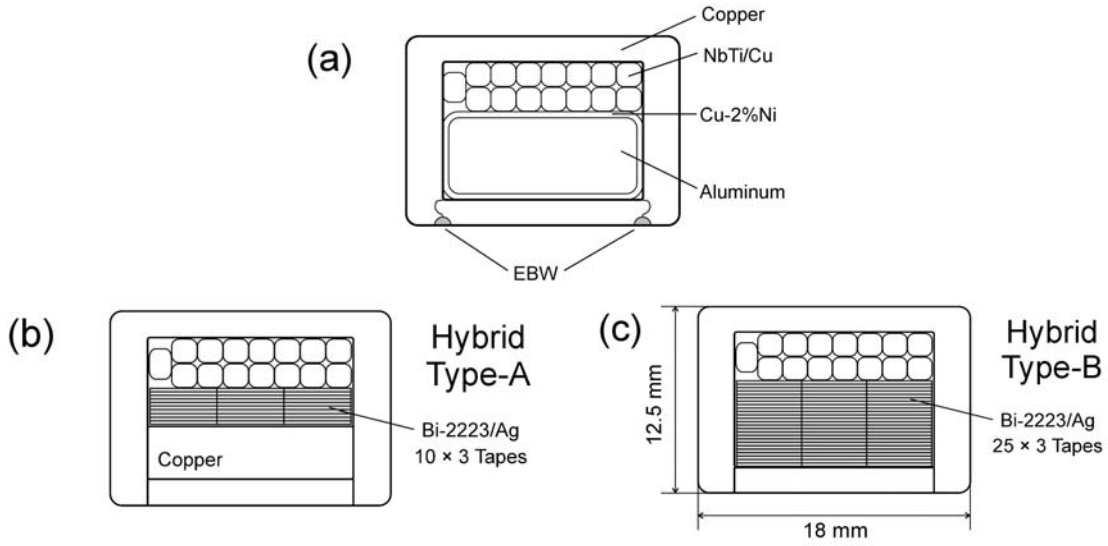

Fig. 3.15: Cross-sectional views of (a) Original LHD helical coil conductor; (b) Type-A hybrid conductor; (c) Type-B hybrid conductor.

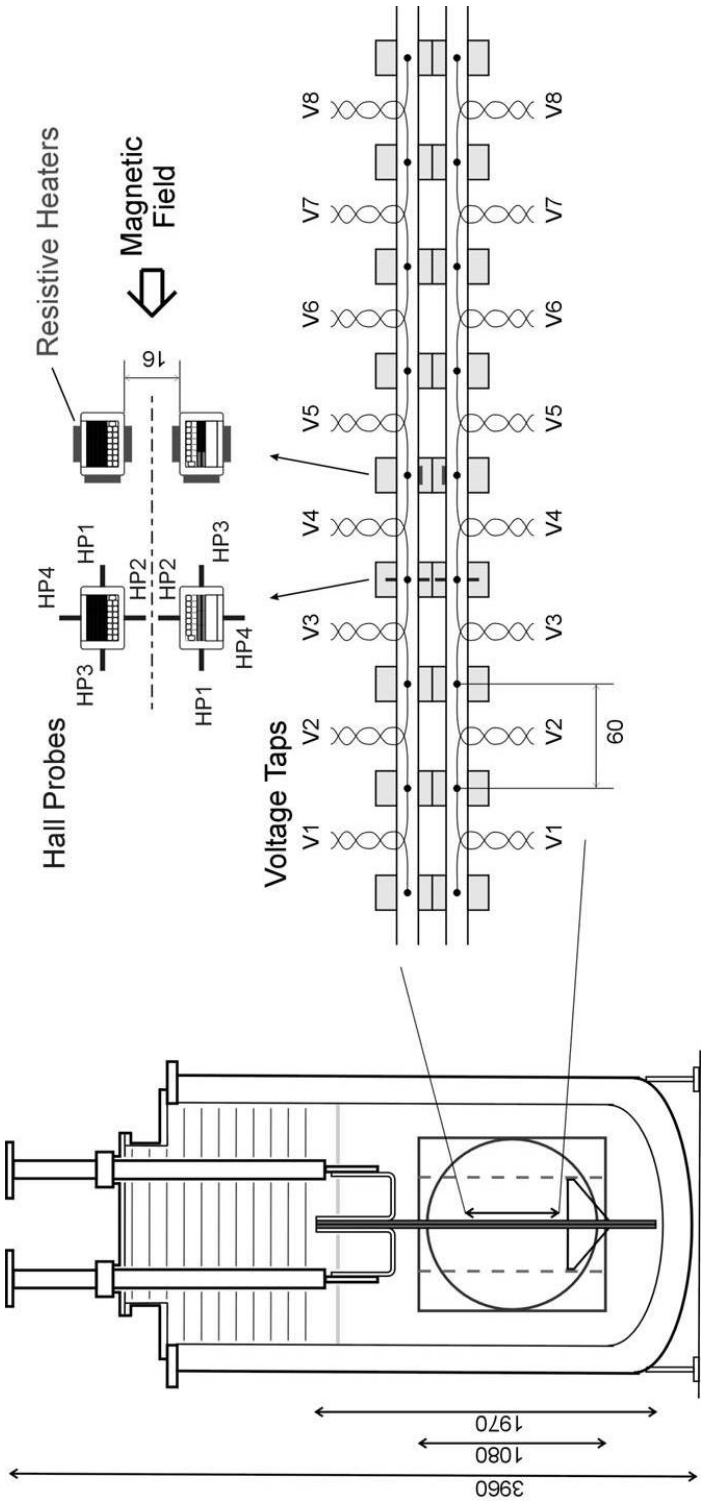

Fig. 3.16: Schematic illustration of the superconductor testing facility (left) and distribution of diagnostic sensors of the short samples made of two hybrid conductors (right). Unit: mm.

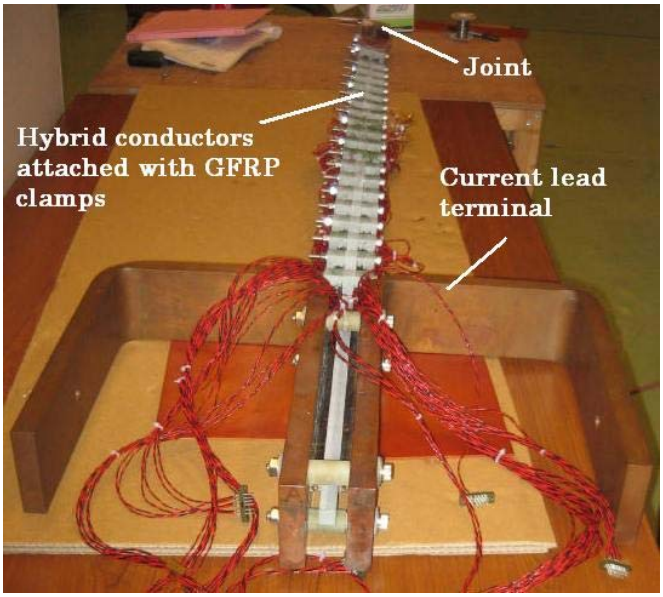

(a)

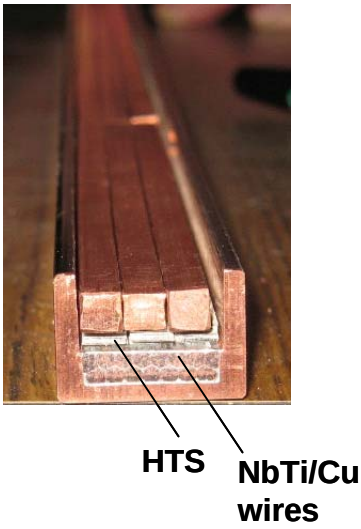

(b)

Fig. 3.17: Photograph of the (a) hybrid conductor sample; (b) type-A hybrid conductor.

Table 3.2: Specifications of LTS/HTS hybrid conductors

Conductors	Items	Parameters
Original Conductor	Superconductor	NbTi
	Strands	ϕ1.74 mm × 15
	Filaments	ϕ47 μm × 726
	Copper to NbTi ratio	0.9 (strand)
	Critical current (density)	21 kA at 7 T (1360 A/mm^2)
	Resistivity of Aluminum	3.8×10^{-11} Ω-m (7 T, 4.2 K)
	Surface treatment	Oxidization
Hybrid Conductors	HTS stabilizer	Bi-2223/Ag tapes
	Critical current of a single HTS tape	114 A at 77 K, self-field
	Number of HTS tapes	Type-A: 30 Type-B: 75
	Critical current of HTS bundles at 4.2 K, 8 T (parallel field)	Type-A: 14.4 kA Type-B: 36 kA

Experimental method and sensors

On the conductor surfaces, a number of voltage taps were attached to monitor normal-zone development. They were situated on the narrower side of the conductor in order to minimize inductive signals due to the change of the current path in the conductors duirng normal-transitions of NbTi/Cu cables. The voltage tap numbers are indicated in Fig. 3.16. In order to strictly specify the cooling perimeter and to sustain the large electromagnetic force, GFRP blocks were used as clamps. The cooling perimeter of 67% was selected in order to match the situation in the innermost windings of the LHD helical coils. Thin film resistive heaters were attached to the conductor surfaces to initiate a quench in stability tests. In order to monitor the change of the current path during normal-transition processes, an array of Hall probes were installed around the conductors.

The fabricated short samples were then installed into the cryostat of the superconductor testing facility, which consists of 9 T split coils (diameter ~1 m), a pair of current-leads (maximum 100 kA capacity) and 75 kA DC power supplies. The uniform magnetic field (above 90% level) can be applied for about 250 mm length at the sample centers.

Initially, the conductors were charged up to the desired current and then resistive heaters were switched ON to inject the heat into the conductor to initiate a normal-zone. As we expected, the transport current was supplied to the LTS part of the hybrid conductor. It is confirmed by the Hall sensors measurements and numerical calculations, which are discussed in the following sections. We had applied Cernox temperature sensors near the heaters to measure the temperature evolutions but unfortunately, the temperature sensors were lost during the experiments and therefore no data of temperature development could be gathered in the present experiment.

3.4.2 Experimental results and analyses

Figure 3.18 shows typical waveforms of the voltage tap signals observed with the Type-B hybrid conductor during a stability test. The bias magnetic field was 7 T and the transport current was 13.0 kA, which corresponds to the target point of the LHD helical coils. A heater pulse of 40 ms was injected and a normal-transition was observed. Here, only the voltage tap signals of V5, V6, V7 and V8 are plotted and we should note that the normal-zone started from the heater position of V5. We observed that the normal-zone propagation was almost symmetrical and the waveforms of V4 to V1 looked almost the same as those of V5 to V8 (and hence for simplicity they are not plotted in Fig. 3.18). It should be noted that the voltage waveforms indicate that the normal-zone formed a traveling normal-zone. Because of the limited length of the uniform magnetic field, the V8 signal looks already a bit smaller and the profile of the traveling normal-zone is not very clear in the present test.

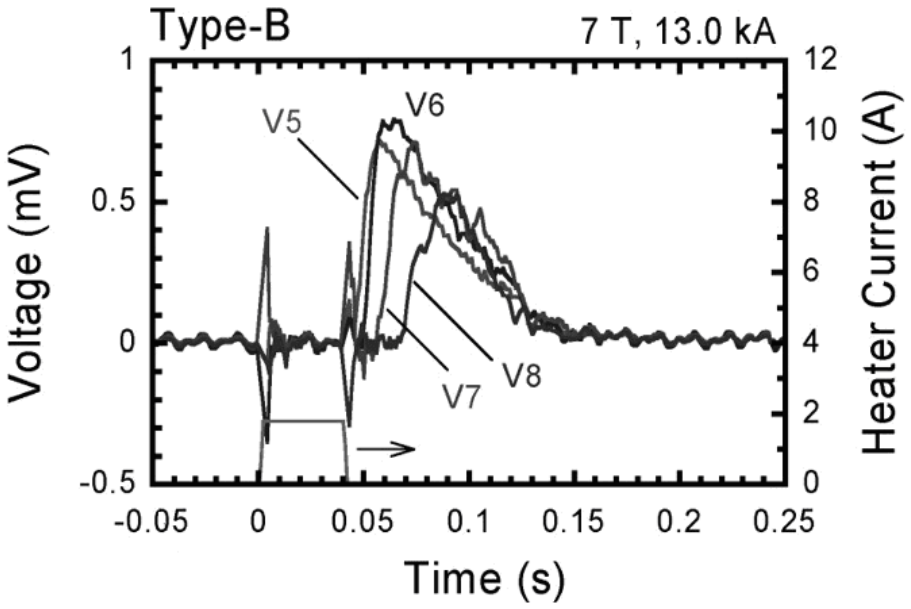

Fig. 3.18: Typical waveforms from the voltage taps observed at 7 T, 13 kA for the Type-B hybrid conductor.

Normal zone propagation velocity

From the time delay between the normal-transitions at voltage tap positions between V3-V2 and V6-V7, we evaluated the propagation velocity and the result is plotted as a function of the sample current in Fig. 3.19. As is seen in Fig. 3.19, the conductor experiences normal-zone propagations even from the sample current of ~8 kA. In the low current region of 8-11 kA, the normal-zone appeared only up to V3 and V6 positions, and the propagation velocity could not be properly evaluated.

Though the generated normal-zone showed propagation, we may consider that the cryogenic stability of the hybrid conductors is sufficiently high. This can be confirmed by comparing the voltage waveforms of the hybrid conductors with those obtained with the original aluminum-stabilized conductor used for the LHD helical coils. Figure 3.20 shows such an example at 8 T, 15 kA. It was observed for the original conductor that the current of 15 kA was well above the minimum propagation current so that the normal-zone propagated and it never disappeared even with the limited length of the uniform magnetic field. On the contrary, the hybrid conductor showed a very short transition and recovered back to the superconducting state within 0.2 s in this case.

Figure 3.21 summarizes the relationship between the duration of the observed normal-zone (at the heater position) and the sample current. It is clearly seen that the duration of the generated normal-transition is about 0.1 s at the current of 13 kA (target point of the LHD conductor). Thus, we may state that hybrid conductors show good stability compared to conventional metal-stabilized conductors of the similar size.

On the other hand, regarding the mechanism of the normal-transition with the present hybrid conductors, we consider that it is caused by the current diffusion process itself from the LTS cable to the bundle of HTS stabilizer. As the transport current diffuses into the bundle, there is a change of the magnetic flux and electric field is hence generated and the joule heat is released. This is a physical process similar to flux jumping in superconducting filaments. Then, the heat release during the current transfer is unavoidable as far as a thick stabilizer is used even if its resistivity is very low. Therefore, it is strongly recommended that stabilizers should be used in pieces and not in bulk.

In Fig. 3.21, it is seen that when the current exceeds 15 kA, the duration of a normal-transition becomes rapidly longer for the hybrid conductor Type-A. This current was already higher than the critical current of Bi-2223/Ag cables with 30 tapes at the temperature higher than critical temperature of the NbTi/Cu cable, which is necessary to quench the current carrying NbTi/Cu part of the hybrid conductor. As discussed before, though the sample was equipped with Cernox temperature sensors, they were lost during the experiment and the actual temperature of the conductors could not be measured. For the Type-B conductor, there is no such a bend in the curve of Fig. 3.21, since the critical current is supposed to be much higher. Due to a minor failure in the facility, the transport current could not be increased further in this experiment, and the limit of the hybrid conductors (where the HTS tapes will also experience a quench) could not be examined so far.

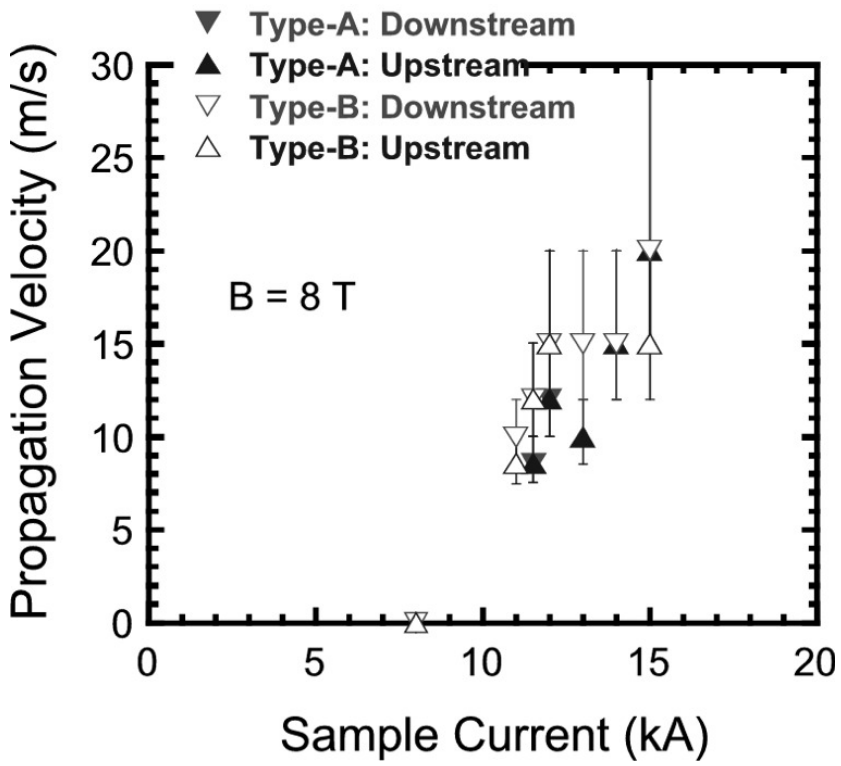

Fig. 3.19: Propagation velocity as a function of the sample current. "Upstream" and "Downstream" refer to the upstream and downstream directions of the sample current.

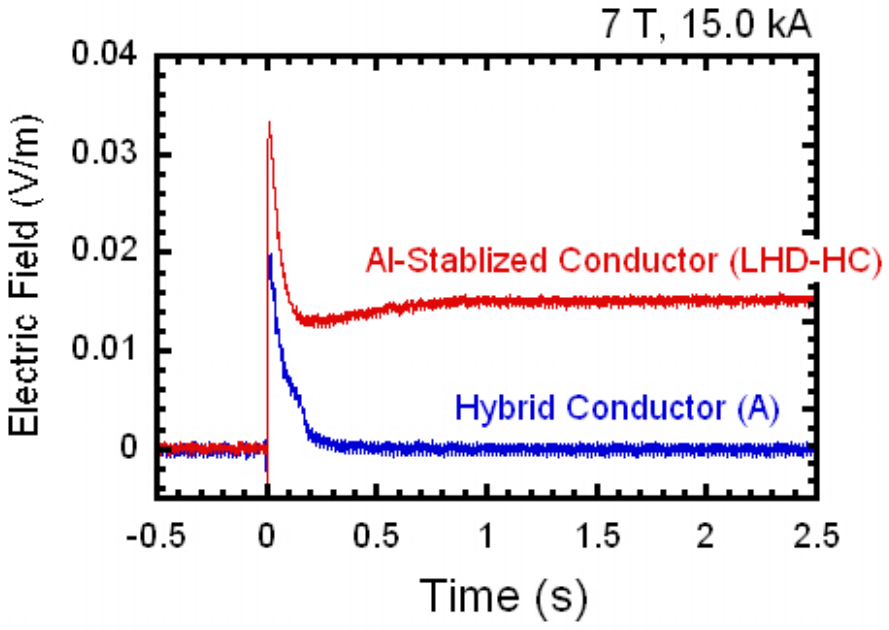

Fig. 3.20: Comparison of the voltage waveforms (at the heater positions) between the hybrid conductor Type-A and the original aluminum-stabilized conductor at 7 T, 15 kA.

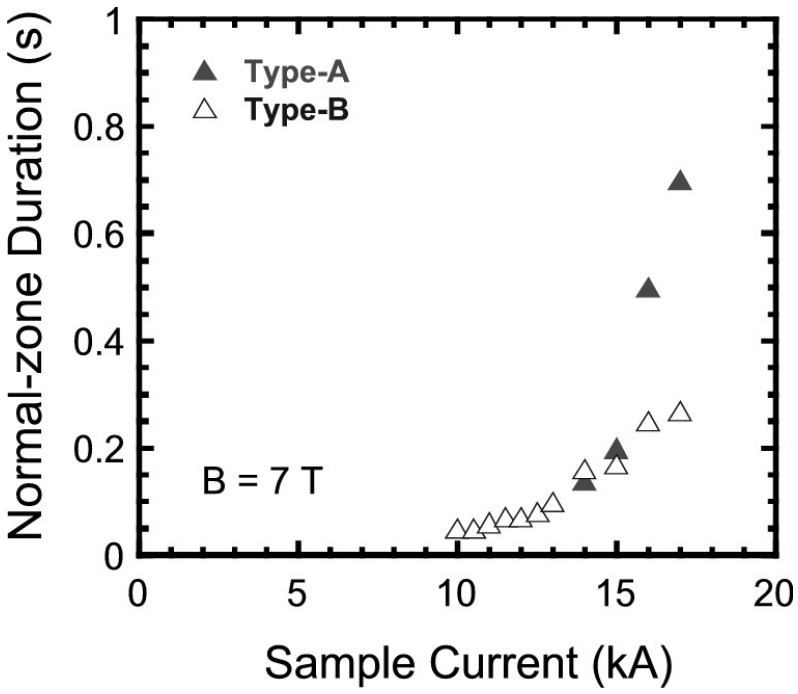

Fig. 3.21: Duration of the observed normal-transition as a function of the sample current.

Current distribution and stability of the conductor

For determining the current distribution inside the conductor in steady state and transient conditions, an array of four Hall sensors around the conductor cross-section was attached on each conductor near the thin film resistive heaters' location as shown in Fig. 3.16.

Figure 3.22 shows the Hall sensors, HP1 and HP2, signals at 7 T and 13 kA for hybrid conductor Type-B after the heat input from thin film heaters. The Hall sensor signals are normalized by steady state signals. As is seen in Fig. 3.22, the Hall probe signals indicate that the transport current actually transferred from the quenching NbTi/Cu cable to the HTS stabilizer within the same time period of the voltage generation. It is also clear that after the transfer of the current, it takes a rather long time (time constant >10 s) for the transport current to come back to the NbTi/Cu strands from the HTS bundle. The time constant should be determined by the joint resistance and inductance of the circuit formed by the NbTi/Cu cable and the HTS stabilizer.

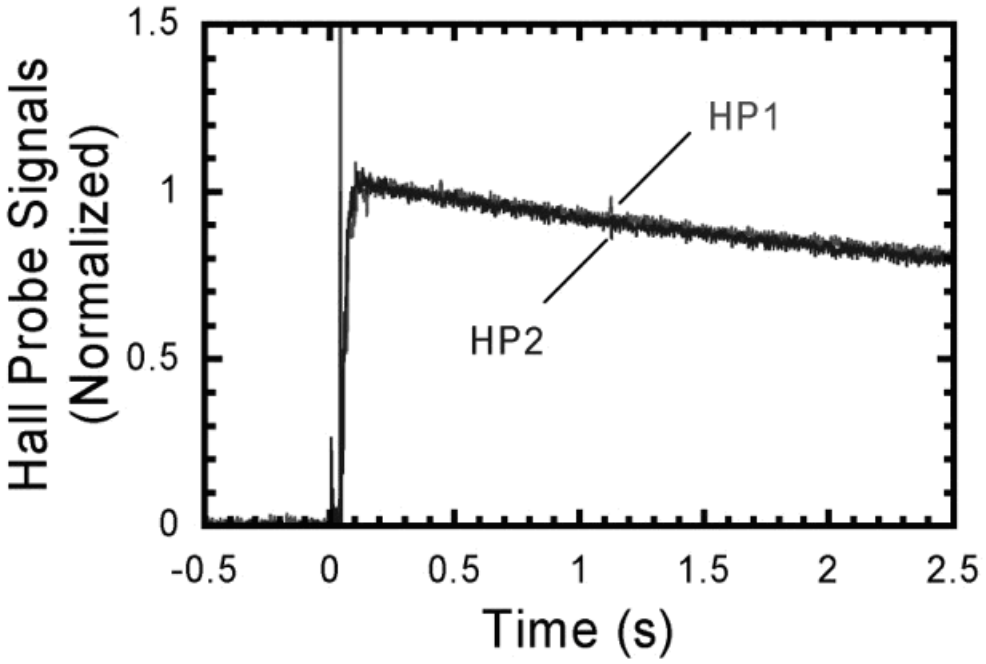

Fig. 3.22: Waveforms of the Hall probe signals observed at 7 T, 13 kA for the Type-B hybrid conductor.

The numerical calculations along with the Hall sensor measurements have been carried out to determine the current distribution in the conductor. Figure 3.23 shows the HP2 and HP4 sensors measurement results at 16 kA and 7 T for hybrid conductor Type-A. The changes in magnetic fields (from steady state condition) at HP2 and HP4 locations after a heat input are plotted.

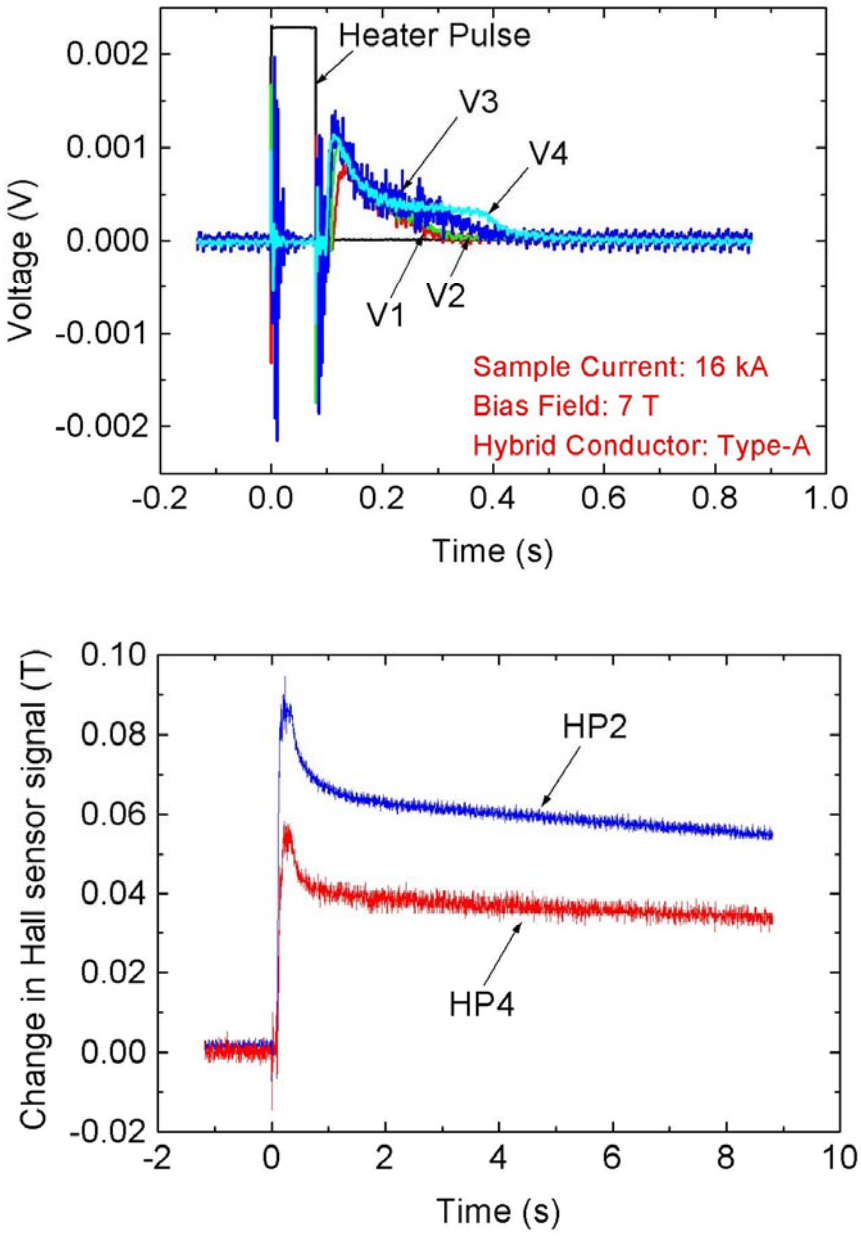

Fig. 3.23: Change in magnetic field at HP2 location at 7 T and 16 kA for Type-A hybrid conductor after a heat input to the conductor.

The experimentally measured change in magnetic fields at HP2 and HP4 are 0.90 T and 0.056 T respectively.

Figure 3.24 and 3.25 show the magnetic fields at HP2 and HP4 locations when 16 kA current is carried by only LTS part and only HTS part of the hybrid conductor respectively. The field calculations are carried out by 2-D FEM software.

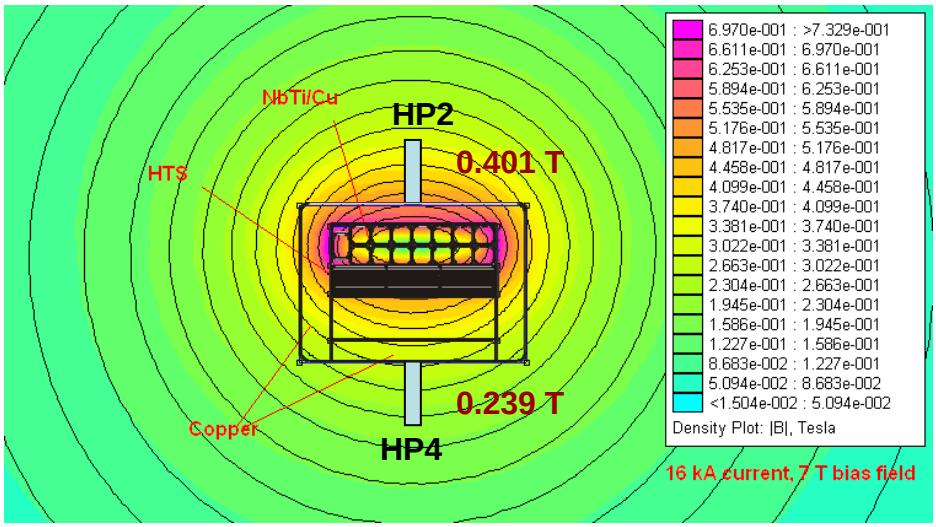

Fig. 3.24: Calculated magnetic fields at HP2 and HP4 locations in Type-A hybrid conductor when transport current is carried by LTS part only.

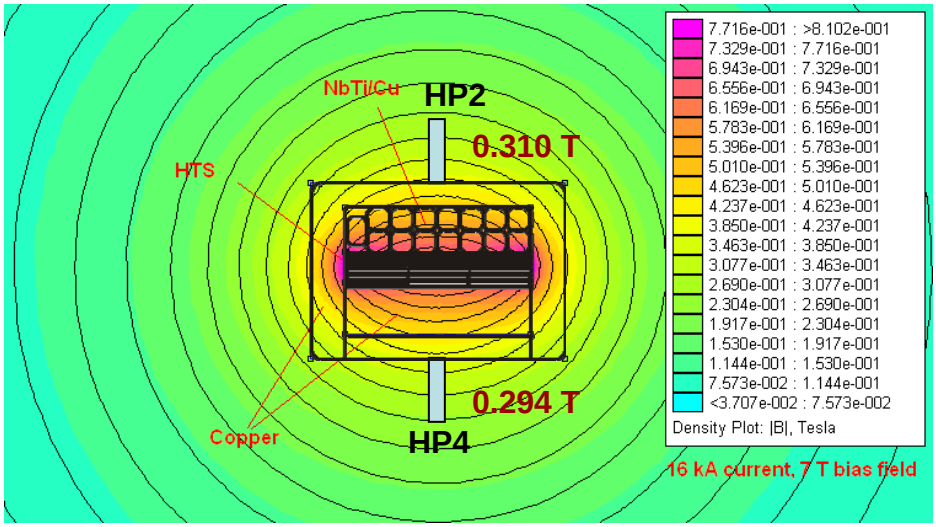

Fig. 3.25: Calculated magnetic fields at HP2 and HP4 locations in Type-A hybrid conductor when transport current is carried by HTS part only.

The calculated change in magnetic fields at HP2 and HP4 are 0.091 and 0.055 T respectively which agree well with experimentally observed values.

Hence, this analysis clearly indicates that current is initially carried by LTS part of the hybrid conductor and then transfers from LTS to HTS part after the heat input from thin film heaters. As discussed before, current has to transfer from LTS to HTS layers just layer by layer from nearest to farthest layer of HTS and therefore HTS part experiences the extreme non-uniform current distribution. It has been found that even though the transport current was more than the critical current of the HTS cables in hybrid conductor, especially Type-A, the conductor did not quench fully. It clearly indicates that stability of the HTS conductor is quite high even with extreme non-uniform current distribution. Therefore, these results suggest that non-uniform current distribution may not be a concern in full-scale HTS conductors as far as the stability is concerned. However, the direct investigation of effect of non-uniform current distribution on the stability of the HTS conductors in high fields and elevated temperatures (for example 15 T and 20 K) might be necessary.

3.5 Summary

An innovative approach was devised to examine the effect of non-uniform current distribution on the stability of HTS conductors by proposing the concept of LTS/HTS hybrid conductors. The proposed hybrid conductor was the world's first superconducting conductor utilizing LTS and HTS together. The second motivation of the proposed hybrid conductor was to improve the cryogenic stability of the solid type conductors, which usually suffer from long magnetic diffusion time constants in the stabilizers such as pure aluminum. Broadly, the following conclusions can be drawn.

1. The proof-of-principle experiments on small scale hybrid conductors and large scale hybrid conductors prepared by modifying the LHD helical coil conductor clearly suggest that the stability can be improved significantly if

HTS is used as a stabilizer in place of conventional metal stabilizer such as pure aluminum.

2. The HTS part in hybrid conductors experienced the extreme non-uniform current distribution by transferring the transport current from LTS to HTS part after a heat input.
3. Even though the transport current was more than critical current of the HTS cables in hybrid conductor (Type-A) and current distribution was an extreme case of non-uniformity, the conductor did not quench fully. This result suggests that non-uniform current distribution may not be a problem with HTS conductors from stability point of view.
4. Consequently, hybrid conductor results support the idea of simple stacking configuration of full-scale HTS conductors for fusion reactor magnets as far as the stability of the conductor is concerned. The non-uniform current distribution might be a natural consequence of inductance mismatching in simple stacked HTS conductors.
5. Direct observation of the effects of non-uniform current distribution on the stability of a full scale HTS conductor with simple stacking in high magnetic field and elevated temperatures (e.g. 15 T and 20 K) is recommended.

Chapter 4

Development of 10 kA-class HTS conductors

High temperature superconductors (HTS) are being considered for high field magnets in fusion reactors due to their good performances in high magnetic field and elevated temperature operations [4.1] – [4.8]. Toward the development of a 100 kA-class HTS conductor for fusion energy reactor magnets such as the LHD-type fusion reactor FFHR, it is necessary to first validate the design concept by studying reduced-scale HTS conductors. For this purpose, 10 kA-class HTS conductors were developed with simple stacking configuration and were extensively examined in various operating conditions. This chapter discusses the details of the 10 kA-class HTS conductor development and tests.

4.1 HTS conductor samples

We developed two 10 kA-class (at 20 K, 8 T) HTS conductors using Bi-2223/Ag and YBCO HTS tapes and tested them separately. Due to the unavailability of long length YBCO tapes, we started with Bi-2223/Ag HTS conductor development, as the Bi-2223/Ag tapes were available in long lengths commercially. Figure 4.1 shows the cross-sectional views of the bare and insulated HTS conductors. For fabricating the Bi-2223/Ag HTS conductor, about 1 m long Bi-2223/Ag HTS tape pieces were cut. The Bi-2223 HTS conductor was made by simply stacking and soldering 34 numbers of Bi-2223/Ag tapes (4.2 mm wide, 0.22 mm thick) inside a copper sheath of an outer size 12.0 mm × 7.5 mm. Table 4.1 shows the parameters of the Bi-2223/Ag tape and the Bi-2223 HTS conductor.

Table 4.1:Parameters of Bi-2223/Ag tape and HTS conductor

	Items	Parameters
Bi-2223/Ag tape	Silver to Superconductor ratio	1.7
	Dimensions	4.2 mm (width) × 0.22 mm (thickness)
	Critical Current (at self-field, 77 K)	140 A
	Index value	18
	Supplier	Sumitomo Electric, Japan
Bi-2223/Ag HTS conductor	Overall size	12.0 mm × 7.5 mm
	Number of Bi-2223/Ag tapes	34 (in two bundles)
	Assembly method	Simple stacking using 60Pb-40Sn solder
	Copper sheath thickness	1.5 mm (3 sides), 2.0 mm (closing plate)

Figure 4.2 shows the I_c-B-T characteristics of the Bi-2223/Ag tapes used in the HTS conductors [4.9]. These I_c-B-T characteristics are produced by the supplier and are used to calculate the critical currents of the HTS conductor with self-field effects discussed in the following sections.

On the other hand, for the YBCO conductor, the 10 mm wide and 0.12 mm thick HTS tapes were used. The HTS conductor was developed by combining GdBCO tapes together with YBCO tapes. We note that the YBCO and GdBCO tapes used for our HTS conductor were provided by International Superconductivity Technology Center (ISTEC) and Fujikura Ltd. under the support of the New Energy and Industrial Technology Development Organization (NEDO) as Collaborative Research and Development of Fundamental Technologies for Superconductivity Applications. Both the YBCO and GdBCO tapes are produced by using IBAD and PLD technology. The YBCO and GdBCO tapes in our HTS conductor may be considered equivalent to each other as their sizes, architecture and production method are same and their critical currents (at self-field,

77 K) are also almost the same (please see Table 4.2). Eight tapes of each YBCO and GdBCO were used together with 0.1 mm thick copper tapes inside a copper sheath of cross-section 13.0 mm × 7.5 mm. Table 4.2 shows the parameters of the YBCO, GdBCO tapes and the HTS conductor. Even though the YBCO and GdBCO tapes are used together, the conductor is being called as YBCO conductor throughout the discussion.

Due to the high resistive substrate and insulating buffer layers in YBCO and GdBCO tapes, the current transfer from one tape to another tape is difficult. Therefore, to avoid any non-uniformity in the current distribution among the HTS tapes, an innovative technique was used to supply uniform current to each YBCO and GdBCO tape in the conductor. The Bi-2223/Ag tapes (4.2 mm wide, 0.22 mm thick, I_c: 140 A at self-field and 77 K) were connected with each YBCO and GdBCO tapes inside the conductor at the current lead side as well as the joint side. Together with YBCO and GdBCO tapes, the copper tapes of 0.1 mm thickness were used primarily to match the thickness with Bi-2223/Ag tapes and therefore avoiding any bending of the YBCO and GdBCO tapes at the Bi-2223/Ag to YBCO (GdBCO) joints inside the conductor. A schematic view of the lateral section of the conductor is shown in Fig. 4.3 (a). The overlap length between the Bi-2223/Ag tape and YBCO or GdBCO tape was chosen to be 15 mm to reduce the joint resistance and hence the joule heating of the conductor. A schematic top view of the assembly of the Bi-2223/Ag tapes with 8 numbers of YBCO or GdBCO is shown in Fig. 4.3 (b). One side of the assembly is shown with Bi-2223/Ag tapes overlapped with YBCO or GdBCO tapes whereas the other side is shown without Bi-2223/Ag tapes for better understanding of the assembly.

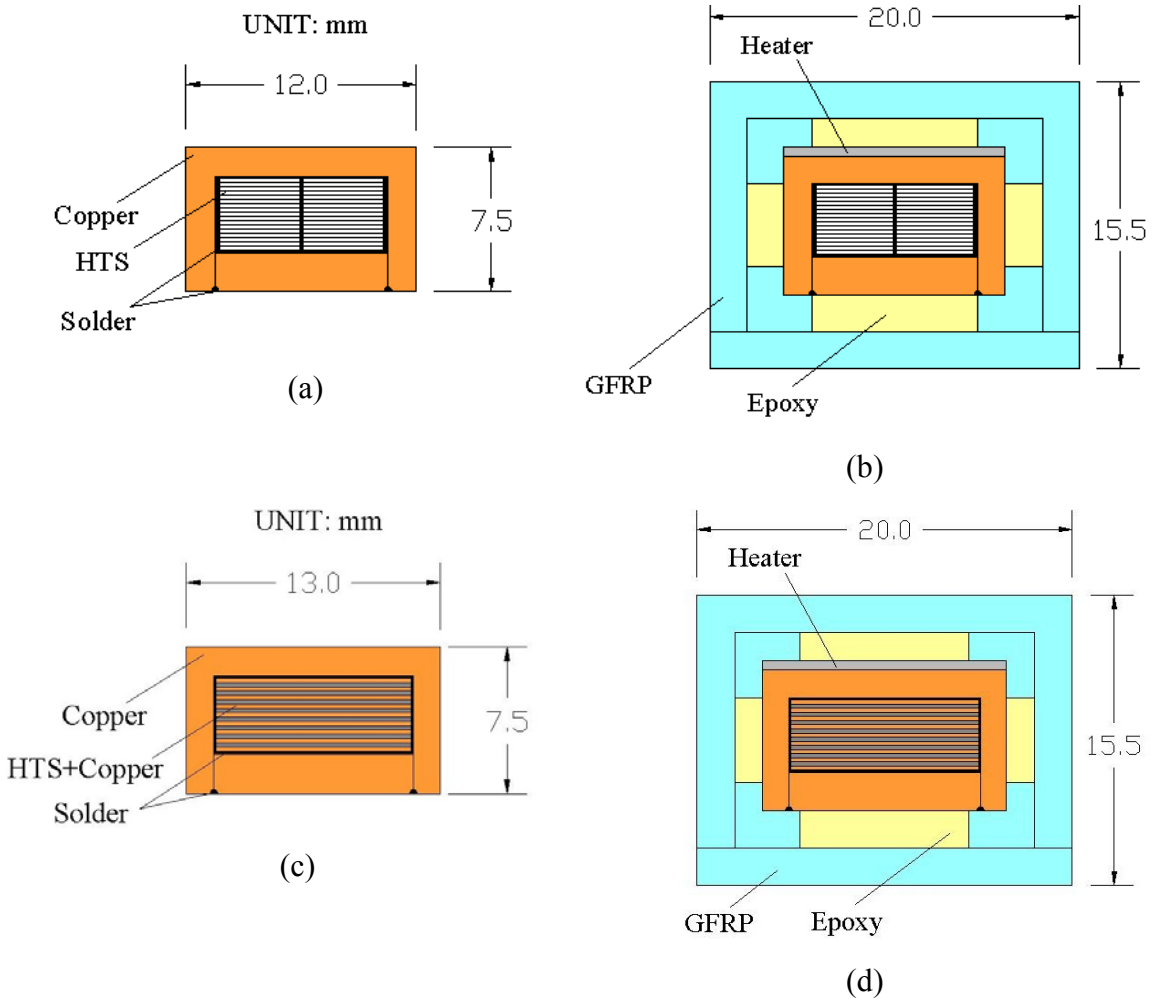

Fig. 4.1: Cross-sectional views of (a) a 10 kA-class Bi-2223/Ag HTS conductor; (b) Bi-2223/Ag HTS conductor with GFRP and epoxy insulation; (c) a 10 kA-class REBCO HTS conductor; (d) REBCO HTS conductor with GFRP and epoxy insulation. In REBCO HTS conductor, 8 tapes of each YBCO and GdBCO are combined with 0.1 mm thick copper tapes.

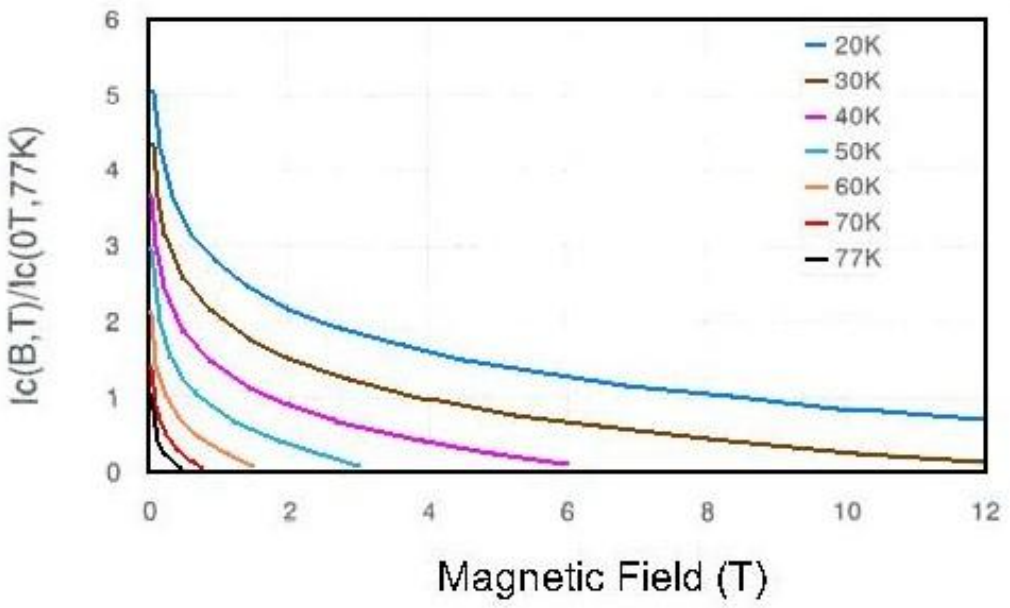

(a)

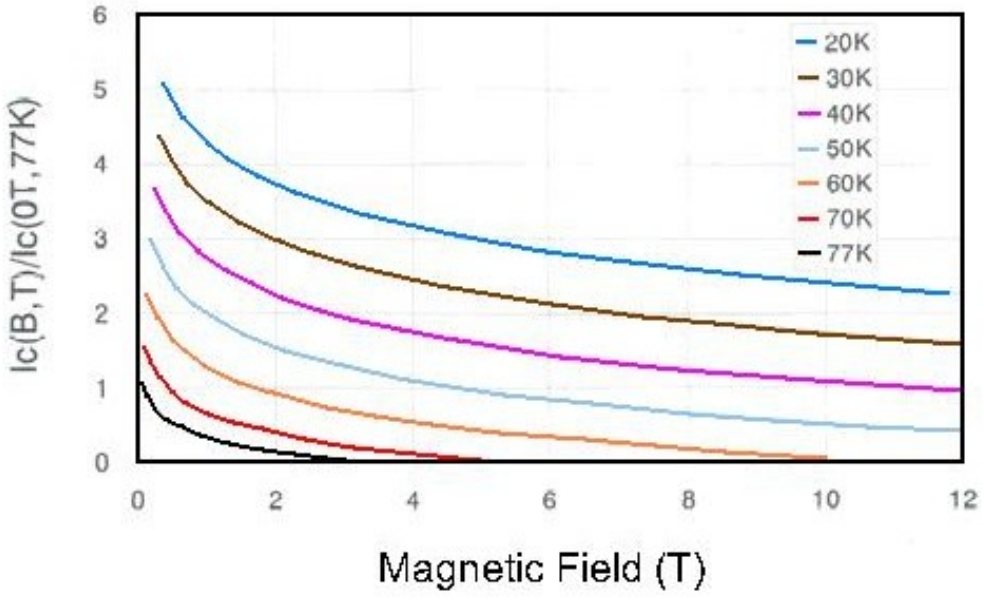

(b)

Fig. 4.2: I_c-B-T characteristics of Bi-2223/Ag tapes in (a) perpendicular field; (b) parallel field to the ab-plane of the tapes.

Table 4.2:Parameters of YBCO, GdBCO tapes and the HTS conductor

	Items	Parameters
YBCO tape	Dimensions	10 mm (width) × 0.12 mm (thickness)
	Tape Architecture	Ag (19 μm)/$Y_1Ba_2Cu_3O_{7-x}$ (2.4 μm)/CeO_2 (0.34 μm)/$Gd_2Zr_2O_7$ (0.71 μm)/HastelloyC-276 (100 μm)
	Critical Current (at self-field, 77 K)	~210 A
	Fabrication method	IBAD and PLD
GdBCO tape	Dimensions	10 mm (width) × 0.12 mm (thickness)
	Tape Architecture	Ag (20 μm)/$Gd_1Ba_2Cu_3O_y$ (1.0 μm)/CeO_2 (1.0 μm)/$Gd_2Zr_2O_7$ (1.4 μm)/HastelloyC-276 (100 μm)
	Critical Current (at self-field, 77 K)	~190 A
	Fabrication method	IBAD and PLD
HTS conductor	Overall size	13 mm (width) × 7.5 mm (thickness)
	Number of tapes	8 (YBCO) + 8 (GdBCO) + 16 (Copper, 0.1 mm thick, 10 mm wide)
	Assembly method	Simple stacking using 60Pb-40Sn solder
	Copper sheath thickness	1.4 mm (2 sides), 1.5 mm (bottom side), 2.0 mm (closing top plate)

Remark: Bi-2223/Ag tapes are connected with individual YBCO and GdBCO tape inside the conductor to ensure uniform current distribution (as shown in Fig. 4.3). The top part of the conductor with only Bi-2223/Ag tapes was connected to the current lead to supply the current. Similarly, at the bottom part of the conductor, the current transfers from YBCO and GdBCO tapes to the Bi-2223/Ag tapes and then to the other leg of the conductor sample.

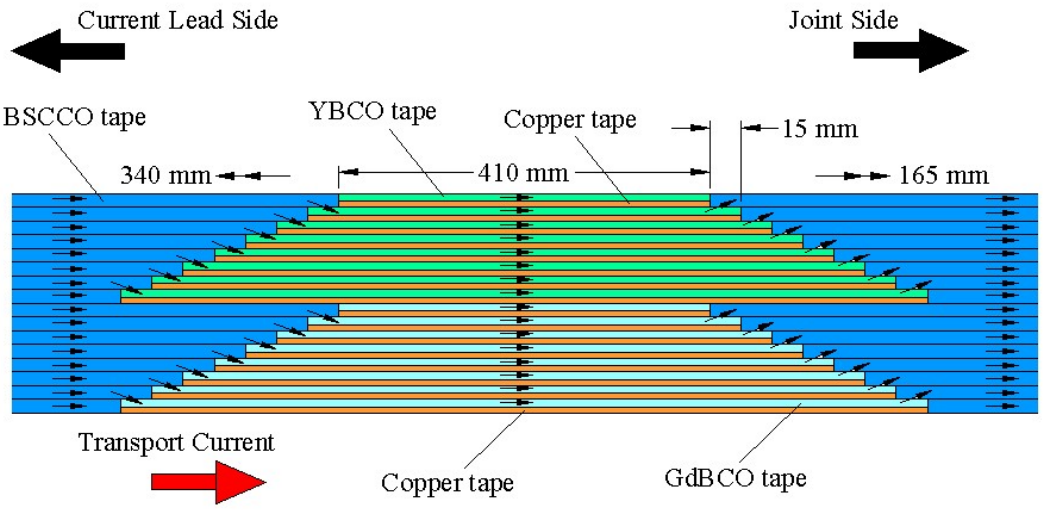

(a)

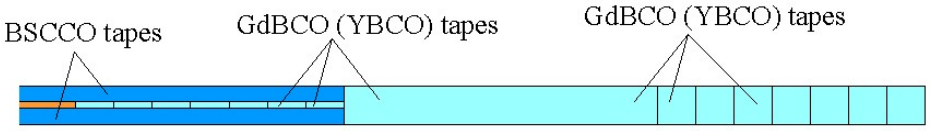

(b)

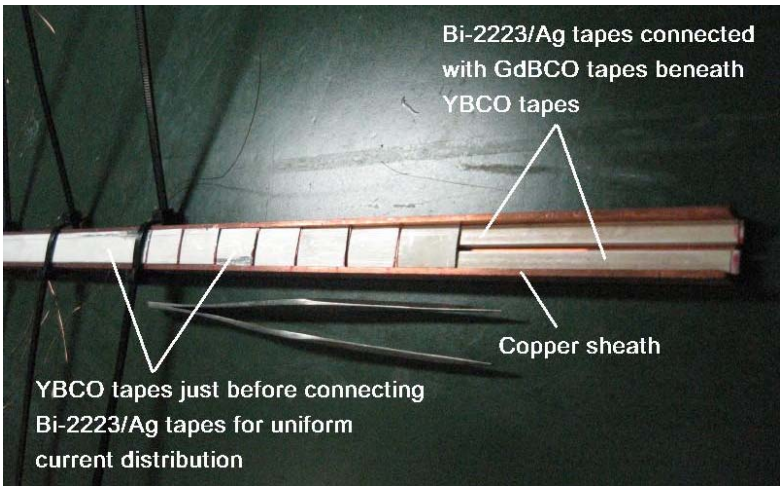

(c)

Fig. 4.3: (a) Schematic view of the lateral section of the YBCO conductor showing the connections between Bi-2223/Ag tapes and YBCO and GdBCO tapes to ensure uniform current distribution in the conductor; (b) top view of the assembly of 8 numbers of YBCO or GdBCO tapes with Bi-2223/Ag tapes inside the conductor. The other side is shown without Bi-2223/Ag tapes for better understanding of the assembly, (c) photo of the YBCO conductor during assembly.

The developed HTS conductors were tested in 8-T split coil facility, which provides a testing bore of 30 mm × 50 mm only. Due to the limited space availability, one innovative method was developed to test the HTS conductors at elevated temperatures up to 30 K. For this purpose, the stainless steel heaters were attached to the surface of the HTS conductor to elevate the temperature and to reduce the heat loss to surrounding liquid helium, the HTS conductor was then insulated by epoxy and GFRP. Therefore, Fig. 4.1 (c) shows the GFRP insulated HTS conductor equipped with stainless steel heaters. The details of the test methods are discussed in the following sections.

4.2 Experimental set-up

The 10 kA-class HTS conductors were tested in the 8-T split coil facility using a pair of 30 kA conventional current leads. The details of the experimental test facility and samples are discussed in this section.

4.2.1 Experimental sample and diagnostics

The HTS conductor samples of about 1-m length were fabricated in hairpin configurations and were tested in a bias field of 8 T, parallel to ab-plane of the HTS tapes. Figure 4.4 shows the HTS conductor test sample installed with 8 T split coil and in the cryostat.

The test conductor leg of the sample was thermally insulated using epoxy and GFRP and therefore was conduction-cooled by liquid helium from the ends. The HTS conductor was tested at 4.2 K as well as at elevated temperature up to 30 K. Figure 4.5 shows the HTS conductor test sample details. Figure 4.6 shows that the fabricated HTS conductor and prepared conductor sample in hairpin configuration.

As discussed before, for elevating the conductor temperature, two thin stainless-steel (SS) heaters were attached at the ends of the conductor leaving the central testing section of about 120 mm length as shown in Fig. 4.7. After attaching the heaters, the insulation of the conductor was done using epoxy and GFRP. The other conductor of the

sample was kept un-insulated and therefore was immersed in liquid helium. Both legs of the sample were joined in a praying hand lap joint configuration. The joint was immersed in liquid helium and the bias field at the joint was less than 1 T. Some NbTi strands were also soldered at the joint to reduce the joint resistance. We carried out the critical current measurements, and minimum quench energy (MQE) measurements on the HTS conductors at 4.2 K and elevated temperatures up to 30 K in a bias field of 8 T. For MQE measurements, the thin-film heaters were used to inject the energy into the conductor. The CERNOX temperature sensors were used to monitor the temperature evolution of the conductor during normal-zone propagations. Voltage taps were used to monitor the normal-zone growth along the conductor. Figure 4.8 shows the 8-T split coil facility. Figure 4.9 shows the magnetic field profile on the conductor produced by 8T-split coil.

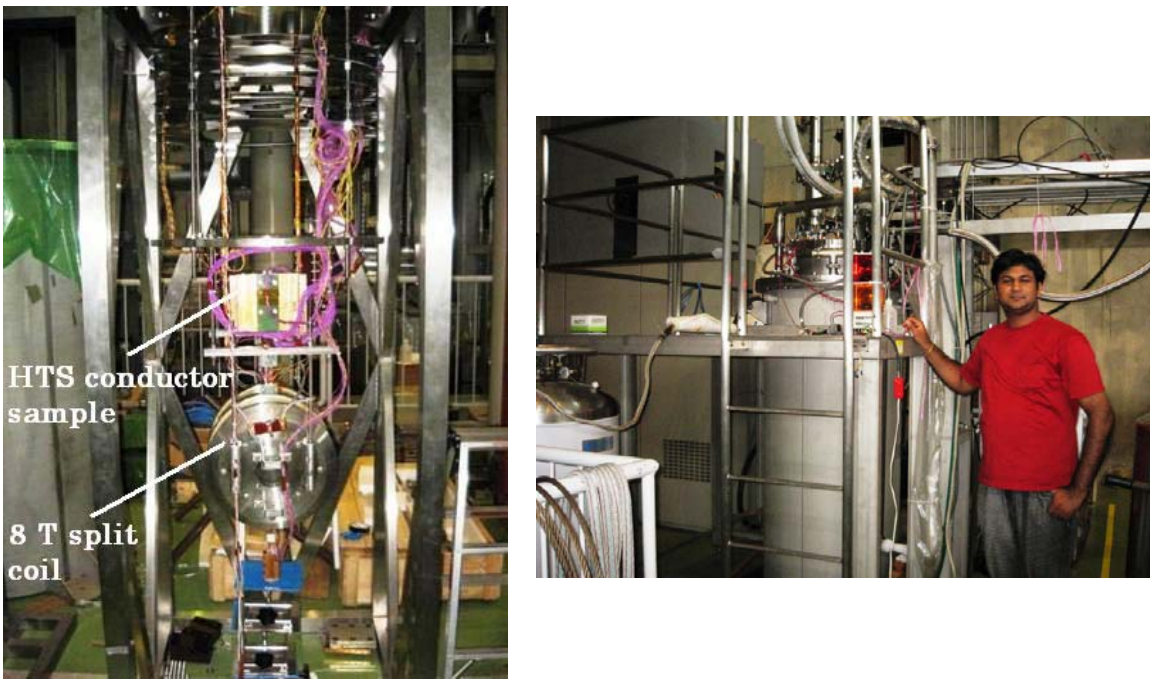

(a) (b)

Fig. 4.4: Photos of (a) HTS conductor sample installed in the 8 T split coil and attached to the 30 kA current leads; (b) HTS conductor sample with split coil installed in cryostat.

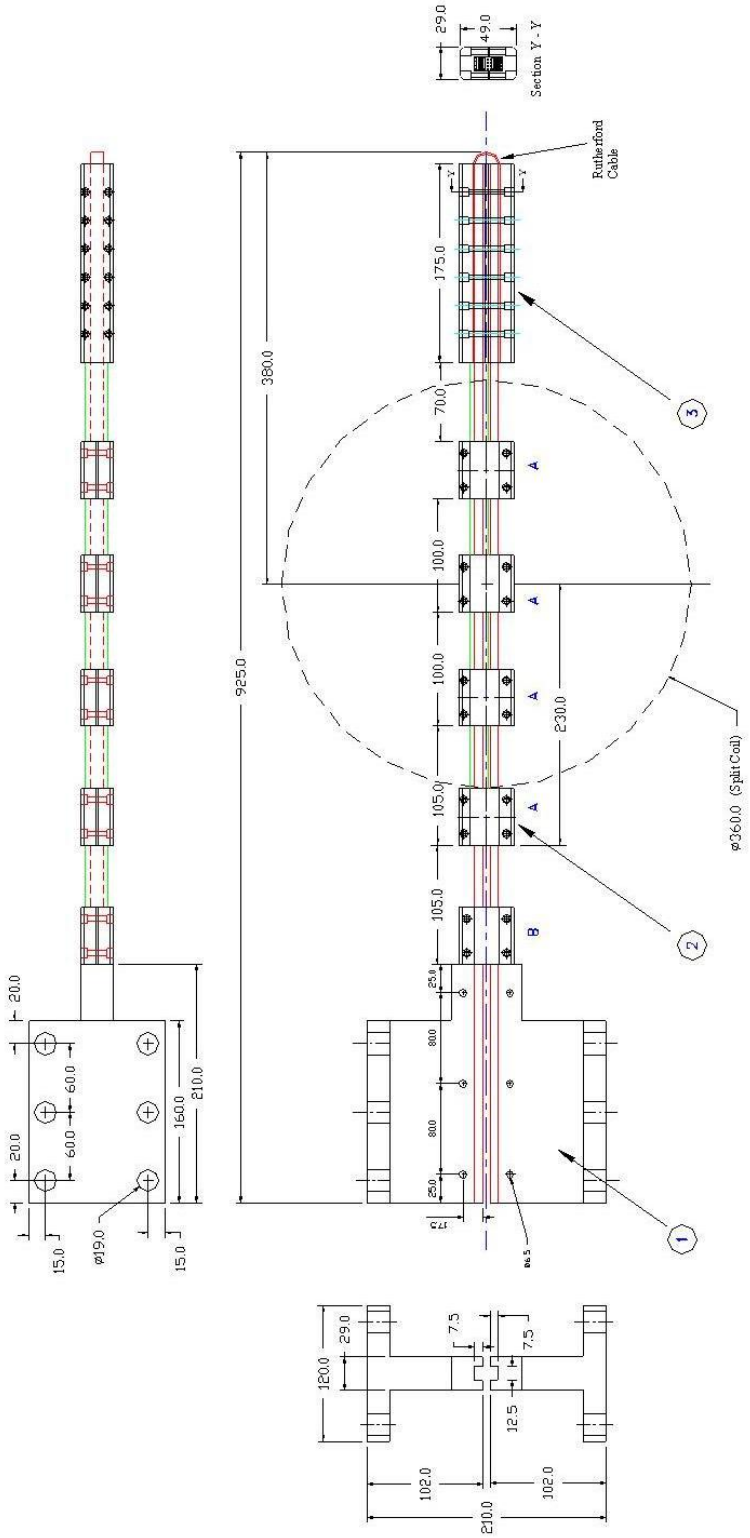

Fig. 4.5: HTS conductor sample in hairpin configuration. (1) Current terminals; (2) GFRP clamps; (3) joint section. Total length of the sample is 925 mm.

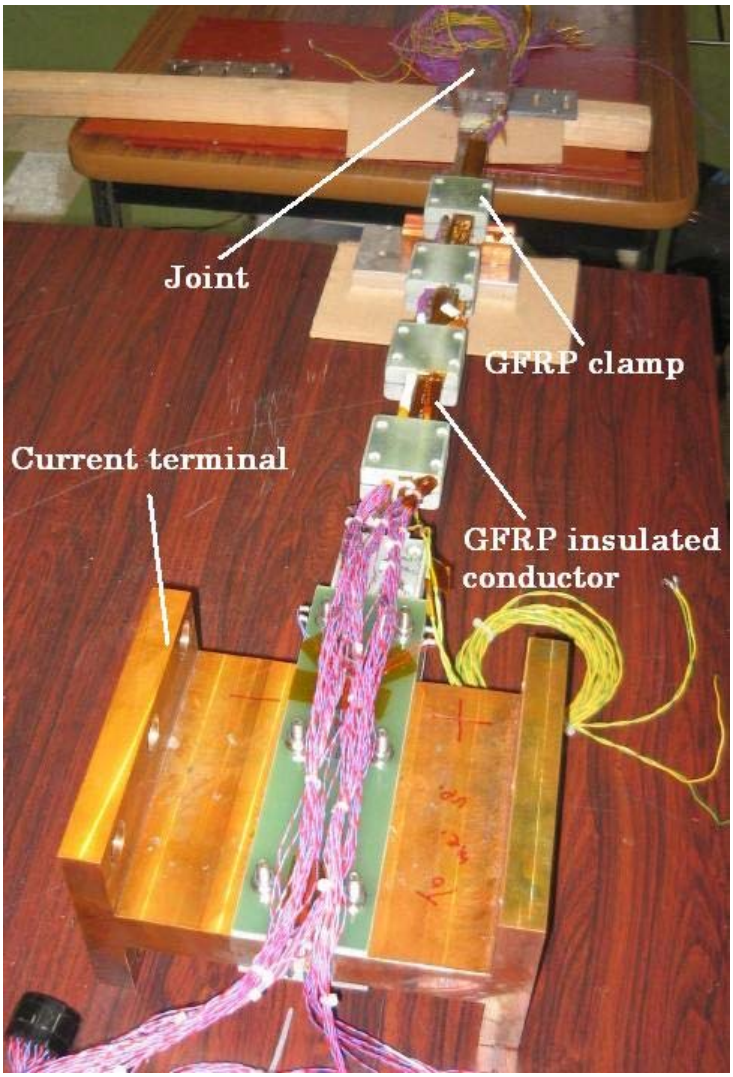

Fig 4.6: Photos of (a) Bi-2223 HTS conductor; (b) Bi-2223 HTS conductor sample.

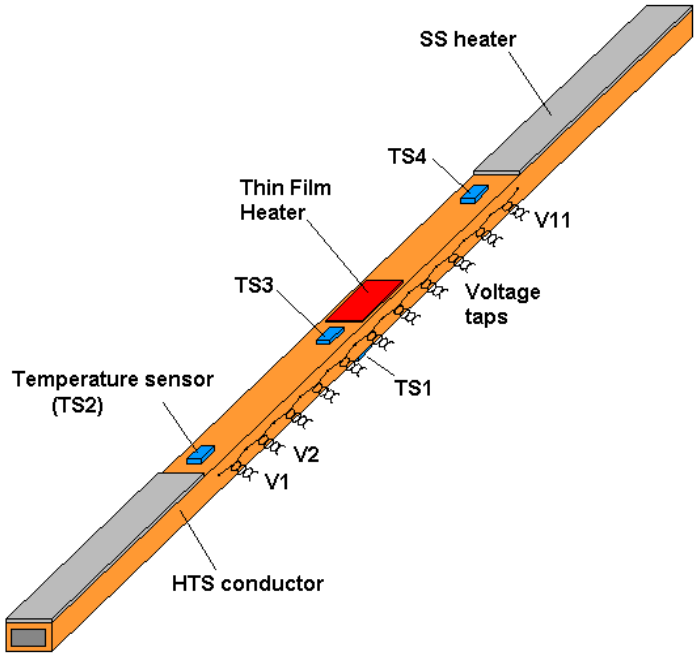

Fig. 4.7: Arrangement of stainless-steel heaters, voltage taps, temperature sensors, and thin-film heaters. V6 voltage taps at the conductor center were used for critical current measurements.

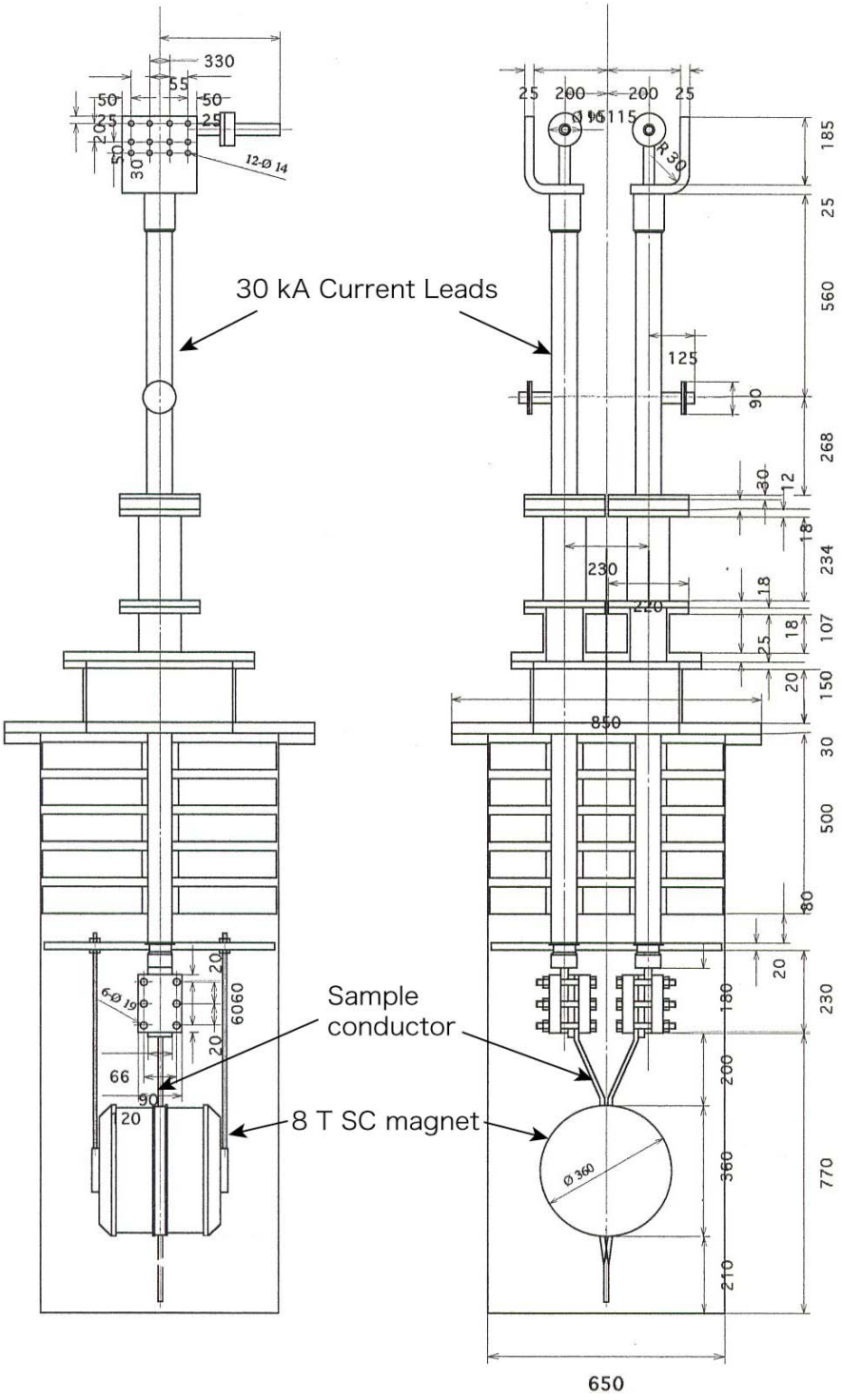

Fig. 4.8: 8-T split coil facility used for HTS conductor tests.

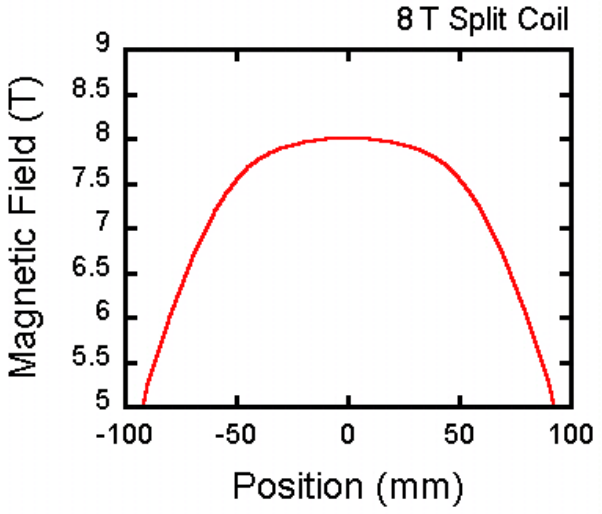

Fig. 4.9: Magnetic field profile generated by the 8-T split coil. The zero position in the horizontal axis indicates the center of the coil.

4.2.2 ANSYS calculations for temperature elevation of the HTS conductors

The ANSYS calculations were carried out to estimate the required heater power to elevate the temperature of the HTS conductor using stainless steel heaters. The 3-D modeling was done in ANSYS and temperature dependent material properties were used for analysis. Figure 4.10 shows the cross-section of the 3-D model of HTS conductor. The "solid 70" finite element was used to model the HTS conductor components.

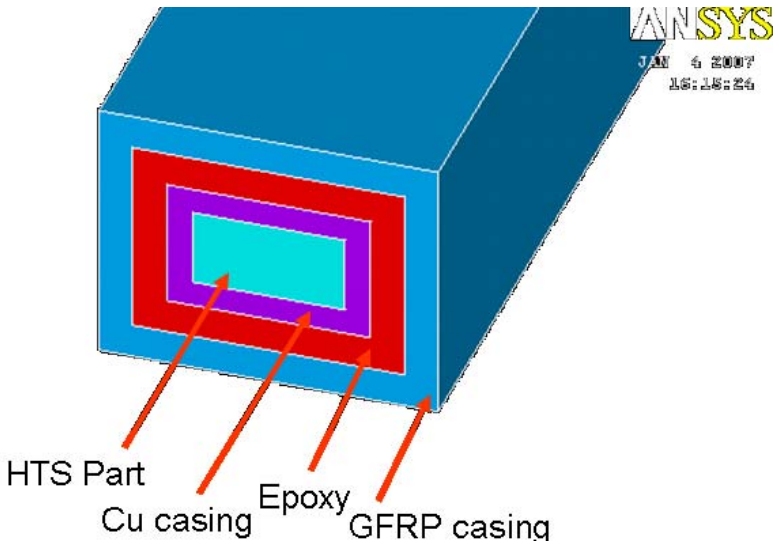

Fig. 4.10: Cross-sectional image of the HTS conductor modeled in ANSYS for temperature elevations calculations.

Figure 4.11 shows the ANSYS results of the temperature distribution along the length of the HTS conductor. The heater power for this calculation is considered to be 17 W for each heater. The two conductor ends and other four surfaces of the GRRP insulation were kept at 4.2 K during calculations, as would be the case in real experiments. According to the calculations, the temperature at the center of the conductor rises up to about 21 K. Figure 4.12 shows the graph of the temperature distribution along the conductor length for more clarity. The temperature in the testing area of about 100 mm is supposed to be uniform within the accuracy of 0.5 K.

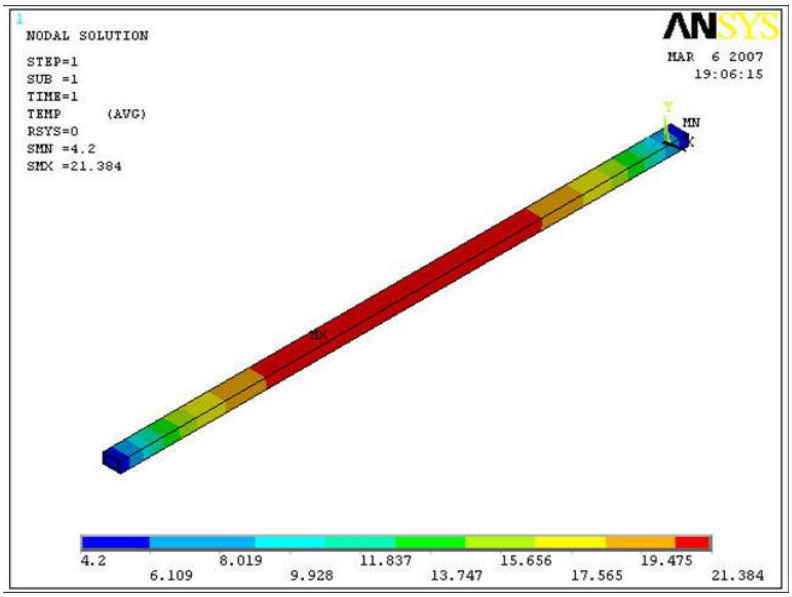

Fig. 4.11: ANSYS results of temperature elevation calculations. The heater wattage was considered as 17 W for each heater.

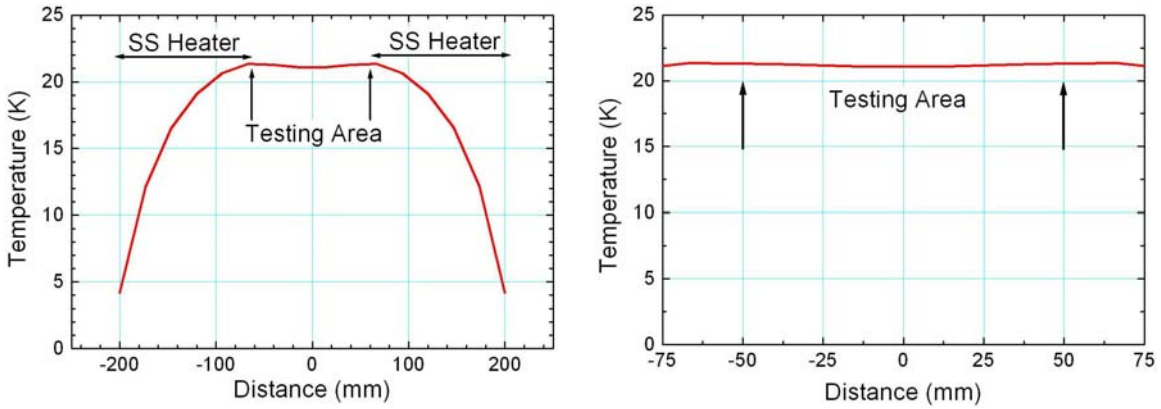

(a) (b)

Fig. 4.12: Temperature distribution along the conductor length for 17 W powers in each heater. The locations of the heaters are mentioned in the graph. Fig. (b) shows the temperature distribution in the test area of about 100 mm.

4.2.3 Temperature elevation experiment in liquid nitrogen with short samples

Before applying the idea to real HTS conductors, it was thought to be necessary to test the concept on short samples in liquid nitrogen. For this purpose short samples were prepared and tested in liquid nitrogen. A copper bar of 1000 mm × 20 mm × 10 mm was equipped with stainless steel heaters and then insulated with PTFE. The testing length was 400 mm by installing the heaters of 150 mm length and keeping central 100 mm without any heater element. All four sides of the sample were covered by PTFE sheets (3.0 mm thick). The PTFE sheets were applied using Araldite adhesive. After the PTFE sheets, the sample was covered by two layers of PTFE tape. Two Pt-Co temperature sensors were installed at the center and at the boundary between two heaters to measure the temperature distribution during the heating of the copper plate. Initially, the whole sample was immersed into the liquid nitrogen and then the heaters were turned on with 10 A current (28 W of each heater at 77 K). Figure 4.13 shows the measurement results. The maximum temperature went up to 92.4 K.

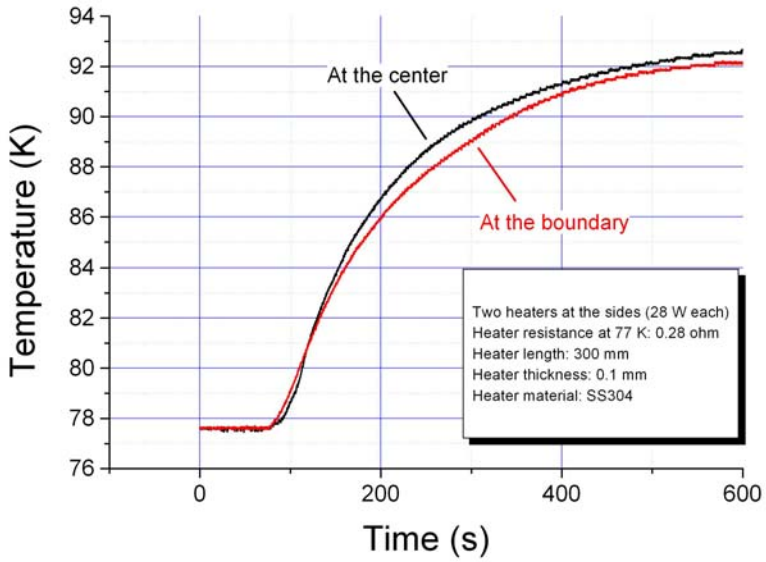

Fig. 4.13: Measured temperatures at the center and at the boundary between two heaters.

(a)

(b)

(c)

Fig. 4.14: (a) Heaters on the copper plate; (b) PTFE insulation on three sides of the copper plate and temperature sensors; (c) insulated sample in the bath.

Figure 4.14 shows some pictures of the sample. The heating of the copper plate was simulated using ANSYS. The three dimensional model with temperature dependent thermal properties was used for the simulations. The "Solid 70" element was used for the modeling of copper plate and PTFE insulation. The fixed temperature of 77 K at all six surfaces exposed to liquid nitrogen was used. A heat generation of 28 W in each heater was applied. The model length was 400 mm, which was equal to the real sample length with insulation. The steady state temperature rise of the copper plate with 56 W heater power is ~ 88.7 K. Figure 4.15 shows the ANSYS model and results.

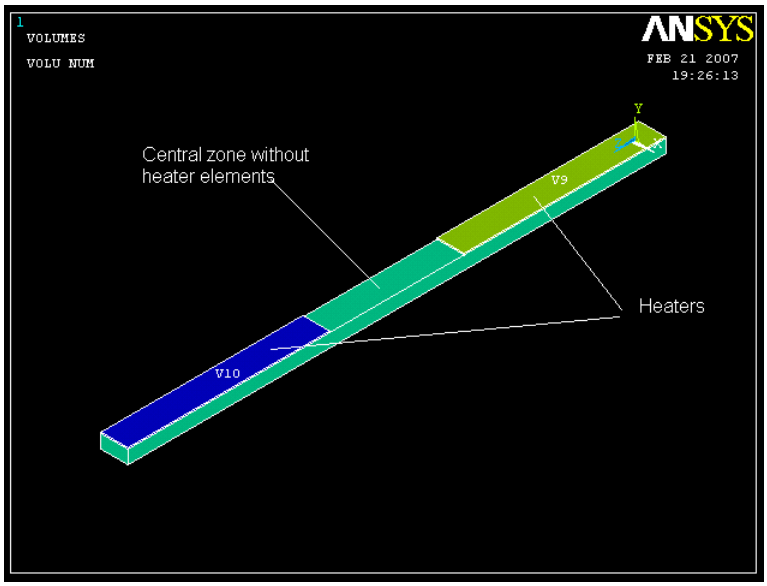

(a)

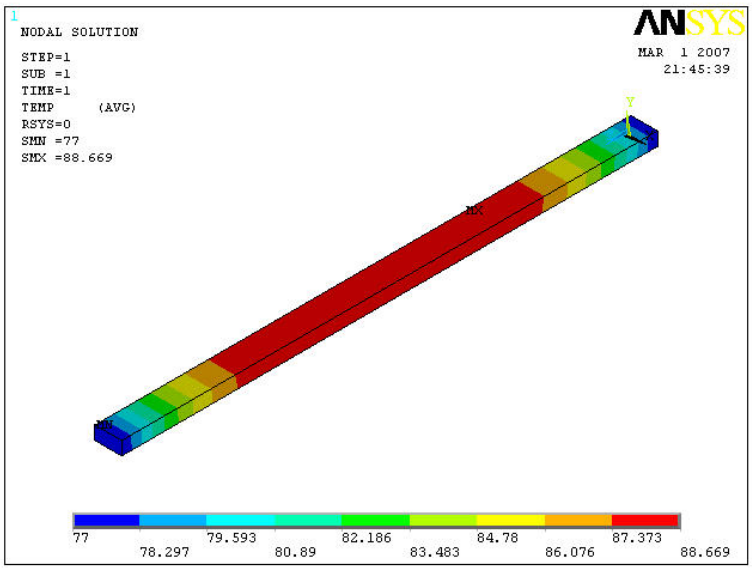

(b)

Fig. 4.15: (a) ANSYS Model with copper plate and heaters (insulation is not shown here); (b) Steady state solution with 56 W heating (two heaters).

The results of the calculations and measurements agree well and then it was decided to apply the same heating method to real HTS conductors.

4.3 Experimental results

The critical current measurements, stability measurements, and ramp rate tests were carried out on the HTS conductors at different operating conditions. This section discusses the experimental results.

4.3.1 Critical currents at different temperatures and 8 T field

Bi-2223/Ag HTS conductor

The critical current measurements were carried out at different temperatures and 8 T bias field parallel to ab-plane. Since the HTS conductors are supposed to be operated in high magnetic fields of more than 12 T or so in a fusion device, the tests were carried out in the maximum available magnetic field of 8 T in our experiments. The critical currents of the HTS conductor were measured using one pair of voltage taps designated as V6 (20 mm spacing) attached at the center of the GFRP-insulated conductor. At the center, two CERNOX temperature sensors (designated as TS1 and TS3) were also attached on two opposite surfaces of the conductor to observe the temperature evolution. The bias magnetic field, parallel to ab-plane of the HTS tapes, was applied using an 8 T split coil. The measured V-I curve of the HTS conductor at 4.2 K and 8 T bias field is shown in Fig. 4.16. The noise signal was observed as soon as the current was applied to the conductor. This was due to the thyristors of the 30 kA power supply. Therefore, the smoothing technique was applied to the raw data to filter out the noise signals before evaluating the critical currents. The raw data as well as the smoothed data are shown in Fig. 4.16. The measured temperature at the center of the conductor is also shown in Fig. 4.16. A non-linear rise in conductor temperature was observed, which exactly follows the non-linear

rise in the voltage. The temperature rise was due to the appearance of flux-flow resistance in the HTS conductor. By the time, the electric field was 1 μV/cm, the temperature of the conductor was about 5.5 K. For evaluating the critical current of the HTS conductor, the experimental data were fitted with a non-linear power law, $E/E_c = (I/I_c)^n$, with E_c = 1 μV/cm criterion. The experimental data were fitted up to 5 μV/cm so that the error due to the temperature change of the conductor was not significant. The evaluated critical current and n-value of the HTS conductor at 8 T and 5.5 K is 14.2 kA and 30 respectively.

The measured V-I curve of the HTS conductor at 10 K in 8T bias field is shown in Fig. 4.17. Before supplying the current into the conductor, the conductor temperature at TS1, TS2, TS3, and TS4 locations was 10.4 K, 12.2 K, 9.9 K, and 9.8 K respectively. At the V6 voltage tap location, the temperature difference across the conductor cross-section was about 0.5K. The similar temperature conditions were established in the conductor for the measurements at 20 K and 30 K. As shown in Fig. 4.17, the conductor temperature kept increasing slowly due to the SS heater power during critical current measurements. Once there was a non-linear rise in the voltage due to the appearance of the flux-flow resistance, the temperature also increased non-linearly. The conductor temperature was about 11 K by the time the electric field was 1 μV/cm. The critical current was evaluated by fitting the experimental data up to about 5 μV/cm with a non-linear power law, $E/E_c = (I/I_c)^n$, with E_c = 1 μV/cm criterion. The evaluated critical current and n-value of the HTS conductor at 8 T and 11 K are 12.9 kA and 19.5, respectively. Similarly, the critical current measurements were done at 20 K, and 30 K in a bias magnetic field of 8T. The critical current and n-values at 22 K and 32 K are 10.5 kA, 17.2 and 8.23 kA, 17 respectively. The measured critical currents show linear dependence on temperature as shown in Fig. 4.18. The simple sum of the critical currents of all the tapes in HTS conductor (without self-field effects) and the calculated critical currents of the HTS conductor using load-line analysis (with self-field effects) [4.11] are also shown in Fig. 4.18.

The calculated critical currents of the HTS conductors agree well with the experimentally observed critical currents.

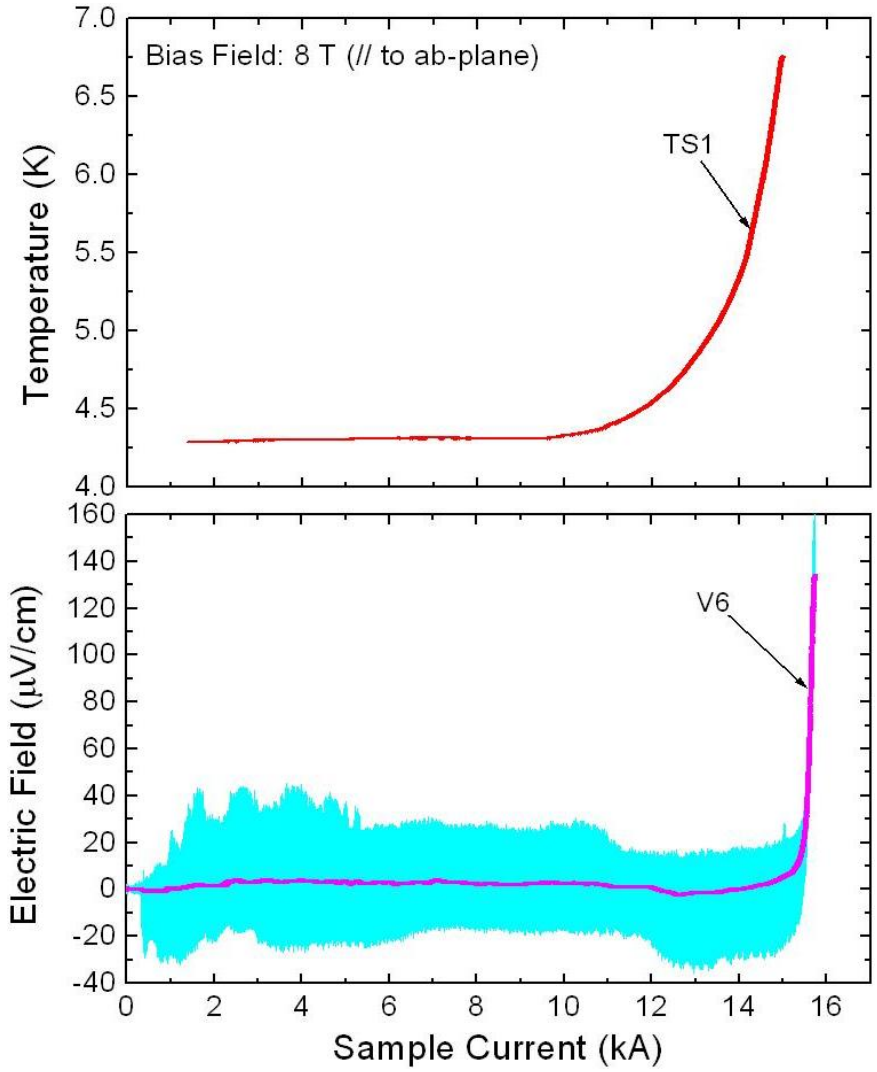

Fig. 4.16: V-I curve of the HTS conductor at 8 T bias field (// to ab-plane) and 4.2 K. The experimental data is fitted with a non-linear power law, $E/E_c = (I/I_c)^n$, with 1 μV/cm criterion. The temperature evolution observed by a CERNOX temperature sensor, TS1, is also shown. The evaluated critical and n-value are 14.2 kA and 30 (at 5.5 K, 8 T) respectively.

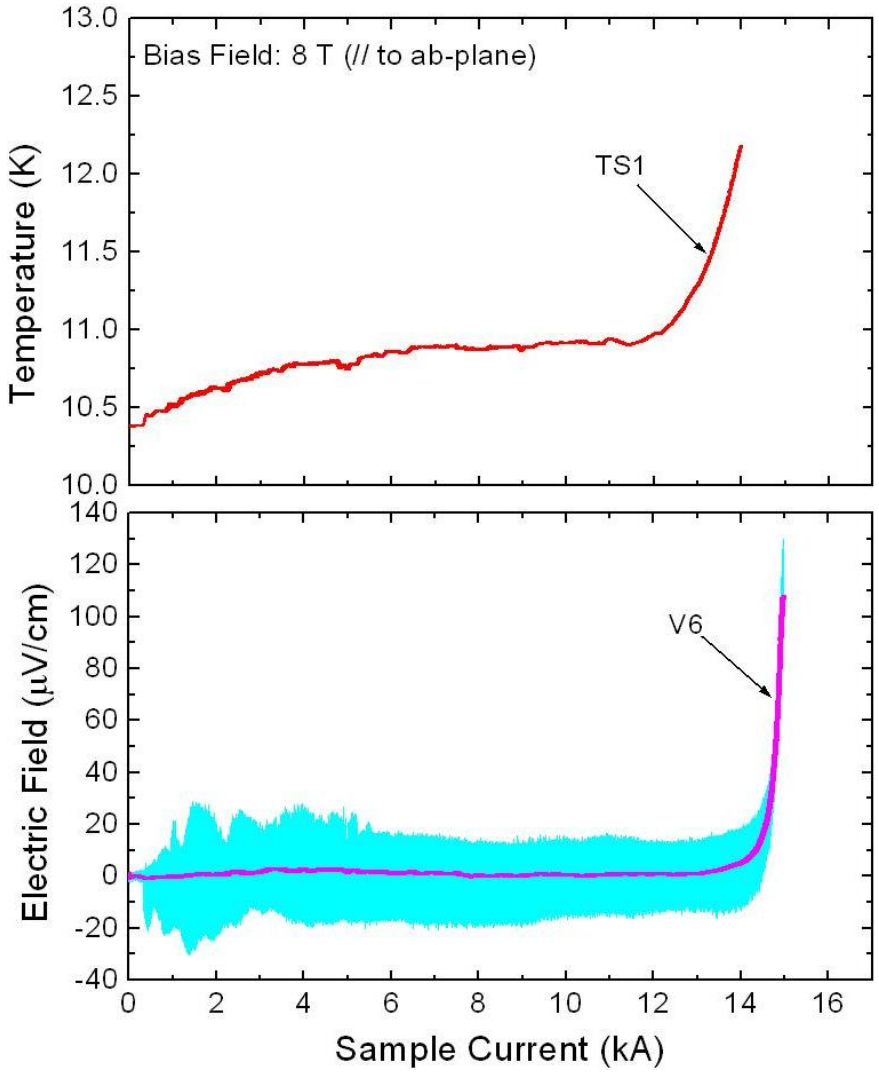

Fig. 4.17: V-I curve of the HTS conductor at 8 T bias field (// to ab-plane) and 10K. The experimental data are fitted with a non-linear power law, $E/E_c = (I/I_c)^n$, with 1 μV/cm criterion. The temperature evolution observed by CERNOX temperature sensor, TS1, is also shown. The evaluated critical and n-value are 12.9 kA and 19.5 (at 11 K, 8 T) respectively.

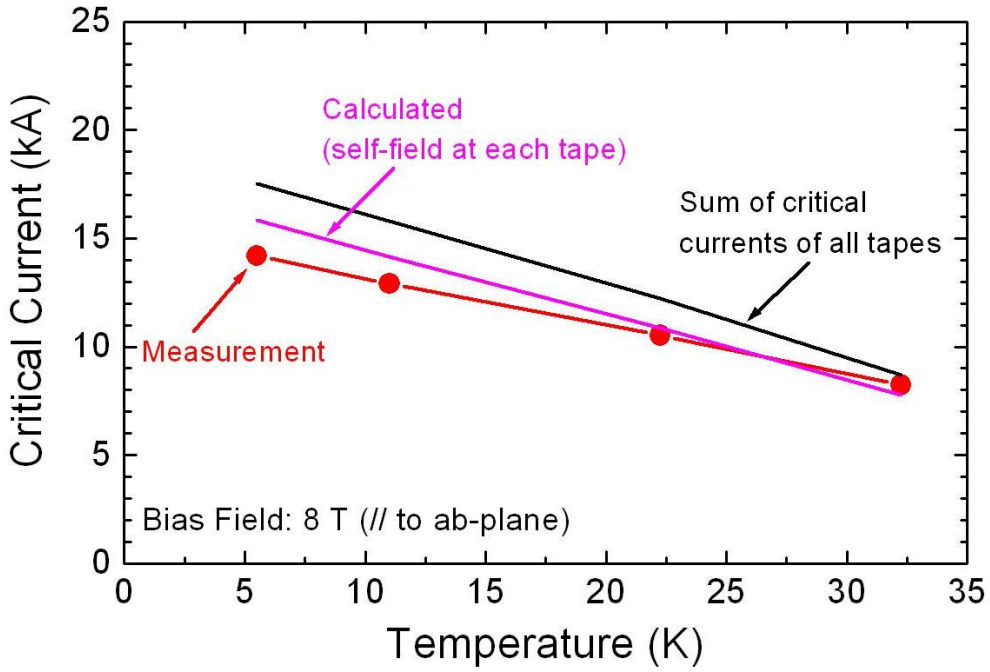

(a)

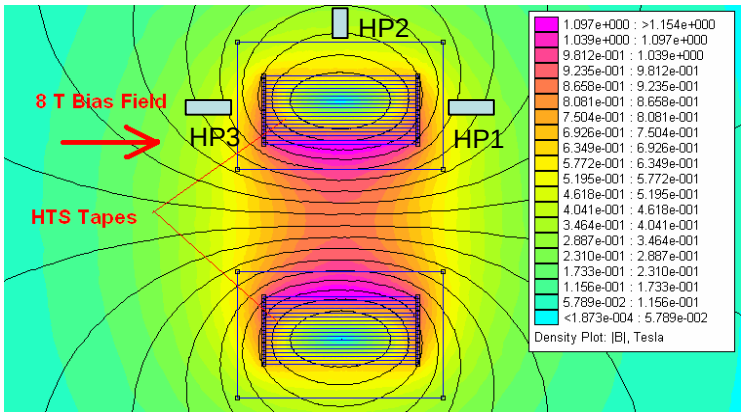

(b)

Fig. 4.18: (a) temperature dependence of the measured critical currents of the HTS conductor. The simple sum of the critical currents of all the HTS tapes in HTS conductor (without self-field effects) and calculated critical currents of the HTS conductor with a load-line analysis (with self-field effects) are also shown; (b) calculated field distribution on the HTS tapes inside the conductors. Each tape is carrying 100 A current.

YBCO HTS conductor

Similar to Bi-2223/Ag HTS conductor, the YBCO conductor was tested by preparing a sample in hairpin configuration. The YBCO conductor was thermally insulated by epoxy and GFRP exactly in the same way as the Bi-2223/Ag conductor sample as discussed before. The other leg of the YBCO conductor sample was actually the Bi-2223/Ag conductor having 34 numbers of Bi-2223/Ag tapes inside the copper sheath. This leg was directly immersed in liquid helium. The joint between YBCO and Bi-2223/Ag conductors at the bottom of the sample was prepared by soldering the NbTi/Cu Rutherford cables between and outside the conductors to reduce the joint resistance as shown in Fig. 4.19. The similar technique was used for Bi-2223/Ag conductor sample as well. The measured joint resistance was less than 2 nano-ohms at 15 kA and 8 T.

The critical currents of the YBCO conductor were measured using one pair of voltage taps attached at the center of the GFRP-insulated conductor. At the center, two CERNOX temperature sensors (designated as TS1 and TS3) were also attached on two opposite surfaces of the conductor to observe the temperature evolution. The bias magnetic field, parallel to ab-plane of the HTS tapes, was applied using an 8 T split coil. The measured V-I curve of the HTS conductor at ~20 K and 8 T bias field is shown in Fig. 4.20. The raw data as well as the smoothed data are shown in Fig. 4.20. The measured temperature at the center of the conductor is also shown in Fig. 4.20. Similar to Bi-2223/Ag conductor, a non-linear rise in YBCO conductor temperature was observed, which exactly follows the non-linear rise in the electric field. The temperature rise was due to the appearance of flux-flow resistance in the conductor. By the time, the electric field was 1 μV/cm, the temperature of the conductor was about 24 K. For evaluating the critical current of the HTS conductor, the experimental data were fitted with a non-linear power law, $E/E_c = (I/I_c)^n$, with E_c = 1 μV/cm criterion. The experimental data were fitted up to 5 μV/cm so that the error due to the temperature change of the conductor was not significant. The evaluated critical current and n-value of the YBCO conductor at 8 T and 24 K is 14.2 kA and 30 respectively.

The measured V-I curve of the HTS conductor at ~10 K in 8T bias field is shown in Fig. 4.21. Once there was a non-linear rise in the electric field due to the appearance of the flux-flow resistance, the temperature also increased non-linearly. The conductor

temperature was about 15.5 K by the time the electric field was 1 μV/cm. The critical current was evaluated by fitting the experimental data up to about 5 μV/cm with a non-linear power law, $E/E_c = (I/I_c)^n$, with E_c = 1 μV/cm criterion. The evaluated critical current and n-value of the HTS conductor at 8 T and 15.5 K are 16.8 kA and 30, respectively. Similarly, the critical current measurements were done at ~25 K in a bias magnetic field of 8T. The evaluated critical current and n-values at 27 K are 12.5 kA and 30 respectively. The conductor temperature could not be raised beyond 25 K due to the current limitation in the S.S. heater power supplies and therefore measurements were restricted to only ~25 K. The critical current measurement at 4.2 K, 8 T was also tried but the other conductor leg of the sample, which was Bi-2223/Ag conductor, showed electric field rise rather than the YBCO conductor. This clearly means the critical current of the YBCO conductor was much higher than the Bi-2223/Ag conductor and therefore the critical current of the YBCO conductor could not be measured at 4.2 K, 8T.

The measured critical currents show linear dependence on temperature as shown in Fig. 4.22. The simple sum of the critical currents of all the tapes in HTS conductor (without self-field effects) and the calculated critical currents of the HTS conductor using load-line analysis (with self-field effects) [4.11] are also shown in Fig. 4.22. The experimental I_c-B-T characteristics of the YBCO and GdBCO tapes are not available and therefore, the percolation model [4.12] has been used to derive these characteristics. Due to the lack of real I_c-B-T characteristics of used YBCO and GdBCO tapes, the agreement between calculated and measured critical currents is not good. To improve the agreement between calculated and experimental results of critical currents, the experiments on the YBCO and GdBCO tapes are planned to be a future task. The derived I_c-B-T characteristics of the YBCO tape (using percolation model), required for our YBCO conductor calculations, are shown in Fig. 4.23. Even though the magnetic field dependence of the critical currents of GdBCO and YBCO tapes might be different from each other, in the present calculations, for simplicity, the I_c-B-T characteristics have been derived by considering the average critical current of 200 A of the YBCO (210 A) and GdBCO (190 A) at self-field and 77 K and therefore, both the tapes have been considered to be equivalent with each other for load line analysis.

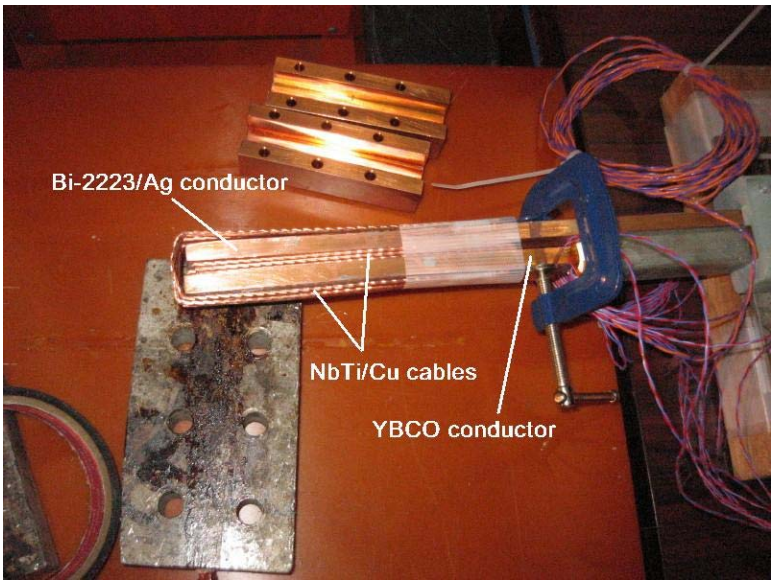

(a)

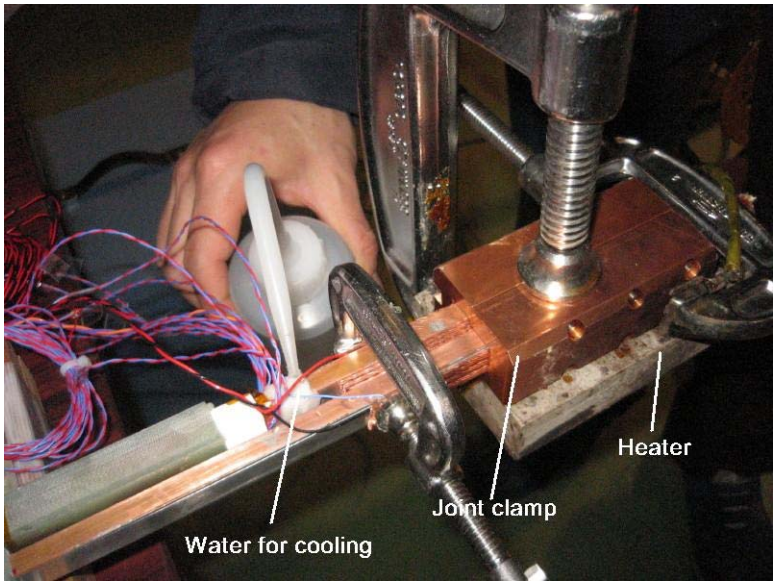

(b)

Fig. 4.19: (a) photo of joint between Bi-2223/Ag and YBCO conductor at the bottom of the sample. The NbTi/Cu cables are used in between and outside the conductors to reduce the joint resistance; (b) joint with clamps and heater attached just before starting the soldering of the joint.

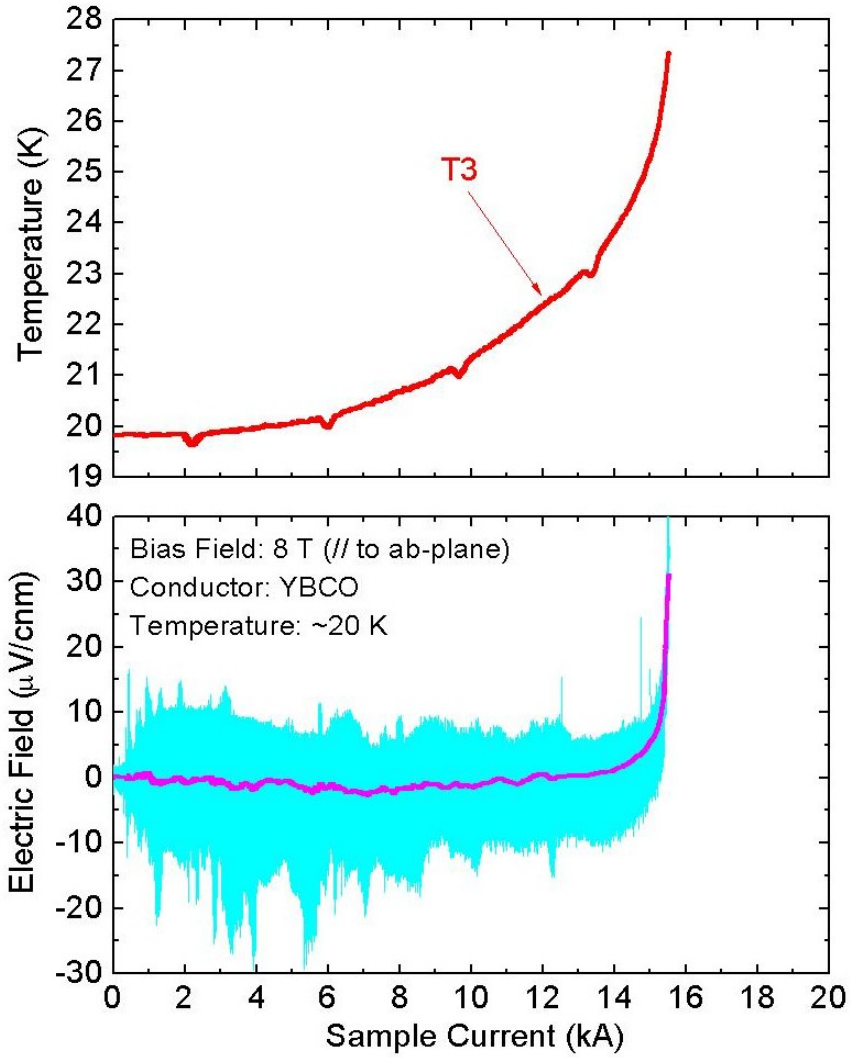

Fig. 4.20: V-I curve of the YBCO conductor at 8 T bias field (// to ab-plane) and ~20 K. The experimental data is fitted with a non-linear power law, $E/E_c = (I/I_c)^n$, with 1 μV/cm criterion. The temperature evolution observed by a CERNOX temperature sensor, TS3, is also shown. The evaluated critical and n-value are 14.2 kA and 30 (at 24 K, 8 T) respectively.

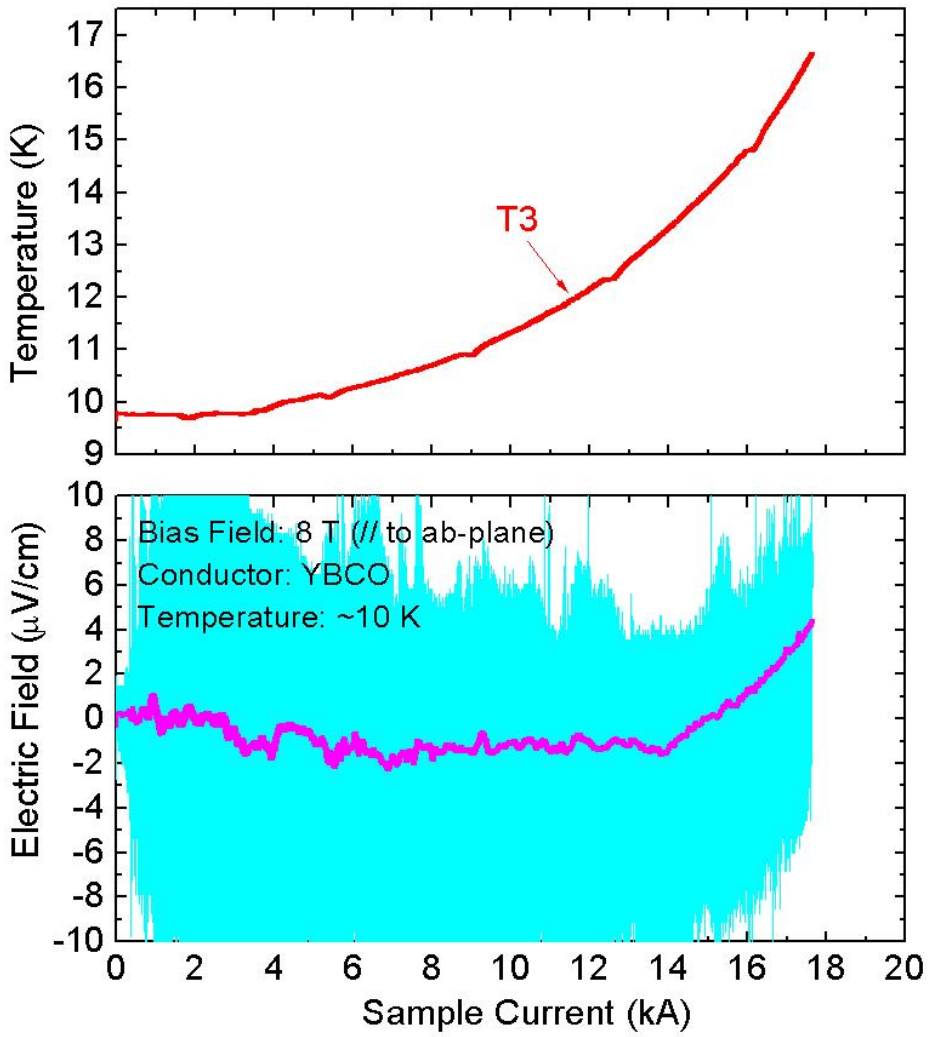

Fig. 4.21: V-I curve of the YBCO conductor at 8 T bias field (// to ab-plane) and ~10 K. The experimental data is fitted with a non-linear power law, $E/E_c = (I/I_c)^n$, with 1 μV/cm criterion. The temperature evolution observed by a CERNOX temperature sensor, TS3, is also shown. The evaluated critical and n-value are 16.8 kA and 30 (at 15.5 K, 8 T) respectively.

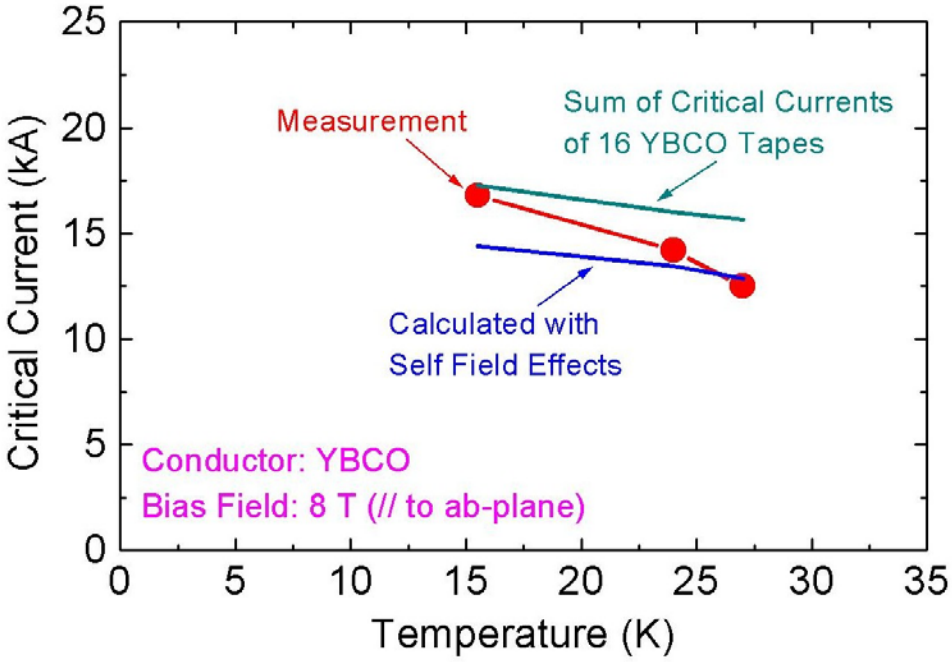

(a)

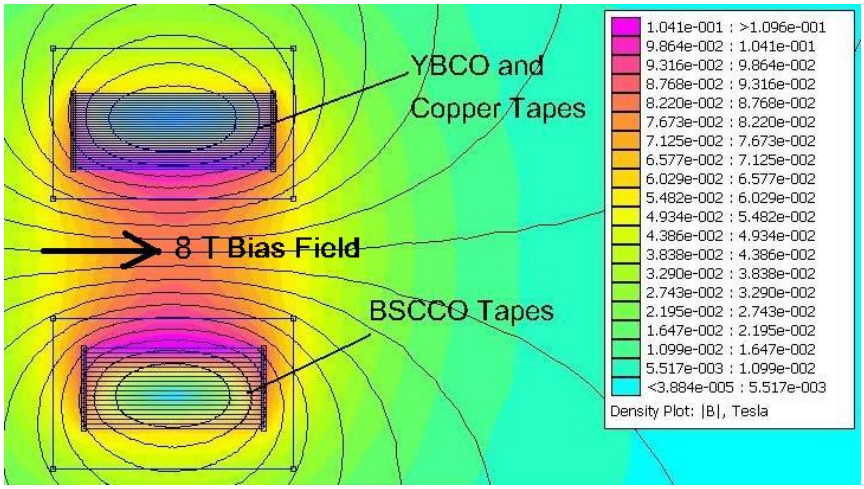

(b)

Fig. 4.22: (a) temperature dependence of the measured critical currents of the YBCO conductor. The simple sum of the critical currents of all the HTS tapes in the conductor (without self-field effects) and calculated critical currents of the YBCO conductor with a load-line analysis (with self-field effects) are also shown; (b) calculated field distribution on the HTS tapes inside the conductors. Each tape is carrying 100 A current.

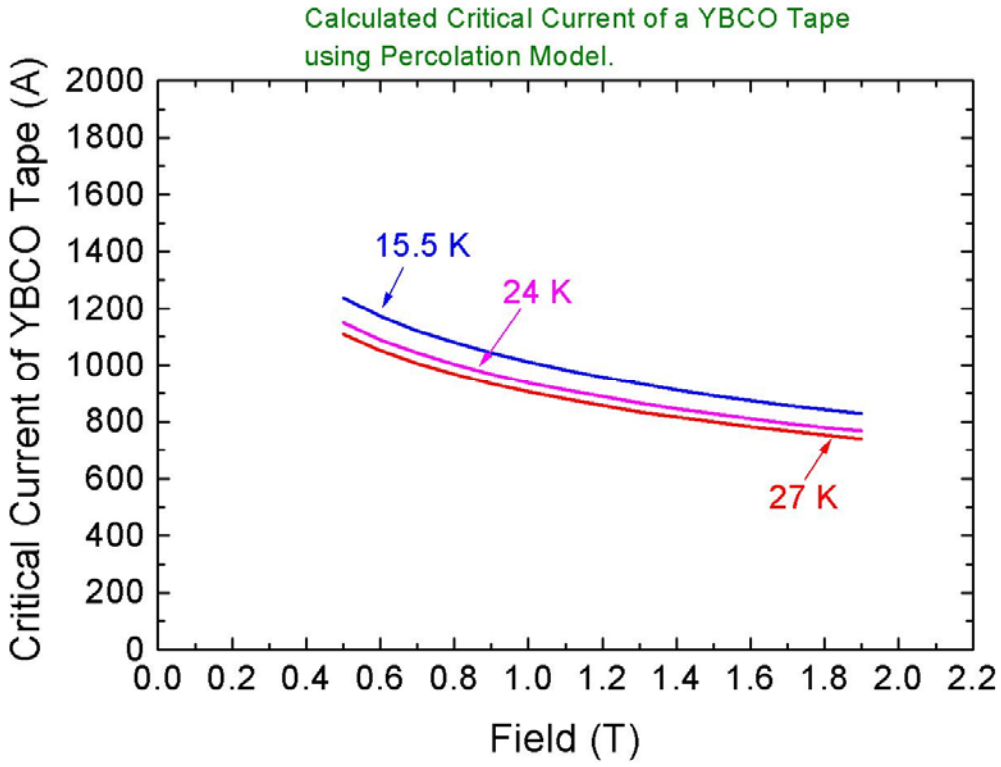

Fig. 4.23: Calculated I_c-B-T characteristics of the YBCO tape using percolation model [4.12].

4.3.2 Minimum quench energy at different currents and temperatures

Bi-2223/Ag HTS conductor

The experiments were carried out to measure the minimum quench energy (MQE) of the GFRP-insulated HTS conductor using the thin-film resistive heaters attached on to the conductor at the center. Several voltage taps attached to the copper sheath of the conductor, as shown in Fig. 4.7, were used to monitor the quench propagation. CERNOX

temperature sensors gave the information about temperature evolution during quench propagation.

These experiments were carried at 4.2 K, 10 K, and 20 K from 13 kA to 9 kA. Using thin film heaters, the energy was deposited into the conductor from ~2122 to ~30490 mJ/cc. The voltage development was observed by several voltage taps but the superconductivity was recovered soon and no thermal runaway was observed. Figure 4.24 shows one example of the voltage developments at 20 K and 10 kA current. The conductor was carrying about 90% of the critical current at 20 K but still conductor did not quench. The temperature rose up to about 35 K at the center, which was more than the current sharing temperature, T_{cs}, (~31 K) of the conductor. The current sharing temperature, Tcs, is calculated by using equation 4.1.

$$T_{cs} = T_{op} + (T_c - T_{op})\left[1 - \frac{I_t}{I_c(T_{op})}\right] \tag{4.1}$$

where T_{op}, T_c, I_t, I_c are the operation temperature, critical temperature, transport current, and critical current at a specified temperature respectively. By considering the linear dependence of critical current on temperature (as shown in Fig. 4.25), the current sharing temperatures have been calculated as shown in Fig. 4.26.

The reason for no quench in HTS conductor might be the good thermal conduction through the copper sheath towards the ends of the conductor, which were immersed in liquid helium at 4.2 K. The maximum input energy was restricted to 30,490 mJ/cc due to the limitation on the power supply and thin-film heaters.

The calculated energy margin and experimental results are shown in Fig. 4.27. The energy margin is calculated by taking into account the conductor materials specific heats from operation temperature to current sharing temperature of the conductor given by equation 4.2 (in J/m^3).

$$E = \int_{T_{op}}^{T_{cs}} C_{cd}\, dT\,(J/m^3) \tag{4.2}$$

The expected stability margin at 20 K and the current loading factor of 0.9 is as high as ~2,000 mJ/cc even with the adiabatic condition. This is almost one order of magnitude higher than that for typical cable-in-conduit conductors. The stability margin of ~2000 mJ/cc can allow the energy release due to the wire motion with a distance of ~4mm caused by the electromagnetic force generated by 100 kA and 13 T. Such a large wire motion of 4 mm is very unlikely to happen in a fusion magnet. This indicates that the HTS magnets can be operated safely with high current loading factor even in adiabatic conditions. The cooling of the conductor gives added advantage to the stability of the conductor as is observed in our experiments.

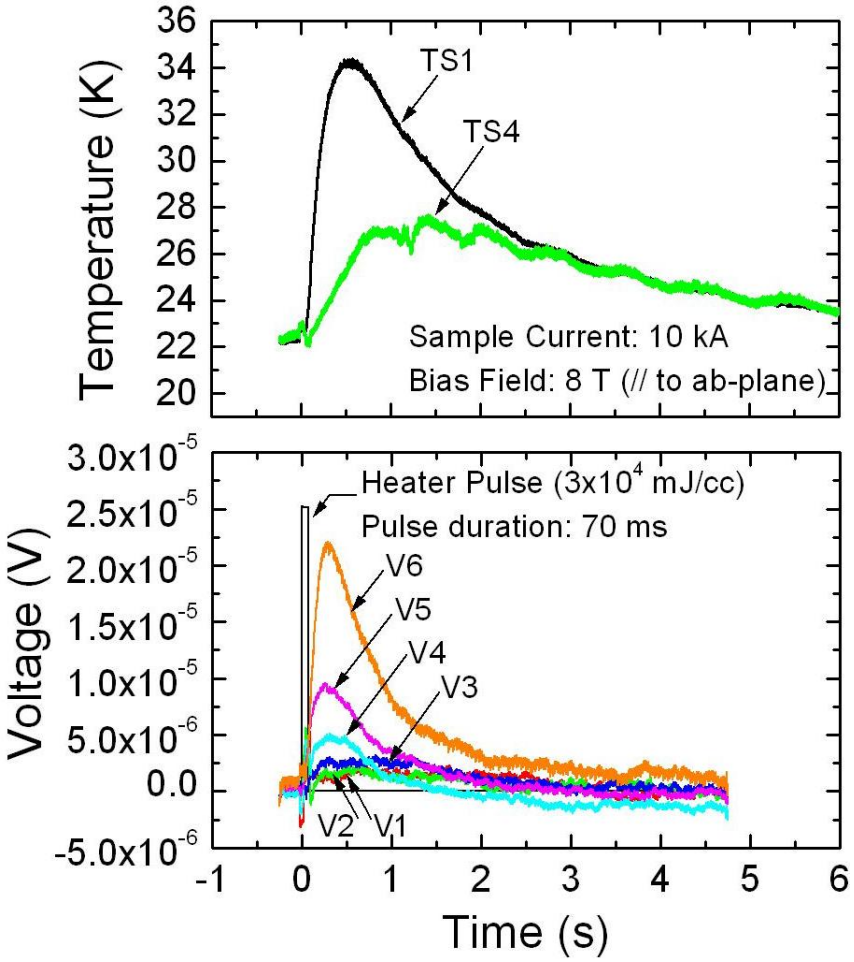

Fig. 4.24: Voltage development in the conductor after a heater pulse of 70 ms duration. Temperature evolution is also shown at the center (TS1) and the boundary (TS4) of the testing area.

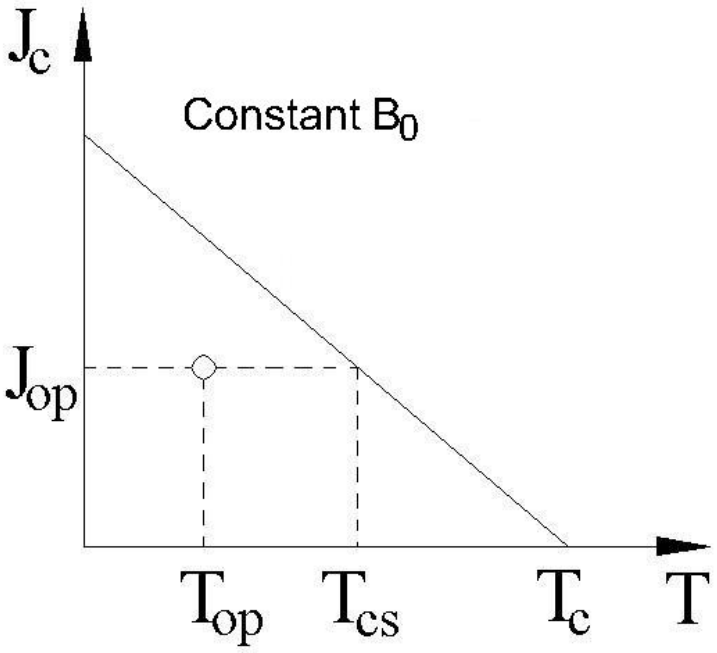

Fig. 4.25: Typical linear temperature dependence of critical current of HTS tape.

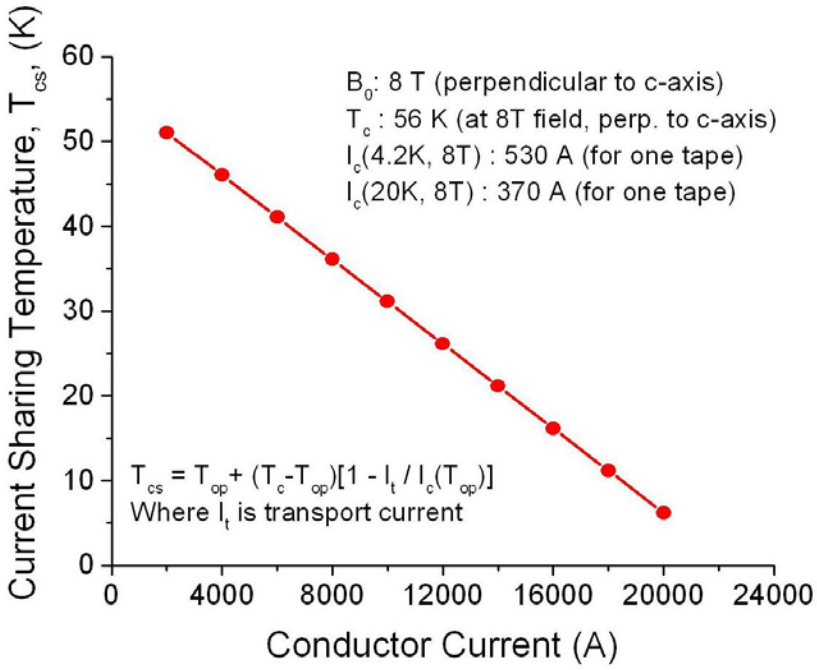

Fig. 4.26: Current sharing temperature of the HTS conductor as a function of transport current.

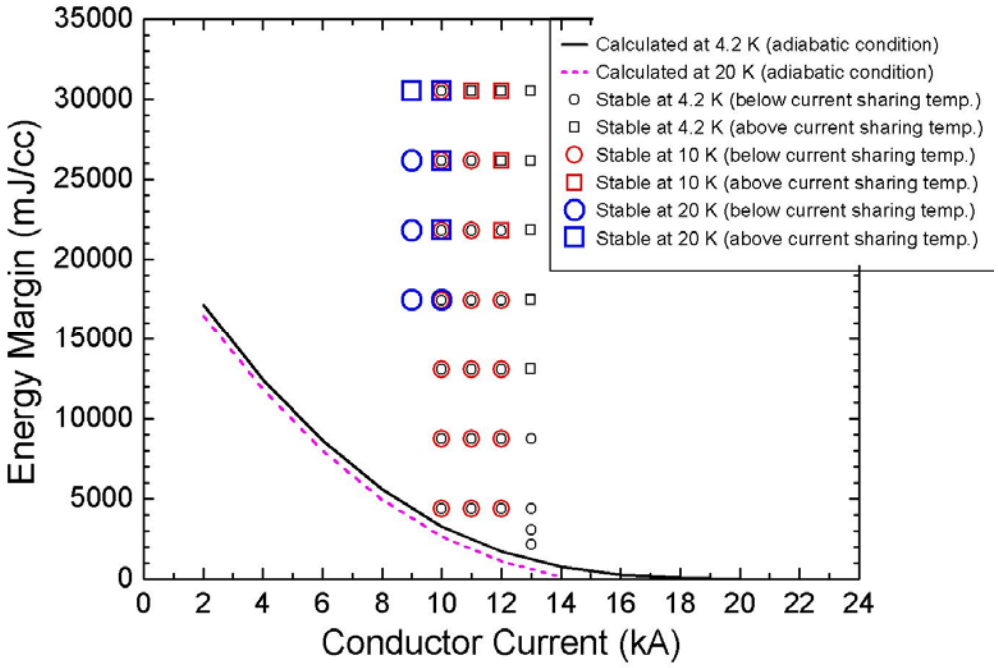

Fig. 4.27: Calculated energy margin of the HTS conductor in adiabatic conditions. The experimental data are also shown. At open circles, the conductor temperature was raised below the current sharing temperature whereas at open squares the conductor temperature was raised above the current sharing temperature after the energy input by thin film heaters. No thermal runaway of the conductor could be observed.

YBCO HTS conductor

The stability experiments were carried out on the GFRP-insulated YBCO HTS conductor as well. Seven pairs of voltage taps (20 mm apart) attached to the copper sheath of the conductor were used to monitor the normal-zone propagation. CERNOX temperature sensors gave the information about temperature evolution during normal-zone propagation.

These experiments were carried at 20 K from 13 kA to 15 kA. Using thin film heaters, the energy was deposited into the conductor from ~2000 to ~87,446 mJ/cc. At 13 kA, the voltage development was observed by several voltage taps but the

superconductivity was recovered soon and no thermal runaway was observed. Figure 4.28 shows one example of the voltage developments at 20 K and 13 kA current. The conductor was carrying about 90% of the critical current at 20 K but still conductor did not quench. The temperature rose up to about 45 K at the center, which was more than the current sharing temperature, T_{cs}, (~33 K) of the conductor. The current sharing temperature, T_{cs}, is calculated by using equation 4.1. The calculated current sharing temperatures are shown in Fig. 4.29.

Similar to Bi-2223/Ag conductor, the reason for no quench in YBCO conductor might be the good thermal conduction through the copper sheath towards the ends of the conductor, which were immersed in liquid helium at 4.2 K. The maximum input energy was restricted to 87,446 mJ/cc due to the limitation on the power supply and thin-film heaters.

The stability tests were carried out at 15 kA as well, which was already more than the critical current (14.2 kA at 20 K and 8 T) of the conductor. Due to the flux-flow resistance, the conductor temperature kept increasing slowly as is clear by the base temperature shown in Fig. 4.30 is more than the set temperature of ~20 K. In this test two heater pulses were fired to initiate a quench in the conductor as shown in Fig. 4.30. After the first heater pulse of 34,625 mJ/cc, the temperature of the conductor rose up to about 40 K but conductor did not quench fully. After about 25 s of the first heater pulse, the second heater pulse of about 43,282 mJ/cc was fired. The conductor temperature rose up to about 45 K and then it kept increasing. The voltage development was also observed corresponding to the temperature rise and a quench of the conductor was observed. This test clearly showed that the HTS conductor was very hard to quench even above the critical current.

The calculated energy margin and experimental results are shown in Fig. 4.31. The energy margin is calculated by taking into account the conductor materials specific heats from operation temperature to current sharing temperature of the conductor given by equation 4.2.

. The stability tests on the HTS conductors clearly suggest that the stability margin of the HTS conductor is quite high compared to LTS cable-in-conduit conductors and

therefore HTS conductors are promising for future fusion magnets from stability point of view.

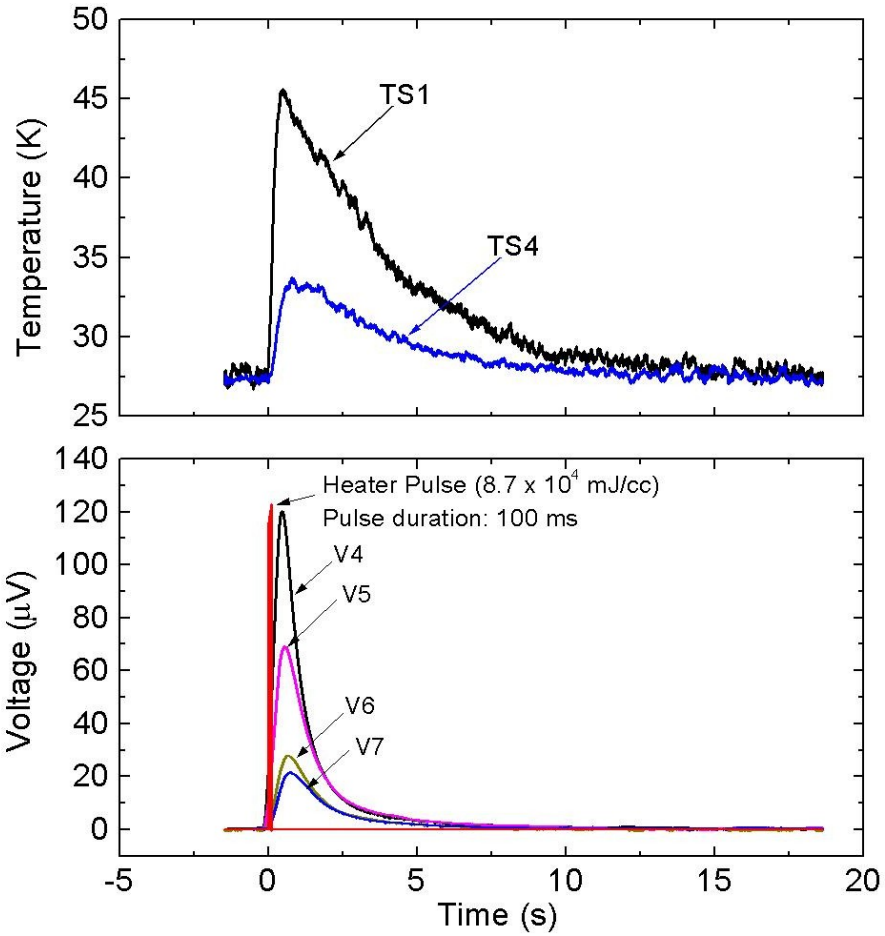

Fig. 4.28: Voltage development in the conductor after a heater pulse of 100 ms duration. Temperature evolution is also shown in the testing area.

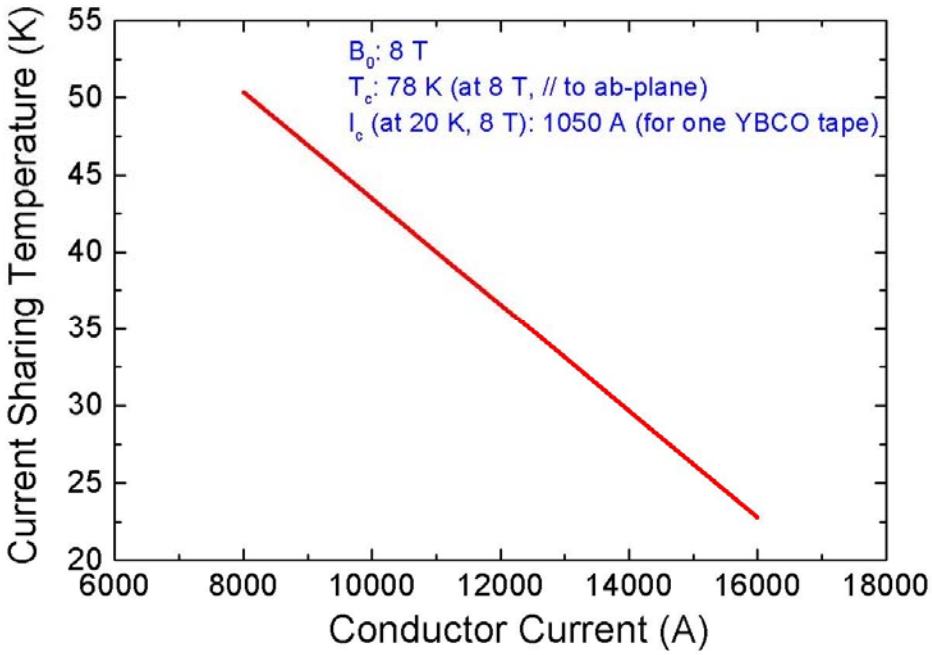

Fig. 4.29: Current sharing temperature of the YBCO conductor as a function of transport current.

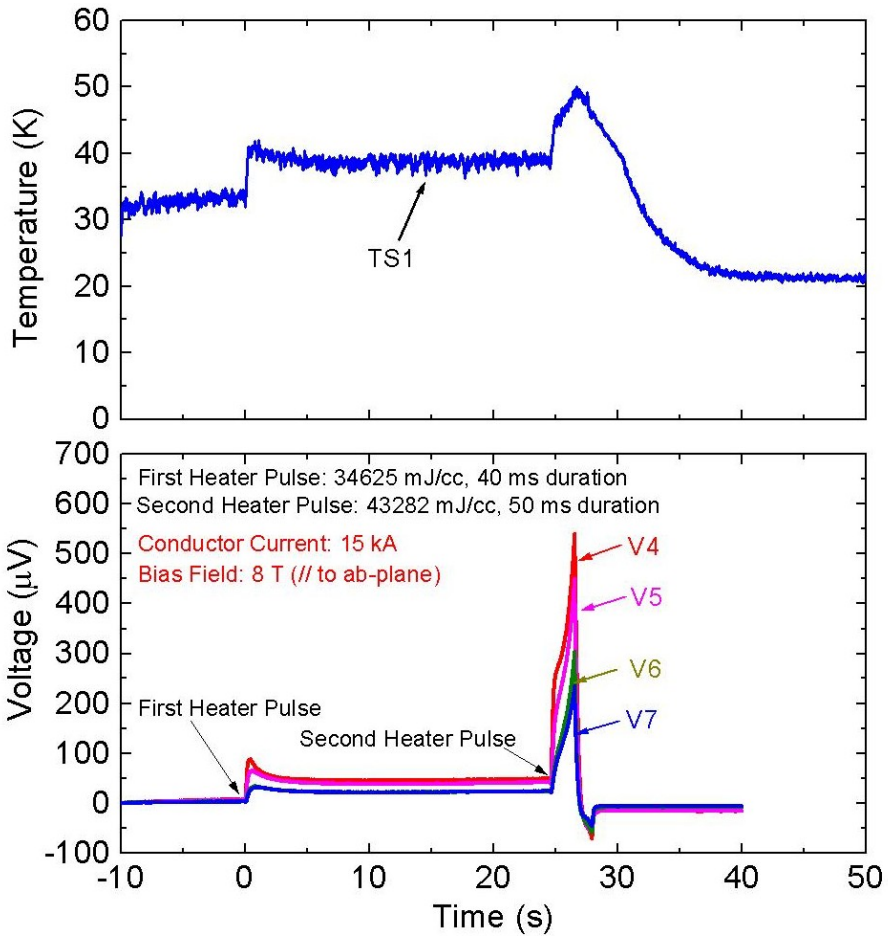

Fig. 4.30: Voltage development in the conductor after a heater pulse of 100 ms duration. Temperature evolution is also shown in the testing area.

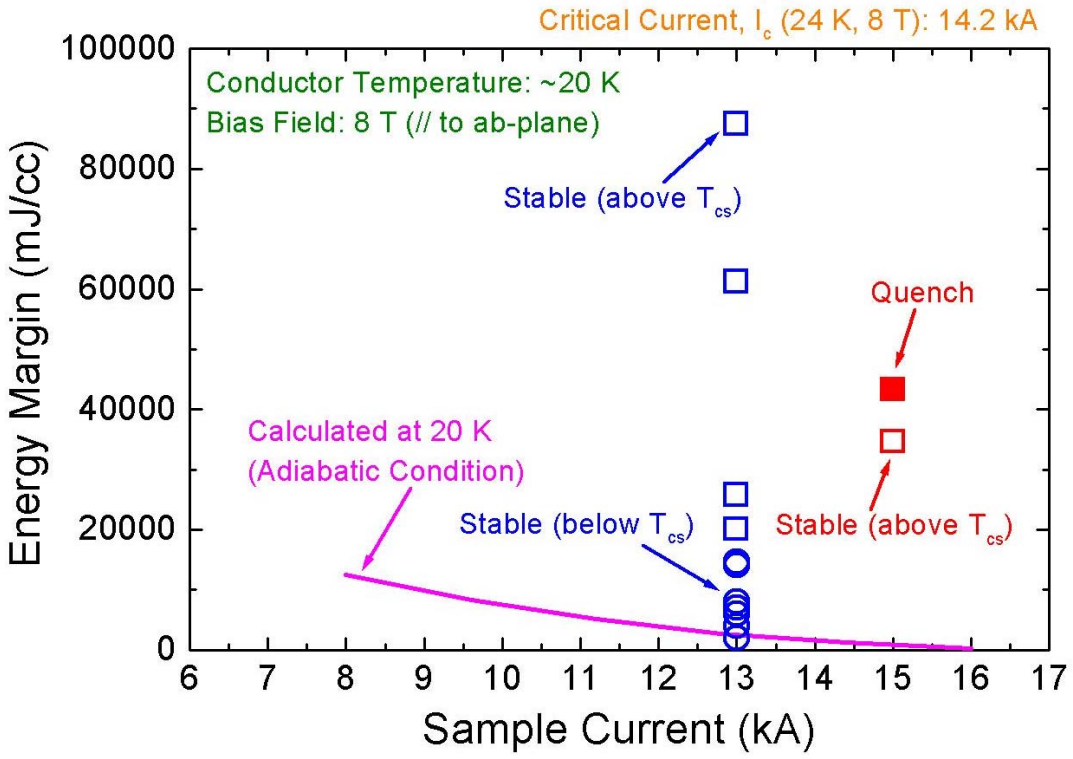

Fig. 4.31: Calculated energy margin of the YBCO conductor in adiabatic conditions. The experimental data are also shown. At open circles, the conductor temperature was raised below the current sharing temperature whereas at open squares the conductor temperature was raised above the current sharing temperature after the energy input by thin film heaters. No thermal runaway of the conductor could be observed at 13 kA whereas a quench was observed at 15 kA.

4.3.3 Ramp rate limitation (RRL) tests at different temperatures

The ramp rate limitation (RRL) tests on the HTS conductors were also carried out. Unlike LTS conductors, the HTS conductor did not show any ramp rate limitation. Unexpectedly, they even showed higher critical currents with higher ramp rates. At higher ramp rates, the time for joule heating by the appearance of flux flow resistance decreases and therefore the rise in conductor temperature also decreases and hence the higher critical current is achieved. Figure 4.32 shows the results of RRL test of Bi-2223/Ag conductor at 4.2 K temperature. Figure 4.33 shows the RRL test results at elevated temperature of ~20 K. The critical current could be measured at 4.4 K at highest ramp rate of 1.5 kA/s as 14.55 kA. At elevated temperature, the critical current was measured to be 10.6 kA at 20.5 K with a ramp rate of 1.5 kA/s. However, at lower ramp rates, due to the joule heating for a rather long time compared to high ramp rate cases, the temperature of the conductor could not be maintained at 4.2, for example in the case of measurements at 4.2 K, and the temperature raised up to 5.5 K by the time the electric field was 1 μV/cm, the criterion for critical currents. The similar temperature rise was observed in case of elevated temperature measurements with lower ramp rates.

The ramp rate tests were carried out on YBCO conductor as well. The tests were carried out only at about 20 K as the critical current measurement was not possible at 4.2 K as discussed earlier. The YBCO conductor as well showed the similar behavior as shown by Bi-2223/Ag conductor. The temperature and electric field development was smaller at high ramp rates. The ramp rate results of YBCO conductor as shown in Fig. 4.34.

HTS conductor showing no ramp rate limitation is a very good result. The performance of the HTS magnet is therefore expected to be quite high compared to LTS conductors even at quite high ramp rates.

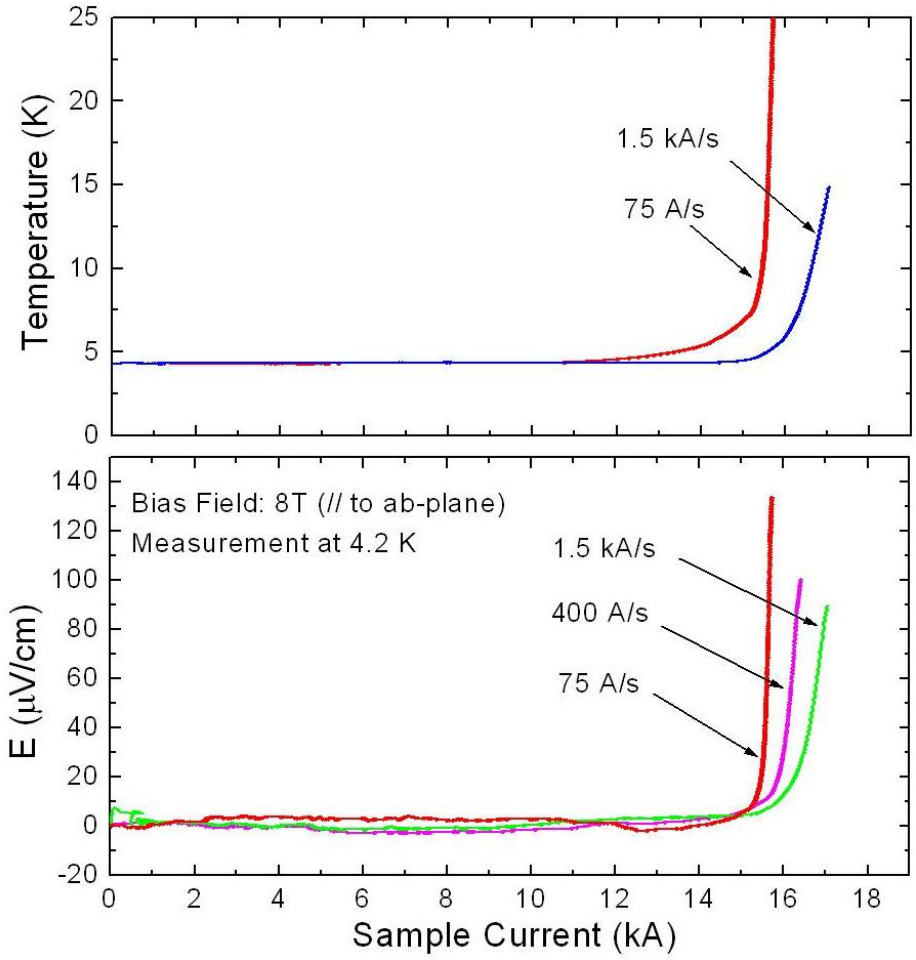

Fig. 4.32: Ramp rate dependence of Bi-2223/Ag conductor at 4.2 K.

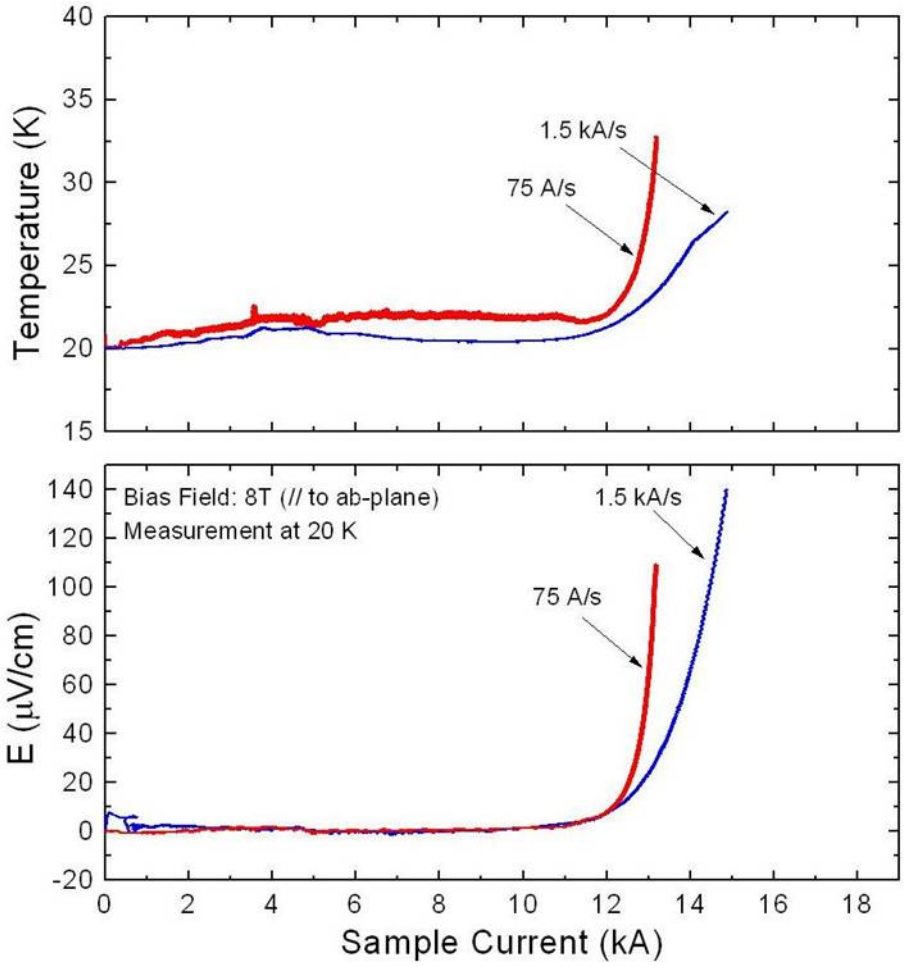

Fig. 4.33: Ramp rate dependence of Bi-2223/Ag conductor at ~20 K.

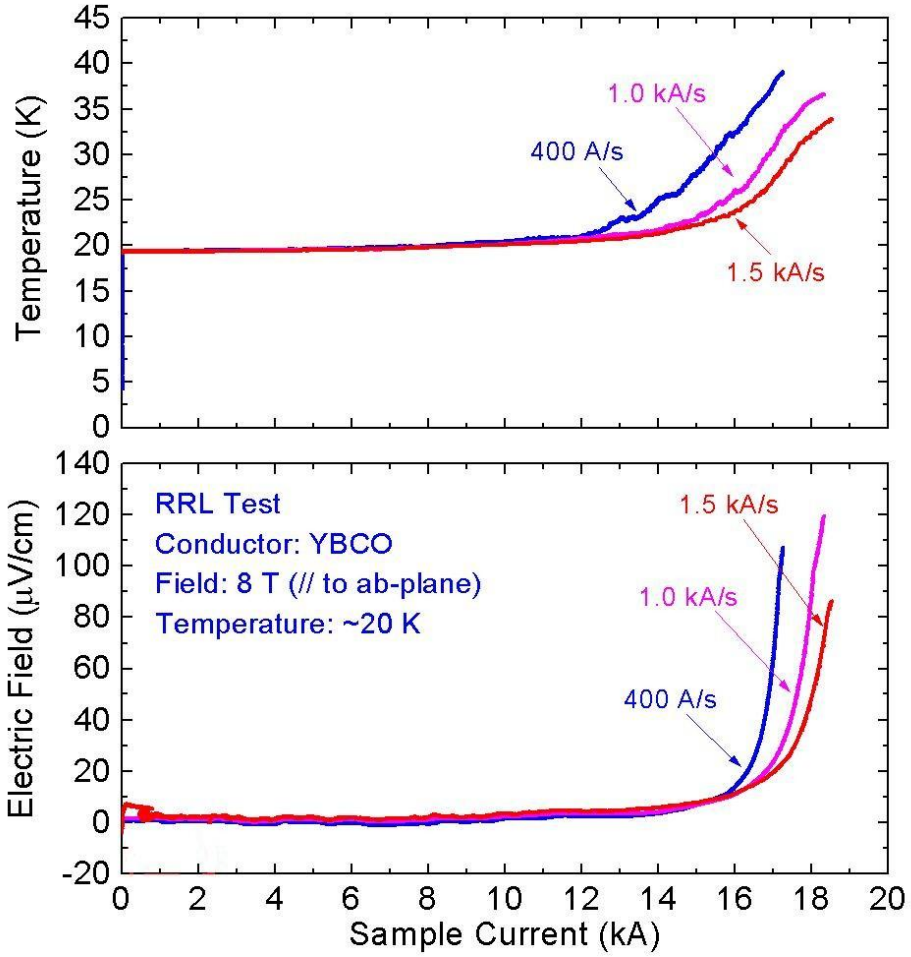

Fig. 4.34: Ramp rate dependence of YBCO conductor at ~20 K.

4.4 Summary

Toward the development of 100 kA-class HTS conductor suitable for fusion reactor magnets, the reduced-scale 10 kA-class HTS conductors have been successfully fabricated and tested. The simple stacking method was applied to reduced-scale 10 kA-class HTS conductors as well as has been proposed for 100 kA-class conductors. The following conclusions can be drawn based on the encouraging results of the 10 kA-class HTS conductors.

1. It is possible to make a HTS conductor by simply stacking the HTS tapes and soldering them inside a metal jacket, such as copper, without degrading the overall performance of the conductor due to mechanical damages during fabrication process. In other words, the fabrication process for simple stacked conductor is quite easy and high performance of the conductor can be achieved.
2. The critical currents of the HTS conductor were observed as per expectations as shown by numerical calculations by taking into account the self-field effects. This shows the success in fabricating the HTS conductor without any degradation.
3. The stability of the HTS conductor has been found to be quite high even with very high current loading of 90% of critical current. The conductor temperature could be raised beyond current sharing temperature but conductor quickly recovered and did not quench fully. The high stability of the conductor with high current loading ensures to realize compact winding with high overall current density, high magnetic field and high stability. In other words, the HTS magnets can provide very safe operations of the fusion reactors without almost any interruption due to the magnet quench.
4. The ramp rate performance of the short samples of HTS conductors has been found to be very encouraging. They did not show any ramp rate dependence unlike the LTS conductors and therefore probably can be effectively used in

the fast ramping magnets such as poloidal field coils or central solenoids of a Tokamak. However, more work is required to conclude on this aspect.

The first results on 10 kA-class HTS conductors are very encouraging. The next chapter discusses the HTS magnet option for LHD-type fusion reactor FFHR.

Chapter 5

Design of HTS magnet option for LHD-type fusion energy reactor FFHR

Force free helical reactor (FFHR) is an LHD-type fusion energy reactor, which is being designed at National Institute for Fusion Science (NIFS) in the framework of inter-university collaborative research [5.1]. Several designs of FFHR-series reactors have been proposed [5.2]. Among them, the latest design FFHR-2m1 has the plasma major radius of 14 m, toroidal field of 6.18 T, maximum field at the conductor 13 T, and fusion power of 1.9 GW. FFHR-2m1 consists of one pair of helical coils and two pairs of poloidal field coils. Already well-developed low temperature superconductors (LTS), such as Nb_3Sn and Nb_3Al are being considered for the helical and poloidal coils of FFHR-2m1. However, recently, the high temperature superconductor (HTS) technology has improved significantly and has shown good prospects for future applications [5.3 – 5.7]. Considering this fact, the HTS has emerged as a competitive candidate for these coils of FFHR [5.8]. HTS conductors are being considered for high field magnets in fusion reactors due to their better performances in high magnetic field and elevated temperature operations [5.9 – 5.13]. In a fusion reactor, the HTS magnets can be operated at ~20 K or higher and therefore reduces the operational cost compared to conventional LTS magnets, which are operated at ~4 K. Secondly, due to the increased specific heat of the HTS conductors at elevated temperatures, they become less prone to quench, and therefore, safer operations of a fusion reactor are possible, which is the most desirable requirement for the magnets. The HTS magnets can be cooled by conduction cooling methods and therefore can avoid the complicated networks of pipings, generally necessary for force flow cooled LTS conductor magnets. The indirect cooling method has been proposed for an aluminum-alloy jacketed Nb_3Sn conductor for the FFHR helical coils [5.14]. The same indirect

cooling technique can be adopted for HTS conductors as well. The increased thermal conductivity of metals at elevated temperatures helps in quickly removing the heat generated in the conductor due to AC losses, mechanical disturbances, nuclear heating and other sources.

The present study is focused on the 100 kA-class HTS conductor designs using YBCO tapes for the helical coils of FFHR. The bird's eye view of the FFHR machine is shown in Fig. 1.36 with major parameter in Table 1.3 of chapter 1. Encouraged by the good results of the 10 kA-class HTS conductor tests, we propose 100 kA-class HTS conductors using simple stacking configuration for the fusion reactor FFHR. The HTS conductor is being considered as one option for the FFHR helical coils along with more conventional LTS conductors using Nb_3Sn, Nb_3A, or V_3Ga. This chapter discusses the typical requirements of the FFHR magnets, design of HTS conductors, and analysis in details.

5.1 HTS conductor designs

The typical operational current of FFHR coils is ~100 kA in a magnetic field of ~13 T. Based on the typical requirements for the FFHR magnets, two designs of HTS conductors are proposed. HTS conductors are proposed on the basis of conduction cooling concept, basically proposed for one of the LTS conductors' option for FFHR [5.14]. Figures 5.1 and 5.2 show one section of the helical coils with the structure and cross-section of the helical coil winding pack of FFHR. Figure 5.3 shows the cross-sectional views of the proposed conductors for the FFHR helical coils. The major specifications of the conductors are shown in Table 5.1.

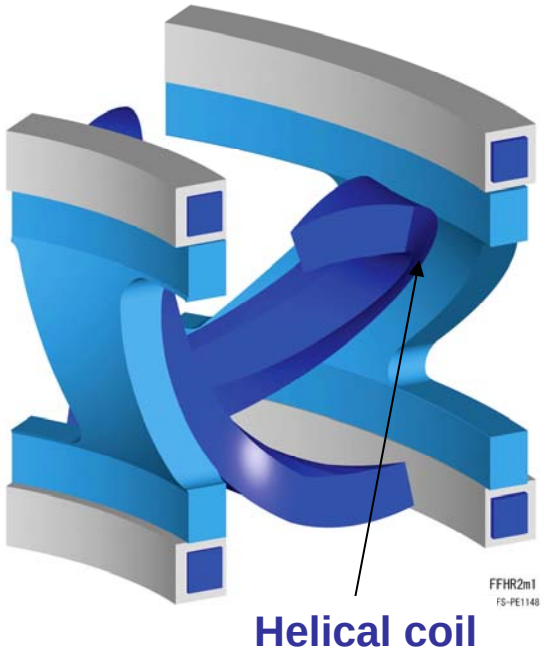

Fig. 5.1: One section of the helical coils of FFHR (Courtesy K. Takahata).

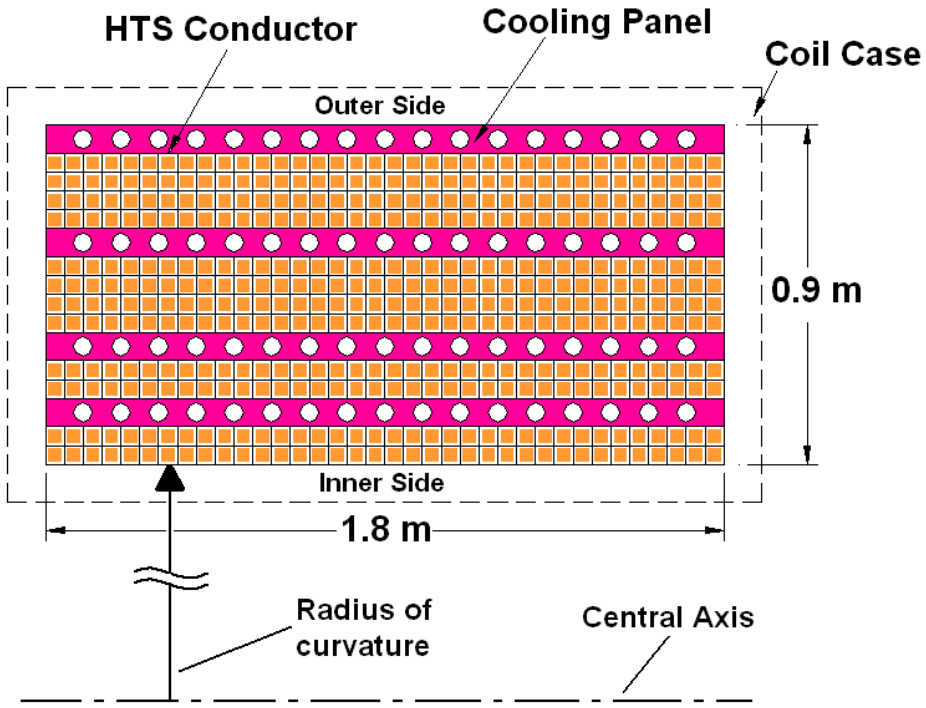

Fig. 5.2: Cross-section of the helical coil winding pack in FFHR.

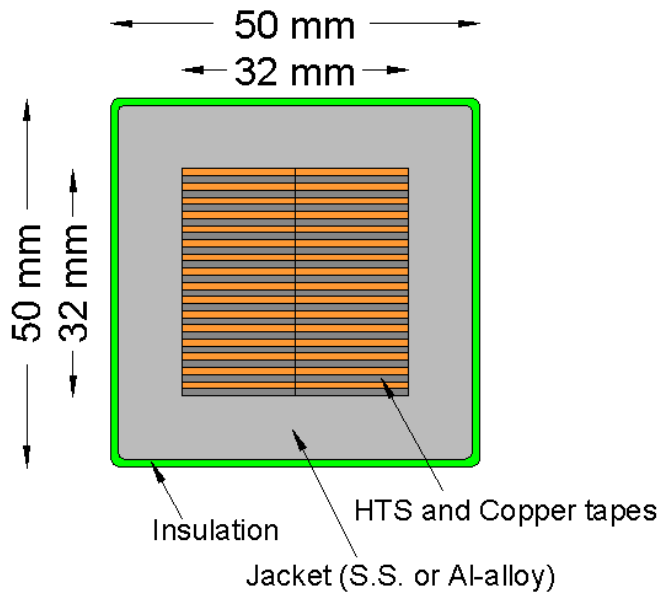

(a) Type-A

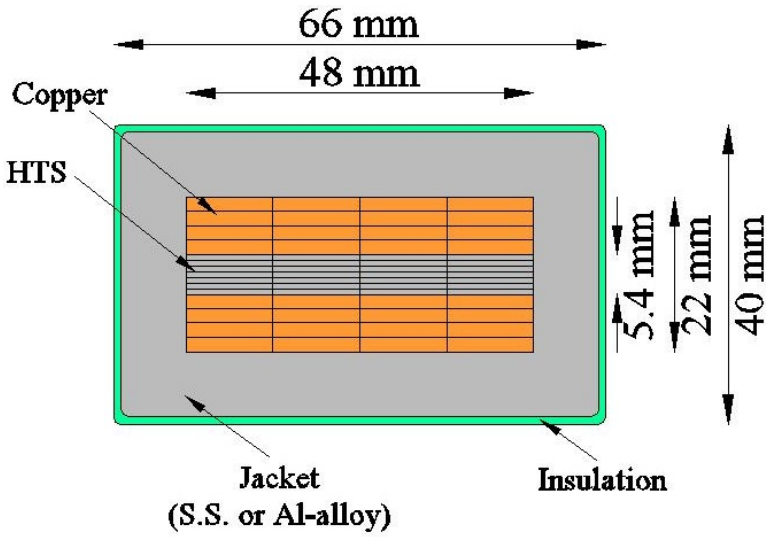

(b) Type-B

Fig. 5.3: Cross-sectional views of the proposed HTS conductors for FFHR helical coils.

Table 5.1: Major specifications of the proposed HTS conductors for the FFHR helical coils

Superconductor	YBCO
Operating Temperature	20 K
Maximum Field	13 T
Operating Current	100 kA
Operating Current Density	~ 40 A/mm^2
Critical Current of the Conductor	~130 kA (13 T, 25 K)
Critical Current of One Tape	100 A/mm-width (25K, 13 T)
Number of Tapes in the Conductor	80 (Type-A) 108 (Type-B)
Dimensions of the HTS Tapes	16 mm × 0.2 mm (Type-A) 12 mm × 0.2 mm (Type-B)
Cu to HTS Ratio	7.0
Bending Strain	0.32 % (Type-A) 0.05 % (Type-B)
Maximum Hoop Stress	~ 380 MPa (at 20 K)
Jacket Material	Aluminum Alloy or Stainless Steel
Cooling Method	Conduction Cooling

As shown in Fig. 5.3, two configurations of the HTS conductors are proposed. The Type-A conductor consists of HTS tapes and copper tapes in the whole cross-section distributed uniformly as shown in Fig. 5.3 (a), to ensure good current distribution from the HTS tapes to copper tapes during normal transition events. However, as shown in Table 5.1, the bending strain is about 0.32 % for this conductor, which is rather large. On the other hand, Type-B conductor consists of HTS tapes just at the center of the cross-section and copper tapes are placed separately at the both sides of the HTS tapes as shown in Fig. 5.3 (b). Since HTS conductors possess high stability by themselves, the additional copper is required for protection point of view, and therefore can be positioned

in either side of the HTS tapes. However, the advantage in the Type-B conductor is that the bending strain reduces to 0.05 %, which is quite smaller than that of the Type-A HTS conductor. The proposed conductors use thick jacket of stainless steel or aluminum-alloy.

As shown in Fig. 5.2, the dimensions of the winding pack (without casing) are 0.9 m × 1.8 m with 12 layers and 36 turns in each layer. The average radius of the curvature of the helical coil is 5.5 m. The built-in cooling panels of 75 mm thickness are envisaged inside the winding pack to provide sufficient cooling to the coil. The coolant such as cold helium gas flows inside the holes provided in cooling panels and cools the conductors by thermal conduction.

The expected steady-state nuclear heat load on the superconducting coils in FFHR is 100 W/m^3 [5.14, 5.15], which should be removed by the coolant effectively. The temperature increase of the conductor, ΔT_{max}, can be estimated by a one-dimensional heat conduction equation,

$$\Delta T_{\max} = \frac{Ql^2}{2\lambda_e} \tag{5.1}$$

where Q is the heat load, l is the distance between cold and hot boundaries, λ_e is the effective thermal conductivity. In Fig. 5.2, the maximum distance between heated conductor and cooling panel, l, is 0.1 m. If the conductor temperature is allowed to be increased by 1 K due to the nuclear heating of 100 W/m^3, the required effective thermal conductivity is 0.5 W/m-K. Figure 5.4 shows the calculated effective thermal conductivity considering different materials over a length of 0.1 m in the winding cross-section. The insulation thickness is taken as 1 mm and its thermal conductivity is 0.1 W/m-K at 20 K. The effective thermal conductivity is calculated by varying the thermal conductivities of the jacket and HTS and copper tapes bundle. In the worst case, when the thermal conductivity of the HTS and copper tapes bundle is considered to be 1 W/m-K and HTS conductor jacket is stainless steel, the effective thermal conductivity comes out to be ~0.85 W/m-K at 20 K. This value is still higher than the required effective thermal conductivity of 0.5 W/m-K, which suggests that stainless steel can also be used in HTS conductors, which was not possible for the LTS counterpart [5.14]. Aluminum-alloy jacket provides higher effective thermal conductivity of ~1 W/m-K at 20 K and therefore is a better option as far as the heat removal is concerned.

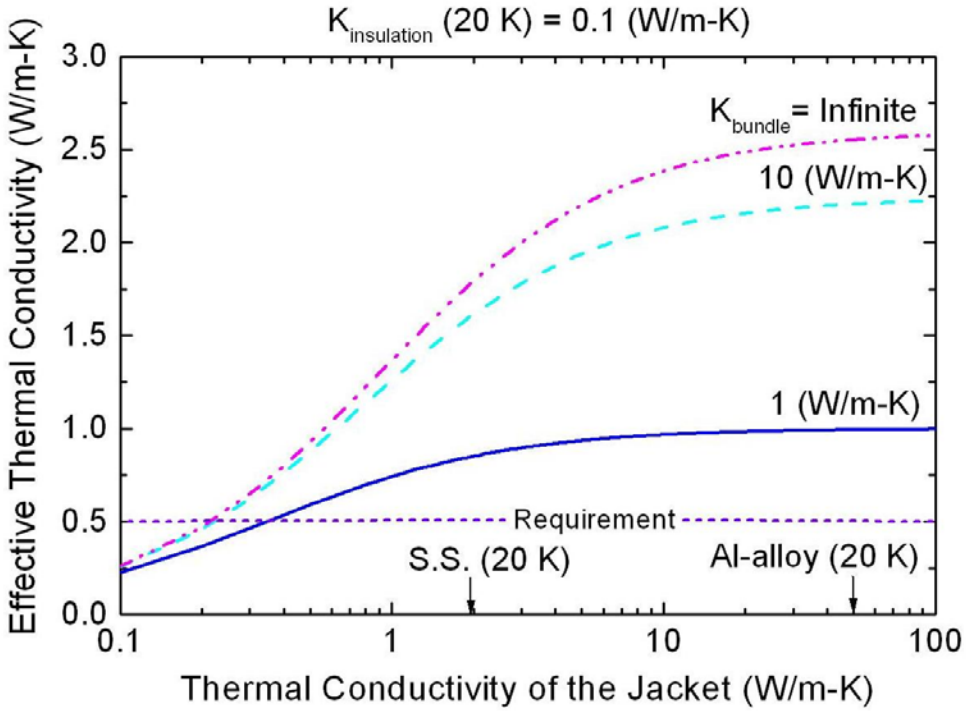

Fig. 5.4: Effective thermal conductivity in the cross-sectional direction of the winding as a function of the thermal conductivities of the jacket and HTS bundle.

5.2 Stress and strain analysis

The helical coils of FFHR will experience large electromagnetic forces and therefore the stress and strain will be developed in the coils. Here, the stress and strain are estimated by considering the coil as an infinite solenoid as a first step, and only the radial forces are taken into account [5.14, 5.16]. Analytical calculations have been done using the following well-known equations for an infinite solenoid winding,

$$\sigma_\theta = \frac{w}{\varepsilon} + \nu \frac{dw}{d\varepsilon} \tag{5.2}$$

$$\sigma_r = \frac{dw}{d\varepsilon} + \nu \frac{w}{\varepsilon} \tag{5.3}$$

$$w = C\varepsilon + \frac{D}{\varepsilon} - \frac{K\varepsilon^2}{3} + \frac{M\varepsilon^3}{8} \tag{5.4}$$

$$K = \frac{(\alpha B_a - B_b)Ja}{\alpha - 1} \tag{5.5}$$

$$M = \frac{(B_a - B_b)Ja}{\alpha - 1} \tag{5.6}$$

$$\varepsilon = \frac{r}{a} \tag{5.7}$$

$$\alpha = \frac{b}{a} \tag{5.8}$$

$$w = \frac{uY}{a(1-v^2)} \tag{5.9}$$

$$BJa = K - M\varepsilon \tag{5.10}$$

where u, Y, a, b, r, B_a, B_b, J, v, σ_θ, σ_r, are the displacement in the radial direction, Young's modulus of the material, inner radius of the winding, outer radius of the winding, distance in the radial direction from the central axis, magnetic field at the inner radius, magnetic field at the outer radius, current density, Poisson's ratio, hoop stress, and radial stress, respectively. The coefficients C and D in Equation (5.4) are determined by the boundary conditions at $r = a$, and b, i.e. $\varepsilon = 1$ and α.

The average radius of the curvature of the helical coil is 5.5 m and therefore the same radius is considered for an infinite solenoid model. The cross-section of the solenoid model is also the same as that of the helical coil shown in Fig. 5.2. The calculated stress and strain, using analytic solutions for an infinite solenoid model, are shown in Fig. 5.5 for the two cases with an aluminum-alloy jacketed conductor and stainless-steel jacketed conductor. For the conductor cross-section, the effective Young's modulus is calculated using the mixture rule considering hardened copper tapes and YBCO tapes with Hastelloy substrates inside either an aluminum-alloy or stainless-steel jacket and GFRP insulation over the HTS conductor. The Young's moduli of copper, HTS tapes, aluminum-alloy, stainless-steel, and GFRP insulation at 20 K are considered to be 140, 200, 80, 200, and 20 GPa, respectively.

The effective Young's moduli for an HTS conductor cross-section are calculated to be 101 and 167 GPa for Al-alloy and stainless-steel jacketed conductors, respectively. The radial stress at the inner and outer radius of the windings is taken to be zero as the boundary conditions. The maximum hoop stress in the stainless-steel cooling panel and aluminum-alloy jacketed HTS conductor are 470 MPa and 250 MPa, respectively. The maximum hoop stress in the conductor is 335 MPa when the HTS conductor jacket is stainless-steel. The stress is always less than the yield strength of the materials at 20 K (380 MPa for Al-alloy and 1050 MPa for stainless-steel), and therefore, the coil is supposed to be safe under large electromagnetic forces in FFHR. The hoop strain is less than 0.2 % for the case with stainless-steel jacket. The bending strain is about 0.32% in FFHR for the conductor design shown in Fig 5.3 (a), and therefore, the total strain would be about 0.5 %. The critical strain for YBCO is about 0.7 %, above which the critical current starts to degrade [5.17]. The HTS conductor design shown in Fig. 5.3 (b) is better to reduce the overall strain in the winding of FFHR.

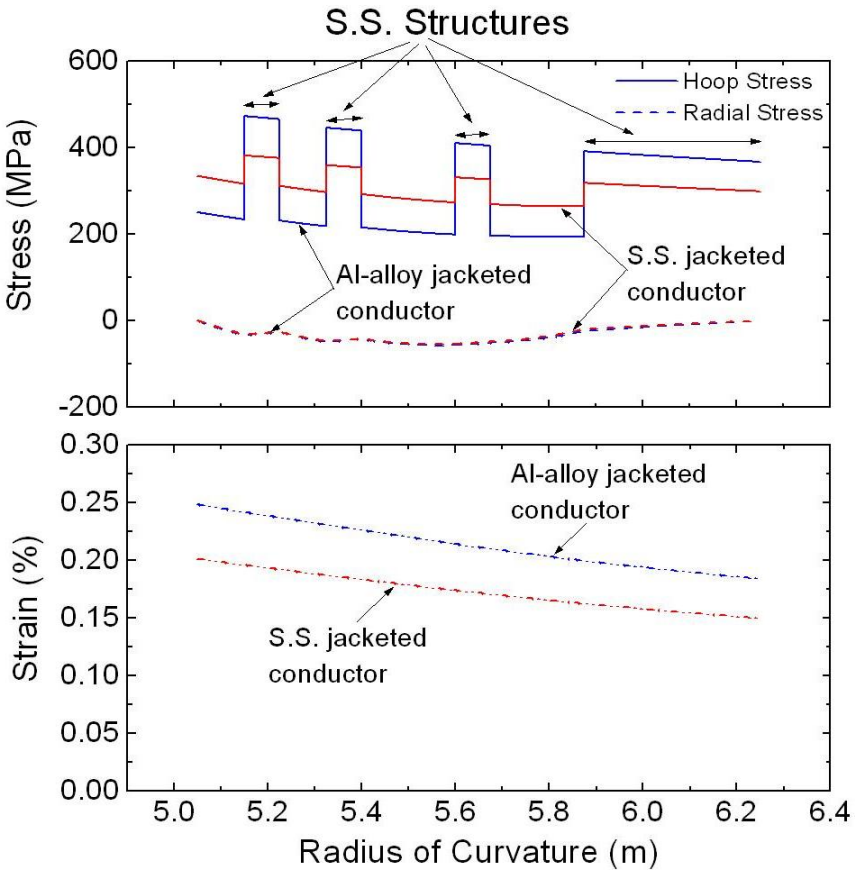

Fig. 5.5: Hoop stress, radial stress, and strain in the helical coil of FFHR. Both options of aluminum-alloy jacketed and stainless steel jacketed HTS conductor are shown.

5.3 Experiments of bending strain on reduced-scale HTS conductor samples

To confirm the bending strain behavior of the HTS conductor designs shown in Fig. 5.3, the bending tests on reduced-scale HTS conductors analogues to 100 kA-class HTS conductors have been carried out. It was believed that the reduced-scale HTS conductor analogues to the rectangular HTS conductor shown in Fig. 5.3 (b) will show higher critical currents for the same bending radius as the expected bending strains would be lower compared to other conductor. The bending strain in a solid conductor is calculated by using equation 5.11.

$$\varepsilon = \frac{t}{2R} \tag{5.11}$$

where ε, t, and R are the bending strain, conductor thickness, and bending radius to the center or neutral axis of the conductor as shown in Fig. 5.6.

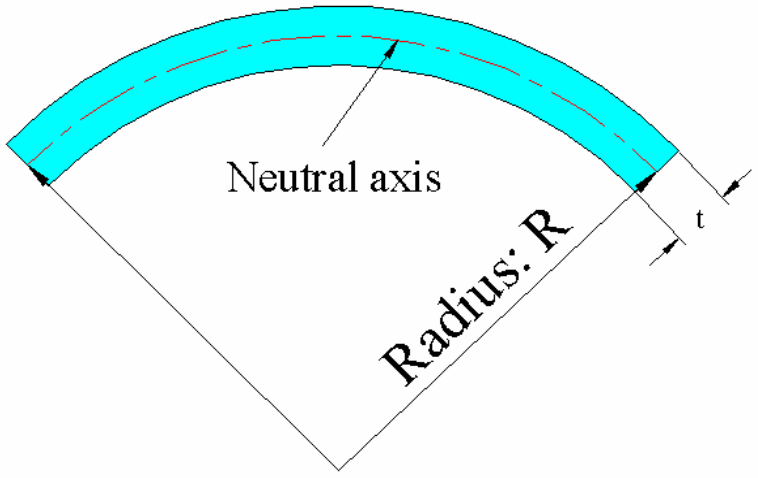

Fig. 5.6: Schematic view of the bent conductor showing the concept of neutral axis to calculate the bending strain using equation 5.11.

Figure 5.7 shows the bending of the proposed HTS conductors with a bending radius of 5.0 m, which is the minimum bending radius in FFHR. As indicated in the figure, the thickness to be used for calculating the bending strain in the HTS tapes of the conductor are 32 mm and 5.4 mm in Type-A and Type-B conductors respectively. Hence, the calculated bending strains in the HTS tapes of Type-A and Type-B conductor are 0.32% and 0.054% respectively.

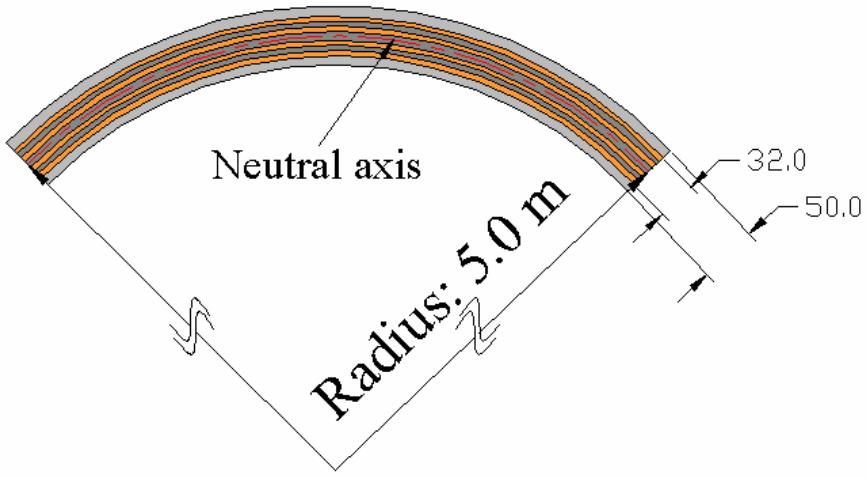

(a)

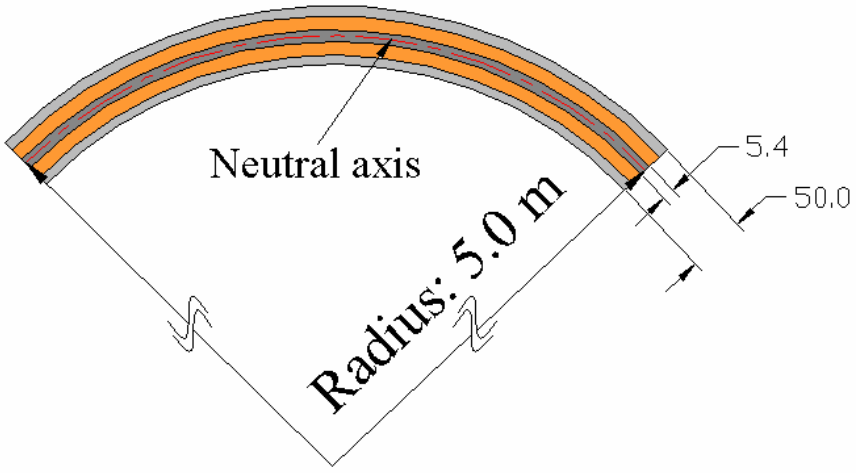

(b)

Fig. 5.7: Schematic view of the proposed HTS conductors with a bending radius of 5.0 m. The thicknesses are different for both conductors to be considered for estimating the bending strains in the HTS tapes of the conductors.

Two reduced-scale HTS conductors are shown in Fig. 5.8 analogues to the proposed 100 kA-class HTS conductors. Four YBCO tapes fabricated by RABiTS technology are used in each conductor. The dimensions of the tape are 0.22 mm (thickness) × 4.2 mm (width) and the critical current is 80 A at 77 K, self-field. Table 5.2 shows the bending diameters and calculated bending strains in the full Type-A and Type-B conductors and in the HTS tapes of the conductors. As is shown in Table 5.2, the expected bending strains in the HTS tapes of the Type-B conductor are much lower than the Type-A conductor for the same bending diameters. The Bakelite formers are used to bend the conductors. The schematic view of the experimental setup is shown in Fig. 5.9.

The critical currents of the HTS conductors were measured by two pairs of voltage taps for each conductor in liquid nitrogen at 77 K and in self-field after bending the conductor using the Bakelite former starting from the largest bending radius former to the smallest bending radius former. The voltage taps were attached in the central part of the conductors and the tap lengths were 200 mm and 400 mm. Figure 5.10 shows some photos of the samples. Figure 5.11 shows some photos of the samples during experiments.

Table 5.2: Bending diameters and strains in the full Type-A or Type-B HTS conductors and in the HTS tapes of the reduced-scale Type-A and Type-B HTS conductors

Bending Diameter (mm)	ε (%), full Type-A or Type-B conductor	ε (%), HTS tapes of the reduced-scale Type-A conductor	ε (%), HTS tapes of the reduced-scale Type-B conductor
2440	0.283	0.2	0.036
1220	0.566	0.4	0.072
813	0.849	0.6	0.11
610	1.131	0.8	0.144
488	1.414	1.0	0.18

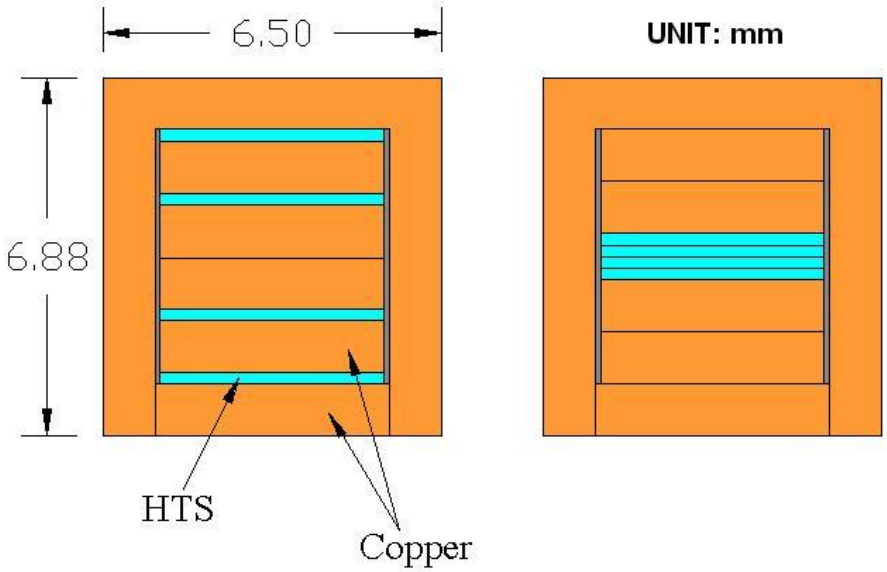

Fig. 5.8: Cross-sectional views of the reduced-scale HTS conductors, analogues to the proposed 100 kA-class HTS conductors, for being tests.

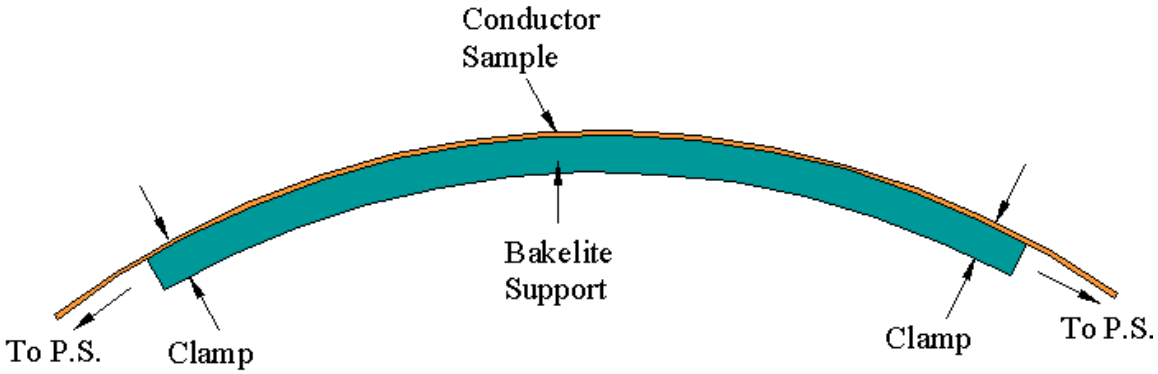

Fig. 5.9: Schematic view of the experimental setup for bending tests on the reduced-scale HTS conductors.

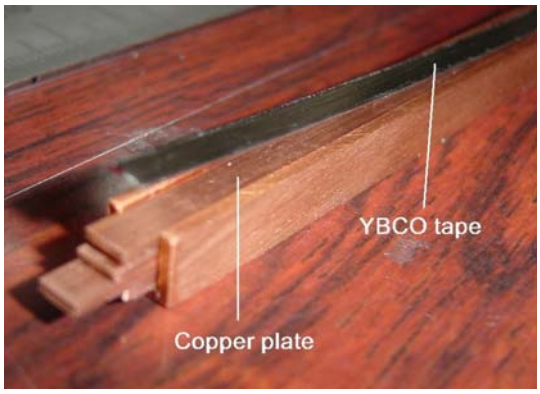

(a)

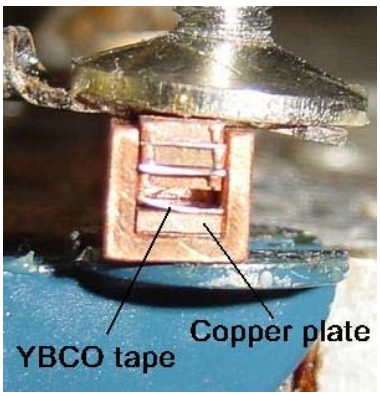

(b)

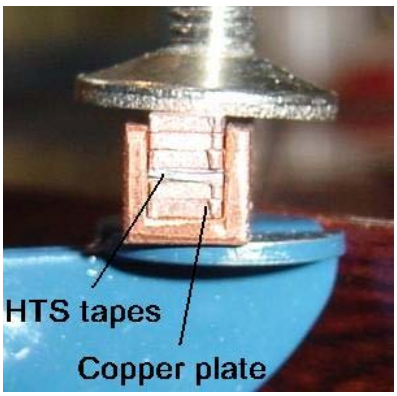

(c)

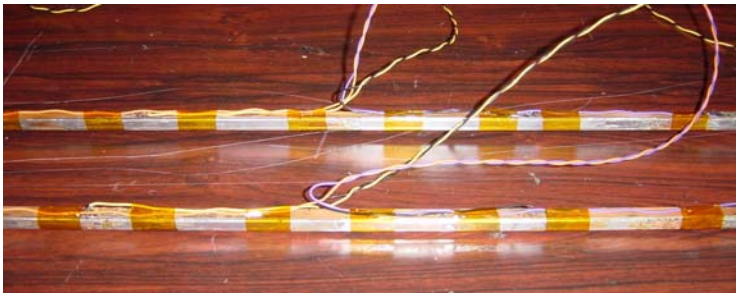

(d)

Fig. 5.10: Photos of (a) type-A conductor during preparation; (b) type-A conductor just before soldering; (c) type-B conductor just before soldering; (d) prepared conductors with voltage taps for critical current measurements.

(a)

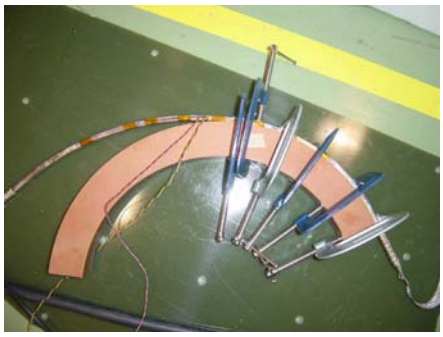

(b)

(c)

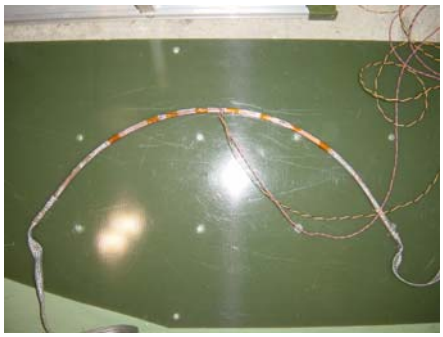

(d)

Fig. 5.11: (a) conductor bent against Bakelite former of outer radius of 2440 mm; (b) conductor bent against Bakelite former of smallest outer radius (488 mm); (c) conductor in LN_2 bath with former; (d) conductor after removal from smallest bending radius former.

The experimental results of the bending tests are shown in Fig. 5.12. As shown in Fig. 5.12, the degradation in critical current of the type-A conductor is significant with increased conductor bending strain. However, the degradation in the critical current of the type-B conductor is almost nothing, as was expected and discussed above. These experimental results clearly indicate that by having the HTS tapes in the central part of the conductor, the bending strain in the HTS tapes can be reduced even though the bending strain in the whole conductor is higher. From these experimental results, one can say that the conductor bending strain of 0.4% (expected conductor bending strain in

FFHR coils) should not create any degradation in the conductor critical current by adopting type-B conductor configuration.

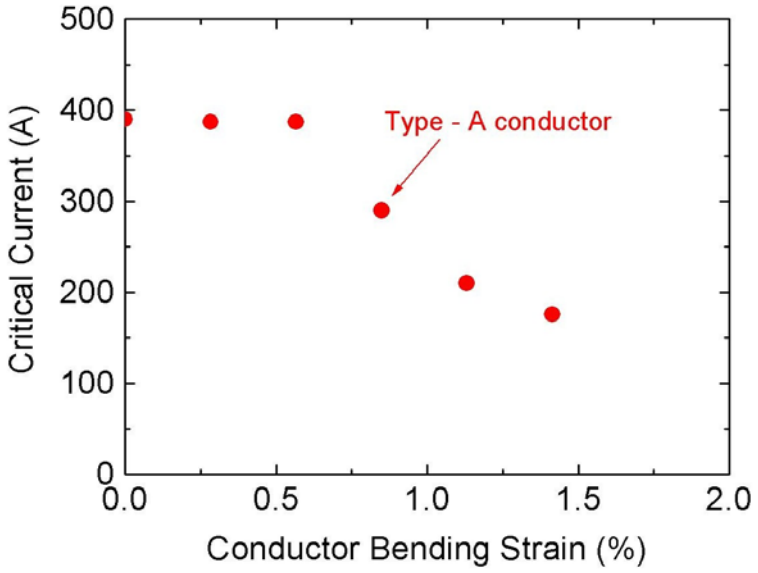

(a)

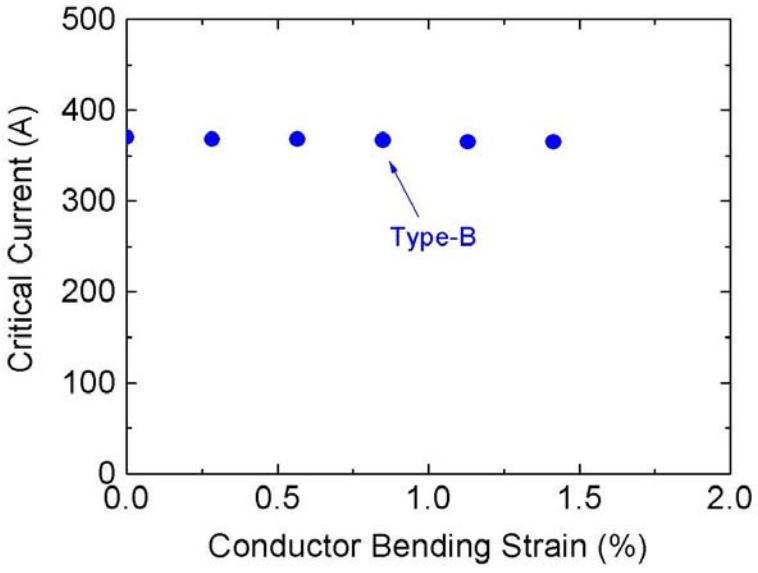

(b)

Fig. 5.12: Experimental results of bending tests on (a) reduced-scale type-A conductor; (b) reduced-scale type-B conductor.

To simulate the spooling-straightening-winding process of the conductor, the conductors were straightened and then re-bent in opposite direction (worse bending condition). The critical currents of both the conductors were measured with different conductor bending strains. The experimental results of opposite bending along with first bending are shown in Fig. 5.13.

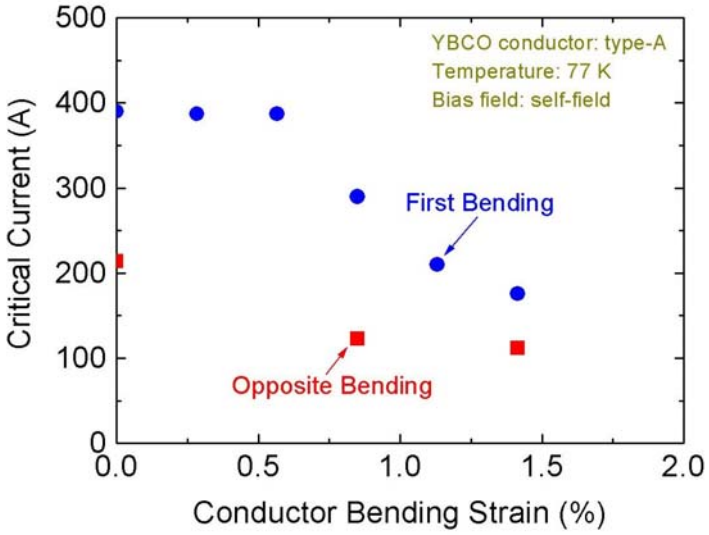

(a)

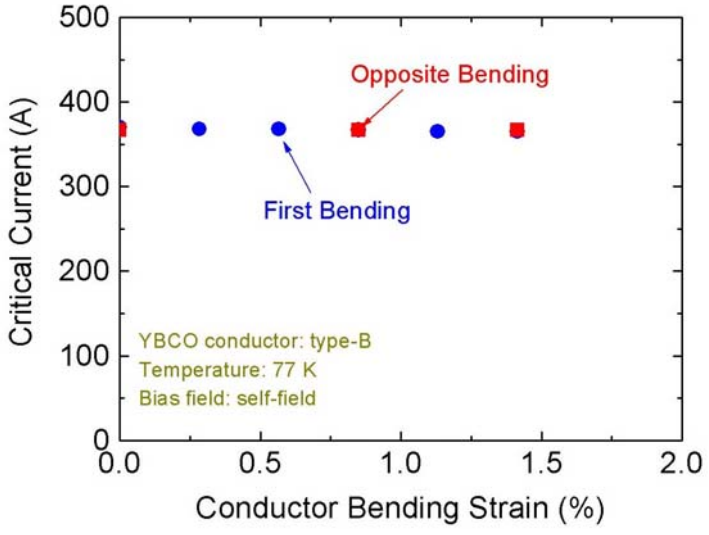

(b)

Fig. 5.13: Experimental results of opposite bending tests on (a) type-A conductor; (b) type-B conductor.

The opposite bending tests revealed that the type-B configuration is better than the type-A configuration from winding point of view.

5.4 Analysis on AC losses

The AC losses during the ramping of coils are always a concern for any superconducting magnet. The ramp rate should be chosen in such a way that the temperature rise of the magnet is small due to AC losses and the magnet does not quench. The smaller losses are required to reduce the load on the refrigeration system as well. The hysteresis losses are the dominant contribution in HTS conductor magnets. Figure 5.14 shows the hysteresis losses per unit volume as a function of excitation time up to the peak field of 13 T at the conductor in the FFHR helical coil. The bundle of HTS tapes behaves as a superconducting slab and therefore the hysteresis losses are calculated using a slab model and Bean critical state model [5.18]. As shown in Fig. 5.14, for hysteresis losses equivalent to steady-state nuclear heating of 100 W/m^3 at the coil windings, the excitation time should be about 13 hours, which is acceptable for the operation of fusion reactors.

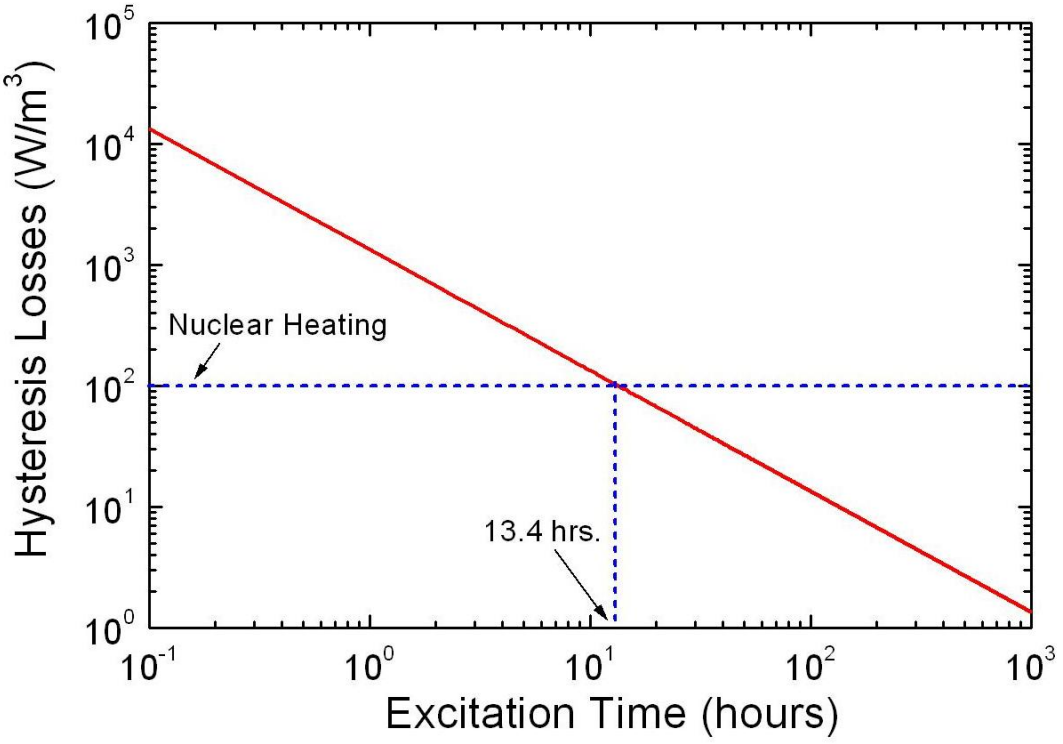

Fig. 5.14: Hysteresis losses as a function of the excitation time up to the peak field of 13 T in the FFHR helical coil.

Figure 5.15 shows the dependence of hysteresis loss on HTS tape width. Generally, the hysteresis loss per cycle increases by increasing the size of the superconductor material inside the conductor. However, it decreases again once the superconductor size is sufficiently large. The bundle of HTS tapes behaves as a superconducting slab and therefore the hysteresis losses are calculated using a slab model and Bean critical state model [5.18]. The calculated hysteresis losses as a function of YBCO tape width are shown in Fig. 5.15 for a varying field up to 13 T perpendicular to the tape surface. The critical current density of YBCO tape is considered as a constant value of 15000 A/mm^2 from 0 T to 13 T [5.9]. As shown in Fig. 5.12, the hysteresis losses increase first by increasing the size of the superconductor but then they start decreasing once the YBCO tape size is about 1 mm. The hysteresis losses of a 100 mm wide YBCO tape are smaller than 1 mm wide tape.

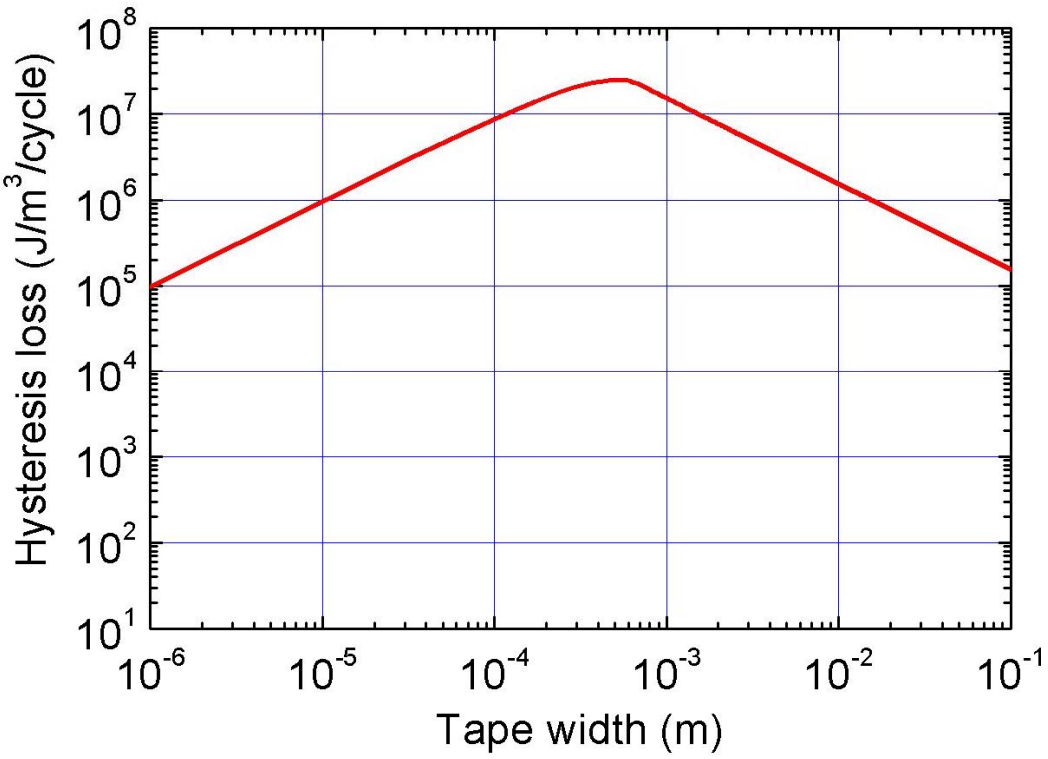

Fig. 5.15: Dependence of hysteresis losses on tape width.

5.5 Analysis on quench detection

Due to the increased specific heat of the materials at elevated temperatures, the thermal diffusivity becomes smaller and therefore the quench propagation also becomes slower. Hence, the voltage development in HTS conductors at elevated temperatures is very slow and the quench detection becomes difficult. This is one of the biggest problems in HTS conductors. Figure 5.16 shows the voltage across the conductor as a function of the conductor length at different temperatures and 100 kA current. At 45 K, the conductor length is about 6 m to observe a voltage of 100 mV whereas it is about 2.5 m at 50 K. The required length further reduces with increased temperature.

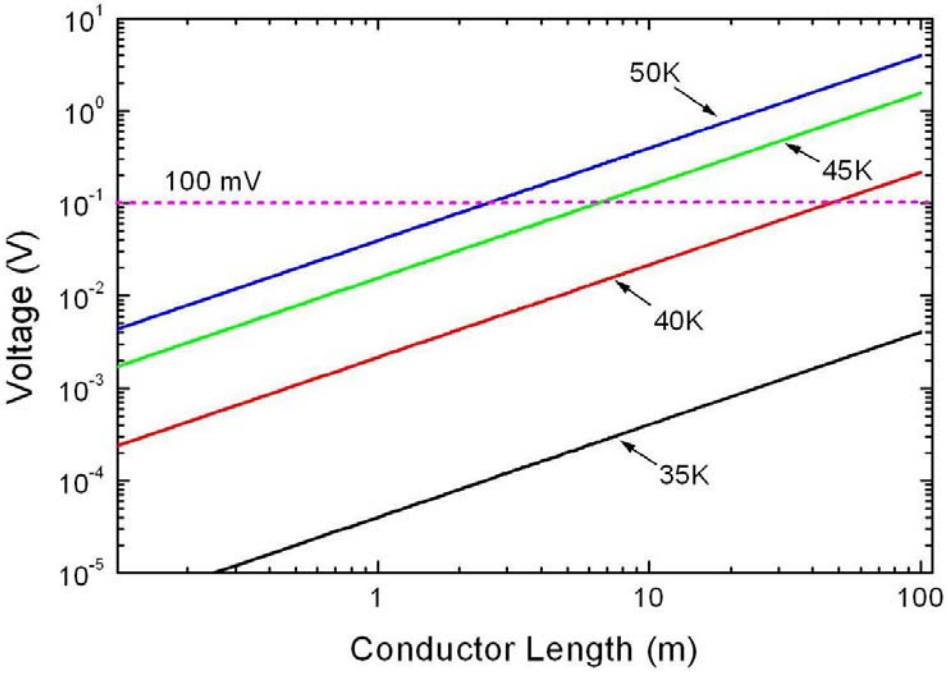

Fig. 5.16: Voltage development as a function of the conductor length at different temperatures and 100 kA current.

5.6 Analysis on hot-spot temperature and quench protection

Figure 5.17 shows the final hot-spot temperature with different jacket materials in the adiabatic condition. The coil current is 100 kA at the initial temperature of 25 K and the stored magnetic energy is dumped into an external resistor with a time constant of 20 s after the quench detection. The percolation model [5.19] and non-linear power law have been used to model the current in HTS tapes. The field and temperature dependent properties of the materials and HTS tapes have been considered for these calculations.

Figure 5.17 suggests that stainless steel jacket for HTS conductor allows higher initial hot-spot temperature (for a condition of final hot-spot temperature less than 150 K)

before dumping. This means that less conductor length is required to develop larger voltage as shown in Fig. 5.16, and therefore quench can be detected rather quickly and easily with stainless steel jacketed HTS conductor.

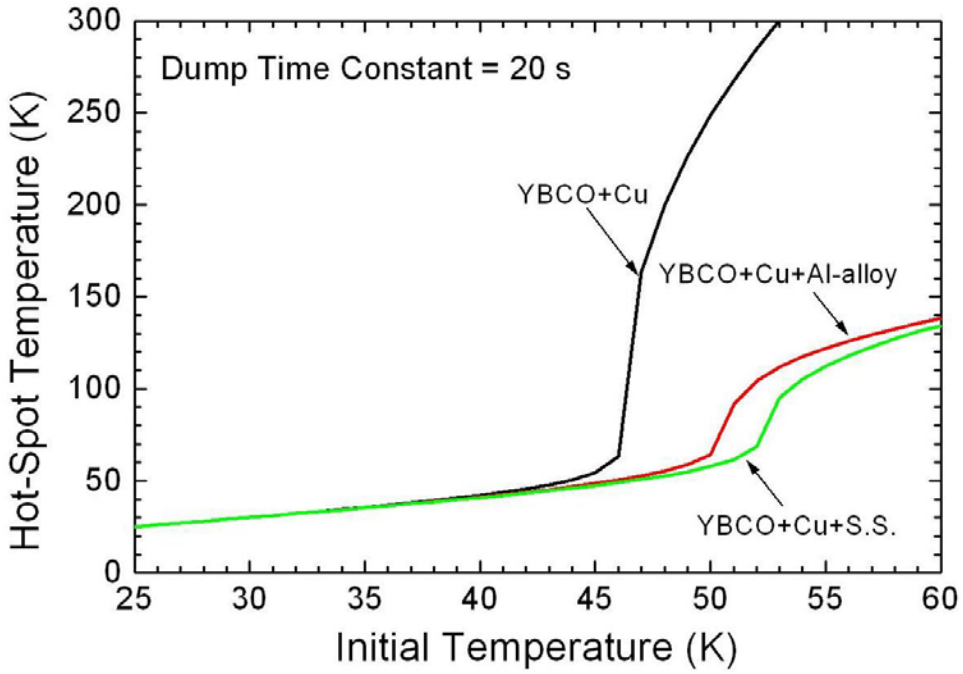

Fig. 5.17: Final hot-spot temperature as a function of the initial hot-spot temperature (just before dumping) and jacket materials.

5.7 Analysis on error magnetic fields due to shielding currents and proposal of grading of the HTS conductor in FFHR

Large shielding currents can be developed inside the HTS tapes due to the change of the magnetic field, which may deteriorate the field accuracy inside the plasma volume. The situation becomes worse when the HTS tapes are not transposed as in the currently

proposed HTS conductor. This is why the shielding currents are unwanted and should be avoided as much as possible. However, we have carried out simple analyses to understand the effect of shielding currents in FFHR. Here, we deal with shielding currents generated in two ways: one is within the YBCO film and the other is through the layers of the HTS tapes in the conductor.

We first analyze the shielding currents in YBCO film due to the field component perpendicular to the YBCO film. Figure 5.18 shows a cross-sectional image of a solenoid using type-B HTS conductor (shown in the left side in the Fig. 5.18) with a transport current. The magnetic field lines generated by the solenoid are also indicated.

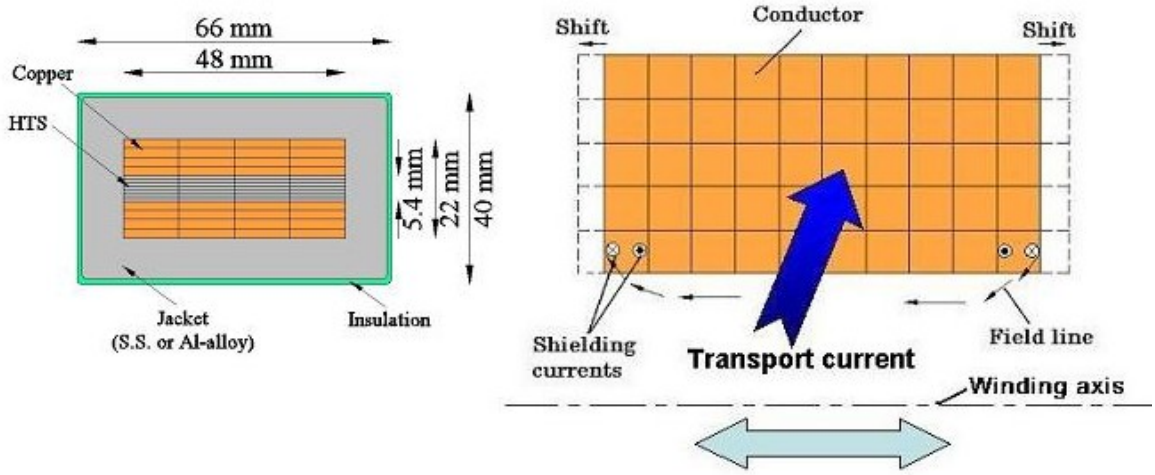

Fig. 5.18: Schematic of shielding currents in the conductors of a solenoid winding. The two-headed arrow shows the direction of the shift in current center.

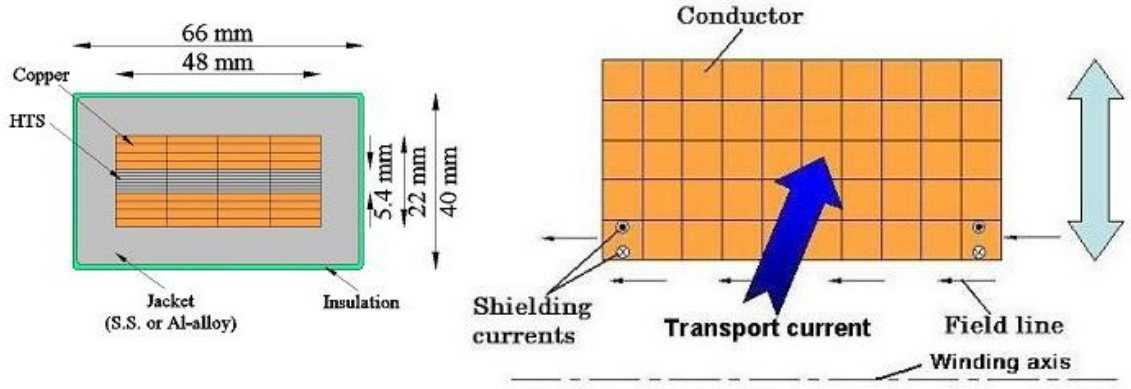

Fig. 5.19: Schematic of shielding currents in the conductors of a solenoid winding. The two-headed arrow shows the direction of the shift in current center.

The field is parallel to the conductor in the central region whereas it is perpendicular to the conductor in the edge regions of the solenoid. As the field is changed at the conductor, the shielding currents are induced in the conductor due to the diamagnetism of the superconductor. The shielding currents make a loop inside the conductor by flowing along and opposite to the transport current. The directions of the shielding currents are shown by cross (along the transport current) and dot (opposite to the transport current) in the conductors in Fig. 5.18. Due to these shielding currents, the current center in a conductor can be assumed to be shifted along the length of the solenoid, which is shown by un-shaded area in Fig. 5.18. Hence, the effective coil length can be considered a bit longer than the actual one. The similar explanations can be applied to the FFHR helical coils. The innermost layer in FFHR experiences about 13 T field with 100 kA transport current. The critical current of the conductor at 13 T and 25 K is about 130 kA. Therefore, a maximum of 15 kA of the shielding current can flow in a conductor in one direction, which is equivalent to ~6 mm of the HTS tape (I_c: 100 A/mm-width of the HTS tape). This means the current center can be assumed to be shifted by ~6 mm from both sides of the winding. Hence, the effective width of the FFHR coil can be treated as 1800 mm + 12 mm. The change of 12 mm over a width of 1800 mm is about 0.67 %, which does not change the magnetic field profile significantly inside the plasma

volume and therefore can be acceptable. However, in the lower field regions, the critical currents could be much higher and therefore the effective shift of the current center might be significant. To solve this problem, the concept of conductor grading can be applied. For lower field regions, the HTS tapes in the conductor are chosen in such a way that the effective critical current is again about 130 kA. Hence, the effective width of the coil can be maintained uniform and minimum throughout the layers and therefore the effect of the shielding currents can be minimized in the plasma volume.

The error fields generated by a shift in the current center perpendicular to the winding axis are also considered. The shift in the current center might be due the non-uniform current distribution of the transport current in the conductor or due to the shielding current generated by parallel field components as shown in Fig. 5.19. Since the HTS tapes thickness in the conductor is about 5.4 mm, the shift in the current center cannot be more than ±2.7 mm in any case, which is within the winding accuracy of ±8 mm for FFHR helical coils. Hence, the shielding currents or a shift in the current center in the perpendicular direction to the HTS tape surface should not be a problem in FFHR helical coils.

As discussed above, even though the shielding currents in FFHR helical coils should not be a problem, another idea to avoid the problem of shielding currents is also considered. To nullify the effect of shielding currents (or diamagnetic effect), the ferromagnetic materials can be incorporated inside the conductor itself [5.20]. This idea was first applied to SSC wires. Figure 5.20 shows the experimental results of the magnetization with and without ferromagnetic Ni inside the wire itself. As it is shown in Fig. 5.20, the diamagnetic effect of the superconductors is cancelled at about 0.33 T field.

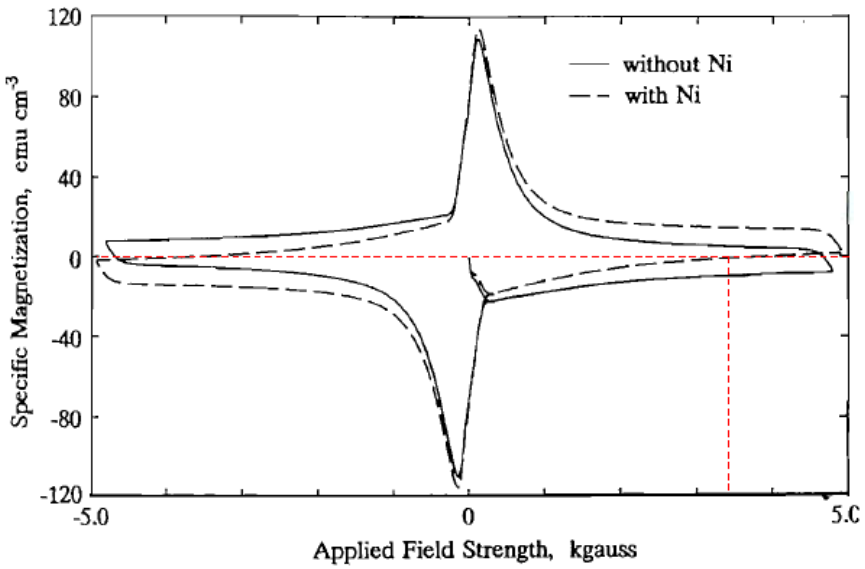

Fig. 5.20: Magnetization of the SSC wire with and without ferromagnetic nickel [5.19].

To cancel the diamagnetic effect of the superconductors, the magnetic moment by ferromagnetic materials should be exactly equal to the diamagnetic moment at a specified magnetic field. For this requirement, the following equation should be satisfied,

$$M_{ferro}V_{ferro} = -M_{sc}V_{sc} \tag{5.12}$$

where M_{ferro}, M_{sc} are magnetic moments per unit volume of the ferromagnetic material and superconductor, respectively. The V_{ferro}, V_{sc} are the total volume of the ferromagnetic material and superconductor in the wire, respectively.

The magnetic moment for a HTS conductor can be given by (for the unit length of the conductor).

$$M_{sc}V_{sc} = \left(\frac{I_c - I_{op}}{2}\right)\left(\frac{w_{sc}}{2}\right) \tag{5.13}$$

where w_{sc} is the width of the HTS tape.

For the FFHR conductor (Type-B), the magnetic moment at 13 T, 25 K can be calculated as

$$M_{sc}V_{sc} = (\frac{130-100}{2}) \times 10^{3} \times (\frac{48}{2}) \times 10^{-3} = 360 \ \text{Am}^2$$

The magnetic moment per unit volume of pure nickel (ferromagnetic material) is 478 $\times 10^3$ A/m. So, using equation 5.12, one can find the required volume of the ferromagnetic material for compensation.

The area, A_{ferro}, (as the length has been considered as one unit) of the ferromagnetic material comes out to be 0.753 $\times 10^{-3}$ m^2. Since the width of the conductor (inside the jacket) is 48 mm, the thickness of the pure Ni should be 15.7 mm for complete compensation. If we use iron, which has a magnetic moment (per unit volume) of 1750 $\times$ 10^3 A/m, then required thickness of the iron tapes would be about 4.3 mm only. Incorporating the ferromagnetic material of 4.3 mm thickness or even 15.7 mm in case of pure nickel is not a problem and hence the shielding current problem can be avoided. The calculation shown above is at 13 T and 25 K. The similar calculations can be done for lower fields as well with graded HTS conductors as discussed before and hence the complete compensation can be achieved at lower fields as well. Thus, the shielding current compensation can be done over a wide range of magnetic field.

For the shielding currents through the layers of HTS tapes, we may consider that these shielding currents are equivalent as the shift of the current center. The shift in current center in the radial direction of the winding is less than 5 mm for the Type-B conductor due to thin layers of HTS tapes, which is within the tolerance of winding accuracy and therefore may not be considered as a serious problem.

5.8 Proposal of segmented helical coils

It may not be easy to realize a continuous winding of the huge helical coils in FFHR, therefore, the segmented helical coils might be a viable choice to wind the helical coils with a number of joints between segments as shown in Fig. 5.21 [5.20]. Due to the elevated temperature operation of HTS coils, the surplus refrigeration power can be used to take away the heat generated by the joints between the helical coil segments. Since the HTS conductor has large temperature margin, the temperature rise of a few Kelvin due to the joints may not be a big concern for the stability of the coils. Figure 5.22 shows the maximum temperature rise of the conductor as a function of heating density calculated by Equation 5.1. Both the options of stainless steel jacketed and aluminum-alloy jacketed conductors have been considered. For a temperature rise of 5 K of the conductor, the heating density of about 990 W/m^3 on the windings can be allowed. This means a joint resistance of about 3 nΩ is acceptable as the number of joints between the conductors in one helical coil, made by 10 segments, is 4320. For about 8000 joints in two helical coils with a joint resistance of 3 nΩ, additional required electrical power would be about 15 MW (at 100 kA current in the coil) considering a specific power (input power per watt of refrigeration) of 60 for the refrigeration system at 20 K. However, the experimentally measured joint resistance with an overlap length of 50 mm of 10 mm wide YBCO tapes is about 6 nΩ at 77 K and self-field. The similar joint resistance or even lower can be expected at 20 K under some magnetic field as the joints in FFHR coils will be experiencing some magnetic field. Therefore, the joint resistance between two YBCO conductors having 100 tapes might be expected to be about 6/100 or 0.06 nΩ, which is much lower than the allowed joint resistance of 3 nΩ as discussed above. Hence, the actual required additional power to cool the joints would be only about 300 kW. The joints between the conductors might be mechanical joints or simple soldered lap joints. A conceptual illustration of a soldered joint configuration is shown in Fig. 5.23. The HTS tapes are cut in step-like structures and then overlapped and joined with YBCO sides facing with each other.

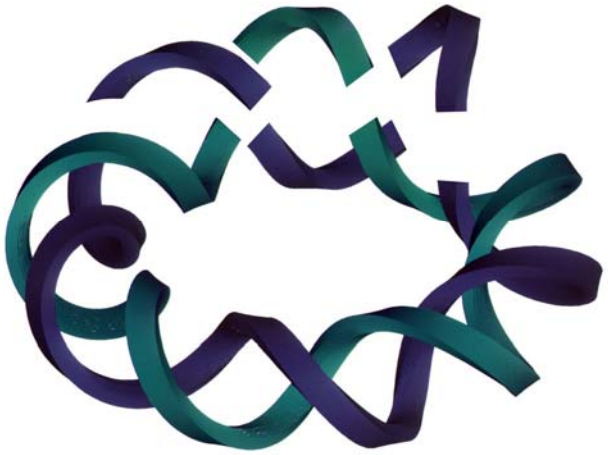

Fig. 5.21: Schematic of segmented helical coils.

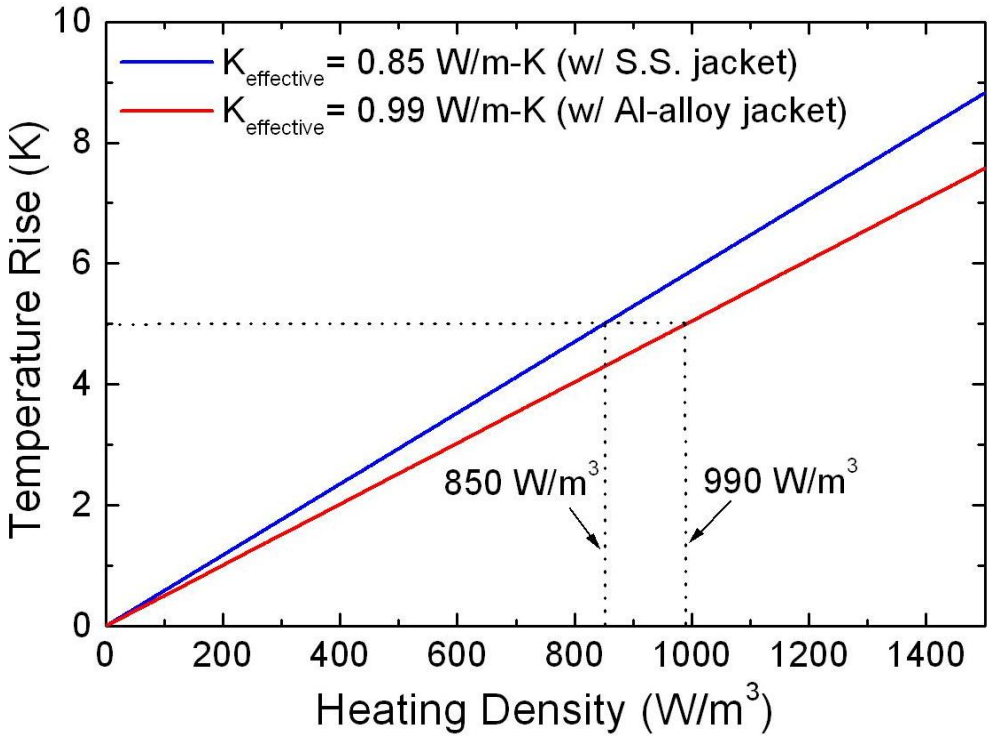

Fig. 5.22: Maximum temperature rise of the conductor as a function of the continuous heating density on the helical coil windings.

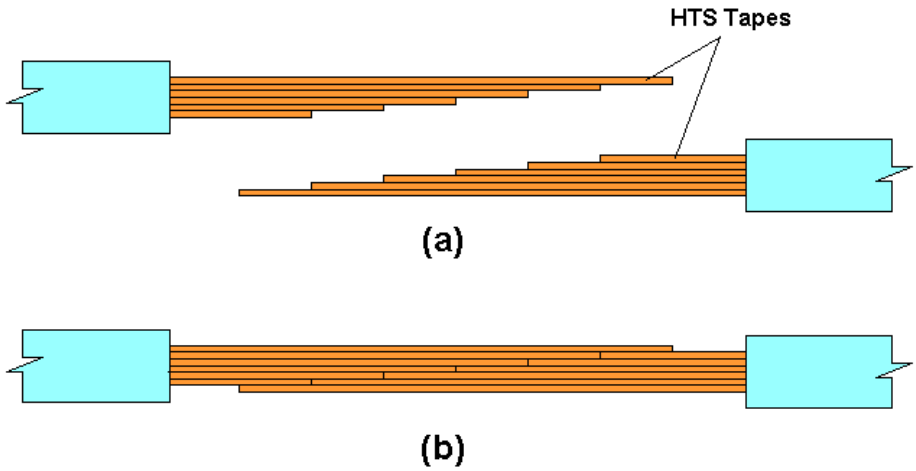

Fig. 5.23: (a) HTS tapes cut in step-like structure; (b) lap joint between HTS tapes.

5.9 Issues to be solved in HTS conductors and near future expectations

Though the progress of HTS conductors is quite good in recent years, there are still many issues to be solved. Some of them are listed here.

1. Mechanical strength of the HTS tapes should be improved.
2. AC losses should be decreased though it may not be a big concern for DC magnets for fusion reactors.
3. Due to the larger filament size, large shielding currents can flow in HTS tapes. These shielding currents may create error fields in the plasma region of a fusion device and may create problems for plasma confinement. Therefore shielding currents should be minimized.
4. Cabling techniques should be worked out for large-current capacity long length conductors.
5. Winding techniques using HTS conductors should be worked out.

6. Presently, the HTS wire cost is quite high. It should be reduced at least up to the level of presently available LTS conductors.
7. Due to the elevated temperature operation, the normal zone propagation speed is slow in HTS conductors, which make quench detection difficult. Therefore, good schemes of quench detection and protection should be worked out.
8. New innovative cooling schemes should be worked out to make the HTS conductor based magnets stable and cost effective.

5.10 Summary

The feasibility study of HTS conductor option for the LHD-type fusion energy reactor FFHR has started. A preliminary design of the HTS conductor is proposed, which seems to be suitable for the FFHR helical coils.

Quench detection and stress calculations suggest that stainless steel should be adopted as a jacket material for the conductor. On the other hand, aluminum-alloy might be a better choice from the winding point of view being a softer material compared to stainless steel.

In the present design, copper to HTS tape ratio has been chosen to be 7 from the protection point of view in case of quench in the magnet. The hot-spot temperature remains below 150 K with a dump time constant of 20 s.

The bending strain tests on the reduced-scale HTS conductors analogues to type-A and type-B configurations clearly indicated that the type-B configuration should be adopted from the winding point of view. The conductor bending strain of 0.4% in FFHR coils should not be a problem from the viewpoint of critical current degradation.

Segmented helical coils with mechanical or soldered joints might be a viable choice due to the large temperature margin of the HTS conductor and available surplus refrigeration power, which is a big advantage of HTS conductors over their LTS counterparts.

The 10 kA-class HTS conductors with Bi-2223/Ag and YBCO HTS tapes have been successfully fabricated and tested at 4.2 K and elevated temperatures up to 30 K as discussed in Chapter 4.

More studies, such as error fields due to the shielding currents, current distribution in the conductor, and AC losses are planned to be done on the HTS conductors.

Chapter 6

Conclusions

The fusion energy reactors such as FFHR cannot allow their huge magnets (storing more than 100 GJ of magnetic energy) to quench and therefore, there is a need to develop high stability conductors to have safer operations. Compared to low temperature superconductors (LTS), HTS conductors possess rather higher stability as they can be operated at elevated temperatures of 20 K or higher, which assures higher specific heats and therefore lower risk of quench even with indirect cooling scheme. In addition to high stability, high critical current density is expected for HTS materials in high magnetic fields even at elevated temperatures. Moreover, lower refrigeration power is required due to elevated temperature operations. Owing to these advantages, HTS conductors are considered to be a potential candidate for future fusion energy reactor magnets. However, no large-current (> 10 kA) capacity HTS conductor that can be used for magnet windings (not for current-leads) has been developed yet, especially with tape-form HTS wires. Toward the development of large-current capacity HTS conductors, feasibility studies of large-current capacity HTS conductors suitable for fusion energy reactors have been carried out in this thesis.

Due to the high critical temperatures, HTS conductors can be operated at elevated temperatures of 20 K or higher with sufficiently high critical current density under high magnetic fields. However, the HTS magnets are supposed to be operated in conduction cooling mode and no coolant is directly available to the conductor to quickly take away the heat. Therefore, it is an important task to examine the stability of HTS conductors in conduction cooling condition, whereas for the LTS conductors coolant is generally in direct contact with the conductor.

Hence, the stability of conductors has been found to be the prime issue for safe and reliable operation of the magnets and fusion reactor itself. Thus, the stability of the HTS conductor has been the focus point of this thesis study.

In this thesis, a simple stacked 100 kA-class HTS conductor has been proposed. Due to the inductance mismatching, the formation of non-uniform current distribution might be a natural consequence. It is well known that non-uniform current distribution degrades the stability of LTS conductors, especially with insulated strand conductors such as the DPC coil conductor, where quick current redistribution is a problem. Since, the proposed HTS conductor has no insulation between wires, the current redistribution among the wires is supposed to be good and therefore the degradation of the stability due to non-uniform current distribution should be less. However, this idea was required to be examined on a full-scale conductor. Therefore, before starting the real HTS conductor development, the effect of non-uniform current distribution on the stability was examined by using a LTS cable-in-conduit conductor with un-insulated strands. The controlled non-uniform current distribution was introduced artificially using an innovative but complicated current feeder system with thin film resistive heaters. In our experiments, we found that the stability margin of the conductor reduced significantly due to the introduction of non-uniform current distribution, which indicates that non-uniform current distribution is a problem even for un-insulated strand conductors where current redistribution among strands takes place rather easily. We found that with non-uniform current distribution, the stability margin reduced by more than one order of magnitude, especially in the transition region between the well-cooled and ill-cooled regions. The limiting current, which separates the well-cooled and ill-cooled regions, was found to be shifted toward the lower current values due to non-uniform current distribution. We have carried out numerical calculations to simulate the experimental data of stability margin with uniform and non-uniform current distributions and found good consistency between experimental and calculated results.

We carried out ramp rate limitation (RRL) experiments as well and found that the quench current reduced due to non-uniform current distribution for faster ramp rates ranging from 100 A/s to 800 A/s. Hence, our experiments of stability margin measurements with non-uniform current distribution on un-insulated strand LTS cable-in-conduit conductor clearly suggest that non-uniform current distribution is an important factor to be considered for large-current capacity conductors. Therefore, the effect of non-uniform current distribution on the stability of HTS conductors should also be

examined even though the stability of HTS conductors is supposed to be quite high compared to LTS conductors.

Then, we proposed a unique and innovative experimental method to examine the effect of non-uniform current distribution on the stability of HTS conductors by preparing LTS/HTS hybrid conductors. In a hybrid conductor, layers of Bi-2223/Ag HTS tapes were soldered to form a stabilizer for the LTS wires. Once a normal-zone appears in the LTS wires, the transport current transfers into the HTS part from one layer to another and so on. This is supposed to be a case of extreme non-uniform current distribution in the HTS part. In our experiments at 4.2 K and 7 T bias field, we found that even with this extreme non-uniform current distribution, the HTS part was stable and the conductor did not quench fully even though the transport current was close to the critical current of the HTS part in the hybrid conductor. These experimental results suggest that non-uniform current distribution may not be a problem for the stability of HTS conductors even though many of the HTS wires carry the currents equal to the critical currents. However, examination of this problem by direct experiments on real full HTS conductors might be an important future task.

Apart from the investigation of effect the of non-uniform current distribution on the stability of HTS conductors, the second purpose of the hybrid conductor concept was to improve the stability of the solid type LTS conductors by replacing conventional pure metal stabilizers by HTS. In our experiments, it was confirmed that the stability of the solid type LTS conductor could be increased significantly using the LTS/HTS hybrid concept. The LTS/HTS hybrid conductor was the world's first superconducting conductor with overall high stability utilizing both LTS and HTS conductors together.

The experiments on the LTS/HTS hybrid conductors confirmed that non-uniform current distribution may not be a problem for HTS conductors and therefore the freedom of conductor configuration can be increased for HTS conductors. Thus, we proposed a large-current capacity HTS conductors consisting of simple stacks of HTS wires, which are presently available in tape forms. This is regarded as a new but a controversial proposal, since simple stacking of superconducting strands without transpositions has never been allowed for LTS conductors. As a first step, we fabricated 10 kA-class (at 20 K, 8 T) HTS conductors using Bi-2223/Ag and YBCO tapes and tested them separately.

The conductors were prepared by stacking HTS tapes and then soldering them inside copper jackets. The conductor sizes were 12 mm (width) × 7.5 mm (thickness) for Bi-2223/Ag conductor and 13 mm (width) × 7.5 mm (thickness) for YBCO conductor, respectively. An innovative technique was applied to test the HTS conductors at different temperatures from 4.2 K to 30 K. Thin stainless steel heaters were attached to the conductor surfaces to elevate the temperature and then conductors were insulated by epoxy and GFRP to obtain similar conduction cooling conditions as in future magnets made of HTS conductors. We measured the critical currents of the HTS conductors at 4.2 K, 10 K, 20 K, and 30 K and the results were found to be close to our expectations. We calculated the critical currents of the HTS conductors at different temperatures and a bias field of 8 T (parallel to the *ab*-plane of the HTS tapes) by taking account of the self-field generated by the transport current in the conductors. The calculated results are found to be in good agreement with the measured critical current, which shows no degradation in HTS conductors due to the handling during the fabrication process. The critical currents of the YBCO conductor were found to be higher than Bi-2223/Ag conductor under a bias field of 8 T (// to ab-plane of the HTS tapes).

The stability margin of the HTS conductors was also measured at different temperatures. The conductors were found to be highly stable, as it was expected from the high heat capacity of the conductors at elevated temperatures. The stability test results suggest that HTS conductors possess much higher stability margin compared to their LTS counterparts, and therefore, are the potential candidates for stable operations of future fusion energy reactors.

We also carried out ramp rate limitation (RRL) tests on the HTS conductors. The results are very encouraging. The conductor did not show any ramp rate limitation behavior even at 1.5 kA/s ramp rate, which was completely different from the observations in the CICC experiment described above. For HTS conductors, the critical currents were found to increase by increasing the ramp rate. This was because the conductor temperature showed lower increase due to the shorter duration of joule heating associated with the appearance of the flux-flow resistance. Hence, our preliminary results suggest that RRL may not be a problem for HTS conductors unlike the LTS counterparts. It is considered that the increase of stability also gives this improvement.

Looking at the encouraging results of 10 kA-class HTS conductors, we have started the HTS conductor design as an option for the helical coils of the LHD-type fusion energy reactor FFHR. We have carried out several studies such as structural, AC losses, quench detection and protection, error fields due to shielding currents, etc. on the proposed 100 kA-class HTS conductors using YBCO tapes. We have considered stainless-steel or aluminum-alloy as the jacket material options for the HTS conductors. It is found that stainless-steel jacket is more suitable due to its higher strength and larger heat capacity. Our preliminary results suggest that HTS conductors might be promising candidates for the helical coils of FFHR. However, when considering the application of HTS conductors for fusion magnets, more studies on many difficult issues, such as the error magnetic fields generated by superconducting shielding currents in HTS tapes and how to make robust coil structures using fragile HTS materials, should be done. One also has to optimize the cooling method for HTS coils. At the same time, owing to the higher stability of HTS conductors, a new design philosophy for HTS coils should be established unlike the conventional counterpart for LTS coils, which are primarily based on the cryogenic stability. In these connections, an innovative idea of having rather thin layers of HTS wires within the conductor is also proposed in the present study. By having such a configuration, the bending strain can be minimized to be ~0.05% level so that the winding of coils using these conductors is feasible. Moreover, the problem of error magnetic field, generated by shielding currents in individual HTS tapes and by the occurrence of non-uniform current distribution due to inductance mismatching among layers of HTS tapes, is considered to be equivalent as the shift of current centers in the conductors. If the HTS part can be confined in thin layers, the current shift is supposed to be in an acceptable level within the tolerance of winding accuracy.

Through this thesis, it has been found that considering HTS conductors to be used for fusion energy reactor magnets is feasible, though a number of issues associated with their development should be solved one by one.

Appendix A

Brief introduction of superconductors

The fundamentals of superconductors are briefly discussed in this section.

A.1 Superconductivity and types of superconductors

The electrical resistance of some metals and metallic compounds suddenly drops to "zero" at critical temperature, T_c. This phenomenon was first discovered by Kamerlingh Onnens in 1911 when he tried to measure the electrical resistance of liquid metal mercury at liquid helium temperature, 4.2 K. He found that the electrical resistance of mercury suddenly drops to "zero" at 4.2 K. Later on, the phenomenon of disappearance of electrical resistance was named superconductivity and the material showing this phenomenon was called as superconductor. Kamerlingh Onnens received the Nobel Prize for physics in 1913 for this discovery.

On the contrary, many high conductivity metals such as copper, silver, platinum do not show superconductivity at low temperatures and their electrical resistances do not drop to zero.

The BCS theory first explained the phenomenon of superconductivity successfully [A.1]. According to the BCS theory, the current in superconductors is carried by copper pairs, which are formed by coupling of two electrons of exactly opposite momentum and spin. The glue between two electrons of a cooper pair is provided by lattice elastic waves, called phonons. The distance between the two electrons of a cooper pair is called the coherence length, ξ, and is large in pure metals. For example, it is 18000 Å and 2300 Å in pure aluminum and pure tin, respectively. The coherence length is smaller in impure metals and alloys. For example, it is in the range of 100 Å in NbTi alloy.

As the momenta are opposite for both the electrons in a cooper pair, the net momentum is zero. By the de Broglie principle (a wave is always associated with a

particle), the associated wave to cooper pair has an infinite wavelength (physically, the wavelength is actually of the order of the size of the superconductor sample). It means that the cooper pairs cannot be scattered by the usual scatterers of individual electrons as a wave is diffused only if there is fluctuation of the number of scattering centers within a volume of the size of the wavelength. Since there is no scattering of cooper pairs in superconductors, therefore they show zero resistance to the electrical current unlike the normal metals.

Following the discovery of the disappearance of electrical resistance in superconductors, a more fundamental aspect of superconductivity was discovered by Meissner and Ochsenfeld in 1933, when they observed that a superconductor, placed in a weak field (less than the critical field, B_c), completely expels the field from the superconductor and shows perfect diamagnetism. This expulsion of the magnetic field is referred to as the Meissner effect [A.2, A.3].

Looking rather closely at the surface of a superconductor, one finds that the Meissner effect does not occur exactly, and that the magnetic field penetrates a rather small but finite distance into the superconductor. This distance is called London penetration depth, λ, after F. and H. London, and usually amounts to a few hundred angstroms [A.4]. For example, it is 500 Å and 510 Å in pure aluminum and pure tin respectively. According to F. and H. London's hypothesis, the shielding currents are established at the surface of a superconductor to produce exactly the same but opposite magnetic field to cancel out the external magnetic field and this is how a superconductor expels the external magnetic field and achieves perfect diamagnetism. In the thin layer of shielding current, the magnetic field penetrates and decays exponentially.

In large external magnetic fields (more than critical field, B_c), the superconductivity vanishes and the field penetrates into the superconductor. These kinds of superconductors are called as Type-I superconductors (or soft superconductors) [A.4]. Below critical field, B_c, the magnetization is exactly the same but opposite to the external field whereas it vanishes to zero at and above B_c.

The critical magnetic field for Type-I superconductors is generally very small and therefore they cannot be used in practical applications. There exists another class of superconductors, which is called Type-II superconductors (or hard superconductors)

[A.4]. These types of superconductors allow magnetic fields to penetrate without the loss of superconductivity. For Type-II superconductors, there are two critical fields: the lower B_{c1} and upper B_{c2}. The field is completely expelled up to B_{c1} only and superconductors show perfect diamagnetism and behave like Type-I superconductors. Above B_{c1}, the field penetrates partially until the upper critical field B_{c2} is reached. Above B_{c2}, the superconductor becomes a normal conductor. Between B_{c1} and B_{c2}, the superconductor is in mixed state. The magnetic behavior of Type-II superconductors is shown in Fig. A1.1.

For the applied field at $B_{c1} < B < B_{c2}$, the magnetic flux partially penetrates the superconductor in the form of tiny microscopic filaments called vortices as shown in Fig. A1.2 [A.5]. The diameter of a vortex in conventional superconductors is typically 100 nm. It consists of a normal core, in which the magnetic field is large, surrounded by a superconducting region in which a persistent supercurrent flows, which maintains the field within the core. Each vortex carries a minimum possible quantum of magnetic flux, Φ_0, given by

$$\Phi_0 = \frac{h}{2e} = 2.067 \times 10^{-15} \text{ [Wb]} \tag{A1.1}$$

where h is the Plank constant and e is the electron charge. The magnetic induction B is directly related to n, the number of vortices per unit area.

$$B = n\Phi_0 \tag{A1.2}$$

Due to this partial flux penetration, the superconductor can withstand strong applied magnetic fields without returning to the normal state. Superconductivity persists in the mixed state up to the upper critical field, B_{c2}, which is sometimes as high as 60 T or even ~150 T in high temperature superconductors, and therefore, Type-II superconductors are of practical importance in high magnetic field applications.

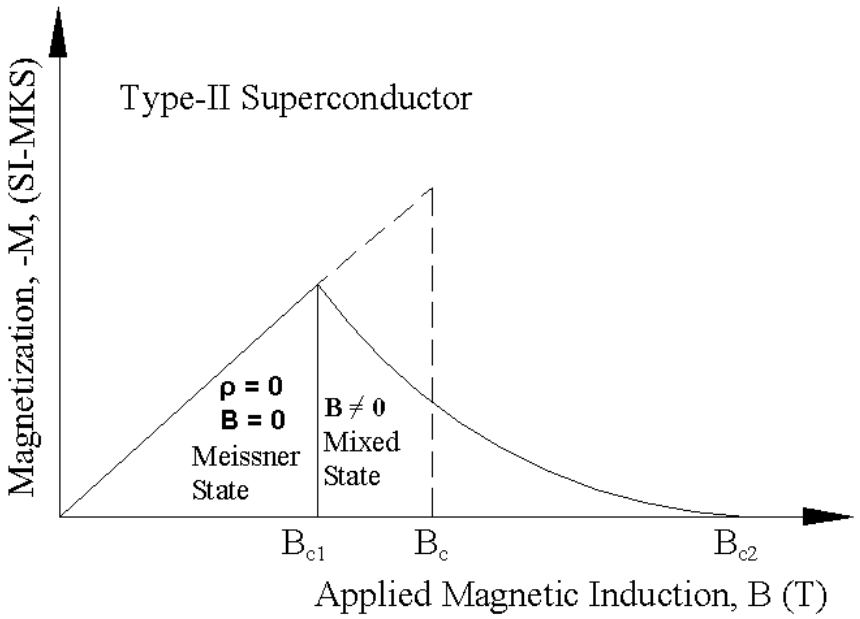

Fig. A1.1: Magnetization of Type-II superconductor as a function of external magnetic field density. Above critical field density, B_{c1}, the flux starts to penetrate and superconductor is said to be in mixed state. Above B_{c2}, superconductivity is lost.

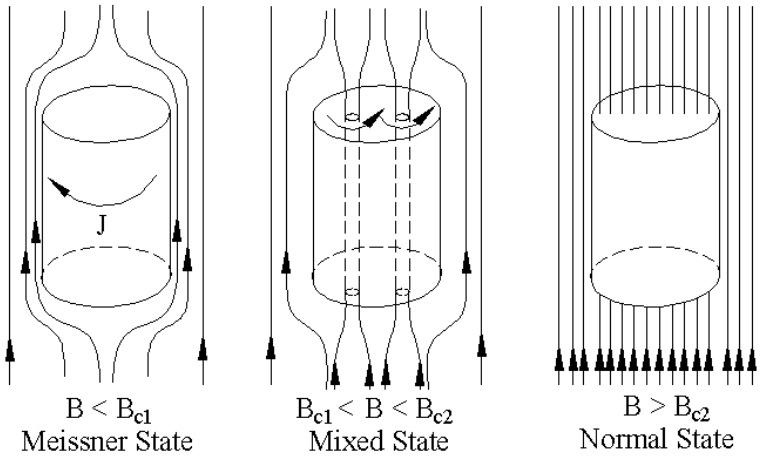

Fig. A1.2: Different stages of Type-II superconductors in external magnetic field. Below B_{c1}, the superconductor is in Meissner state and shows perfect diamagnetism. Between B_{c1} and B_{c2}, the flux is penetrated into the superconductor in the form of quantized vortices and the superconductor is said to be in mixed state. Above B_{c2}, superconductivity is lost and flux completely penetrates the material.

A.2 Characteristics of superconductors

There are several important characteristics of superconductors as discussed below.

Energy gap

At temperatures below the critical temperature, T_c, the heat capacity of a superconductor varies as

$$C_v(T < T_c) \sim \exp\left(-\frac{\Delta}{k_B T}\right) \tag{A2.1}$$

$E_g = 2\Delta$ is a constant for a given material and is called the energy gap; k_B is the Boltzmann constant [A.5]. Such temperature dependence is characteristic of a system that has an energy gap in its spectrum of allowed energy states. The relation between Δ and T_c is given by the BCS theory as $2\Delta = 3.5\, k_B\, T_c$.

In semiconductors, the gap in the energy spectrum corresponds to the energy difference between the valence and the conduction band whereas in superconductors 2Δ corresponds to the energy needed to break a cooper pair and is of the order of 1 meV for conventional superconductors at $T_c < 20$ K.

Coherence and penetration lengths

As discussed above, the coherence and penetration lengths are two characteristic lengths of superconductors [A.4]. The coherence length, ξ, is the interaction length of two electrons in a cooper pair in a superconductor whereas the penetration length is a measure of field penetration into the superconductor in the Meissner state. For Type-I superconductors, the coherence length is larger than penetration length, whereas it is reverse for Type-II superconductors. The ratio of two characteristic lengths is called the Ginzburg-Landau parameter, $\kappa = \lambda/\xi$. It is an important parameter that characterizes whether the material is Type-I or Type-II superconductor. If $\kappa < 0.7$, the material is a Type-I superconductor, whereas for $\kappa > 0.7$, the material is Type-II superconductor. In the latter case, the magnetic flux penetrates into the superconductor in the form of

cylindrical tubes called vortices. A Vortex has a radius of λ and destroy superconductivity locally within a cylinder of radius ξ.

Critical current density and index number

So, far we have discussed the temperature and magnetic field properties of the superconductors but not the current flowing in them. Type-I and Type-II superconductors show very different magnetic and current carrying properties as well. Type-II superconductors have much higher critical current densities compared to Type-I, and therefore, Type-II superconductors are of practical importance.

The current density is the current divided by the cross-sectional area through which it flows. Superconductors have the critical temperature, T_c, the critical magnetic field, B_c. They have the critical current density, J_c; upper limit of the current density beyond which the superconductor cannot sustain current without energy dissipation. For practical superconductors, the electric field, E, as a function of J, generally given by the following non-linear power law [A.6].

$$E = E_c \left(\frac{J}{J_c} \right)^n \tag{A2.2}$$

where E_c is the electric field that defines the critical current density, J_c. Generally, E_c is defined at 0.1 μV/cm or 1 μV/cm for practical superconductors. The index for the current density, n, is called the index number and is infinite for ideal superconductors. For real superconductors ($n < \infty$), it should be noted that the electric field is not zero even below J_c but reduces to a level too small to be measured easily in practice as shown in Fig. A2.1, where E is plotted as a function of J corresponding to three superconductors having the same J_c but different index numbers. Note that for $J < J_c$, $E = 0$ for $n = \infty$ superconductor whereas for finite index numbers (n_1 and n_2), and one obtains some finite values of electric fields as $0 < E_1 < E_2$ (for $n_1 > n_2$). For low temperature superconductors, the index number is typically in the range of 40 ~ 50, whereas it is in the range of 10 ~ 30 for high temperature superconductors.

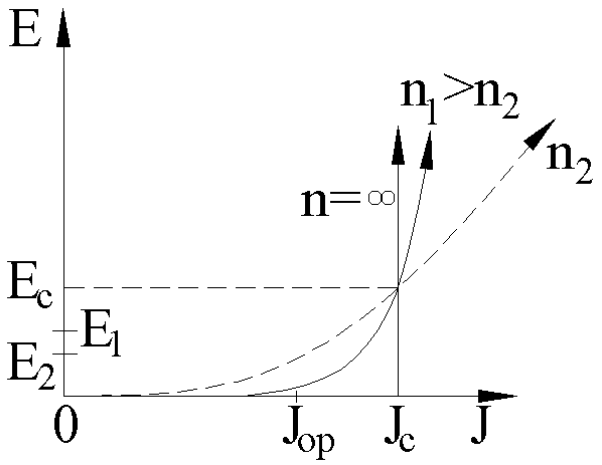

Fig. A2.1: Typical E-J characteristics of the practical superconductors for three different index numbers '*n*'. $n = \infty$ plot is for ideal superconductor whereas other two curves for n_1 and n_2 are for real superconductors. Index number n_1 curve is closer to low temperature superconductors whereas index number n_2 curve is closer to high temperature superconductors.

T-B-J characteristics

Below the certain critical temperature, T_c, the superconducting material shows the complete absence of electrical resistivity for the passage of direct current. In addition to T_c, the critical magnetic field, B_c and critical current density, J_c are other two parameters that define the critical surface (shown in Fig. A2.2), inside which the superconducting phase exists and outside the normal resistivity state [A.7]. T_c and B_c are the thermodynamic properties that for a given superconducting material are invariant to metallurgical processing whereas J_c is not. These three properties (T_c, B_c, and J_c) of a superconductor are connected with each other and an increase in anyone of these properties invariably produces decrease in other two. B_c and T_c are connected through a parabolic function given as

$$B_c \propto \left[1 - \left(\frac{T}{T_c}\right)^2\right] \tag{A2.3}$$

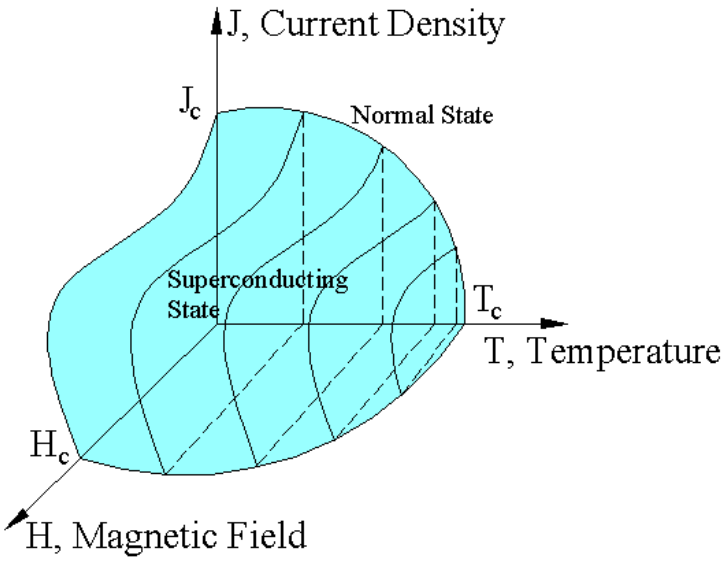

Fig. A2.2: The relationship between temperature, magnetic field and critical current in a superconductor. Anywhere inside the surface, the material is superconducting.

J_c is a decreasing function of temperature and, at T_c, it drops to zero. The operating temperature of typical superconductors is the boiling temperature of liquid helium (4.2 K) at which quite high current density (~ 10^{10} A/m^2 at 5 T for Nb_3Sn) is achievable.

The critical current density, J_c, is a metallurgical property of a superconductor and can be enhanced just by metallurgical processes. This enhanced J_c performance is generally attributed to a "pinning" force that counteracts the Lorentz force acting on the vortices. The pinning force is provided by pinning centers that are created in crystal structures by material impurities, metallurgical processes such as cold working. The field dependence of J_c was studies by Kim and others and they found a basic equation by equating the Lorentz force to the pinning force

$$J_c = \frac{\alpha_c}{B + B_0} \tag{A2.4}$$

where α_c and B_0 are constants.

Bean critical state model

Bean critical state model introduces a hypothesis that whenever a current, I, flows in a superconducting wire, the current density at the outside surface will immediately jump up to the critical current density, J_c and the superconductor is said to be in the "critical state" [A.7]. To transport more current, the shallow layer (with critical current density, J_c) thickens, again carrying, J_c, but over a larger cross-section. In this way, the current is always flowing with critical current density, J_c, but only the outer portion of the superconductor carries a current other than zero. In the annular ring where current J_c is flowing, $\partial B_\theta(r)/\partial r = J_c$ (from Maxwell's equation), a constant, and is zero elsewhere. Thus, B varies linearly with r from surface to the inside of the superconducting wire. The shapes of B and J are sketched in Fig. 2.3. Even though J_c decreases with magnetic field in all real superconductors, the Bean critical state model primarily assumes J_c to be field independent.

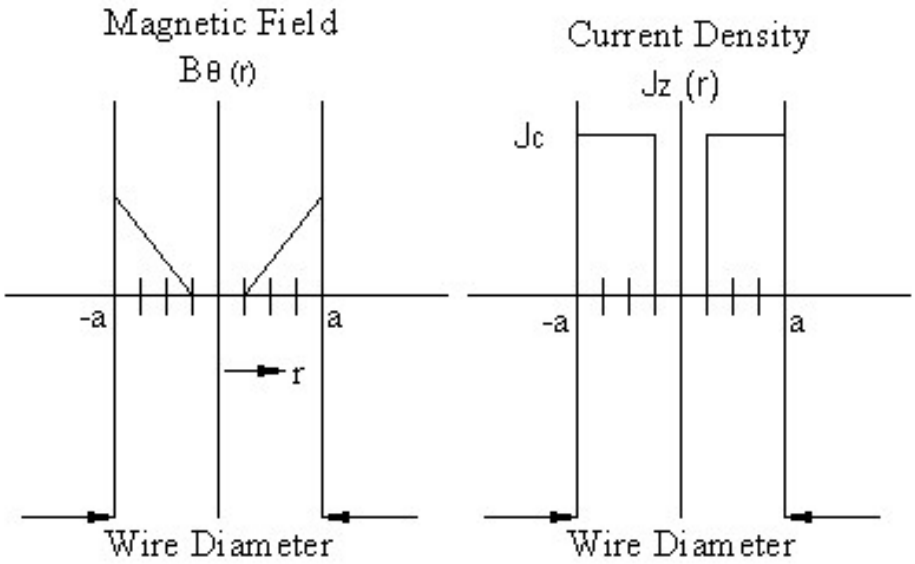

Fig. A2.3: Magnetic field and current distribution in a superconducting wire according to the Bean critical state model.

Hysteresis in superconductors

The magnetic behavior of materials is represented by plotting the magnetization, M, versus the applied field, B. When M depends only upon the present value of B, then the material returns to its initial magnetic state when the applied field returns to its initial state and no energy is dissipated. In practice, copper behaves this way. However, superconductors do not behave in this way, and hysteresis arises from flux pinning. When there is no flux pinning, there is no irreversibility; that is the magnetic behavior of the superconductors is perfectly reversible. This is the case for Type-I superconductors. The practical Type-II superconductors, however, show magnetic hysteresis as shown in Fig. A2.4 [A.7]. Up to B_{c1}, the magnetization is almost perfectly diamagnetic but increasing B leads to extensive flux penetration, M decreases, and at B_{c2}, the penetration is complete. In the superconducting state, much of the flux is pinned inside the superconductor. As external field is decreased, the internal magnetic field remains elevated. Since $B = \mu_0(H+M)$, this means that M rises to a positive value.

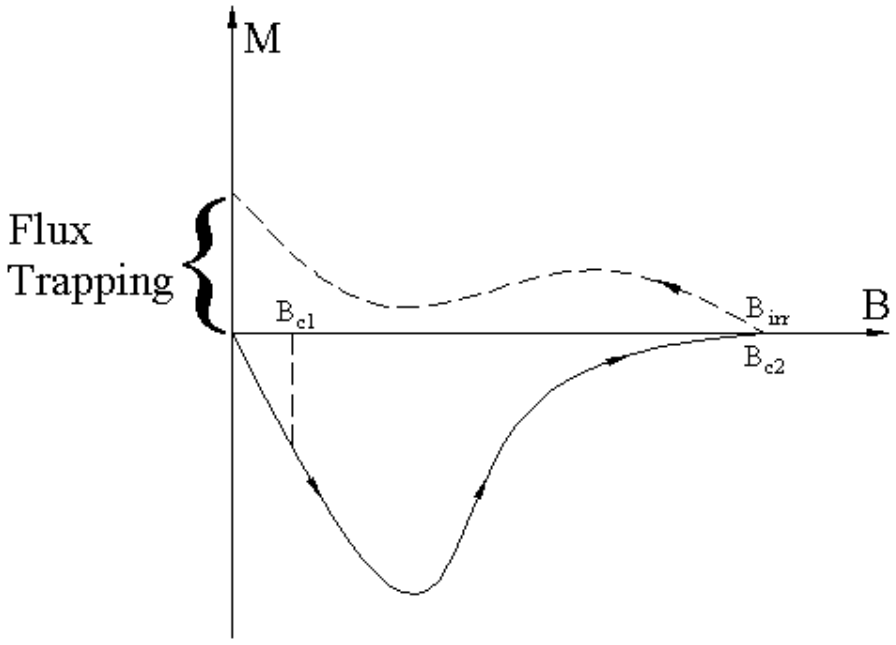

Fig. A2.4: Hysteresis of a realistic Type-II superconductor. The field at which irreversibility sets in, B_{irr}, is virtually the same as B_{c2}.

Further decline in H is accompanied by changes in M that leave B finite even when $H = 0$, which is due to flux trapping in the material and the magnetic energy associated with the field change converts into the heat. This permanent magnetism remains until the temperature is changed.

Appendix B

Design of heat exchangers for the INNOCENTS experiments

The design calculations for the heat exchangers used in the INNOCENTS experiments are discussed in this section.

Heat Exchangers in the INNOCENTS experiments

In INNOCENTS (INstabilities due to artificial NOn-uniform Current distribution experimENTS) experiments, two types of heat exchangers (counter flow heat exchanger and simple single pipe immersed in liquid helium heat exchanger) were used to have supercritical helium flowing inside the CICC at 0.4 MPa pressure and 4.2 K temperature. Figure B.1 shows the schematic of one unit of the single pipe heat exchanger used in INNOCENTS experiments.

Table B.1: Specifications of the counter flow heat exchanger

OD of the inner pipe	6 mm
OD of the outer pipe	10 mm
Number of units in heat exchanger	2
Number of spirals in one unit	15
Spiral diameter	~ 50 mm
Pitch	20 mm
Length of the one unit	350 mm
Approximate pipe length of one spiral	160 mm
Approximate pipe length in one unit	160 mm x 15 = 2400 mm
Total pipe length in heat exchanger (2 units)	4800 mm

Table B.2: Specifications of the single pipe heat exchanger

OD of the pipe	10 mm
Number of heat exchangers	2
Number of units in one heat exchanger	6 (12 in two heat exchangers)
Number of spirals in one unit	15
Spiral diameter	~ 50 mm
Pitch	20 mm
Approximate pipe length of one spiral	160 mm
Approximate pipe length in one unit	160 mm x 15 = 2400 mm
U transition lengths from one spiral unit to another spiral unit	120 mm x 2 + 240 mm x 3 = 960 mm
Total pipe length in one heat exchanger	2400 mm x 6 + 960 mm = 15360 mm
Total pipe length in two heat exchangers	15360 mm x 2 = 30720 mm

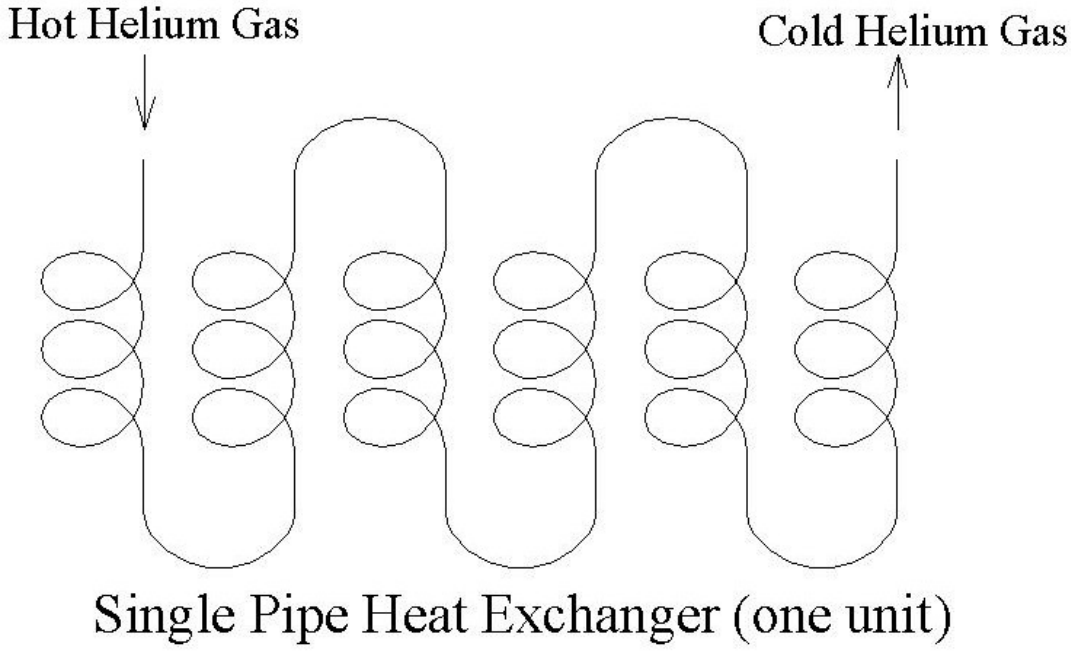

Fig. B.1: Schematic of the single pipe heat exchanger used in INNOCENTS experiments.

Cooling of the helium gas stream (flowing inside the single pipe heat exchanger) by a liquid helium bath

As shown in Fig. B.2, the hot helium gas is cooled by a bath of liquid helium when helium gas flows inside a copper pipe immersed in liquid helium bath.

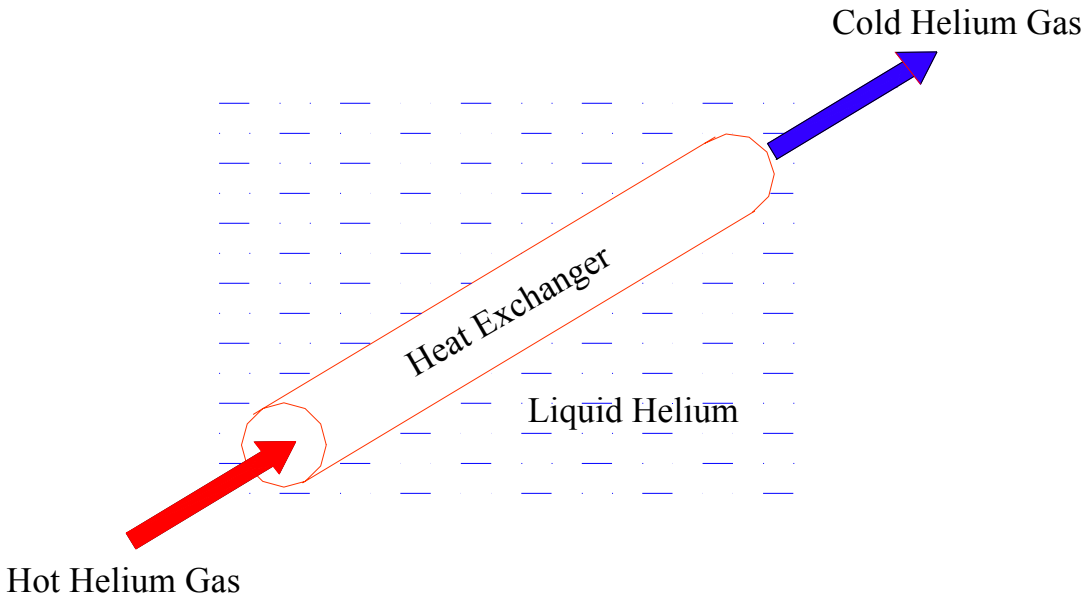

Fig. B.2: Schematic of a heat exchanger.

The required length of the pipe, L, for required gas outlet temperature, T_0, is given by [B.1]

$$L = \frac{\dot{m} C_p}{hS} \ln\left(\frac{T_L - T'}{T_0 - T'}\right) \qquad \text{(B.1)}$$

where, $\dot{m}$ is the gas mass flow rate (Kg/s), C_p is the specific heat of gas at the inlet (J/Kg-K), h is heat transfer coefficient (W/m^2-K), S is pipe's internal perimeter (m^2), T_L is gas inlet temperature (K), and T' is bath temperature (K).

The heat transfer coefficient, h, is given by

$$h = \frac{0.023}{\mathrm{Pr}^{0.6}} C_p \frac{G^{0.8}\eta^{0.2}}{D^{0.2}} \quad \text{(B.2)}$$

where, η is the gas viscosity, D is the pipe's inner diameter, Pr is the Prandtl's number.

$$G = \frac{4\dot{m}}{\pi D^2},\ \mathrm{Pr} = \eta C_p / \lambda \quad \text{(B.3)}$$

where λ is the thermal conductivity of the gas.

Using equations (B.2), and (B.3), and the following parameters for He gas at 300 K and 0.4 MPa,

D = 8 mm, η = 19.94 x 10^{-6} Pa-s, C_p = 5193 J/Kg-K, λ = 0.1562 W/m-K, $\dot{m}$ = 1.5 g/s (max.), one finds the heat transfer coefficient, h, as 695.5 W/m^2-K.

Total pipe length, L, in single pipe heat exchangers in INNOCENTS experiments is approx. 31 m. Using L=31m, and other parameters in equation (B.1), one finds

$\ln(\frac{300-4.2}{T_0-4.2}) = 69.5$, which gives T_0 - 4.2 ≈ 0 or T_0 = 4.2 K.

Please note that we have used gas specific heat and viscosity data at 300 K. From equation (B.2), it is clear that h/C_p has weak dependence on temperature (from viscosity, η) and therefore, the error in outlet temperature of the gas (from equation (B.1)) is small, especially when the pipe length is large.

We can do the reverse calculation as well to find out the necessary pipe length for cooling the He gas up to 4.2 K using liquid helium bath.

Let us take T_0 = 4.2 K, T' = 4.2 K, T_L = 300 K.

The average temperature is approx. 150 K. The gas properties at 150 K are

η = 12.53 x 10^{-6} Pa-s, C_p = 5194 J/K-Kg, λ = 0.097 W/m-K

This gives Prandtl number, Pr, as 0.67 or $\mathrm{Pr}^{0.6}$ = 0.786

By equation (B.2) h/C_p comes out to be 0.122. Using these values in equation (B.1), one finds the necessary pipe length as ~6.2 m. Hence one can conclude that 31 m of pipe length in INNOCENTS experiments to achieve 4.2 K supercritical helium was more than enough. No counter flow heat exchanger is required for this purpose but of course it reduces the heat load on the liquid helium bath.

Pressure drop calculations

The pressure drop in a smooth pipe is given by

$$\Delta P = 0.5\Psi \frac{LG^2}{D\rho} \tag{B.4}$$

where ρ is density of the fluid, and

$$\Psi = 64(\frac{\eta}{GD}) = \frac{64}{\mathrm{Re}} \tag{B.5a}$$

for laminar flow and

$$\Psi = 0.316(\frac{GD}{\eta})^{-0.25} \tag{B.5b}$$

for turbulent flow.

$$\mathrm{Re} = \frac{GD}{\eta} = \frac{4\dot{m}}{\pi D\eta} \tag{B.6}$$

If Re >> 2300 then it is turbulent flow otherwise laminar flow.

At average temperature of 150 K, the Reynolds number, *Re*, comes out to be as 19000, which is much higher then 2300 i.e. the flow is turbulent.

Therefore, Ψ is calculated using equation (B.5b) and it comes out to be as 0.0269.

From equation (B.3), 'G' comes out to be 29.86 Kg/m^{2}s.

The helium gas density, ρ, at 150 K and 0.4 MPa is 1.28 Kg/m^3.

Now, the pressure drop is calculated using equation (B.4).

$$\frac{\Delta P}{L} = 0.5 \times 0.0269 \frac{(29.86)^2}{8 \times 10^{-3} \times 1.28} = 1171 \text{ Pa/m}$$

For 6 m long pipe (needed to get 4.2 K temperature He as calculated above), the pressure drop is 7026 Pa i.e. ~0.07 atm.

Please note that the above calculation is rough calculation but enough to have an idea of pressure drop and outlet temperature in single pipe heat exchangers in INNOCENTS experiments.

Appendix C

Magnetic field calculations for the experiments on small-scale LTS/HTS hybrid conductors

The magnetic field calculations for the experiments on small-scale LTS/HTS hybrid conductors are discussed in this section.

Estimation of the number of turns of the bias field coil

The magnetic field of the 9 T solenoid coil is numerically calculated by assuming a uniform volumetric current distribution in the winding package (as shown in Fig. C.1). In order to provide a central magnetic field of 9 T, it is found that the total current of 1544091.7 A is required within the winding region. Since the nominal current of the superconducting wire is 49.0 A, the number of turns can be estimated as 31512.

Current density: 1544091.7/(176×48.25) ~ 181.83 A/mm^2
Estimated cross-sectional area of the wire: 49/181.83 ~ 0.2695 mm^2
Estimated size of the wire: 0.519 mm × 0.519 mm
Estimated number of layers: 93
Estimated number of turns in one layer: 339

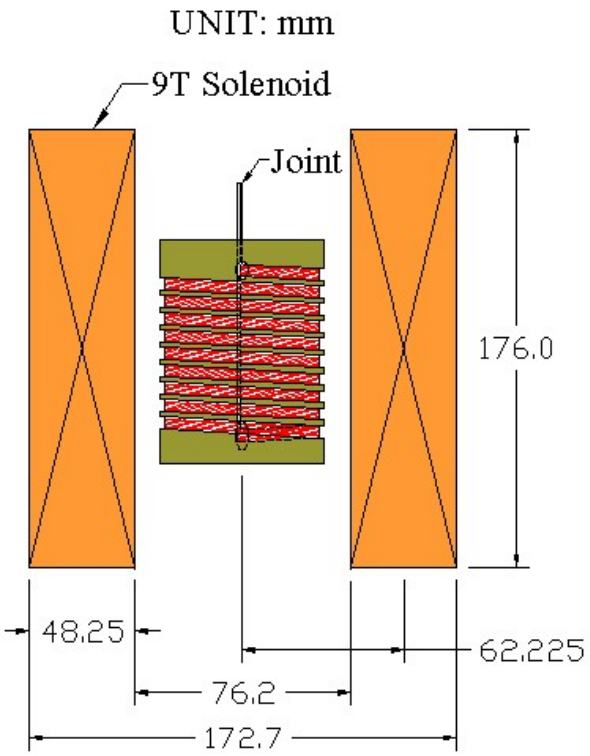

Fig. C.1 Configuration of the sample coil and bias coil.

Estimation of the inductances

The sample coil is a 9 turn helically wound solenoid with an LTS/HTS hybrid superconductor, as is illustrated in Fig. C.2. Both ends of the conductor are jointed together by solder so that the coil forms a short circuit. Here this coil is modeled to be a simple coil with a single layer winding equally divided into 9 turns. Then, the self-inductance the sample coil and the mutual inductance between the sample coil and the bias coil are calculated to be given as follows:

Self-inductance of the sample coil: 3.6 μH
Mutual-inductance between the sample coil and bias coil: 5.23 mH

Then, in order to induce 1000 A in the sample coil, the current and field change of the bias coil are given as follows:

Required current change: $3.6 \times 10^{-3}/5.23 \times 1000 = 0.688$ A

Required field change: $0.69/49 \times 9 = 0.127$ T

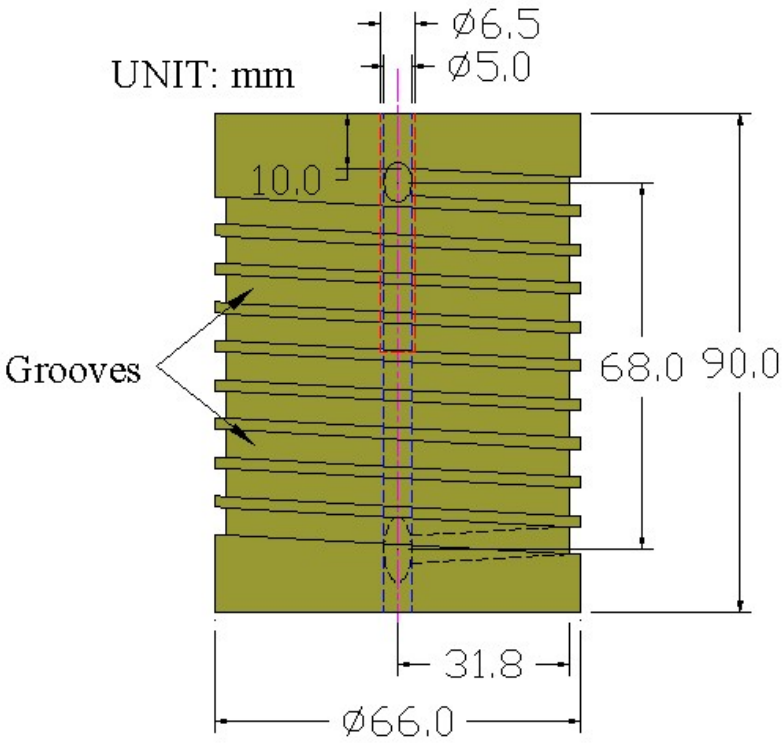

Fig. C.2 Side view of the sample coil. The winding is consisting of 9 turns.

Calculation of the magnetic field generated by the sample coil

The magnetic field generated by the sample coil can be precisely calculated based on Bio-Savart's law by giving the helical path of the winding [C.1]. The trajectory of the helical path used for the numerical calculation is shown in Fig. C.3, and it shows good agreement with the design of the bobbin as shown in Fig. C.4.

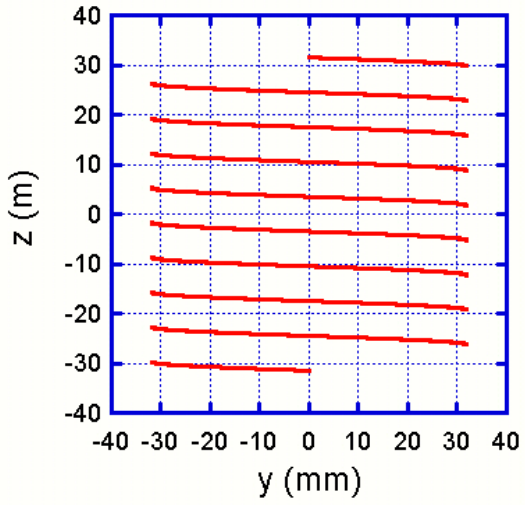

Fig. C.3 Trajectory of the helical path of the sample coil used for the numerical calculation. Only the positive region of x-axis is plotted.

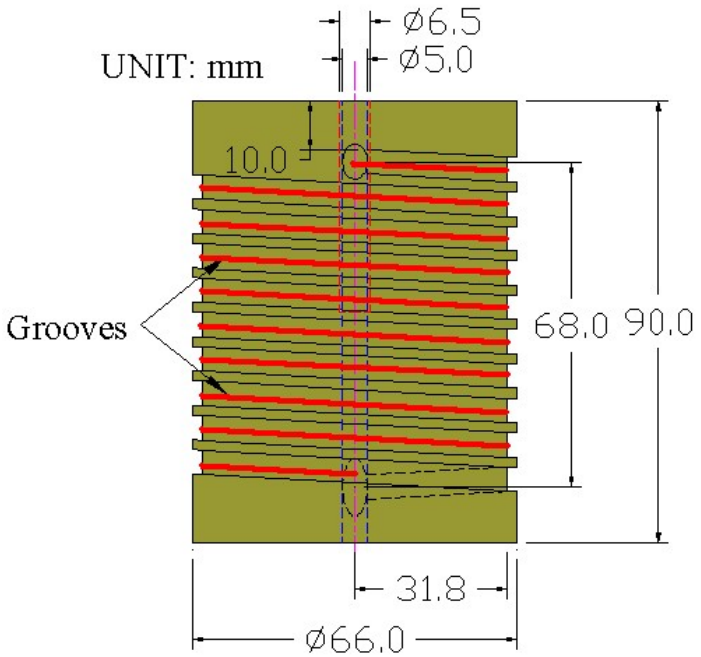

Fig. C.4 Comparison between the drawing of the coil bobbin and the trajectory of the winding used for the calculation.

The result of the magnetic field calculation is shown in Fig. C.5 when the coil current of 1000 A is induced in the sample coil. With this condition, the magnetic field at the center of the coil is given as -0.126 T, which shows good agreement with the value estimated by the mutual coupling between the sample coil and the bias coil. Here the current direction is assumed to be in the positive direction of the vertical axis. On the other hand, it should be noted that even though the coil winding shown in the above figures is specified in counter clockwise direction, the actually prepared one is in the clockwise direction. Thus, if the current is again given in the positive direction, the magnetic field becomes positive in the real experiment.

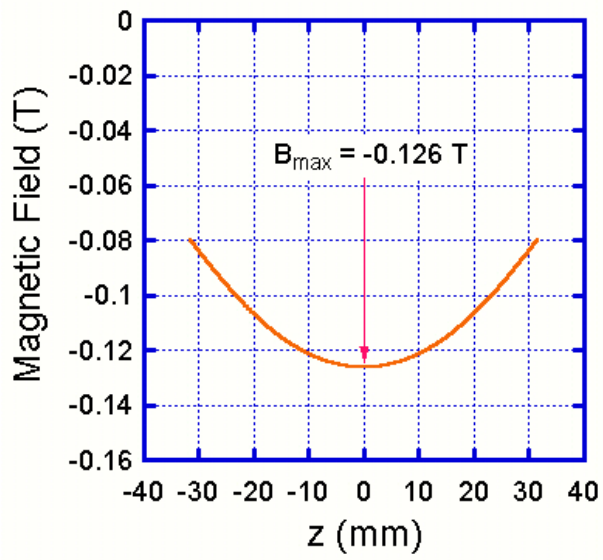

Fig. C.5 Calculated magnetic field (vertical component) along the axis of the sample coil when the current of 1000 A is induced. The coil winding is assumed to be in the counter clockwise direction.

Appendix D

Critical current analysis of the HTS conductors

The analysis for estimating the self-field effects on the critical currents of the HTS conductors has been discussed in this section.

Self-field effects on critical currents of HTS conductor

Bi-2223/Ag HTS conductor

The self-field effects on critical currents of the Bi-2223/Ag conductor have been calculated. The HTS conductor was tested in a bias field of 8 T (// to ab-plane of the HTS tapes) in conduction-cooled conditions. Table D.1 shows the measured values of critical currents at different temperatures. The calculated critical currents of HTS conductor (simple sum of critical currents of all the tapes in HTS conductor) are also shown for comparison. The difference between calculated and measured critical currents of HTS conductor are believed to be due to the self-fields created by the conductor (especially the self-field parallel to c-axis of the HTS tapes).

Table D.1: Measured critical currents of the HTS conductor

T (K)	B (T), parallel to ab-plane of the HTS tape	Calculated N × Ic (single tape) (kA)	Measured I_c of HTS conductor (kA)
5.5	8	17.51	14.2
11	8	15.81	12.9
22	8	12.24	10.5
32	8	8.71	8.23

The load line analysis has been performed to take into account the self-field (// to c-axis) for the critical current calculations of the HTS conductor.

Before load line analysis, let us discuss about the angular dependence of the critical currents of BSCCO HTS tapes [please see reference D.1 for details]. As we know, the grains in HTS tapes are misaligned and the ab-planes of the grains are perfectly parallel to the HTS tape surface. Fig. D.1 shows the grain misalignment angle 'φ' and magnetic field angle 'α'.

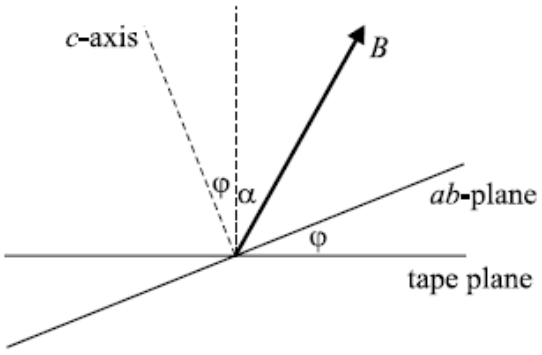

Fig. D.1: Definition of the field angle α and misalignment angle φ.

One scaling function *f(α)*, independent of magnetic field magnitude, is defined as follows.

$$f(\alpha) = \frac{B_{\perp,\mathrm{eff}}(\alpha)}{B_{\perp,\mathrm{eff}}(0^\circ)} = \frac{\int_{\varphi=-90^\circ}^{90^\circ} G(\varphi)\,|\cos(\alpha+\varphi)|\,\mathrm{d}\varphi}{\int_{\varphi=-90^\circ}^{90^\circ} G(\varphi)\,|\cos(\varphi)|\,\mathrm{d}\varphi}.$$

$$G(\varphi) = \frac{1}{\sigma\sqrt{2\pi}} \mathrm{e}^{-(\varphi^2/2\sigma^2)}, \quad -90^\circ \leqslant \varphi < 90^\circ,$$

where σ is the standard deviation in the grain alignment angle.

The effective perpendicular field component $B_{\perp,eff}$ is the same for an applied magnetic field with magnitude B and orientation α as for a field with magnitude $B \times f(\alpha)$ that is applied perpendicular to the tape surface. From the assumption that the critical current only depends on the field components applied perpendicular to the ab-plane of the grains, it follows directly that

$$I_c(B,\alpha) = I_c(B \times f(\alpha), 0^\circ) \equiv I_c(B^*, 0^\circ)$$

Where B^* is the scaled field amplitude. This means that if we know the scaling function $f(\alpha)$ for the field orientation of α, the effective field perpendicular to the tape surface can immediately be calculated. Hence, eventually, the critical current characteristics of HTS tape in perpendicular fields are enough to estimate the critical currents with different orientation angles α. Fig. D.2 shows one example [from reference D.1] of the critical currents of HTS tape with different field orientations. Using scaling function $f(\alpha)$, it is shown that all the points fall on a single curve.

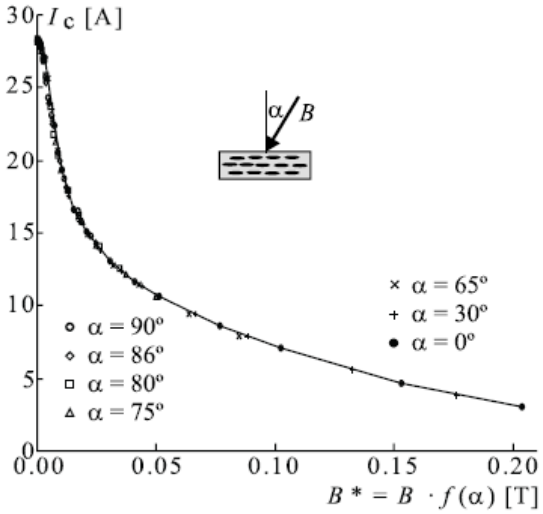

Fig. D.2: Critical currents as a function of scaled magnetic field $B^*=B \times f(\alpha)$. Symbols are measured data.

From above discussion, we find that the equivalent perpendicular field component (to HTS tape surface) can be estimated for a parallel field component by equaling the critical currents for both orientations at a particular temperature.

In our HTS conductor experiment, the 8 T field was parallel to the tape surface. By comparing the critical currents of the HTS tape in perpendicular and parallel field orientations, we find that equivalent perpendicular field component is about 1.3 T for 8 T parallel field component. Therefore, the bias field of 8 T can be treated as if it was 1.3 T field, perpendicular to the tape surface. The self-field produced by the conductor itself is the additional field to this 1.3 T. Only the perpendicular component of the self-field is being considered for the load line analysis as the parallel field component is cancelled due to the change of direction for top and bottom HTS tapes in the HTS conductor. Figure D.3 shows the self-field lines created by HTS conductors. The current is each tape is considered as 500 A.

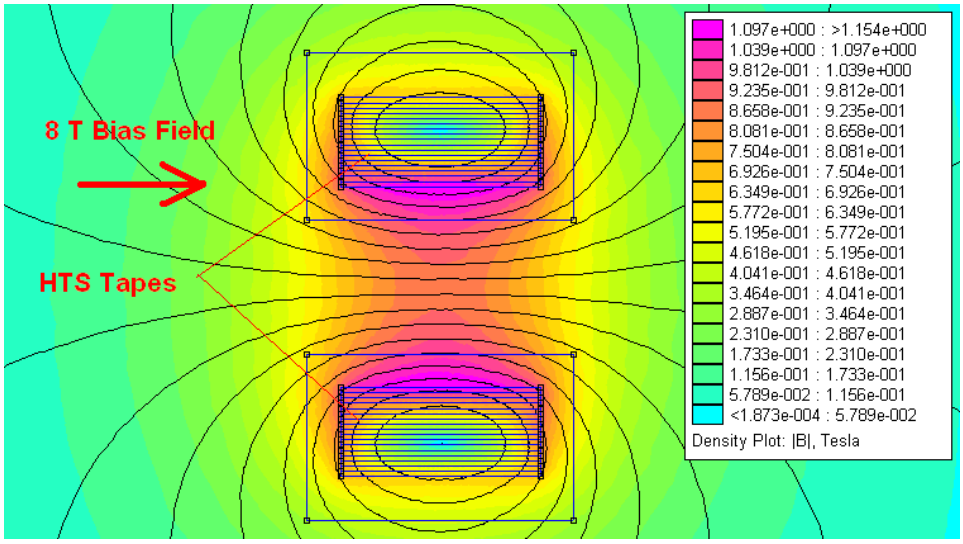

Fig. D.3: Self-field lines created by HTS conductors. Each tape current is set as 500 A.

The calculated constant of maximum perpendicular field is 8.54 x 10^{-4} TA^{-1} (for 34 tapes in two bundles configuration). The reciprocal value of this constant gives the slope of the load line I_{cr} = 1171 x B (perpendicular). Fig. D.4 shows the load line on the plot of I_c vs. $B\perp$ of the HTS tape for different temperatures. The I_c vs. $B\perp$ plots in Fig. D.4 have been deduced from data sheets by Sumitomo Electric. The load line is shifted due to the effective bias field of 1.3 T (equivalent to 8 T bias field parallel to tape surface) and therefore cuts the horizontal axis at 1.3 T. The intersection points of the load line and I_c characteristics curves of the HTS tape are the critical currents of the HTS tape at that particular temperature. In Fig. D.4, shown critical currents on the vertical axis are normalized with the critical current at 0 T field and 77 K temperature, which is 140 A for the HTS tapes used in our HTS conductor. This data is also provided by the supplier Sumitomo Electric. The calculated critical currents from Fig. D.4 are shown in Table D.2 along with the measured critical currents and simple sum of the critical currents of the HTS tapes in the conductor.

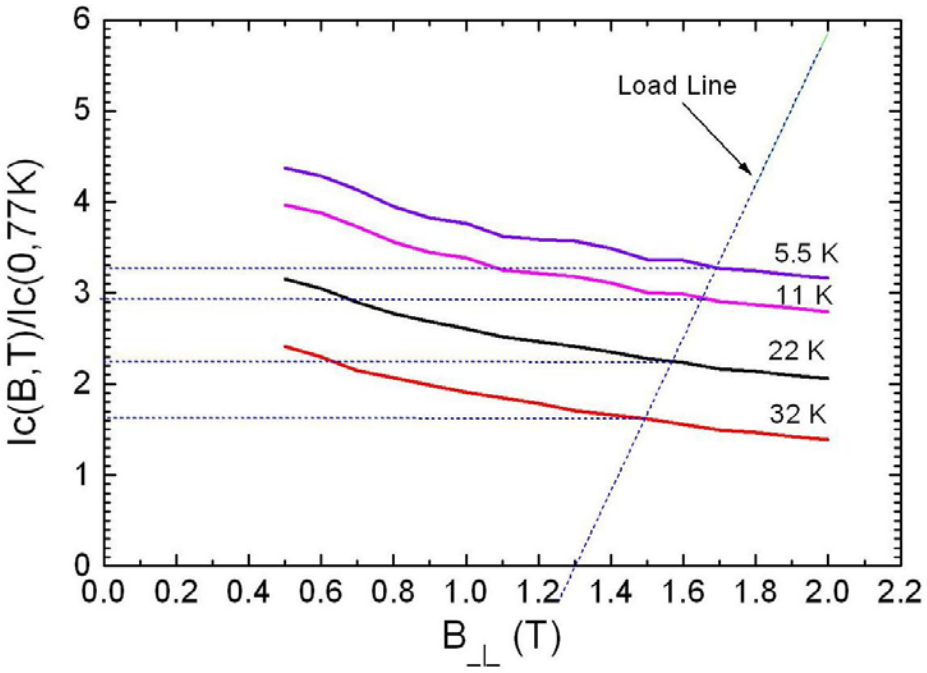

Fig. D.4: Load line on the Ic (normalized) vs. B⊥ plot of the HTS tape. The load line is for a configuration of 34 HTS tapes in 2 bundles. The effective bias field of 1.3 T (perpendicular to tape surface) is also considered in plotting the load line.

Table D.2: Measured and calculated critical currents of the HTS conductor

T (K)	B (T), parallel to ab-plane of the HTS tape	Calculated N × Ic (single tape) (kA)	Calculated N × Ic (single tape) with self-field effect (kA)	Measured I_c of HTS conductor (kA)
5.5	8	17.51	15.47	14.2
11	8	15.81	13.80	12.9
22	8	12.24	10.57	10.5
32	8	8.71	7.62	8.23

As show in Table D.2, the calculated critical currents of the HTS conductor with self-field effects are closer to the measured critical currents. Still there is some difference between calculated and measured critical currents. The reasons might be,

1. All the HTS tapes have been considered with uniform critical current properties. However, there might be some difference between each tape, which may affect the calculated results.
2. The critical currents are calculated from deduced I_c vs. $B\perp$ curves. There might be small errors in deduced I_c vs. $B\perp$ curves, which may affect the calculated critical currents.
3. The conductor temperature was measured at the surface. There might be a temperature difference between surface and inner tapes, which may affect the calculated results.

The reason of the discrepancy between calculated and measured critical currents is not very clear. However, it has been shown that the self-field plays a significant role for critical current estimations. The differences between calculated critical currents and measured ones are not large and can be accepted within few percent of error bars.

YBCO HTS conductor

The self-field effects on the critical currents of the YBCO conductor have been calculated. The YBCO conductor was tested in a bias field of 8 T (// to ab-plane of the YBCO tapes) in conduction-cooled conditions. Table D.3 shows the measured values of critical currents at different temperatures. The calculated critical currents of YBCO conductor (simple sum of critical currents of all the tapes in YBCO conductor without self-field effect) are also shown for comparison. The difference between calculated and measured critical currents of the YBCO conductor are believed to be due to the self-field created by the conductor (especially the self-field parallel to the c-axis of the YBCO tapes). The tested HTS conductor consists of YBCO and GdBCO tapes (8 tapes each). The critical currents are 210 and 190 A at 77 K and self-field, respectively. We note that both these

tapes were provided by International Superconductivity Technology Center (ISTEC) and Fujikura Ltd. under the support by the New Energy and Industrial Technology Development Organization (NEDO) as Collaborative Research and Development of Fundamental Technologies for Superconductivity Applications. Here, we assume that these tapes are identical to each other in our present analysis.

Table D.3: Measured critical currents of the YBCO conductor

T (K)	B (T), parallel to ab-plane of the YBCO tape	Calculated Ic (single tape) × N (kA)	Measured I_c of YBCO conductor (kA)
15.5	8	17.28	16.8
24	8	16.03	14.2
27	8	15.68	12.5

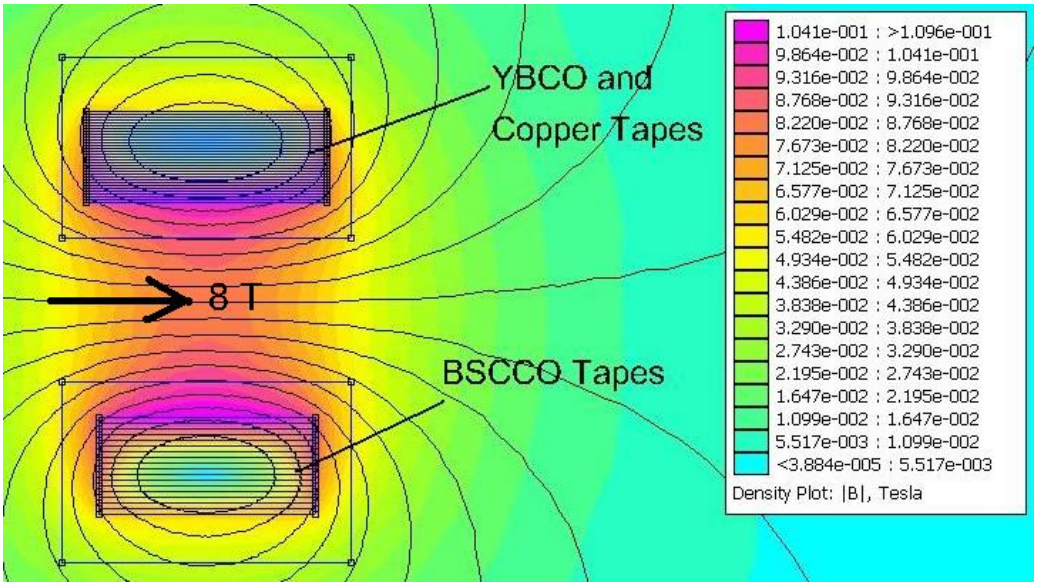

Fig. D.5: Self-field lines created by YBCO and BSCCO conductors. Each YBCO and GdBCO tape current is set as 100 A.

The load line analysis has been performed to take into account the self-field (// to c-axis) effects for the critical current calculations of the HTS conductor in the similar way as discussed for Bi-2223/Ag conductor.

In our YBCO conductor experiment, the 8 T field was parallel to the tape surface. By comparing the critical currents of the YBCO tape in perpendicular and parallel field orientations [Reference D.2, Fig. 2], we find that equivalent perpendicular field component is about 0.8 T for 8 T parallel field component. Therefore, the bias field of 8 T can be treated as if it was 0.8 T field, perpendicular to the tape surface. The self-field produced by the conductor itself is the additional field to this 0.8 T. Only the perpendicular component of the self-field is being considered for the load line analysis as the parallel field component is cancelled due to the change of direction for top and bottom YBCO tapes in the YBCO conductor. Figure D.5 shows the self-field lines created by YBCO conductors. The current is each tape is considered as 100 A. The calculated constant of maximum perpendicular field is 7.66×10^{-4} TA^{-1} (for 16 YBCO and GdBCO tapes with copper tapes). The reciprocal value of this constant gives the slope of the load line $I_{cr} = 1305 \times B$ (perpendicular). Figure D.6 shows the load line on the plot of I_c vs. $B\perp$ of the HTS tape for different temperatures. The I_c vs. $B\perp$ plots in Fig. D.6 have been produced using percolation model by taking the reference of the critical current of 210 A at 77 K and self-field. The load line is shifted due to the effective bias field of 0.8 T (equivalent to 8 T bias field parallel to tape surface) and therefore cuts the horizontal axis at 0.8 T. The intersection points of the load line and I_c characteristics curves of the YBCO tape are the critical currents of the YBCO tape at that particular temperature. The calculated critical currents from Fig. D.6 are shown in Table D.4 along with the measured critical currents and simple sum of the critical currents of the YBCO tapes in the conductor.

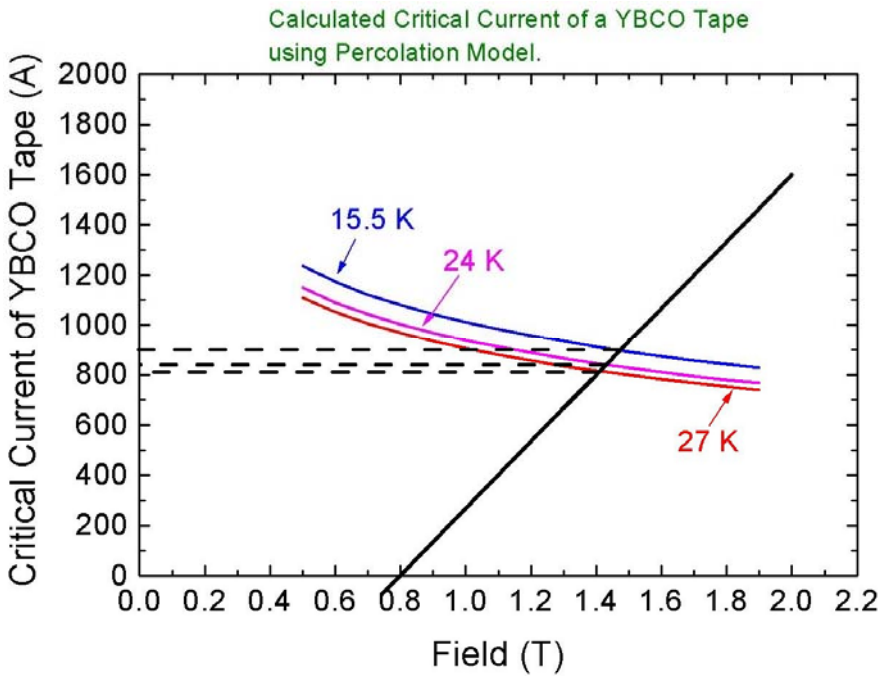

Fig. D.6: Load line on the Ic vs. B⊥ plot of the YBCO tape. The load line is for a configuration of 16 YBCO tapes with copper tapes. The effective bias field of 0.8 T (perpendicular to tape surface) is also considered in plotting the load line.

TABLE D.4: Measured and calculated critical currents of the YBCO conductor

T (K)	B (T), parallel to ab-plane of the HTS tape	Calculated N × Ic (single tape) (kA)	Calculated N × Ic (single tape) with self-field effect (kA)	Measured I_c of HTS conductor (kA)
15.5	8	17.28	14.4	16.8
24	8	16.03	13.44	14.2
27	8	15.68	12.88	12.5

As show in Table D.4 and Fig. D.7, the calculated critical currents of the YBCO conductor with self-field effects are not in good agreement with measured critical currents. The reasons might be,

1. The YBCO and GdBCO tapes (8 tapes each) have been used in the tested YBCO conductor. For the calculations, the YBCO and GdBCO tapes have been considered with identical properties. However, there should be some differences between these tapes [D.3, D.4], which should affect the calculated results.
2. The critical currents are calculated from the calculated I_c vs. $B\perp$ curves using percolation model. There might be errors in calculated I_c vs. $B\perp$ curves, which may affect the calculated critical currents. The experimental data of YBCO and GdBCO tapes critical current seems to be necessary to improve the results and therefore, the experiments on YBCO and GdBCO tapes are planned to be done as a future task.

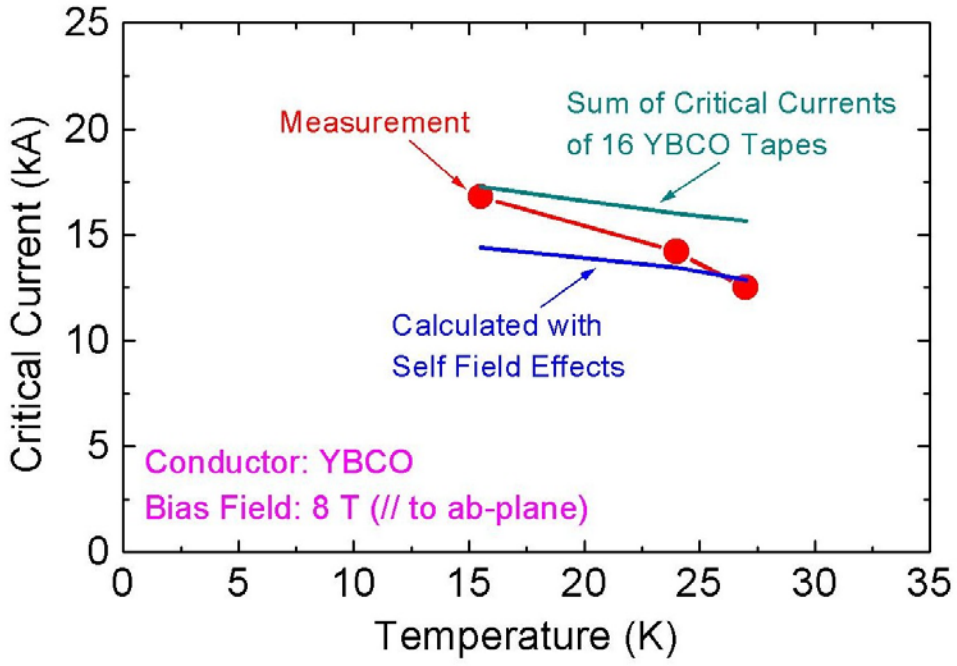

Fig. D.7: Measured and calculated critical currents of the YBCO conductor.

The reason of the discrepancy between calculated and measured critical currents is not very clear. However, it has been shown that the self-field plays a significant role for critical current estimations.

References

[1.1] Yukikazu Iwasa, Case Studies in Superconducting Magnets, Plenum Press, (1994).

[1.2] Martin N. Wilson, Superconducting Magnets, Clarendon Press Oxford, (1983).

[1.3] N. Koizumi et al., Development of advanced Nb_3Al superconductors for a fusion demo plant, Nuclear Fusion 45 (2005) pp. 431.

[1.4] Y. Hishinuma et al., Fabrication and superconducting properties of PIT-V3Ga mono-cored wires using high Ga content Cu–Ga compound powders, Supercond. Sci. Technol. 20 (2007) pp. 569.

[1.5] G.M. Ozeryansky, E. Gregory, A new internal tin Nb_3Sn conductor made by a novel manufacturing process, IEEE Transactions on Magnetics 27 (1991) pp. 1755.

[1.6] M.O. Hoenig and D.B. Montgomery, Dense supercritical helium cooled superconductors for large high field stabilized magnets, IEEE Transactions on Magnetics 11 (1975) pp. 569.

[1.7] E Salpietro, Status of the ITER magnets, Supercond. Sci. Technol. 19 (2006) pp. S84.

[1.8] T. Satow, O. Motojima, Performance of the LHD magnet system, IEEE Trans. on Appl. Supercond.12 (2002) pp. 629.

[1.9] J.G. Bednorz and K.A. Mueller, Z. Phys. B – Condensed Matter 64 (1986) pp. 189.

[1.10] M.K. Wu, et al., Superconductivity at 93 K in a new mixed phase Y-Ba-Cu-O compound system at ambient pressure, Phys. Rev. Lett. 58 (1987) pp. 908.

[1.11] H. Maeda et. al, A new high-T_c oxide superconductor without a rare earth element, Jap. J. Appl. Phys. 27 (1988) pp. L209.

[1.12] Sumitomo Electric, Japan (http://www.sei.co.jp/super/).

[1.13] T. Isono et al., Development of 10 kA class Bi2212 conductor for fusion application, IEEE Trans. on Appl. Supercond. 13 (2003) pp. 1512.

[1.14] Y. Yamada, M. Mogi and K. Sato, Examples and future prospects of high-temperature superconductor products, SEI Technical Review · Number 65 · October (2007) pp. 51.

[1.15] International Superconductivity Technology Center (ISTEC), Japan (http://www.istec.or.jp/index-E.html).
[1.16] Thomas P. Sheahen, Introduction to High-Temperature Superconductivity, Plenum Press, (1994).
[1.17] A. Goyal, D. P. Norton, J. D. Budai, M. Paranthaman et al., High critical current density superconducting tapes by epitaxial deposition of YBa2Cu3Ox thick films on biaxially textured metals, Appl. Phys. Lett. 69 (1996) pp. 1795.
[1.18] American Superconductor, USA (http://www.amsc.com/).
[1.19] H. Krauth et al., Design of the EURATOM test coil for the large coil task, Symposium on Engineering Problems of Fusion Research, 8th, San Francisco, Calif., November 13-16, 1979, Proceedings. 3 (1979) pp. 1169.
[1.20] Y.C. Saxena, SST-1 Team, Present status of the SST-1 project, Nuclear Fusion 40 (2000) pp. 1069.
[1.21] G. S.Lee et al., The design of the KSTAR tokamak, Fusion Eng. Design 46 (1999) pp. 405.
[1.22] Wu Weiyue et al., Assembly of the superconducting tokamak EAST, Journal of the Korean Physical Society 49 (2006) pp. S14.
[1.23] K. Kizu et al., Conceptual Design of magnet system for JT-60 super advanced (JT-60SA), IEEE Trans. on Appl. Supercond.17 (2007) pp. 1348.
[1.24] N. Yanagi et al., Stability test results on the aluminum stabilized superconductor for the helical coils of LHD, IEEE Trans. on Appl. Supercond. 9 (1999) pp. 1113.
[1.25] K. Takahata et al., Stability of cable-in-conduit superconductors for large helical device, IEEE Trans. on Appl. Supercond. 3 (1993) pp. 511.
[1.26] J. Baldzuhn et al., Coil tests and superconductor code calculations for the stellarator W7-X coils, Cryogenics 46 (2006) pp. 507.
[1.27] A. Ulbricht, J. L. Duchateau, W. H. Fietz, D. Ciazynski, H. Fillunger, S. Fink et al., The ITER toroidal field model coil project, Fusion Eng. Design 73 (2005) pp. 189.
[1.28] N. Martovetsky, M. Takayasu, J. Minervini, T. Isono, M. Sugimoto, T. Kato et al., Test of the ITER TF insert and central solenoid model coil, IEEE Trans. on Appl. Supercond. 13 (2003) pp. 1441.

[1.29] N. Mitchell, Summary, assessment and implications of the ITER model coil test results, Fusion Eng. Design 66-68 (2003) pp. 971.
[1.30] M. Huguet and the ITER International Team and Participant Teams, The ITER magnets: preparation for full size construction based on the results of the model coil programme, Nuclear Fusion 43 (2003) pp. 352.
[1.31] Z. Yoshida, Y. Ogawa et al., First plasma in the RT-1 device, Plasma and Fusion Research: Rapid Communications 1 (2006) pp. 008-1.
[1.32] N. Yanagi et al., Excitation test results of the HTS floating coil for the Mini-RT project, IEEE Trans. on Appl. Supercond. 13 (2003) pp. 1504.
[1.33] Joel H. Schultz et al., The levitated dipole experiment (LDX) magnet system, IEEE Trans. on Appl. Supercond. 9 (1999) pp. 378.
[1.34] Toshio Uede et al., Evaluation of superconducting current feeder system for the large helical device (LHD), IEEE Trans. on Appl. Supercond. 11 (2001) pp. 2563.
[1.35] K. Yoshida et al., Updating the design of the feeder components for the ITER magnet system, Fusion Eng. Design 75–79 (2005) pp. 241.
[1.36] T. Mito et al., Development of high temperature superconducting current feeders for a large-scale superconducting experimental fusion system, IEEE Trans. on Appl. Supercond. 11 (2001) pp. 2611.
[1.37] J. R. Miller et al., Design and development of a pair of 10 kA HTS current leads for the NHMFL 45 hybrid magnet system, IEEE Trans. on Appl. Supercond. 15 (2005) pp. 1492.
[1.38] Toshinari Ando, Design of a 60-kA HTS current lead for fusion magnets and its R&D, IEEE Trans. on Appl. Supercond. 11 (2001) pp. 2535.
[1.39] R. Heller et al., Experimental results of a 70 kA high temperature superconductor current lead demonstrator for the ITER magnet system, IEEE Trans. on Appl. Supercond. 15 (2005) pp. 1496.
[1.40] K. Okuno et al., Superconducting magnet system in a fusion reactor, Journal of Nuclear Materials 329–333 (2004) pp. 141.
[1.41] N. Koizumi, K. Okuno, Y. Takahashi, H. Tsuji, and S. Shimamoto, Stabilized operation of 30 kA NbTi demo poloidal coil (DPC-U) with uniform current distribution in conductors, Cryogenics 34 (1994) pp. 1015.

[1.42] N. Koizumi, K. Okuno, Y. Takahashi, H. Tsuji, M. Nishi, K. Yoshida et al., Experimental results on instability caused by non-uniform current distribution in the 30 kA NbTi demo poloidal coil (DPC-U) conductor, Cryogenics 34 (1994) pp. 155.
[1.43] N. Koizumi, Y. Takahashi, M. Nishi, T. Isono, H. Tsuji, M. Ono et al., Ramp-rate limitation due to current imbalance in a large cable-in-conduit conductor consisting of chrome-plated strands, Cryogenics 37 (1997) pp. 441.
[1.44] N. Koizumi, K. Okuno, Y. Takahashi, H. Tsuji, and S. Shimamoto, Current imbalance due to induced circulation currents in a large cable-in-conduit superconductor, Cryogenics 36 (1996) pp. 409.
[1.45] K. Seo et al., Avalanche-like quenches in cable in conduit conductors, Journal of the Korean Physical Society 49 (2006) pp. S276.
[1.46] N. Mitchell, Analysis of non-uniform current distribution effects in multistage cable-in-conduit conductors, Cryogenics 39 (1999) pp. 539.
[1.47] K. Seo, T. Mito, J.R. Miller, S. Kawabata, T. Ichihara, and M. Hasegawa, Analysis of joint-resistance-induced non-uniform current distribution, IEEE Trans. on Appl. Supercond. 15 (2005) pp. 1595.
[1.48] V.S. Vysotsky, M. Takayasu, M. Ferri, and J.V. Minervini, New method of current distribution studies for ramp rate stability of multistrand superconducting cables, IEEE Trans. on Appl. Supercond. 5 (1995) pp. 580.
[1.49] N. Amemiya et al., Experimental study on current re-distribution and stability of multi-strand superconducting cables, IEEE Trans. on Appl. Supercond. 7 (1997) pp. 942.
[1.50] CRYOCOMP Version 3.06, Cryodata Inc.
[1.51] J. R. Hull, Potential for use of high-temperature superconductors in fusion reactors, Jour. Nucl. Materials 191-194 (1992) pp. 520.
[1.52] T. Isono, N. Koizumi, K. Okuno, R. Kurihara, S. Nishio, K. Tobita, Design study of superconducting coils for the fusion DEMO plant at JAERI, Fusion Eng. Design 81 (2006) pp. 1257.
[1.53] G. Janeschitz, L. Boccaccini, W. H. Fietz, W. Goldacker, T. Ihli, R. Meyder et al., Development of fusion technology for DEMO in Forschungszentrum Karlsruhe, Fusion Eng. Design 81 (2006) pp. 2661.

[1.54] P. Komarek, Potential and desire for HTS application in thermonuclear fusion, Fusion Eng. Design 81 (2006) pp. 2287.
[1.55] A. Sagara et al., Conceptual design activities and key issues on LHD-type reactor FFHR, Fusion Eng. Design 81 (2006) pp. 2703.

[2.1] P. J. Lee, Engineering Superconductivity, Wiley–Inter science Publications, 2001.
[2.2] L. Bottura, Limiting current and stability of cable-in-conduit conductors, Cryogenics 34 (1994) pp. 787.
[2.3] Y.C. Saxena, SST-1 Team, Present status of the SST-1 project, Nuclear Fusion 40 (2000) pp. 1069.
[2.4] F. Hosono, S. Inaba, K. Chida, K. Kamata, S. Pradhan, and Y.C. Saxena, Performance of cable-in-conduit conductors for SST-1 at IPR, Hitachi Cable Review, No. 20, (2001) pp. 101.
[2.5] M. O. Hoenig, A. G. Montgomery, S. J. Waldman, "Cryostability in force-cooled superconducting cables", IEEE Transactions on Magnetics 15 (1979) pp. 792.
[2.6] J. Yamamoto, T. Mito, K. Takahata, S. Yamada, N. Yanagi, I. Ohtake et al., Superconducting test facility of NIFS for large helical device, Fusion Eng. Design 20 (1993) pp. 147.
[2.7] Yukikazu Iwasa, Case Studies in Superconducting Magnets, Plenum Press, (1994).
[2.8] Martin N. Wilson, Superconducting Magnets, Clarendon Press Oxford, (1983) pp. 204.
[2.9] N. Koizumi, Y. Takahashi, M. Nishi, T. Isono, H. Tsuji, M. Ono et al., Ramp-rate limitation due to current imbalance in a large cable-in-conduit conductor consisting of chrome-plated strands, Cryogenics 37 (1997) pp. 441.
[2.10] M. Takayasu, M. Ferri, C. Y. Gung, T. **A.** Painter, M. M. Steeves and J.V. Minervini, Measurements of ramp-rate limitation of cable-in-conduit conductors, IEEE Trans. on Appl. Supercond. 3 (1993) pp. 456.
[2.11] Sangkwon Jeong et al., Experimental investigation to overcome the ramp-rate limitation of CICC superconducting magnets, IEEE Trans. on Appl. Supercond. 11 (2001) pp. 1689.

[2.12] L. Krempasky and C. Schmidt, Ramp-rate limitation in large superconducting magnets due to ‘supercurrents’, Cryogenics 36 (1996) pp. 471.
[2.13] GANDALF: A computer code for quench analysis of dual flow CICC’s, http://botturl.web.cern.ch/botturl/CryoSoft/manuals/Gandalf_2.2.pdf.
[2.14] C. Schmidt, Transient heat transfer to a closed volume of He I and its influence on superconductor stability, Cryogenics 31 (1991) pp. 618.
[2.15] K. Seo et al., Avalanche-like quenches in cable in conduit conductors, Journal of the Korean Physical Society 49 (2006) pp. S276.
[2.16] K. Seo, T. Mito, J.R. Miller, S. Kawabata, T. Ichihara, and M. Hasegawa, Analysis of joint-resistance-induced non-uniform current distribution, IEEE Trans. on Appl. Supercond. 15 (2005) pp. 1595.

[3.1] O. Motojima, K. Akaishi, H. Chikaraishi, et al., Progress summary of LHD engineering design and construction, Nuclear Fusion 40 (2000) pp. 599.
[3.2] H. Kaneko, Insulation of highly conductive metal in composite stabilizer for reduction of Hall current across surface, Cryogenics 33 (1993) pp. 1077.
[3.3] J.M. Pfotenhauer, M.K. Abdelsalam, F. Bodker, et al., Test results from SMES proof of principle experiment, IEEE Transactions on Magnetics 27 (1991) pp. 1704.
[3.4] N. Yanagi, S. Imagawa, Y. Hishinuma, et al., Asymmetrical normal-zone propagation observed in the aluminum-stabilized superconductor for the LHD helical coils, IEEE Trans. on Appl. Supercond. 14 (2004) pp. 1507.
[3.5] S. Imagawa, N. Yanagi, H. Sekiguchi, et al., Performance of the helical coils for the large helical device in six years' operation, IEEE Trans. on Appl. Supercond. 14 (2004) pp. 1388.
[3.6] L. Masur, D. Parker, M. Tanner, E., et al., Long length manufacturing of high performance BSCCO-2223 tape for the Detroit Edison power cable project, IEEE Trans. on Appl. Supercond. 11 (2001) pp. 3256.
[3.7] T. Kaneko, T. Hikata, M. Ueyama, et al., Status of Bi-2223 tapes performance and development, IEEE Trans. on Appl. Supercond. 9 (1999) pp. 2465.
[3.8] Sumitomo Electric, Japan (http://www.sei.co.jp/super/).

[4.1] J. R. Hull, Potential for use of high-temperature superconductors in fusion reactors, Jour. Nucl. Materials 191-194 (1992) pp. 520.
[4.2] T. Isono, N. Koizumi, K. Okuno, R. Kurihara, S. Nishio, K. Tobita, Design study of superconducting coils for the fusion DEMO plant at JAERI, Fusion Eng. Design 81 (2006) pp. 1257.
[4.3] G. Janeschitz, L. Boccaccini, W. H. Fietz, W. Goldacker, T. Ihli, R. Meyder et al., Development of fusion technology for DEMO in Forschungszentrum Karlsruhe, Fusion Eng. Design 81 (2006) pp. 2661.
[4.4] P. Komarek, Potential and desire for HTS application in thermonuclear fusion, Fusion Eng. Design 81 (2006) pp. 2287.
[4.5] L. Bromberg, M. Tekula, L. A. El-Guebaly and R. Miller, Options for the use of high temperature superconductor in tokamak fusion reactor designs, Fusion Eng. Design 54 (2001) pp. 167.
[4.6] T. Ando, S. Nishio, H. Yoshimura, IEEE Trans. Appl. Supercond. 14 (2004) pp. 1481.
[4.7] H. Hashizume et al., J.Plasma Fusion Res. Series 5 (2001) pp. 532.
[4.8] W Goldacker et al., J. Phys. Conf. Ser. 43 (2006) pp. 901.
[4.9] Sumitomo Electric, Japan (http://www.sei.co.jp/super/).
[4.10] W. Nah, H. Hwangbo, J. Ye, J. Joo et al., Load line analysis of Bi-2223 tape stacked cable for self field effects, IEEE Trans. on Appl. Supercond. 10 (2000) pp. 1158.
[4.11] T. Kiss et al., Critical current properties in HTS tapes, Physica-C 392-396 (2003) pp. 1053.

[5.1] A. Sagara et al., Conceptual design activities and key issues on LHD-type reactor FFHR, Fusion Eng. Design 81 (2006) pp. 2703.
[5.2] A. Sagara et al., Improved structure and long-life blanket concepts for heliotron reactors, Nuclear Fusion 45 (2005) pp. 258.
[5.3] J. R. Hull, Potential for use of high-temperature superconductors in fusion reactors, Jour. Nucl. Materials 191-194 (1992) pp. 520.
[5.4] G. Janeschitz, L. Boccaccini, W. H. Fietz, W. Goldacker, T. Ihli, R. Meyder et al., Development of fusion technology for DEMO in Forschungszentrum Karlsruhe, Fusion

Eng. Design 81 (2006) pp. 2661.
[5.5] P. Komarek, Potential and desire for HTS application in thermonuclear fusion, Fusion Eng. Design 81 (2006) pp. 2287.
[5.6] W.H. Fietz et al., High temperature superconductors for the ITER magnet system and beyond, Fusion Eng. Design 75-79 (2005) pp. 105.
[5.7] L. Bromberg, M. Tekula, L. A. El-Guebaly and R. Miller, Options for the use of high temperature superconductor in tokamak fusion reactor designs, Fusion Eng. Design 54 (2001) pp. 167.
[5.8] T. Hemmi et al., Annual Report of National Institute for Fusion Science, ISSN 0917-1185 (2007) pp. 278.
[5.9] T. Ando et al., Design of the TF coil for a tokamak fusion power reactor with YBCO tape superconductors, presented at SOFE 2005.
[5.10] F. Dahlgren et al., ARIES-AT magnet systems, Fusion Eng. Design 80 (2006) pp. 139.
[5.11] T. Isono, N. Koizumi, K. Okuno, R. Kurihara, S. Nishio, K. Tobita, Design study of superconducting coils for the fusion DEMO plant at JAERI, Fusion Eng. Design 81 (2006) pp. 1257.
[5.12] W Goldacker et al., J. Phys. Conf. Ser. 43 (2006) pp. 901.
[5.13] T. Isono et al., IEEE Trans. on Appl. Supercond. 13 (2003) pp. 1512.
[5.14] K. Takahata et al., Conceptual design of an indirect-cooled superconducting magnet for the LHD-type fusion reactor FFHR, Fusion Eng. Design 82 (2007) pp. 1487.
[5.15] A. Sagara et al., Carbon tiles as spectral-shifter for long-life liquid blanket in LHD-type reactor FFHR, Fusion Eng. Design 81 (2006) pp. 1299.
[5.16] M. N. Wilson, Superconducting Magnets, (Clarendon Press, Oxford, 1983) pp. 41.
[5.17] K. Shikimachi et al., Journal of Physics: Conference Series 43 (2006) pp. 547.
[5.18] M. N. Wilson, Superconducting Magnets, (Clarendon Press, Oxford, 1983) pp. 162.

[5.19] T. Kiss et al., Critical current properties in HTS tapes, Physica-C 392-396 (2003) pp. 1053.
[5.20] E.W. Collings et al., Design of coupled or uncoupled multifilamentary SSC-Type strands with almost zero retained magnetization at fields near 0.3 T, Adv. Cryo. Eng. 36

(1990) pp. 247.
[5.21] H. Hashizume et al., J. Plasma Fusion Res. Series 5 (2001) pp. 532.

[A.1] J. Bardeen, L. N. Cooper, and J. R. Schrieffer, Theory of Superconductivity, Phys. Rev. 108 (1957) pp. 1175.
[A.2] H.K. Onnes, Commun. Phys. Lab. 12 (1911) pp. 120.
[A.3] W. Meissner and R. Ochsenfeld, Naturwiss. 21 **(**1933) pp**.** 787.
[A.4] Charles Kittel, Introduction to Solid State Physics, 7th Ed., Wiley, (1996).
[A.5] Michel Cyrot, Davor Pavuna, Introduction to Superconductivity and High-T_c Materials, World Scientific, (1992).
[A.6] Yukikazu Iwasa, Case Studies in Superconducting Magnets, Plenum Press, (1994).
[A.7] Thomas P. Sheahen, Introduction to High-Temperature Superconductivity, Plenum Press, (1994).

[B.1] G. K. White, Experimental Techniques in Low Temperature Physics, (Clarendon Press, Oxford, 1979) pp. 58.

[C.1] R. L. Coren, Basic Engineering Electromagnetics, (Printice Hall, Englewood Cliffs, N.J., 1989) pp. 144.

[D.1] O. van der Meer, B. Ten Haken, H.H.J. ten Kate, “A model to describe the angular dependence of the critical current in a Bi-2223/Ag superconducting tape”, Physica C 357-360 (2001) pp. 1174.
[D.2] J. H. Kim et al. “Magnetic field dependence of Y-123 coated conductor and Bi-2223 tape at 4.2 K”, Physica C 426-431 (2005) pp. 1103.
[D.3] K. Takahashi et al. “Investigation of thick PLD-GdBCO and ZrO2 doped GdBCO coated conductors with high critical current on PLD-CeO2 capped IBAD-GZO substrate tapes”, Supercond. Sci. Technol. 19 (2006) pp. 924-929.
[D.4] A. Kinoshita et al. “Development of a thick GdBCO and ZrO2-doped GdBCO film with a high critical current on a PLD-CeO2/IBAD-GZO metal substrate”, Physica C 463-465 (2007) pp. 630-632.